technische universität
dortmund

Silver clusters deposited into polymers, aerogels and ionic liquids studied with X-ray and optical spectroscopy

Dissertation

zur Erlangung des Doktorgrades der Naturwissenschaften der
Fakultät Physik der Technischen Universität Dortmund

vorgelegt von
Dipl. Phys. David Christopher Engemann

Angefertigt am
Lehrstuhl für Experimentelle Physik I
Fakultät Physik
Technische Universität Dortmund

Dortmund, November 2014

Gutachter:

Erstgutachter: apl. Prof. Dr. Heinz Hövel

Zweitgutachter: Prof. Dr. Thomas Weis

Contents

Abstract

Nanoparticles are quoted as a future technology. Especially silver (Ag) nanoparticles exhibit a great potential due to their optical activity and their anti-microbial behaviour. The deposition of clusters (consisting of about 250 Ag atoms) enables the functionalization of the clusters before they are deposited into or onto a substrate. The properties and the potential areas of application for those clusters vary with the kind of the substrate. In the present thesis Ag clusters were deposited into three different substrates by a supersonic nozzle expansion source. These are silica aerogel (SiO2 aerogel), polydimethylsiloxane (PDMS) and the room temperature ionic liquid 1-butyl-3-methylimidazolium hexafluorophosphate (BMIM PF6). Especially the properties of the clusters in the room temperature ionic liquid are of great interest due to the emerging scientific interest in those green solvents. The optical, structural, chemical and electronic properties were investigated using X-ray (X-ray absorption near edge structure, XANES) and optical (UV-Vis) spectroscopy. By plasmon resonance spectroscopy it was found that clusters in PDMS can be used as sensors to detect the presence of toxic H2S. Furthermore their shape in PDMS can be considered as spherical. The deposition of clusters into silica aerogel enables the investigation of high amounts of separated clusters. This is necessary for XANES experiments. These experiments yielded information on the density of unoccupied states of the clusters and showed differences in the 4d band structure between cluster and bulk material. Additionally the electronic structures of clusters partially transformed to Ag2O and Ag2S were investigated. The deposition of clusters into BMIM PF6 enabled the investigation of the fundamental properties of Ag clusters in the ionic liquid without the presence of any chemical additives as used in wet chemistry productions. It was found that the stability of the clusters in the ionic liquid is strongly influenced by the purity of the ionic liquid and its temperature. Moreover the clusters can be fragmented by X-ray radiation which results in a XANES spectrum of micro clusters.

1 Introduction

Nanoparticles are named as a future technology. Nevertheless, applications of nano-materials date back to about 3500 years ago. At the time people in ancient Egypt used metal compounds in molten glass to make the glass coloured [Kreibig and Vollmer, 1995].

However, a qualitative theory which describes the processes which take place when light hits metal nanoparticles, or also called clusters, was given by MIE at the beginning of the last century [Mie, 1908]. With the emergence of various cluster sources, detailed experimental investigations of these particles became possible. Those experiments can be compared with modern computational methods to form working physical models of those systems. One example is the extension of X-ray absorption spectroscopy by so-called FEFF calculations [Rehr and Albers, 2000].

Fundamental research on clusters becomes more and more application-oriented. The goal is to functionalize the clusters to accomplish various functions. The fields of applications of those functionalized clusters can vary from medicine through to the use of clusters in catalytic processes.

HAES et al. reported the possibility to use silver clusters with sizes of the magnitude 100 nm as an assay for Alzheimer's disease [Haes et al., 2004]. One of the most driven fields of research is the effort to use metal NP in cancer therapy [Pissuwan et al., 2006]. Furthermore, the antimicrobial properties of silver can be used for treatment of E. coli bacteria colonies which can trigger diseases in human bodies [Kim et al., 2007].

NOUR et al. used Ag NP/PDMS composites to reduce H_2S from CH_4 and CO_2 gas streams [Nour et al., 2014]. The particular properties of nanostructure materials get use especially for the example of gold. While bulk gold is chemical inactive, gold nanoparticles on a TiO_2 surface can be used for the oxidation of the highly toxic CO to the less toxic CO_2 [Green et al., 2011].

In all applications the clusters have to be in contact with an embedding medium. This could be a solid surface, a matrix or a liquid. In the present thesis Ag clusters were deposited into three kinds of matrix materials. The first one is a polymer (Polydimethylsiloxane), the second is an aerogel (SiO_2 aerogel) and the third a room temperature ionic liquid (1-butyl-3-methylimidazolium hexafluorophosphate). Fundamental and special properties of the Ag clusters were deduced by UV-Vis spectroscopy and X-ray absorption spectroscopy measurements. The focus is on the electronic structure and properties of the Ag clusters.

In the present thesis the **second chapter** contains the necessary theoretical background.

The **first section** describes the structural properties of Ag clusters. Herein especially the geometric and electronic properties are discussed. It will be shown why the structure of a cluster differs from the structure of solid and what kind of structures are expected.

The **second section** deals with the optical and electronic properties of the weakly bound electrons in a cluster. The interaction of light with a dielectric sphere and also a spheroid, is discussed. The fundamental Mie theory will then be specialised to small silver clusters (wavelength $\gg$ cluster diameter) and their optical extinction spectra will be calculated for various configurations (spherical cluster, spheroidal cluster, cluster with shell, cluster in embedding medium).

In the **third section** the properties of the tight bound electrons are discussed. This is connected with the fine structure of the atoms in a cluster and is the basis of the X-ray absorption near edge structure spectroscopy which is also discussed in this section.

In the **third chapter** the experimental implementation is presented.

The **first section** of this chapter deals with the embedding materials Polydimethylsiloxane (PDMS), 1-butyl-3-methylimidazolium hexafluorophosphate (BMIM PF_6) and silica aerogel (SiO_2 aerogel).

The **second section** gives a description of the laboratory setup.

Section three and **four** describe the experimental implementation of the optical and X-ray measurements, respectively.

The **fourth, fifth** and **sixth chapter** are on the experiments on Ag clusters in PDMS, silica aerogel and BMIM PF_6, respectively. Here the experiments will be presented and the results are discussed.

Chapter six summarises the results of the thesis and gives some outlook to future experiments.

2 Theory

2.1 Silver clusters

Silver (Ag) is a transition metal with the atom number 47, an atomic mass of $m_{\mathrm{Ag}} = 107.868\,\mathrm{g/mol}$ and an electronic configuration of $[\mathrm{Kr}]4\mathrm{d}^{10}5\mathrm{s}^{1}$. Therefore, its oxidation numbers are I and II. Under normal conditions it is a solid body with a face-centred cubic (fcc) crystal structure. At a temperature of 1235 K Ag is melting. It is known as a good electric conductor ($15.87\,\mathrm{n\Omega \cdot m}$) and an optical active medium. Nevertheless, the properties of Ag can change dramatically when decreasing the system from a solid with 10^{23} atoms to a cluster with about 10^{2} atoms. For example, the geometric structure of an Ag cluster changes from fcc to icosahedral with decreasing size [de Heer, 1993].

2.1.1 Geometric magic clusters

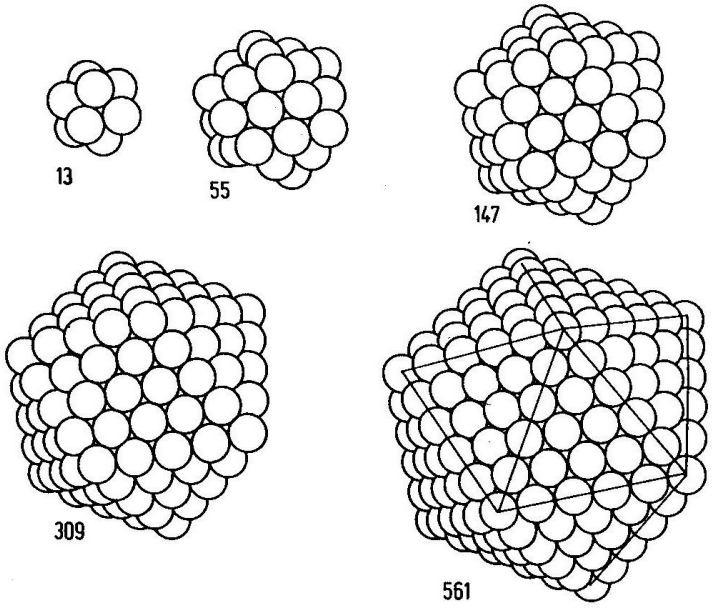

Figure 2.1: Clusters of different sizes and icosahedral geometry [Haberland et al., 2006]. The clusters have a perfect icosahedral symmetry if their geometric shells are closed. Such configurations are also called Mackay icosahedrons [Mackay, 1962], and the number of atoms of a cluster with closed icosahedral shells can be determined by (2.1)

When reducing the size of a bulk system down to molecular scale, clusters of a distinct size are particularly stable if their atoms arrange in special shapes. The so-called Mackay icosahedrons [Mackay, 1962] are geometrically high symmetric bodies which enable energy minimisations for many clusters when their shells are closed. Figure 2.1 shows the closed shell structure of clusters of different sizes. Because of their high stability these clusters are also known as geometric magic clusters.

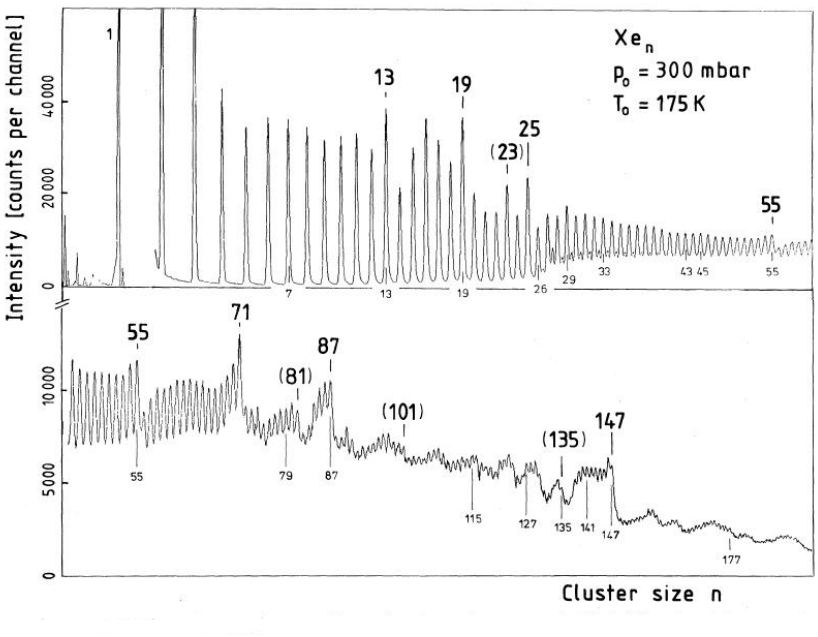

Figure 2.2: The mass spectrum of Xe clusters [Echt et al., 1981] in gas phase exhibits some strong intensities which can be ascribed to the higher stability of clusters with closed icosahedral shells.

These icosahedra were experimentally verified in 1981 by ECHT [Echt et al., 1981] with mass spectroscopy of xenon (Xe) clusters in the gas phase. This is shown in Figure 2.2. The intensity in the mass spectrum decreases abruptly after an icosahedral shell has been filled ($N = 13, 55, 147$). The other strong intensities must be assigned to symmetric shapes which are not discussed here. The number N of atoms for a cluster with k closed icosahedral shells can be calculated by equation (2.1) [Mackay, 1962]

$$N = 1 + \sum_{i=1}^{k} \left(10 \cdot i^2 + 2\right) \ . \tag{2.1}$$

MARTIN et al. [Martin et al., 1991] observed mass selected sodium clusters with geometric closed shell structures like cuboctahedra or icosahedra which especially occur for big clusters consisting of more than 1500 atoms. For clusters with less than 1500 atoms, filled electronic shells dominate the configuration of the clusters (section 2.1.2). Because of their similar electronic configurations, experiments on the mass spectra of sodium clusters yield adequate information on the mass spectra of silver clusters [von Issendorff, 2011].[1]

2.1.2 Electronic magic clusters

While the stability of bigger clusters is dominated by geometric aspects and closed shells of atoms, the stability of smaller metal clusters is dominated by the electronic behaviour of the valence electrons in the clusters. Especially alkali metal clusters exhibit a strong dependence on their electronic configuration. In 1983/1984 KNIGHT et al. performed experiments on mass selected sodium clusters Na_N and observed strong intensities in mass spectra of clusters consisting of $N = 8, 20, 40, 58, 92$ atoms (Figure 2.3).

[1] At this point it should be remarked that the shape of clusters of different composition and size are still a line of current research. This becomes more important when dealing with clusters deposited on surfaces or embedded in matrices.

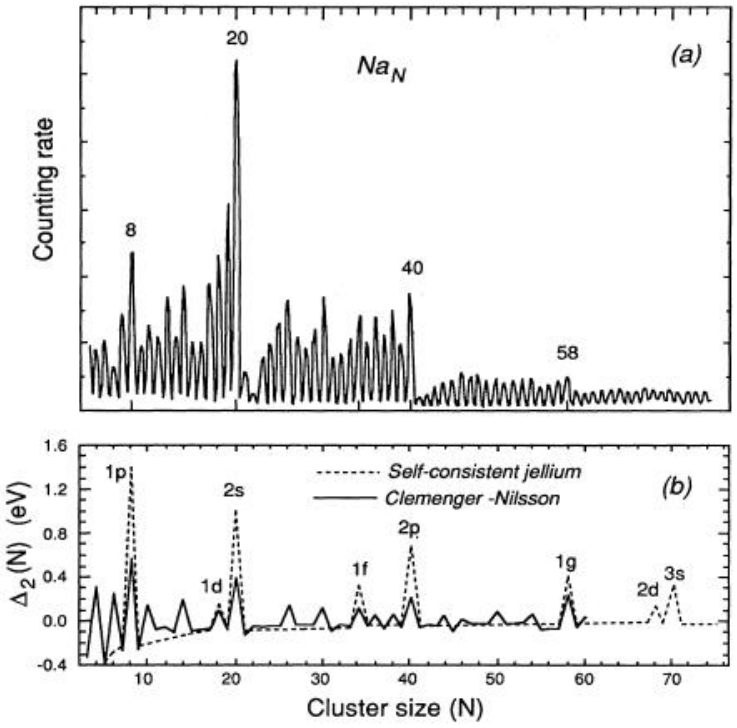

Figure 2.3: (a) Spectrum of mass selected Na_N clusters. The strong intensities correspond to sodium clusters with closed electronic shell configuration in the jellium model. (b) Calculated change of the electronic energy of adjacent clusters. When this calculation predicts a strong change, an electronic shell is filled. The calculations were carried out for clusters in self-consisting jellium model and Clemenger-Nilsson-model [de Heer, 1993].

This can be explained by the so-called jellium model. The jellium model is a simple but effective model for metal clusters. Here the complicated Coulomb potentials of the nucleus cores and the inner electrons of the atoms are replaced by an effective, spherical one-particle potential ρ_0 (Figure 2.4). Thus the valence electrons, which are responsible for molecular or cluster bonding, feel an effective force in the centre of the cluster. This problem can be handled similar to the hydrogen atom which leads to electronic shells of the cluster with main quantum numbers ν, l (Figure 2.5).

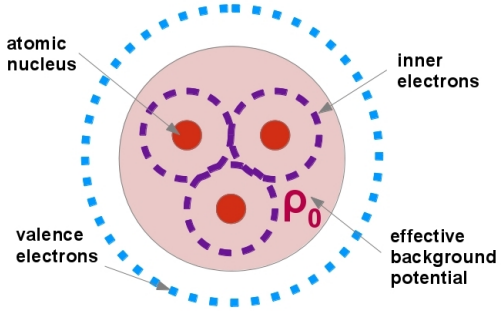

Figure 2.4: In the jellium model, the nucleus core and the inner electrons are replaced by an effective background potential. So the valence electrons only feel an effective potential localised in the centre of the cluster. This model results in a central potential problem similar to the hydrogen atom.

Figure 2.5 illustrates the occupation of the different quantum levels. Depending on the effective potentials the energy and the order of the quantum levels can change. Herein the quantum numbers

should not be mistaken for atomic quantum numbers from the hydrogen atom. It is typical to use the quantum numbers known from nuclear physics due to the strong similarities between clusters and nucleons.

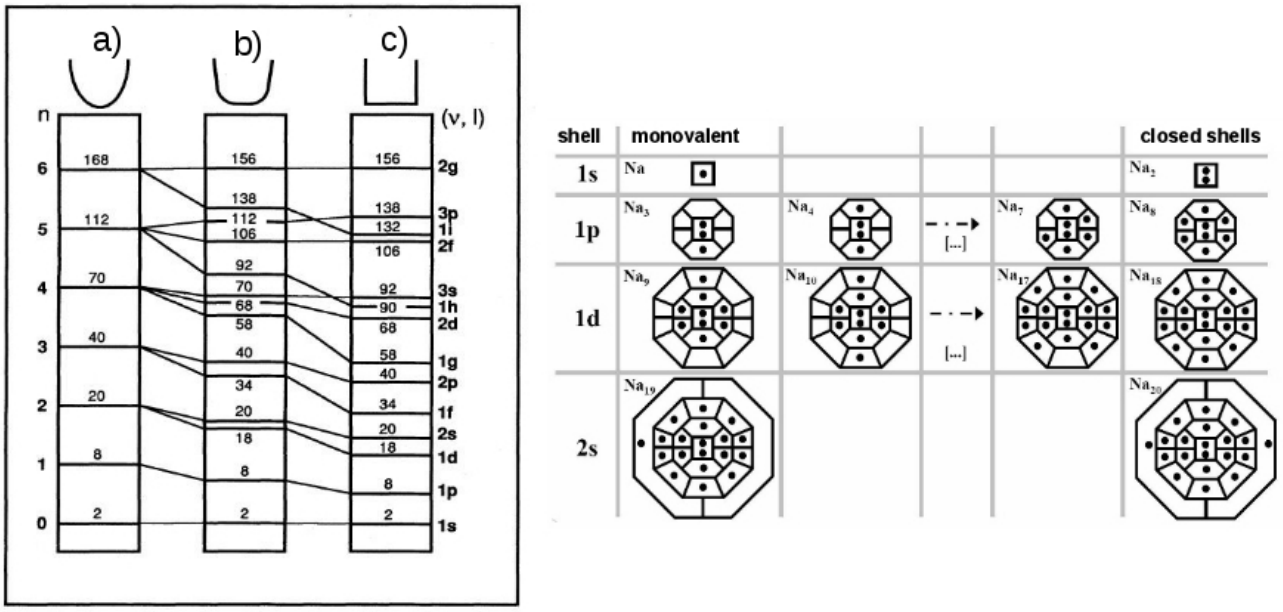

Figure 2.5: Left: First and secondary cluster quantum numbers of the electrons in clusters with different effective single particle potentials: a) harmonic oscillator, c) box potential and b) superposition of a harmonic oscillator and box potential [de Heer, 1993]. Right: The jellium model with a harmonic oscillator potential yields electronic cluster shells similar to the electron orbitals known of the hydrogen atom [Heiz and Schneider, 1999].

While a cluster with closed electronic shells seems to be perfectly spherical, a cluster with one more electron exhibits a distortion. Due to the low potential energy of a cluster with closed electron shells, one more electron will occupy an energetically higher orbital. This energetically higher cluster state degrades the stability of the cluster which manifests in a lower intensity in mass spectrum. When dealing with Na or Ag clusters, every atom contributes one valence electron to the cluster.

Furthermore, the Jahn-Teller-theorem [Jahn and Teller, 1937] implies that a cluster with an open shell lowers its energy by distortion. In 1985 CLEMENGER adapted a formalism from NILSSON [Nilsson, 1955] to describe the distortion of a cluster quantitative. In this Clemenger-Nilsson-model [Clemenger, 1985], the effective potential of the cluster in the jellium model is set to a three-dimensional harmonic oscillator potential with axial distortion and a small inhomogeneity:

$$H = \frac{\vec{p}}{2m} + \frac{1}{2}m\omega_0^2\Omega_\perp^2\left(x^2+y^2\right) + \frac{1}{2}m\omega_0^2\Omega_z^2 - U\hbar\omega_0\left(l^2 - \frac{1}{2}n(n+3)\right) \tag{2.2}$$

$$\Omega_\perp = \left(\frac{2+\delta}{2-\delta}\right)^{1/3} \quad , \quad \Omega_z = \left(\frac{2+\delta}{2-\delta}\right)^{-2/3} .$$

The inhomogeneous l^2 term causes a split of the degeneracy of different angular momentums with the same total oscillator quantum number n. For Na clusters as discussed in the work of CLEMENGER, it is $0.04 < U < 0.08$. ω_0 is the characteristic oscillation frequency of a spherical oscillator ($U = 0, \delta = 0$). δ is the parameter of distortion.
The results of this model are shown in Figure 2.7. The shape of a cluster depending on the number of electrons in an unfilled shell changes from prolate to oblate (Figure 2.7 left).

The value δ, for which the sum of the single particle energies is minimal (N-atom cluster), is assigned to the ground state and plotted in Figure 2.7 right. Variations in the total energy $E(N)$ of a cluster consisting of N atoms can be calculated by

$$\Delta_2(N) = \frac{3}{4}\left((E(N+1) - E(N)) - (E(N) - E(N-1))\right).$$

The intensity of these variations as a function of cluster size is shown in Figure 2.3 b) (solid line). So, intensities in the mass spectrum, which cannot be explained by the simple jellium model, can be explained by the Clemenger-Nilsson-model.

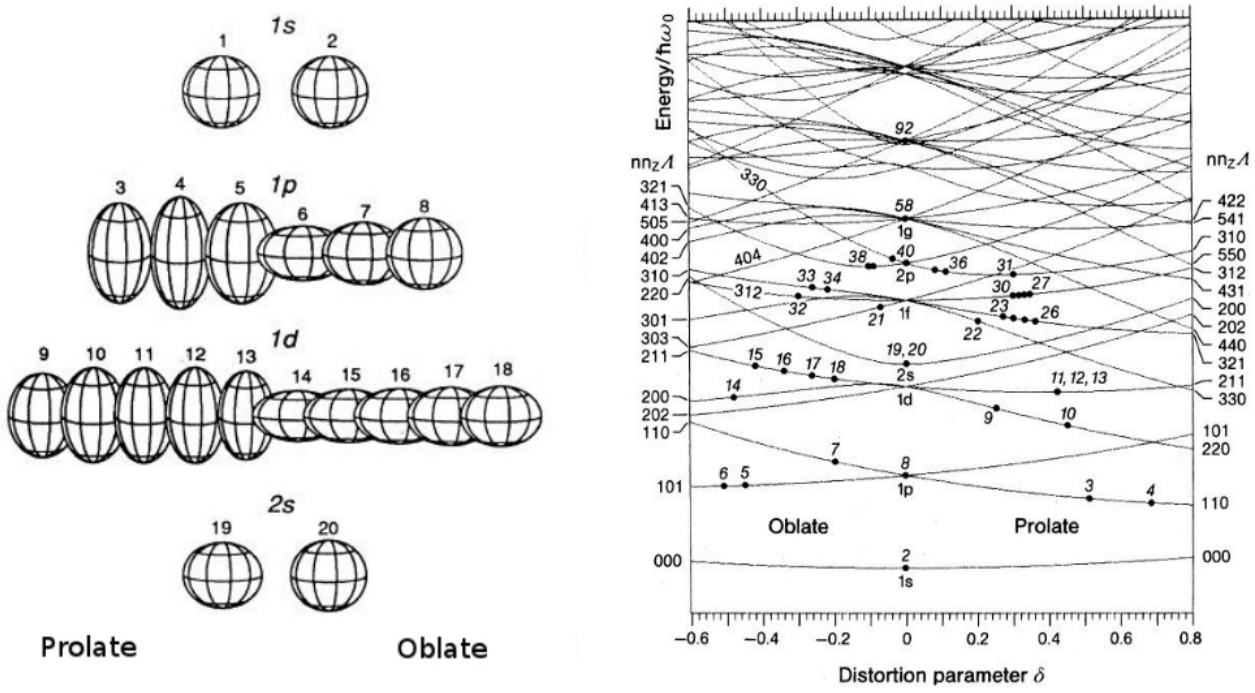

Figure 2.6: The electronic displacement in open shells results in a distortion of the clusters (left) [de Heer, 1993]. This behaviour is known from the molecular physics as Jahn-Teller-theorem. In nuclear physics, this is described by the Nilsson model [Nilsson, 1955] which was adapted by CLEMENGER [Clemenger, 1985] to yield an explanation for the distortion of clusters.

As Ag is similar in electronic configuration to Na, especially in the jellium model where only the valence electrons are of importance, most qualitative considerations of this chapter can be transferred to Ag clusters.

Agglomerated, coalesced and aggregated clusters

Deposited clusters are able to interact with their next neighbours. If the distance between the clusters is as small as the diameter of the clusters, the clusters can agglomerate, coalesce or aggregate. The meaning of these terms in the present thesis is specified below.

Agglomeration is called the forming of various structures, where the single clusters do not change their shape. Coalescence is taking place if the clusters on a surface converge to islands [Grönhagen, 2011]. The shape of a single clusters is not conserved. Aggregation is a process similar to coalescence. However in the present thesis, the term aggregation is used to describe the coalescence process in a liquid. The different terms, coalescence and aggregation, should indicate the different favoured structures on a surface or in a liquid. On a surface coalesced clusters often form islands while in a liquid spherical structures can be preferred, depending on the used liquid [Smetana et al., 2005].

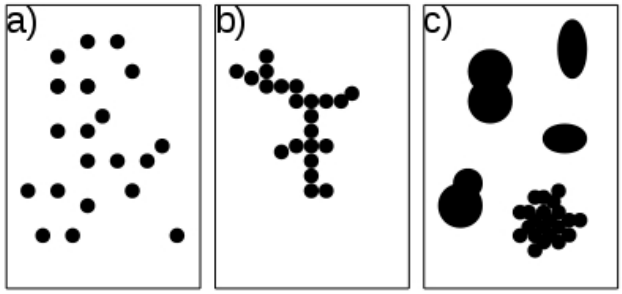

Figure 2.7: Illustration of a) single clusters, b) agglomerated clusters and c) coalesced clusters on a surface.

2.2 Optical properties of Ag clusters

In this section an introduction to the optical properties of Ag clusters should be given. These properties are dominated by quasi free and weakly bound electrons in the clusters and the geometry of the clusters. This section starts with a brief to the Maxwell equations to define the used symbols and formulas. Below SI units are used. Then the Mie theory is introduced and the used approximations and boundary conditions presented. Finally, the equations for the theoretical extinction cross sections of the clusters will be derived and discussed by simulated extinction spectra.

2.2.1 Maxwell equations in matter

The Maxwell equations for an electric $\vec{E}$ and a magnetic $\vec{B}$ field are the fundamental laws of electrodynamic. They describe the behaviour of electromagnetic fields in vacuum and also in matter. Every electromagnetic field has to satisfy the Maxwell equations:

$$\begin{aligned} \nabla \cdot \vec{E} &= \frac{\rho_q}{\epsilon_0} & \nabla \cdot \vec{B} &= 0 \\ \nabla \times \vec{E} &= -\frac{\partial \vec{B}}{\partial t} & \nabla \times \vec{B} &= \mu_0 \vec{J} - \frac{1}{c^2}\frac{\partial \vec{E}}{\partial t} \end{aligned} \tag{2.3}$$

These are the Maxwell equations in vacuum in differential form for time dependent fields. ρ_q is the density of free charges which are the sources of electric fields and $\vec{J} = \varrho^{-1}\vec{E}$ is the electric current of the free charges which is proportional to the electric conductivity ϱ^{-1}. In the presence of matter the equations have to be modified because an external field can generate additional internal fields.

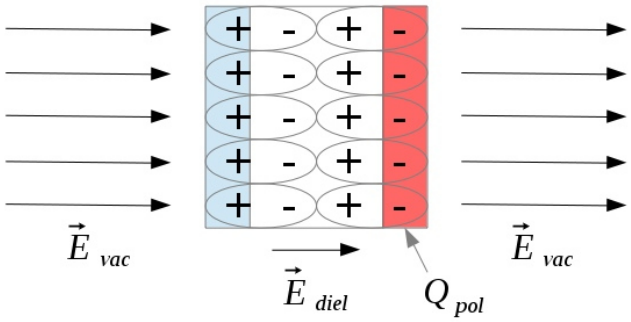

Figure 2.8: The external field E_{vac} causes shifts of the charges in the dielectric medium. In the centre of the medium the charges compensate each other, but at the surface there are net charges. These net charges weaken the external field so that the internal field $\vec{E}_{diel}$ is not as strong as the external one (after [Demtröder, 2013]).

Figure 2.8 illustrates the behaviour of electric fields in matter. The external electric field causes a shift of the charges. While the charges inside the matter compensate each other, there are net charges at the surfaces A of the penetrating and escaping field. The sum of these charges is given by the polarisation charge Q_{pol} [Demtröder, 2013]. The absolute value of the charge per area is called polarisation $P = Q_{pol}/A$. The volume integration of $\nabla \cdot \vec{E}$ in 2.3 using Gauss's theorem yields $E \cdot A = Q/\epsilon_0$, where ϵ_0 is the permittivity of free space. Thus the field inside the medium is

$$\vec{E}_{diel} = \vec{E}_{vac} - \vec{E}_{pol} = \vec{E}_{vac} - \frac{\vec{P}}{\epsilon_0} \ . \tag{2.4}$$

As $\vec{P}$ only depends on the properties of the medium and the electric field inside the medium, it can be explained for weak fields by

$$\vec{P}/\epsilon_0 = \chi \cdot \vec{E}_{diel} \ . \tag{2.5}$$

χ is called dielectric susceptibility and is in general a complex tensor which depends on different variables. With the dielectric function[2]

$$\varepsilon = 1 + \chi \tag{2.6}$$

the dielectric displacement can be defined by

$$\vec{D} = \epsilon_0 \vec{E}_{diel} + \vec{P} = \epsilon_0 \varepsilon \vec{E}_{diel} = \epsilon_0 \vec{E}_{vac}. \tag{2.7}$$

Similar considerations for the magnetisability M of magnetic materials with the permeability $\mu = 1 + \chi_{mag}$ (where χ_{mag} is the magnetic susceptibility) in a magnetic field B lead to

$$\vec{H} = \frac{1}{\mu_0}\vec{B} - \vec{M} = \frac{\vec{B}}{\mu_0 \mu} = \frac{\vec{B}}{\mu_0(1 + \chi_{mag})} \ . \tag{2.8}$$

μ_0 is the vacuum permittivity. The dielectric displacement $\vec{D}$ and the $\vec{H}$ field also satisfy the Maxwell equations [Nolting, 2001]. Thus the fundamental description of electromagnetic fields and waves in matter are given by:

the Maxwell equations in matter,

$$\nabla \cdot \vec{D} = \rho_q \tag{2.9}$$

$$\nabla \cdot \vec{B} = 0 \tag{2.10}$$

$$\nabla \times \vec{E} = -\frac{\partial \vec{B}}{\partial t} \tag{2.11}$$

$$\nabla \times \vec{H} = \vec{J} - \frac{\partial \vec{D}}{\partial t} \tag{2.12}$$

the constitutive medium dependent relations and

$$\vec{J} = \varrho^{-1}\vec{E} \tag{2.13}$$

$$\vec{B} = \mu\mu_0\vec{H} \tag{2.14}$$

$$\vec{P} = \epsilon_0 \chi \vec{E} \tag{2.15}$$

the influence of the polarisation and magnetisation on the fields.

$$\vec{D} = \epsilon_0 \vec{E} + \vec{P} \tag{2.16}$$

$$\vec{H} = \frac{\vec{B}}{\mu_0} - \vec{M} \tag{2.17}$$

In the absence of matter, χ_{diel} and χ_{mag} become zero and the Maxwell equations in matter simplify to the Maxwell equations in vacuum (2.3).

Because of the negligible magnetic effects of the substrates investigated in this thesis, the magnetic properties will not be discussed any further in the following sections. Furthermore, in the energetic range of visible light, the magnetic permeability of silver is $\mu = 1$.

[2] $\varepsilon = \epsilon/\epsilon_0$ is mostly called relative dielectric function.

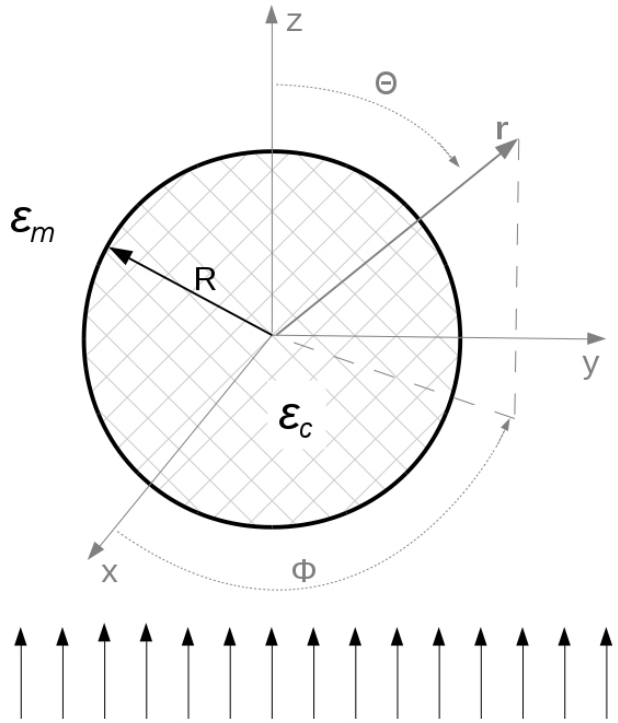

Figure 2.9: Sphere in embedding media with a uniform electric field.

2.2.2 Mie theory

In this section a short introduction into the Mie theory should be given. The theory is a short summary of the presentation by BOHREN and HUFFMAN [Bohren and Huffman, 2004]. The theory of MIE [Mie, 1908] deals with the scattering of light on small particles. To describe the problem of light scattered at a small spherical particle, it is a good access to start with an electromagnetic wave in vacuum. For this, the Maxwell equations of time harmonic fields are

$$\begin{aligned} \vec{\nabla} \cdot \vec{E} &= 0 & \vec{\nabla} \cdot \vec{H} &= 0 \\ \vec{\nabla} \times \vec{E} &= i\omega\mu\mu_0\vec{H} & \vec{\nabla} \times \vec{H} &= -i\omega\varepsilon\epsilon_0\vec{E}\ . \end{aligned} \tag{2.18}$$

In this case, with $k = \frac{\omega}{c}$, the electromagnetic field has to satisfy the wave equations

$$\vec{\nabla}^2\vec{E} + k^2\vec{E} = 0 \qquad \vec{\nabla}^2\vec{H} + k^2\vec{H} = 0\ . \tag{2.19}$$

These equations can be solved by the vector fields $\vec{M}$ and $\vec{N}$

$$\vec{M} = \vec{\nabla} \times (\vec{c}\psi) \qquad \vec{N} = \frac{\vec{\nabla} \times \vec{M}}{k} \tag{2.20}$$

where ψ is a scalar function, $\vec{c}$ a constant vector and $\vec{M}$ and $\vec{N}$ satisfy

$$\vec{\nabla} \times \vec{N} = k\vec{M}\ . \tag{2.21}$$

These fields enable a compact solution of the Maxwell equations. Because of the spherical problem, the vector-wave-equations are written in spherical coordinates. The vector fields will be inserted in the spherical vector-wave-equation. This yields a partial differential equation which will be solved by a separation approach $\psi(r, \theta, \phi) = \xi(r)\Theta(\theta)\Phi(\phi)$. The function $\Phi(\phi)$, with $0 \leq \phi \leq 2\pi$, is solved by $\sin(m\phi)$ and $\cos(m\phi)$ with eigenvalues m. The $\Theta(\theta)$ function, with $0 \leq \theta \leq \pi$ is solved by the Legendre

polynomials $P_n^m(cos\theta)$. The solutions for $\xi(r)$ are the spherical Bessel functions $j_n(kr)$ and $y_n(kr)$[3] and also the combinations of these functions $h_n^{(1)}(kr) = j_n(kr) + iy_n(kr)$ and $h_n^{(2)}(kr) = j_n(kr) - iy_n(kr)$, the Hankel functions. Thus, the generating function ψ of the vector fields $\vec{M}$ and $\vec{N}$ in spherical coordinates is given by the even (e) and odd (o) functions

$$\begin{aligned}\psi_{emn} &= \cos m\phi P_n^m(\cos\theta) z_n(kr) \ , \\ \psi_{omn} &= \sin m\phi P_n^m(\cos\theta) z_n(kr) \ ,\end{aligned} \tag{2.22}$$

where $z_n(kr)$ is any of the Bessel functions $j_n,\ y_n,\ h_n^{(1)},\ h_n^{(2)}$. The vector fields $\vec{M}_{emn}$, $\vec{M}_{omn}$, $\vec{N}_{emn}$ and $\vec{N}_{omn}$ follow by insertion of (2.22) in (2.20) and are given in [Bohren and Huffman, 2004]. With these generating functions, a plane wave can be constructed in spherical coordinates by building a superposition of the resulting vector fields.

The problem of the interaction of an electromagnetic wave with a spherical particle leads to three waves for the electric and three waves for the magnetic components: the impinging waves $\vec{E}_i$ and $\vec{H}_i$, the scattered waves $\vec{E}_{sc}$ and $\vec{H}_{sc}$ and the waves inside the cluster $\vec{E}_c$ and $\vec{H}_c$. The requirement that the tangential components of the E and H fields are continuous at the boundary of the particle lead to the boundary conditions

$$(\vec{E}_i + \vec{E}_{sc} - \vec{E}_c) \times \vec{e}_r = 0 = (\vec{H}_i + \vec{H}_{sc} - \vec{H}_c) \times \vec{e}_r \ . \tag{2.23}$$

The indices i, sc and c mark the incident fields, the scattered fields and the fields inside the particle, respectively. $\vec{e}_r$ is the radial unit vector. This yields with $E_n = i^n E_0(2n+1)/n(n+1)$

$$\vec{E}_c = \sum_{n=1}^{\infty} E_n \left(c_n \vec{M}_{o1n}^{(1)} - i d_n \vec{N}_{e1n}^{(1)} \right) \qquad \vec{H}_c = \frac{-k_c}{\omega \mu_c} \sum_{n=1}^{\infty} E_n \left(d_n \vec{M}_{e1n}^{(1)} - i c_n \vec{N}_{o1n}^{(1)} \right) \tag{2.24}$$

$$\vec{E}_s = \sum_{n=1}^{\infty} E_n \left(i a_n \vec{N}_{e1n}^{(3)} - b_n \vec{M}_{o1n}^{(3)} \right) \qquad \vec{H}_s = \frac{k}{\omega \mu} \sum_{n=1}^{\infty} E_n \left(i b_n \vec{N}_{o1n}^{(3)} + a_n \vec{M}_{e1n}^{(3)} \right) \ , \tag{2.25}$$

where a_n, b_n, c_n and d_n are the coefficients which have to be determined so that (2.23) is satisfied. The subscript (1) indicates that the generating scalar function ψ (2.22) is specified by j_n. Analogically the subscript (3) indicates that ψ (2.22) is specified by $h_n^{(1)}$. The electric and magnetic fields are then sums of spherical harmonics where every n is corresponding to an electromagnetic normal mode, $\vec{M}_n$ and $\vec{N}_n$. The coefficients for every n result from the boundary conditions (2.23) at the position $r = R$, the boundary of the particle.

The scattering cross section σ_{sca} and the extinction cross section σ_{ext} of the particle illuminated by an x-polarised wave are then given by

$$\sigma_{sca} = \frac{W_s}{I_i} = \frac{2\pi}{k^2} \sum_{n=1}^{\infty} (2n+1)(|a_n|^2 + |b_n|^2) \tag{2.26}$$

$$\sigma_{ext} = \frac{W_{ext}}{I_i} = \frac{2\pi}{k^2} \sum_{n=1}^{\infty} (2n+1) \Re\{a_n + b_n\} \ . \tag{2.27}$$

I_i is the incident irradiance and W is the rate at which energy is absorbed or scattered by the particle and calculated by a surface integral $-\int_A \vec{S} \cdot \vec{e}_r dA$ of the pointing vector $\vec{S}$ where $\vec{e}_r$ is the surface normal vector.

[3] y diverges for small arguments

2.2.3 Small spherical particles

In the case of a particle with a diameter $2R$ small compared to the wavelength λ, say $2R \ll \lambda$, the particle only feels an electric field with time varying intensity[4] and the problem becomes easier. The associated scattering problem is known as Rayleigh scattering. As a consequence the spherical Bessel functions expressed as power series are cancelled after the first terms. In the case of $|m|x \ll 1$, i. e. a particle small compared with the wavelength, it is $b_1 \ll a_1$ and

$$a_1 = -\frac{i2x^3}{3}\frac{m^2-1}{m^2+2} \ . \tag{2.28}$$

The arguments x and m are identified as the dimensionless size parameter and the relative wave vector k_c/k ($\sim$ relative refraction index $\tilde{N}_c/\tilde{N}$), respectively:

$$x = kR = \frac{2\pi\tilde{N}R}{\lambda} \quad , \quad m = \frac{k_c}{k} = \frac{\tilde{N}_c}{\tilde{N}} \tag{2.29}$$

Herein N is the refraction index outside in N_c inside the particle. With these approximations the extinction efficiency $Q_{ext} = \sigma_{ext}/\pi R^2 = Q_{abs} + Q_{sca}$ of a particle with the effective surface perpendicular to the incident beam πR^2 and the cross section σ_{ext} is dominated by the absorption efficiency and becomes

$$\begin{aligned} Q_{ext} &= Q_{abs} + Q_{sca} \\ &= 4x\Im\left\{\frac{m^2-1}{m^2+2}\right\} \propto \omega \ . \end{aligned} \tag{2.30}$$

In (2.30), it was assumed that $|m|x \ll 1$ and $(4x^3)\Im\left\{(m^2-1)/(m^2+2)\right\} \ll 1$.[5] Instead of Rayleigh scattering which increases with the fourth degree of frequency ω^4 the absorption in Rayleigh approximation is just proportional to the frequency ω.

This equation yields a correlation between the cross sections and the dielectric function, because

$$\varepsilon_1 = \tilde{n}^2 - \tilde{k}^2 \qquad \varepsilon_2 = 2\tilde{n}\tilde{k} \tag{2.31}$$

$$\tilde{n} = \sqrt{\frac{\sqrt{\varepsilon_1^2+\varepsilon_2^2}+\varepsilon_1}{2}} \qquad \tilde{k} = \sqrt{\frac{\sqrt{\varepsilon_1^2+\varepsilon_2^2}-\varepsilon_1}{2}} \ . \tag{2.32}$$

The complex dielectric function is given by $\varepsilon = \varepsilon_1 + i\varepsilon_2$ and the complex refractive index by $\tilde{N} = \tilde{n} + i\tilde{k}$. The clusters investigated in this thesis have a mean diameter of about $2R = 2\,\text{nm}$ thus the Rayleigh approximation is valid for investigations with light in the visible and also deep UV range. Thus the extinction cross section and the extinction efficiency of a particle surrounded by a medium with the dielectric function ε_m are give by

$$Q_{ext} = 4kR\Im\left\{\frac{\varepsilon-\varepsilon_m}{\varepsilon+2\varepsilon_m}\right\} \tag{2.33}$$

$$\sigma_{ext} = 4\pi kR^3\Im\left\{\frac{\varepsilon-\varepsilon_m}{\varepsilon+2\varepsilon_m}\right\} \ . \tag{2.34}$$

Electrostatic approximation

The polarisability $\vec{p} = \alpha\vec{E}_{diel}$ of a dielectric, spherical and microscopic particle in an electrical field can be calculated by the assumption of molecular dipoles in the particle and a surface charge density at the

[4] The magnetic forces are neglected when not explicitly mentioned.
[5] For more details find [Bohren and Huffman, 2004] chapter 5.1

surface of the particle. This electrostatic approximation ($2R \ll \lambda$) yields a simple formula [Nolting, 2001] which links the molecular polarisability α to the macroscopic dielectric function ε

$$\alpha = \frac{3\epsilon_0}{N_{osc}} \left(\frac{\varepsilon - 1}{\varepsilon + 2} \right) \overset{\substack{n_{osc}=1 \\ V=V_\circ}}{=} 4\pi R^3 \epsilon_0 \left(\frac{\varepsilon - 1}{\varepsilon + 2} \right) \ . \tag{2.35}$$

Herein the number of molecules n_{osc} per volume V is given by $N_{osc} = n_{osc}/V$. In the case of one ($n_{osc} = 1$) spherical ($V_\circ = 4/3\pi R^3$) particle, which is embedded in a medium with the dielectric function ε_m, equation (2.35) becomes [Bohren and Huffman, 2004]

$$\alpha = 4\pi R^3 \left(\frac{\varepsilon - \varepsilon_m}{\varepsilon + 2\varepsilon_m} \right) \ . \tag{2.36}$$

The comparison of (2.34) and (2.36) yields a simple connection between the absorption / extinction cross section and the molecular polarisability. The explanation results from the electrostatic approximation: The assumption of a particle which is small compared with the wavelength of the incident light is corresponding to an electric field which is constant over the volume of the particle. This is the electrostatic approximation which is sometimes also called quasistatic approximation because (2.36) is also valid for time dependent fields, if the frequency is sufficiently small which corresponds to a large wavelength $\lambda \propto \frac{1}{f}$. In such a case, $\vec{p}$ is given by oscillating dipoles (section 2.3.1).

For a complex dielectric function of the particle $\varepsilon = \varepsilon_1 + i\varepsilon_2$ and a real dielectric function of the surrounding medium[6] ε_m, the absorption / extinction cross section becomes

$$\begin{aligned} \sigma_{ext} &= 4\pi k R^3 \Im \left\{ \frac{\varepsilon - \varepsilon_m}{\varepsilon + 2\varepsilon_m} \right\} \\ &= k \cdot \Im\alpha \qquad (2.37) \\ &= \underbrace{4\pi k R^3 \cdot 3}_{9V_0\sqrt{\varepsilon_m}\frac{\omega}{c}} \frac{\varepsilon_2 \varepsilon_m}{(\varepsilon_1 + 2\varepsilon_m)^2 + \varepsilon_2^2} \\ &= 9V_0 \frac{\omega}{c} \varepsilon_m^{\frac{3}{2}} \frac{\varepsilon_2}{(\varepsilon_1 + 2\varepsilon_m)^2 + \varepsilon_2^2} \qquad (2.38) \end{aligned}$$

This is the same result as shown in equation (2.34) by the approximation of

$$|m|x \ll 1 \text{ and } (4x^3)\Im\left\{(m^2-1)/(m^2+2)\right\} \ll 1$$

in Mie theory.

2.2.4 Ellipsoidal particle

The problem of scattering and absorption by an ellipsoidal particle can be handled similarly to the problem of light scattering and absorption by a sphere (section 2.2.2). For this, the scalar wave equation has to be solved in ellipsoidal coordinates. The vector potential functions $\vec{M}$ and $\vec{N}$ can then be derived by the solutions of the scalar potential functions ψ by using (2.20). The resulting electromagnetic fields are superimpositions of these vector fields [Quinten, 2010].

In the Rayleigh approximation, the molecular polarisabilities α_i along the three axes a, b, c[7], corresponding to the indices $i = \{1, 2, 3\}$, is given by

$$\alpha_i = \frac{4}{3}\pi abc \frac{\varepsilon - \varepsilon_m}{\varepsilon_m + L_i(\varepsilon - \varepsilon_m)} \ , \tag{2.39}$$

[6] In Mie theory the dielectric function of the embedding medium has to be real or it should only have a small negligible imaginary part. A strong imaginary part would cause a damping of the electromagnetic wave and the assumption of a free plane wave would not be valid anymore.

[7] Henceforth the radius of a spherical particle is given by R while the semi axes of a spheroid are given by a, b, c.

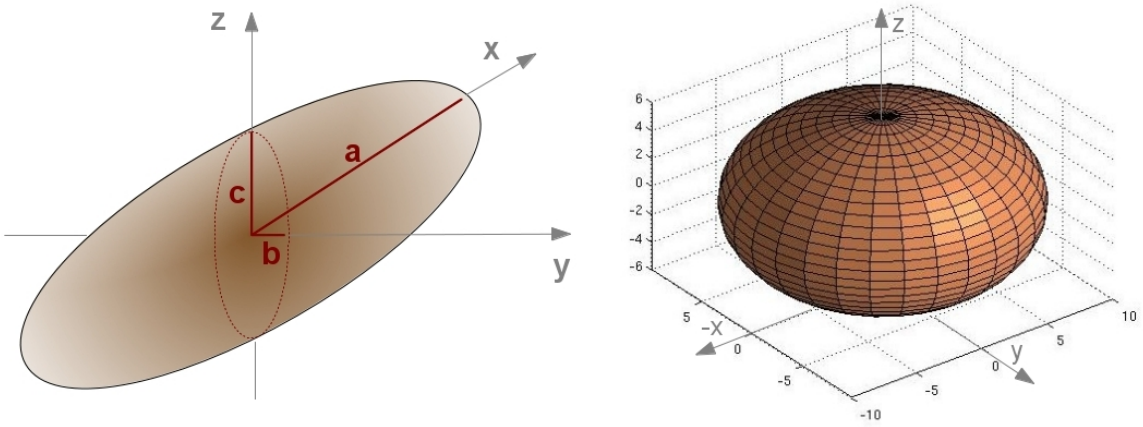

Figure 2.10: Schematic figure of an ellipsoid with three different semi axes $b < c < a$ (left). An ellipsoid with two equal semi major axes $a = b$ and smaller semi minor axis $c = 0.6a$ is plotted in the right figure.

where the geometry factors L_i are connected by $L_1 + L_2 + L_3 = 1$. For deposited and embedded clusters, it is only required to consider oblate spheroids[8] (Figure 2.10 (right)).
In this special case of oblate spheroids ($a = b$), the geometry factors are

$$L_1 = L_2 = \frac{g(e)}{2e^2}\left(\frac{\pi}{2} - \tan^{-1} g(e)\right) - \frac{g^2(e)}{2} \tag{2.40}$$
$$g(e) = \left(\frac{1-e^2}{e^2}\right)^{\frac{1}{2}} \;,\; e^2 = 1 - \frac{c^2}{a^2}$$
$$L_3 = 1 - L_1 - L_2 = 1 - 2L_1 \;.$$

Because of the lower symmetry of a spheroid compared to a sphere, the dipole moment $\vec{p}$, and consequently the extinction cross section σ_{ext}, depends on the orientation of the particle to the incident light. This can be explained by the linear expression

$$\vec{p} = \varepsilon_m \underline{\alpha} \vec{E}_0 \tag{2.41}$$

where $\underline{\alpha}$ becomes a three-dimensional matrix.

By choosing an appropriate setup, the resulting effective polarisability is a linear combination of the polarisabilities along the three axes and depends on the polarisation of the incident light and the orientation of the particle

$$\alpha_{eff} = a_1\alpha_1 + a_2\alpha_2 + a_3\alpha_3 \;. \tag{2.42}$$

The setup often enables the excitation of only two of the three axes. Then it is $a_3 = 0$ and the coefficients a_1 and a_2 follow by trigonometric functions (see Figure 2.19).

2.2.5 Coated particles

The properties of clusters can be tuned by different functionalization procedures. One of these is the stabilisation of clusters in liquid solutions by the formation of ligands. The clusters with complex ligands form a core-shell system which also changes the optical properties of the clusters.

[8] Ellipsoids with two equal axis are called spheroids.

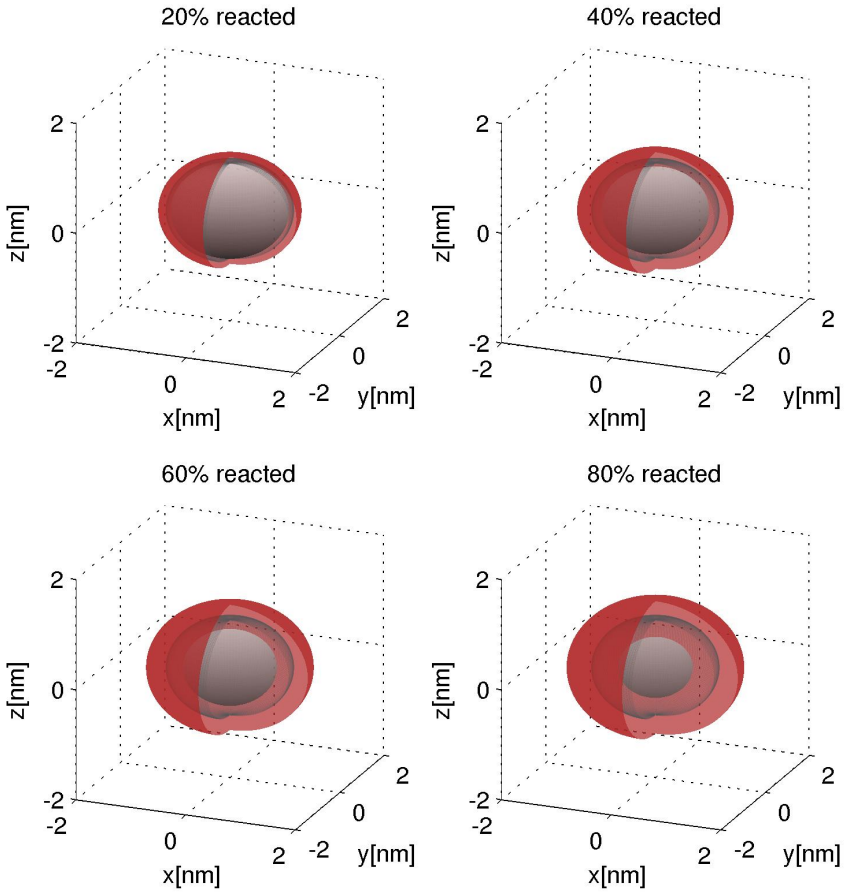

Figure 2.11: Schematic illustration of a spheroidal cluster ($c/a = 0.8$) during a chemical reaction with oxide. The grey spheroid in the centre represents the Ag core and the red one the Ag_2O shell. The transparent grey shell represents the original cluster (with the same volume as a spherical cluster with 2 nm diameter).

An analogue behaviour can be observed after chemical reactions like sulfidation of silver clusters where the outer atoms form a chemical bonding with sulphur atoms. The properties of the resulting (silver) core- (silver sulfide) shell clusters differ from those of pure silver clusters. This problem is handled by introducing a third dielectric function ε_s, which describes the response of the shell material to an applied electromagnetic field. The new boundary conditions with respect to the geometric structure yield an analytical expression for the polarisability.

The dipole moment along the axis j of a spheroidal cluster with a spheroidal shell in an electromagnetic field parallel to the axis j is determined by the polarisability along this axis

$$\alpha_j = V_0 \frac{\left((\varepsilon_s - \varepsilon_m)\left(\varepsilon_s + (\varepsilon_c - \varepsilon_s)\left(L_j^{(c)} - fL_j^{(s)}\right)\right) + f\varepsilon_s(\varepsilon_c - \varepsilon_s)\right)}{\left(\left(\varepsilon_s + (\varepsilon_c - \varepsilon_s)\left(L_j^{(c)} - fL_j^{(s)}\right)\right)\left(\varepsilon_m + (\varepsilon_s - \varepsilon_m)L_j^{(s)}\right) + fL_j^{(s)}\varepsilon_s(\varepsilon_c - \varepsilon_s)\right)} . \tag{2.43}$$

$V_0 = \frac{4}{3}\pi a_{tot} b_{tot} c_{tot}$ is the total volume of the particle and $f = \frac{a_c b_c c_c}{a_{tot} b_{tot} c_{tot}}$ the volume fraction of the inner core on the total volume. The geometrical factors L_j^c of the core and L_j^s of the shell along the j direction are given for a spheroid with $a = b > c$ by equation (2.40).

This equation describes clusters with ligand shells and also with shells formed by chemical reactions. In the last case it has to be mentioned that the volume of the cluster can change during the reaction because of the different densities of the educt and the product material. Thus, at reactions like

oxidation and sulfidation, the volume of the whole cluster increases with increasing reaction state while the volume of the core decreases with increasing reaction state and is zero for a fully reacted cluster. This is illustrated in Figure 2.11 for a spheroidal cluster with an axial ratio of $c/a = 0.8$ and in Figure 2.13 for a spherical cluster. These clusters have the initial volume of a spherical cluster with a diameter of $2R = 2\,\mathrm{nm}$. The simulations were performed for the reaction $4\mathrm{Ag} + \mathrm{O_2} \rightarrow 2\mathrm{Ag_2O}$. Because of approximately the same densities ($\rho_{Ag_2O} = 7.14\,\mathrm{g/cm^3}$, $\rho_{Ag_2S} = 7.23\,\mathrm{g/cm^3}$) and molar masses ($m_{mol,\ Ag_2O} = 231.74\,\mathrm{g/mol}$, $m_{mol,\ Ag_2S} = 247.80\,\mathrm{g/mol}$) of $\mathrm{Ag_2O}$ and $\mathrm{Ag_2S}$, nearly the same changes in volume are expected for a sulfidation of silver clusters. The grey sphere or spheroid in the centre represents the core of the cluster while the red one represents the $\mathrm{Ag_2O}$ shell. The transparent grey shell illustrates the former pure cluster surface.

Figure 2.12 (left) illustrates the changes of the main axis a of a spheroid and the radius R of a sphere depending on the reaction state. The parameters a_{shell} and R_{shell} correspond to the thickness of the shells. These simulations were performed for oxide as the reactant. The total main axis a_{total} and radius R_{total} are the sum of the main axis or the radius of the core and thus the main axis or radius of the originated core-shell cluster.

Figure 2.12 (right) illustrates the volume fractions of the core and the shell ($\mathrm{Ag_2O}$) on the original volume of the unreacted cluster and on the volume of the whole core-shell cluster. The behaviour for a spherical shape is the same like that for a spheroidal shape. It is remarkable, that after 25 % of the original cluster mass is oxidised the volume of the shell on the total core-shell cluster volume is increased to about 50 %.

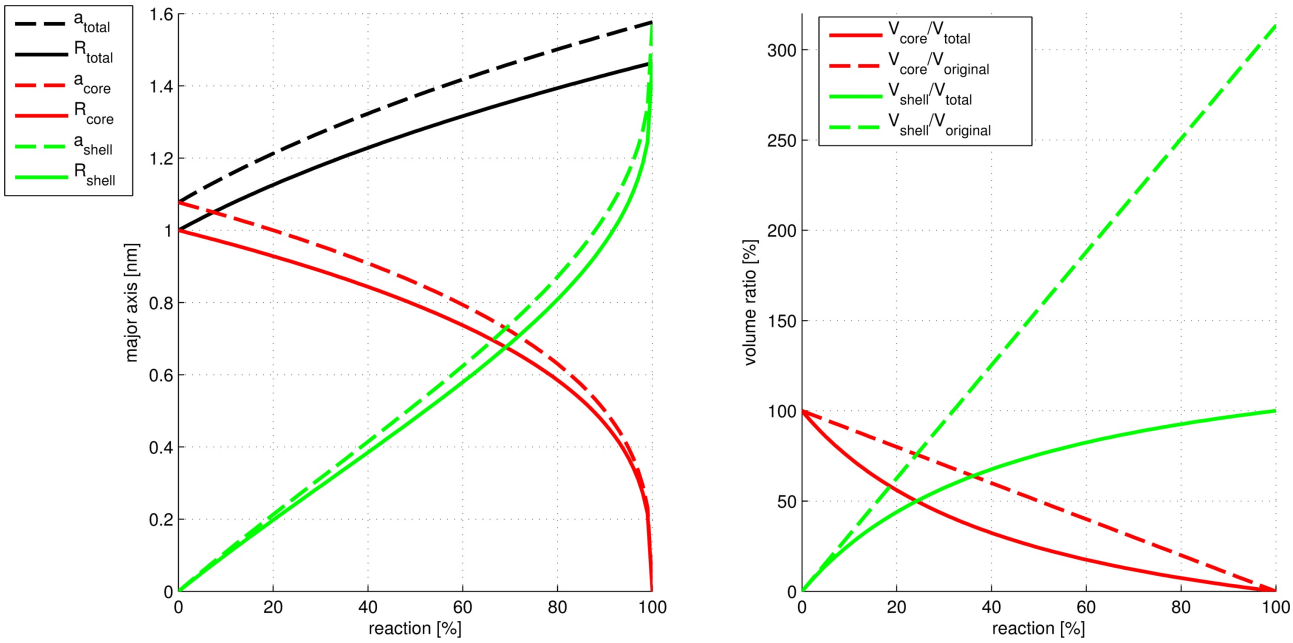

Figure 2.12: Changes of the main axes (dashed lines) and the radii (solid lines) of a spheroidal ($c/a = 0.8$) and spherical cluster in dependence on the reaction state of an oxidation (left). Dependence of the volume amount of the core and the shell of an oxidised cluster on the whole volume (right). The initial volume was the same like that of a spherical cluster with a diameter of 2 nm.

It should be noticed that these considerations are only approximations. The structure of a cluster normally differs from that of bulk material. So the densities of Ag, $\mathrm{Ag_2O}$ and $\mathrm{Ag_2S}$ can vary a bit from those given above.

Coated sphere

In the special case of a coated sphere, the high symmetry of the particle simplifies the problem and makes it independent from the polarisation of the incident light. The geometrical factors are then given by $L_j^{(a)} = L_j^{(b)} = L_j^{(c)} = \frac{1}{3}$ and the polarisabilities $\alpha_1 = \alpha_2 = \alpha_3 = \alpha$ can be determined by

$$\alpha = V_0 \frac{(\varepsilon_s - \varepsilon_m)(\varepsilon_c + 2\varepsilon_s) + f(\varepsilon_c - \varepsilon_s)(\varepsilon_m + 2\varepsilon_s)}{(\varepsilon_s + 2\varepsilon_m)(\varepsilon_c + 2\varepsilon_s) + f(2\varepsilon_s - 2\varepsilon_m)(\varepsilon_c - \varepsilon_s)} \,. \tag{2.44}$$

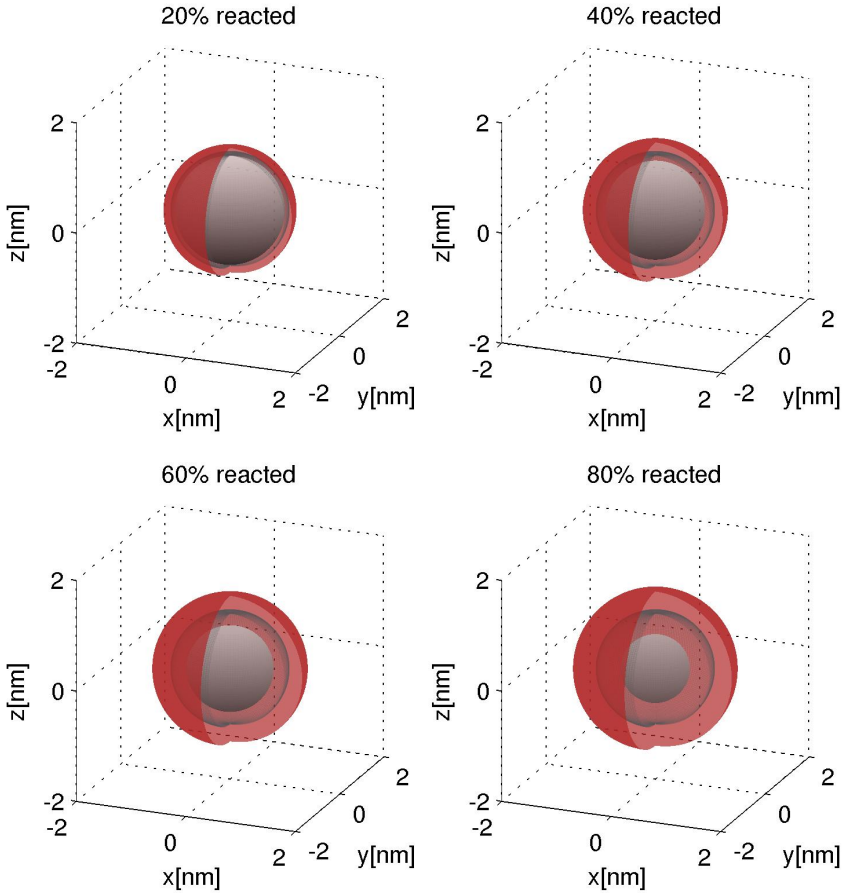

Figure 2.13: Schematic illustration of a spherical cluster ($2R = 2\,\mathrm{nm}$) during a chemical reaction with oxide. The grey spheroid in the centre represents the Ag core and the red one the Ag_2O shell. The transparent grey shell represents the original cluster.

2.3 Electronic properties of weakly bound electrons in Ag clusters

In the previous section the scattering and excitation of spherical and spheroidal particles which are small compared with the wavelength of an impinging electromagnetic field was discussed. As a result, the extinction cross section was given by several equations, only depending on the optical properties of the particle, its shell and the embedding material. For the interaction of light in the visible and UV range, these functions are determined by the properties of the free and weakly bound electrons of the cluster atoms.

2.3.1 Lorentz model

A first approach to the behaviour of electrons in an atom, that respond to an electromagnetic field, can be given by the classical motion equation $m\ddot{\vec{x}} + b\dot{\vec{x}} + K\vec{x} = e\vec{E}$, where m is the mass of a single electron, b a damping constant and K a spring constant. This system corresponds to a bound electron excited by an external force $e\vec{E}$. The solution of this problem is given by

$$\begin{aligned}\vec{x} &= \frac{\frac{e}{m}\vec{E}}{\omega_0^2 - \omega^2 - i\gamma_0\omega} \\ &= \frac{e}{m}\vec{E}\cdot\left(\frac{\omega_0^2-\omega^2}{\left(\omega_0^2-\omega^2\right)^2+\left(\gamma_0\omega\right)^2} + i\frac{\gamma_0\omega}{\left(\omega_0^2-\omega^2\right)^2+\left(\gamma_0\omega\right)^2}\right)\end{aligned} \tag{2.45}$$

with the resonance frequency $\omega_0^2 = K/m$ and the damping constant $\gamma_0 = b/m$. A number of N_{osc} oscillators per unit volume and the dipole $\vec{p} = e\vec{x}$ yield a polarisation of $\vec{P} = N_{osc}\vec{p} = N_{osc}\cdot e\vec{x}$. This leads in connection with equation (2.15) to the susceptibility of an ensemble of independent, bound electrons with the same frequency dependency.[9] ω_0 is the frequency where the amplitude of $\vec{x}$ in (2.45) is maximal for small damping. The dielectric function is then given by

$$\varepsilon_1^{Lorentz} = 1 + \frac{\omega_p^2\left(\omega_0^2-\omega^2\right)}{\left(\omega_0^2-\omega^2\right)^2+\left(\gamma_0\omega\right)^2} \tag{2.46}$$

$$\varepsilon_2^{Lorentz} = \frac{\omega_p^2\gamma_0\omega}{\left(\omega_0^2-\omega^2\right)^2+\left(\gamma_0\omega\right)^2}\ . \tag{2.47}$$

Herein $\omega_p^2 = N_{osc}e^2/m$ is the plasma frequency, which indicates the point where $\varepsilon_1 \approx 0$ in a system where ε only depends on the influences of free electrons i. e. with $\omega_0 = 0$.

2.3.2 Drude model

In solid crystals like metals, semiconductors and some insulators the large number of electrons form a quasi continuum of energy states. These so-called bands follow an energetic order. The energetically highest band with an energy E_c is called conduction band followed by the energetically next highest band, the valence band E_v (Figure 2.14). In the of an insulator, the valance band is completely filled

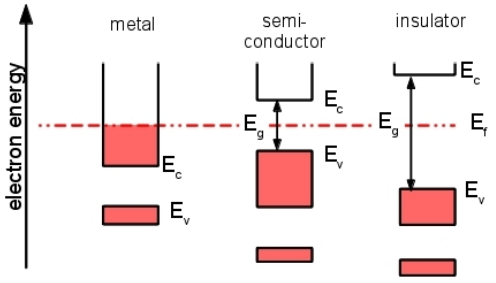

Figure 2.14: Schematic illustration of the energetic levels of conduction and valence band in a metal, a semiconductor and an insulator. In the case of a metal, the Fermi level is energetically located in the conduction band, while in the case of a semiconductor or an insulator the Fermi level is in a gap between the valence and the conduction band.

while the conduction band is completely empty. These states are separated by a band gap E_g. If

[9] This one-oscillator model could be extended to a multiple-oscillator model by replacing ω_0, ω_p and γ of the N_{osc} oscillators with the single resonance and plasma frequencies ω_{0j}, ω_{pj} and γ_j of the jth electron and a summation $\sum_j$ over all electrons.

the Fermi energy E_f is located in this gap, the electrons will not be able to flow when applying an electric field because they cannot reach any unoccupied states. If the band gap decreases, the electrons can be excited from the valance band to the conduction band for example by an impinging photon. Such systems are known as semiconductors. Conductors and metals are denoted by a partially filled conduction band. In this case the Fermi energy is located in the conduction band $E_f \geq E_c$ and the electrons can flow by switching in an unoccupied state in the same band. These electrons are often called quasi free with respect to their possibility to move in the material. Their interaction with the lattice of the crystal is considered by an effective mass of the electrons in the band [Kittel, 1999].

As a result the behaviour of electrons in a solid is not completely described by the Lorentz model, but also has to consider the amount of the quasi free electrons and the possibility of interband transitions.

The physical model to describe these quasi free electrons is the Drude model and, in this case, is a consequence of the Lorentz model when the spring constant is set to be zero $K = 0$ and the mass of the electrons is replaced by the effective mass m_{eff}. The following dielectric function in the Drude model is given by

$$\varepsilon_1^{Drude} = 1 - \frac{\omega_p^2}{\omega^2 + \gamma_0^2} \qquad \varepsilon_2^{Drude} = \frac{\omega_p^2 \gamma_0}{\omega\left(\omega^2 + \gamma_0^2\right)} \ . \tag{2.48}$$

In the case of metals at room temperature and electromagnetic waves in the visible range up to the ultraviolet range, γ is much smaller than ω_p. Thus (2.48) becomes

$$\varepsilon_1^{Drude} \approx 1 - \frac{\omega_p^2}{\omega^2} \qquad \varepsilon_2^{Drude} \approx \frac{\omega_p^2 \gamma_0}{\omega^3} \ . \tag{2.49}$$

The so-called Drude parameters of silver are given by [Kreibig and Fragstein, C. V., 1969, Ehrenreich and Philipp, 1962]:

n	$5.9 \cdot 10^{28} m^{-3}$
m_{eff}	$\approx m_e$
$\hbar\omega_p$	9.08 eV
$\hbar\gamma_0$	0.018 eV

2.3.3 Dielectric function of silver

Silver is a well-conducting metal and can so be described by the Drude model. However, the Drude model does not consider interband transitions of electrons from one occupied band to a higher unoccupied band, in the case of Ag from 4d band to 5sp band. This effect leads to an additional term, the interband susceptibility χ^{inter}, in the dielectric function

$$\varepsilon = 1 + \chi^{Drude}(\omega) + \chi^{inter}(\omega) \ , \tag{2.50}$$

where $1 + \chi^{Drude}(\omega) = \varepsilon^{Drude}(\omega) = \varepsilon_1^{Drude}(\omega) + i\varepsilon_2^{Drude}(\omega)$ is given by (2.48). This interband term can be considered by a real constant of about 2.5 for small energies. For higher energies ($\gtrsim 3\,\mathrm{eV}$), it has to be considered by a complex frequency depending function. The real and imaginary parts of the dielectric function of bulk like silver [Johnson and Christy, 1972] are plotted in Figure 2.15 in comparison with die dielectric function of quasi free electrons calculated by equation (2.48) with the parameters for silver. These transitions from one band to an energetically higher band are permitted for

$$\hbar\omega = E_i(\vec{k}) - E_f(\vec{k}) \tag{2.51}$$

where $\hbar\omega$ is the energy of an exciting photon, E_i and E_f the energy of the initial and the final state and $\vec{k}$ the wave vector in the first Brillouin zone. While the conservation of energy (2.51) is a necessary

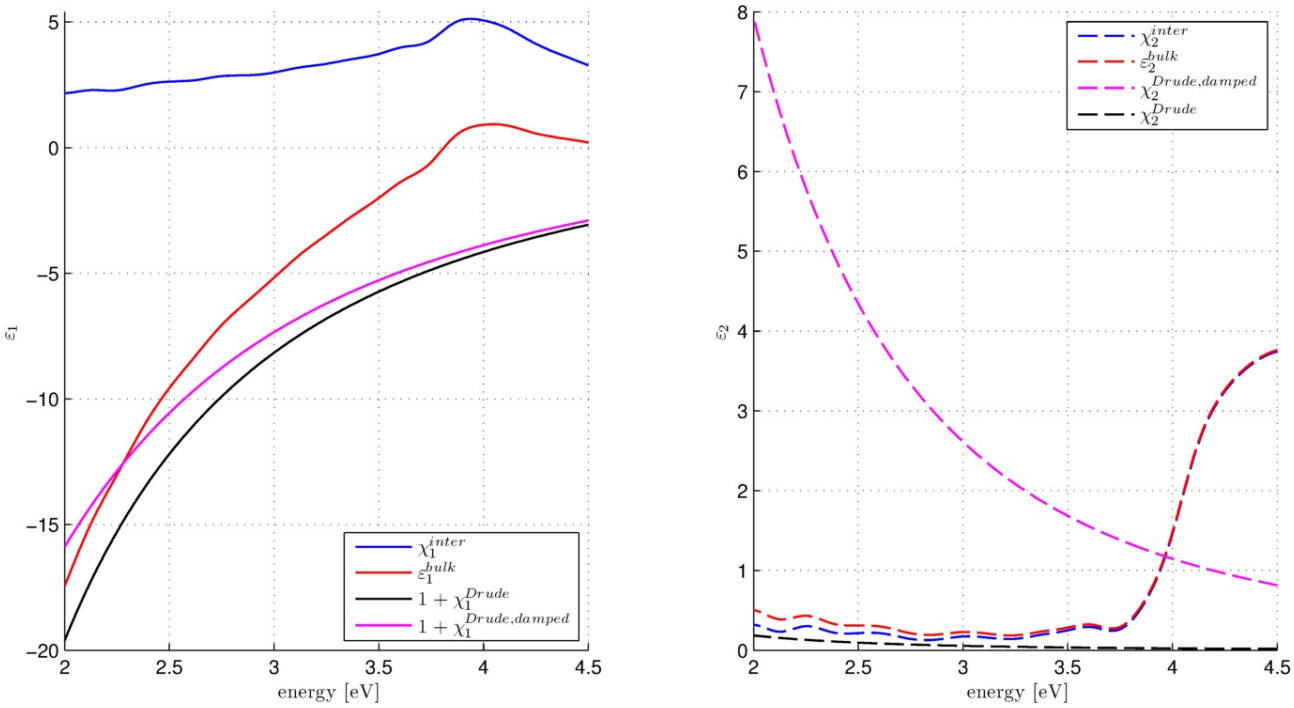

Figure 2.15: The real and imaginary parts of various parts of dielectric functions are plotted in the left and the right figure, respectively. The red lines exhibit the dielectric function of bulk silver after JOHNSON and CHRISTY [Johnson and Christy, 1972]. The dielectric function of quasi free electrons after Drude $1+\chi^{Drude}$, calculated by (2.48), are represented by the black lines. The interband amount follows by $\varepsilon^{bulk} - (1 + \chi^{Drude})$ (blue line). The magenta lines exhibit a Drude dielectric function with additional surface damping $\gamma_0 \to \gamma_0 + \gamma_{surface}$ ($A = 1$, see section 2.3.4).

criterion, the probability of a transition is maximal for points in the Brillouin zone where bands in $\vec{k}$-space are parallel

$$\vec{\nabla}_{\vec{k}} \left(E_i(\vec{k}) - E_f(\vec{k}) \right) = 0 \; . \tag{2.52}$$

These critical points cause singularities in the density of states like the ones known from the Van Hove singularities of crystal phonons [Kittel, 1999]. As a result, the absorption and so the imaginary part of the interband susceptibility $\chi_2(\omega)$ becomes maximally.

The strong influence of the interband susceptibility becomes clear when analysing the energetic position of the plasmon excitation resonance. A resonance of the excitation is found where the extinction cross section (2.38) becomes maximal. This is fulfilled for

$$\varepsilon_1 \approx -2\varepsilon_m \tag{2.53}$$

if ε_2 is not too big and does not vary strongly. Thus the resonance energy of a small silver particle, described by Drude model in vacuum $\varepsilon_m = 1$, is where the black line in Figure 2.15 cuts $\varepsilon_1 = -2$ which is given at $\hbar\omega \approx 5.2\,\mathrm{eV}$. However, the contribution of the interband susceptibility raises the real part of the Drude dielectric function to higher values, so $\varepsilon_1 = -2$ is fulfilled at $\hbar\omega = 3.5\,\mathrm{eV}$. Also the energetic position of the so-called plasma frequency, the frequency where $\varepsilon_1 = 0$, shifts from about $\omega = 9.2\,\mathrm{eV}/\hbar$ to $\omega = 3.8\,\mathrm{eV}/\hbar$ [Quinten, 2010].

2.3.4 Dielectric function of Ag clusters

While the dielectric function of bulk like silver is well known, the dielectric function of small silver particles differs with the size of the particles due to plasmon damping effects at the surface of the particles. The restriction of the mean free path of the electrons in the clusters can be considered by an additional damping constant $\gamma_{surface}$ which is added to the damping constant γ_0 in the Drude or Lorentz model:

$$\gamma = \gamma_0 + \gamma_{surface} = \frac{1}{\tau_\infty} + \frac{1}{\tau_{surface}} = \frac{v_F}{l_\infty} + A \cdot \frac{v_F}{R} \tag{2.54}$$

Herein is $v_F = 1.4 \cdot 10^6\,\mathrm{m/s}$ the Fermi velocity and l_∞ the mean free path of electrons in bulk silver ($l_\infty = 52\,\mathrm{nm}$ for silver at room temperature [Hövel, 1995,Ehrenreich and Philipp, 1962]). The fraction v_F/l_∞ describes a mean collision frequency so that every time τ_∞ an electron in a silver bulk collides with an impact partner. The corresponding damping parameter $\gamma_{surface}$ describes the frequency of the impact processes between the electrons and the surface. A is a dimensionless constant with a magnitude of 1 and is strongly influenced by the cluster-environment interface. The dielectric function can now be calculated by using the dielectric function of a silver bulk, subtracting the Drude dielectric function for silver bulk and adding a modified Drude dielectric function with the damping parameter $\gamma = \gamma_0 + \gamma_{surface}$ [Kreibig and Fragstein, C. V., 1969]:

$$\varepsilon(\omega, R) = \varepsilon^{bulk}(\omega) - \frac{(-\omega_p^2)}{\omega^2 + i\omega\gamma_0} + \frac{(-\omega_p^2)}{\omega^2 + i\omega\left(\gamma_0 + A\frac{v_F}{R}\right)}\,. \tag{2.55}$$

The results of this equation for clusters with different sizes are plotted in Figure 2.16. Figure 2.16

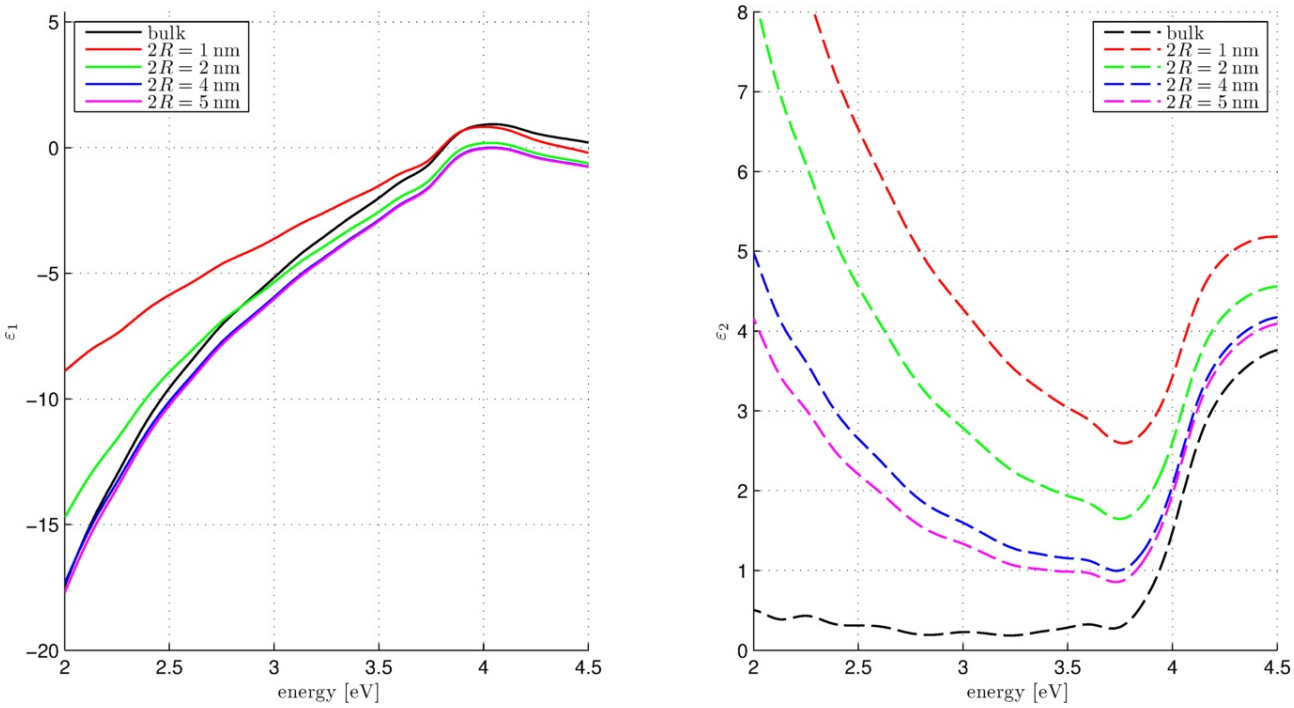

Figure 2.16: The real and the imaginary part of the dielectric function of a silver cluster with the surface damping constant $A = 1$ of sizes from $2R = 1\,\mathrm{nm}$ up to $2R = 5\,\mathrm{nm}$ were calculated by equation (2.55).

illustrates the dependence in size for the real and imaginary part of the dielectric function of Ag clusters with diameters between 1 nm and 5 nm. The size effect is given by the $1/R$ character of the surface damping constant. Corresponding to equations (2.49) for small damping constants, the

influence of γ is marginal for ε_1 for clusters with diameters bigger than 2 nm[10], but still has a strong effect on ε_2.

2.3.5 Plasmon resonance of Ag clusters

The optical extinction of clusters, which are small compared with the wavelength, is also known as the plasmon resonance because here approximately the whole energy, which is absorbed by the particle, is converted to oscillations of the free electrons in the cluster. The easiest case is the absorption by a homogeneous sphere as described by equation (2.38). For a cluster with defined size and dielectric function, the shape and position of the extinction are still depending on the dielectric function on the embedding or surrounding material ε_m. In the case of surrounding material, whose imaginary part of ε_m is negligible and does not vary much, the resonance is localised where it is $\varepsilon_1 \approx -2\varepsilon_m$. The refraction index and therefore the dielectric function for a non absorbing medium is bigger than 1. The plasmon resonance is localised where $\varepsilon_m > -2$ (Figure 2.16). In this region the dielectric function of the cluster is a monotonous increasing function so that the energetic position of the plasmon resonance shifts to lower energies with increasing ε_m.

This behaviour is illustrated in Figure 2.17 for Ag clusters with a diameter of $2R = 2$ nm in vacuum and in fused silica. The dielectric function of vacuum is constantly 1. Thus the resonance is where the green line in Figure 2.16 is $\varepsilon = -2\varepsilon_m = -2$, which is fulfilled for $E \approx 3.5$ eV. The dielectric function of fused silica can be calculated by the Sellmeier equation, an empirical equation which describes the wavelength dependent behaviour of n^2 for optical transparent media, and which is approximately 2.2. So the resonance for Ag cluster in silica is expected where $\varepsilon_1 \approx -4.4$ and thus $E \approx 3.1$ eV.

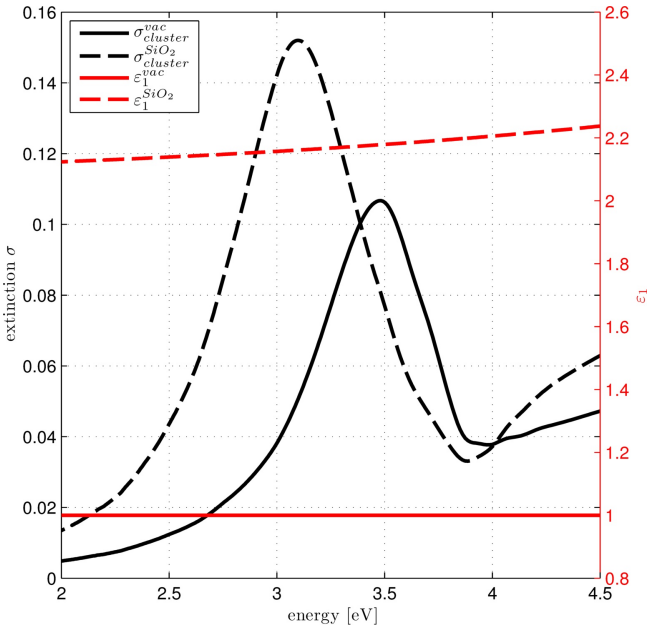

Figure 2.17: Extinction of Ag clusters with a diameter of $2R = 1$ nm in vacuum and fused silica with real dielectric functions ε_1^{vac} and $\varepsilon_1^{SiO_2}$ respectively. $\varepsilon_1^{SiO_2}$ was calculated by the Sellmeier equation and the imaginary parts of the dielectric functions are zero. The resonance positions are at $\varepsilon_1 \approx -2\varepsilon_m$ which is $\varepsilon_1 \approx -2$ for clusters in vacuum and $\varepsilon_1 \approx -4.4$ for clusters in fused silica. From this it can be followed that the energetic position of the extinction maxima is ≈ 3.5 eV for clusters in vacuum and ≈ 3.1 eV for clusters in fused silica (compared to Figure 2.16).

To summarise the previous sections, the optical extinctions of Ag clusters of different sizes, shapes and compositions in vacuum are plotted in Figure 2.18 and should be discussed in detail now. All extinctions are normalised to the corresponding geometric cross section $A_\perp = \pi s^2$ ($s^2 = R_{total}^2$ for a sphere, $s^2 = a_{total} \cdot c_{total}$ for a spheroid). Vacuum was chosen as embedding medium and the surface damping constant is $A = 1$.

In Figure 2.18 a) the extinctions of a single Ag cluster with varying diameters between $2R = 1$ nm and $2R = 5$ nm are plotted. For clusters with diameters $2R = 5$ nm, the dipole approximation 2.38 is fulfilled, for bigger clusters a correction would be necessary. The extinction increases with increasing

[10] For very small clusters $2R < 1$ nm the surface damping $1/R \cdot (Av_F)$ and thus γ becomes dominant and the approximation (2.49) of small damping is no longer valid.

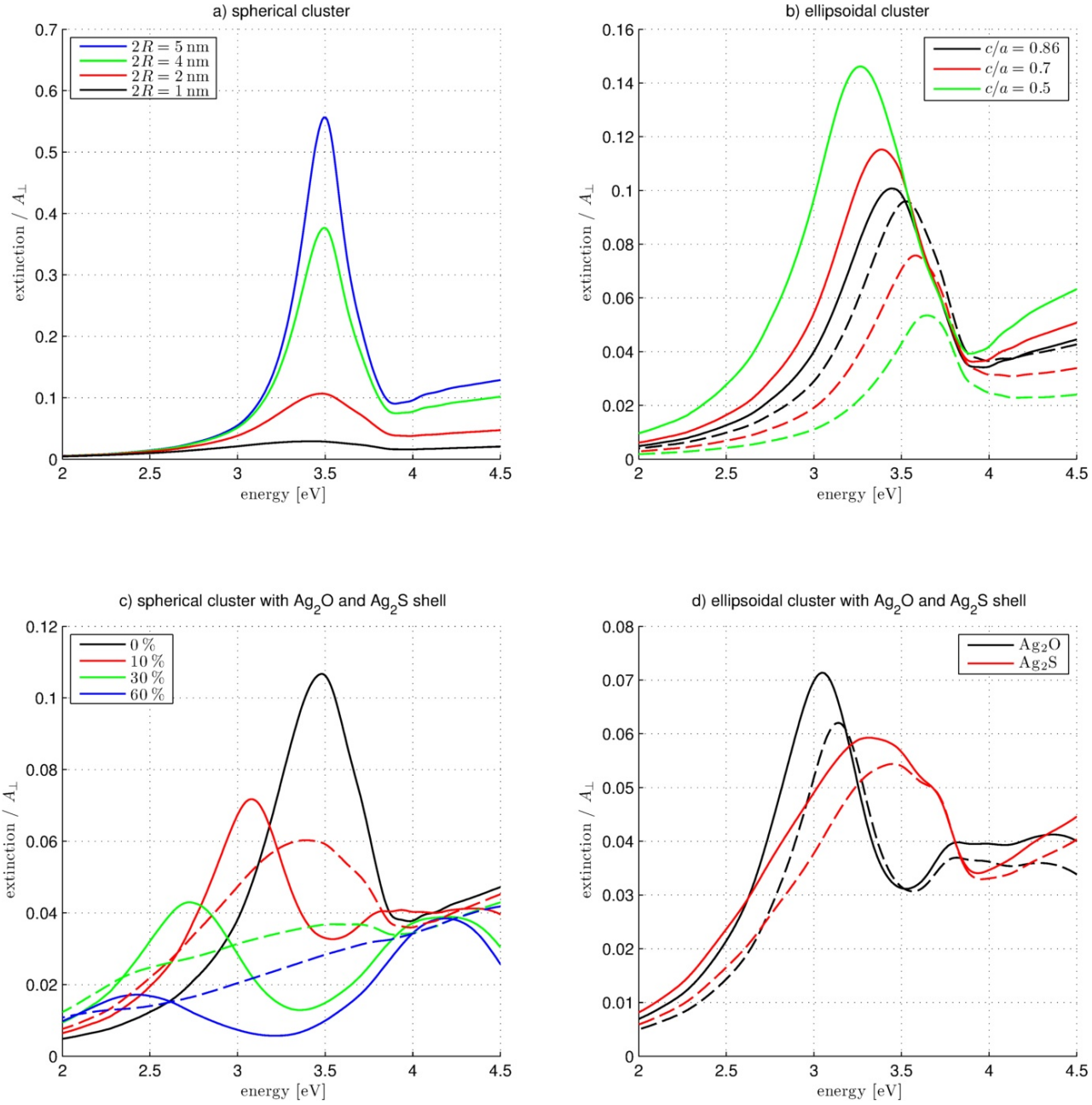

Figure 2.18: a) Spherical cluster in vacuum with different diameters. b) Spheroidal cluster with different axial ratios. The volume of the cluster is equivalent to the volume of a sphere with a diameter of 2 nm. The solid lines represent the extinction of s-polarised light and the dashed lines the extinction of p-polarised light. c) Spherical cluster with an original diameter of 2 nm with shells which were formed after 0 %, 10 %, 30 % and 60 % of the cluster were reacted with sulphur or oxygen. The solid lines represent a cluster with Ag_2O shells and the dashed lines a cluster with Ag_2S shells. d) Combined effects on the extinction of a cluster with the same volume like a cluster with a diameter of 2 nm. The axial ratios were chosen to 0.86. The reaction progress (with S or O) is 10 %. The solid lines represent measurements with s-polarised light and the dashed lines measurements with p-polarised light. All extinction spectra were normalised to the geometric cross section (see text) and simulated for clusters in vacuum $\varepsilon_m = 1$ with $A = 1$.

size of the cluster proportional to R^3 (see (2.38))[11]. The only visible effect is a small shift of the maximum of the extinctions to lower energies for decreasing cluster sizes caused by the dielectric function for Ag clusters (Figure 2.16). Here the resonance condition is fulfilled at lower energies for smaller clusters. Much stronger than the position of the maximum, the full width at half maximum (FWHM) of the extinction changes with the cluster size. The FWHM is determined by the double width between the peak and the position where the low energetic flank has half the intensity of the maximum. This definition is used for all following FWHM determinations. For a small cluster, the FWHM of the extinction is larger than for a large cluster. This is a consequence of the surface damping constant $\gamma_{surface}$. Thus the shape of the extinction spectrum of a large cluster with the diameter $2R_{large}$ can be modified to have the same shape of the spectrum of a small cluster with the diameter $2R_{small}$ by varying A_{large} so that $A_{large}R_{large} = A_{small}R_{small} = const.$ For more detailed discussion about surface damping effects and the FWHM of the cluster extinction spectrum is given in [Hövel, 1995].

Figure 2.18 b) exhibits the extinctions of a spheroidal cluster with the axes $a = b$ and $c < a$. To clarify the effect of the cluster distortion, the extinctions were calculated for impinging s- and p-polarised light. The distortion is given by the axial ratios $c/a = \{0.75; 0.5; 0.25\}$. The lengths of the axes were calculated so that for a given axial ratio the volume of the cluster should be the same like that of a spherical cluster with the diameter $2R = 2\,\mathrm{nm}$. The dielectric function of a cluster with surface damping constant A was also calculated in the way, that the dielectric function of the spheroid corresponds to that of a sphere with the same volume. The setup of this simulation is shown in Figure 2.19. The plane of incidence is given by the $yz-$ plane and the angle between the surface normal of the cluster (dashed line) and the y axis should be $\varphi = 90\,°$. In this system a is along the x axis, b along the y and c along the z axis. The light is polarised and its propagation direction is parallel to the y axis. So the points in the propagation vector represent the s-polarised mode and the strokes the p-polarised mode (solid and dashed lines in Figure 2.18 b) respectively). The plasmon resonance in p-polarisation is shifted to higher energies due to the shorter resonance axis. The plasmon resonance in s-polarisation in contrast is shifted to lower energies. These effects increase with decreasing axial ratio c/a. As explained in Figure 2.18 a) the height of the cluster plasmon resonance increases with increasing electron oscillation axis. In experiments where $\varphi < 90\,°$ the measured cluster extinction spectrum of the p-polarised light also excites parts of the b axis and so contains parts of the s-polarised extinction.

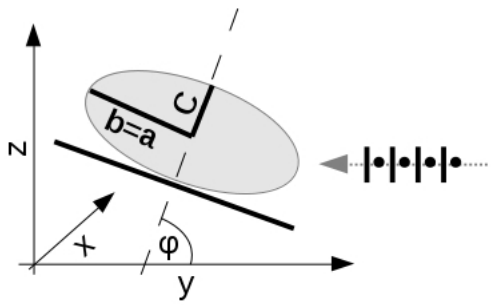

Figure 2.19: Setup for the simulation and experiments with polarised light at distorted clusters. The light propagates along the y axis (grey arrow) in the yz plane and is s-polarised (black dots) or p-polarised (black lines). The surface normal (dotted line) and the y axis comprise an angle of φ.

The changes of extinction spectra of a chemical reacted (with sulphur or oxygen) spherical Ag cluster are plotted in Figure 2.18 c). At a reaction of the Ag cluster with a gas like S or O, the Ag atoms in the outer shells become Ag_2S or Ag_2O. The amount of these shells on the whole cluster is given by the reaction state P which means that the relative mass $P = m_{reacted}/m_{original}$ of the original cluster reacted with the gas. The mass of the core after the reaction is given by $m_{core} = (1 - P)m_{core}$. As

[11] The approximately linear behaviour here is a consequence of the normalisation of the cluster extinction to the geometric cross section.

a consequence the extinction spectrum changes due to the lower radius R_{core} of the core cluster. In contrast the total volume becomes larger because of the lower density of the Ag_2S or Ag_2O shells with an additional thickness d_{shell} (see Figure 2.13).

The solid black line exhibits again the extinction spectrum an Ag cluster with a diameter of $2R = 2\,\text{nm}$. The coloured solid and dashed lines represent the extinction spectra of the cluster reacted with Ag_2O and Ag_2S respectively. Three points can be figured out by these spectra: 1) The shells cause a damping of the plasmon resonance indicated by the decrease of the heights of the extinction maxima with increasing P. Further, the FWHM of the resonance increases with increasing P, which is also an indication for an increasing damping effect. 2) The energetic positions of the extinction spectra shift to lower energies with increasing P. 3) The magnitude of these effects caused by an oxidation differs from that caused by a sulfidation. Therefore, the energetic shift of the extinction maximum cannot be explained alone by a size effect. The change of the core surrounding medium dominates this shift effect. Furthermore, these shifts are very distinct for an oxidation. In Ag clusters with a diameter of $2R = 2\,\text{nm}$ about 50 % of the atoms are surface atoms. So the forming of one Ag_2O shell in this model would correlate with an extinction shift of about 1 eV. In contrast, the same amount of Ag_2S would damp the plasmon resonance so strongly that a plasmon would not be observed anymore. Actually, a 30 % sulfidised Ag cluster has a hardly measurable optical extinction.

The dielectric functions of Ag_2S and Ag_2O bulk were used to describe the influence of the cluster shells. In contrast to Ag bulk, they are no metals and their optical properties are not determined by the mean free path of the electrons. So a modification of the dielectric function, as it was done in (2.55), was not applied here. Furthermore, band structure effects are responsible for the optical properties. Experiments have shown that bulk properties like surface states or band structures remain at low size scales of a few nm [Barke and Hövel, 2003]. The properties of Ag clusters with Ag_2S and Ag_2O shells described by using $\varepsilon_s = \varepsilon^{bulk}_{Ag_2O}$ and $\varepsilon_s = \varepsilon^{bulk}_{Ag_2S}$ yield good agreements with experimental observations.

The combination of the previous discussed effects is shown in Figure 2.18 d). Here the extinction spectra of a 10 % reacted (with oxygen and sulphur) and distorted $c/a = 0.86$[12] Ag cluster are plotted. These spectra differ clearly from that of an idealised spherical cluster without shells in vacuum represented in Figure 2.18 a). The chemical reaction causes a strong shift to lower energies in the case of oxygen. The energetic shift in the case of a reaction with sulphur is small. The widening of the plasmon is dominated by the influence of the dielectric function of the shell.

Effective medium

The previously discussed spectra were simulated for clusters in vacuum $\varepsilon_m = 1$. However, in some matrices, the deposited clusters are not homogeneously surrounded by the matrix material $1 \leq \varepsilon^{eff}_m \leq \varepsilon_m$. This problem can be handled by a first step effective medium approximation

$$\varepsilon^{eff}_m = p\varepsilon^{sub}_m + (1-p)\varepsilon^{env}_m \tag{2.56}$$

where ε^{sub}_m and ε^{env}_m are the dielectric functions of the substrate and the gaseous (or vacuum) environment respectively. p determines the ratio of the cluster surface which is in contact with the substrate or the gaseous (or vacuum) environment.

Furthermore, a complex and frequency-depending dielectric function of the embedding matrix material ε_m would make the system more complicated but it could still be describe analytically [Quinten, 2010].

[12] While depositing clusters on surfaces with the thermal cluster apparatus used in this work, a distortion of $c/a \approx 0.86$ is assumed [Hövel, 1995].

2.3.6 Measurand extinction

In (2.27) the extinction and scattering cross sections were introduced as the energy absorbing and scattering rates per incident irradiance. This energy transfer can be calculated if the optical spectrum of the impinging light $I_0(\omega)$ and of the transmitted light $I(\omega)$ can be measured at the same time[13] and in the same time interval. Then the loss of intensity per energy interval $I_0(\omega) - I(\omega)$ during the measurement is a measure for the extinction.

As the measurement at one single particle is not possible in experiments, most experiments deal with ensembles or layers of particles. If the particles do not interact with each other and the extinction processes can be treated as not correlated, then the transmittance can be described by the Beer-Lambert law

$$I(z) = I_0 \exp\left(-n_{cluster} \cdot \sigma_{ext} \cdot z\right) \ . \tag{2.57}$$

Herein I_0 is the intensity of the incident light, $n_{cluster}$ the number of clusters per volume V, σ_{ext} the extinction cross section and $I(z)$ the intensity of the light at position z. If the sample has the thickness d and I_0 is the intensity of the light before and $I(d)$ behind the sample

$$\ln\left(\frac{I(d)}{I_0}\right) = -n_{cluster} \cdot \sigma_{ext} \cdot d \quad \Rightarrow \quad \sigma_{ext} \propto -\ln\left(\frac{I(d)}{I_0}\right) \tag{2.58}$$

the extinction cross section is not proportional to $I_0 - I$, as motivated before, but proportional to $\ln(I_0) - \ln(I)$. Because σ_{ext} and $\ln(I_0) - \ln(I)$ only differs in a constant factor, the measured extinction is defined as

$$\text{extinction} \equiv -\lg\left(\frac{I}{I_0}\right) \ . \tag{2.59}$$

By comparing (2.59) with (2.58), the extinction can also be written by

$$\begin{aligned} \text{extinction} &= \frac{1}{\ln 10} \cdot n_{cluster} \cdot d \cdot \sigma_{ext} = \frac{1}{\ln 10} \cdot \frac{\sharp\text{cluster}}{V} \cdot \frac{V_{cluster}}{V_{cluster}} \cdot d \cdot \sigma_{ext} \\ &= \underbrace{\frac{1}{\ln 10} \cdot \frac{1}{V_{cluster}} \cdot d_{eff}}_{1/G} \cdot \sigma_{ext} \ . \end{aligned} \tag{2.60}$$

Using (2.60) it is possible to determine the effective clusters coverage by comparing the measured extinction with the theoretically expected cross section σ_{ext} of a single cluster. Proportionality factor G is used to compare measured extinctions with simulated extinction cross sections.

Validity of extinction measurements

Here an important detail is that the reference I_0 should be measured in a way that all other influences to the incident light like scattering or absorption by the surface are considered within the I_0 signal. Especially, if the embedding matrices are not homogeneous, this is experimentally not simple and can cause background signals. Furthermore, this definition of extinction is only valid for separated, not interacting clusters. This is fulfilled for Ag clusters with a mean diameter of $2R = 2\,\text{nm}$ if the distance between two clusters is $R_{NN} > 5R$. It follows from this that for clusters on a plain surface the effective coverage should not exceed 0.16 cluster monolayers (MLs)[14] [Hövel, 1995].

[13] Because modern laboratory light sources have a characteristic spectrum, which does not change significantly during short time intervals, it suffices to measure the spectra of $I_0(\omega)$ before measuring $I(\omega)$.

[14] For more details for the effective coverage of a cluster ML see section 8.1

Electromagnetic coupling of clusters

If the effective deposition quantity of clusters on a plain surface becomes more than 0.16 ML, the clusters have next neighbour distances of $R_{NN} < 5R$ and are no longer separated so they can couple electromagnetically. In this case, a generalized Mie theory (GMT) [Quinten, 2010] could be applied instead of the Mie theory discussed before. As the calculations done in GMT are typically implemented numerically, only the qualitative effects on the plasmon resonances caused by electromagnetic coupling will be discussed in this section.

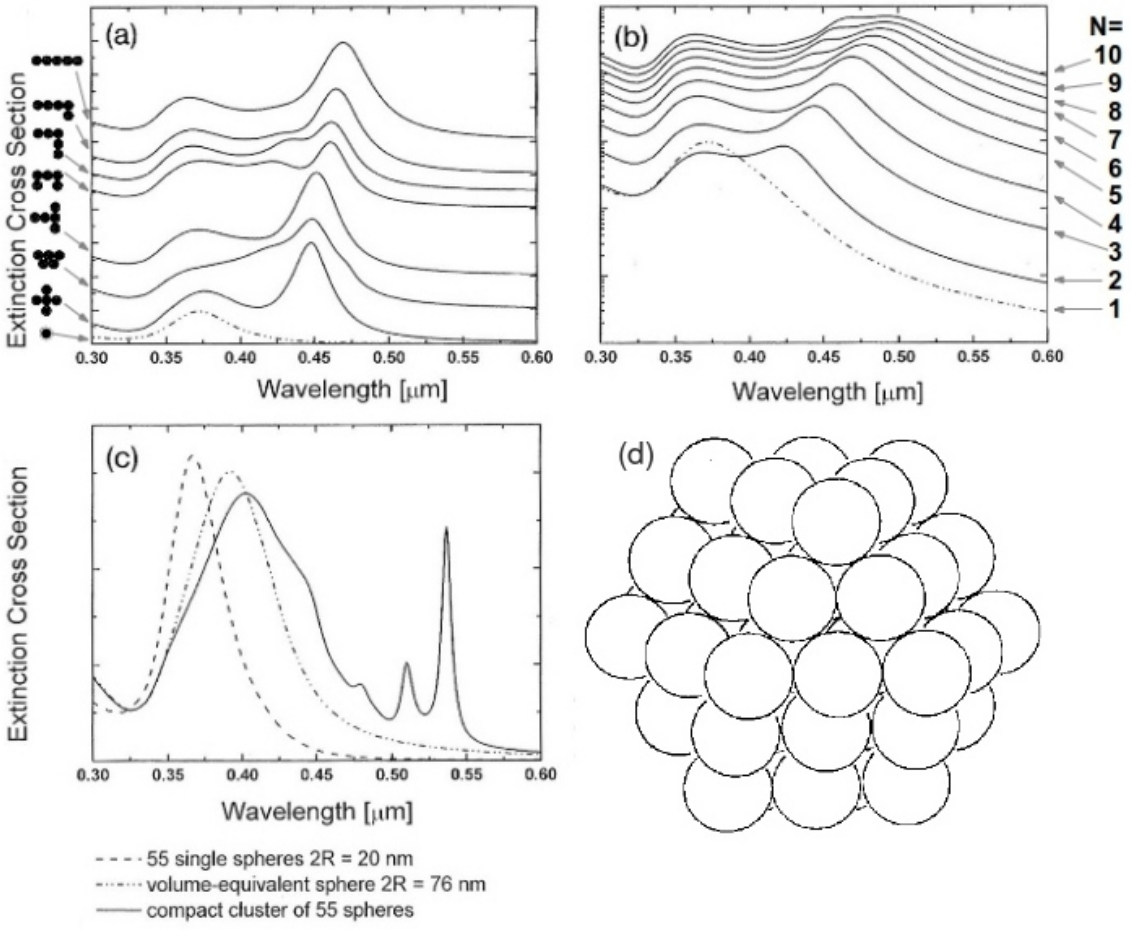

Figure 2.20: Extinction spectra of aggregated clusters with different shapes ($2R = 40\,\text{nm}$) are plotted in figure (a). In (b) extinction spectra of clusters with chain-like structures of different lengths (one cluster ($2R = 40\,\text{nm}$) up to ten clusters) are plotted. In (c) the extinction spectra of 55 single clusters ($2R = 20\,\text{nm}$), 55 clusters arranged in a compact cluster shape (d) and spherical structure ($2R = 76\,\text{nm}$) are shown.

The resonance of a single cluster splits into resonances with mainly lower energies if several clusters aggregate. Additional resonances at higher energies are suppressed because of the closely lying interband transitions which prevent resonances in this region [Quinten, 2010]. This effect causes a red shift of the plasmon resonance. Furthermore, the spectrum of an ensemble of statistically aggregated (and also not aggregated, if $R_{NN} < 5R$) clusters appears broadened due to the superimpositions of the differently split spectra.

In Figure 2.20 (a) the extinction spectra of aggregated Ag clusters with $2R = 40\,\text{nm}$ as a function of the wavelength are shown. The largest split of the extinction is caused by a chain-like arrangement of the aggregated clusters. This behaviour is illustrated in more detail in Figure 2.20 (b). Here chain

like cluster ($2R = 40\,\text{nm}$) aggregates consisting of $N = 1, 2, 3, 4, 5, 6, 7, 8, 9, 10$ clusters are simulated. A clear widening of the split plasmon resonances can be observed with increasing length of the chain. The extinction spectra of a macro cluster consisting of 55 single, spherical clusters ($2R = 20\,\text{nm}$) are represented in Figure 2.20 (c). In comparison to the spectrum of 55 not aggregated, not coupled single clusters, the spectrum is strongly red shifted and its FWHM is about two times of the FWHM of the spectrum of single clusters. If this macro cluster rearranges to a spherical cluster, the shift of the spectrum would be much smaller. But a red shift and an increase of the FWHM is still observable. This is due to the effects of multipoles, beyond of dipoles, in Mie theory.

2.4 X-Ray Absorption Fine Structure (XAFS)

The properties of Ag clusters, which can be attributed to the valence and conduction band electrons, were discussed in the last section. For example measurements can be performed which yield information about chemical reactions, described using a core-shell model. However, these measurements cannot deliver information about the reaction process itself. Further, systems without completely closed cluster shells cannot be described by this model. This model yields also no information about inter atomic distances or the atomic arrangement of the shells.

A powerful tool which yields information about the atomic structure of the clusters and their chemical environment is the X-ray Absorption Spectroscopy (XAS). In XAS an X-ray photon is absorbed by a core level electron and the resulting photoelectron can switch into an unoccupied state in the atom or into the continuum.

The processes taking place in XAS and the information, that can be extracted from XAS, will be discussed in this section. While there are a lot of different XAS techniques, the main attention will be directed to the X-ray Absorption Near Edge Structure (XANES) spectroscopy. In this section the X-ray absorption fine structure of atoms will be presented, followed by the properties of photon absorption processes. The main part of this section is about the processes which take place during XANES experiments and which information they yield. The section closes with a short summary of important facts which have to be considered in XAS experiments.

2.4.1 Excitation of core level electrons

Occupied electronic states in an atom are indicated by the first quantum number $n = 1, 2, 3, ...$, the second (azimuthal) quantum number $l = 0, 1, ..., n-1$ and the magnetic quantum number $m_l = -l, -l+1, ..., 0, ..., l-1, l$. They describe (respectively) the radial orbit, the azimuthal properties of the orbit and the projection from l to the z axis of an electron in a given state. For a full description, also the spin $s = 1/2$ of the electron has to be considered. The spin is the intrinsic angular momentum of an electron and has the orientations $m_s = \pm 1/2$. The angular momentum of the orbit and the spin can couple to a total angular momentum j. The resulting energetic levels are illustrated in Figure 2.21. It can be shown that the mean charge density $\langle \psi_n \,|\, e \,|\, \psi_n \rangle$, where e is the elementary charge, of a fixed fully occupied state n, given by the sum over all permitted l and m_l, is spherically symmetric [Demtröder, 2005]. So, the atomic levels with the same quantum number n are called shells and are indicated by $n = 1 \rightarrow$ K-shell, $n = 2 \rightarrow$ L-shell, $n = 3 \rightarrow$ M-shell and so on. Their energetic order is given by their orbital angular momentum (s, p, d, ...) and their total angular momentum (1/2, 3/2, 5/2, ...). In X-ray spectroscopy, the energetic levels are indicated by the shell and a number which indicates the energetic level in the shell. For example, the lowest state in the L-shell ($n = 2$) is the 2s state and thus indicated by L_1 (compare Figure 2.21). Electrons of occupied states can be excited by a photon (or an electron) and switch into an unoccupied state or the continuum. These processes are shown in Figure 2.22.

If a photon excites an electron from its initial state with energy E_i into an energetically higher unoccupied state with energy E_f, the energy of the photon after this process is $\hbar\omega' = \hbar\omega - (E_f - E_i)$.

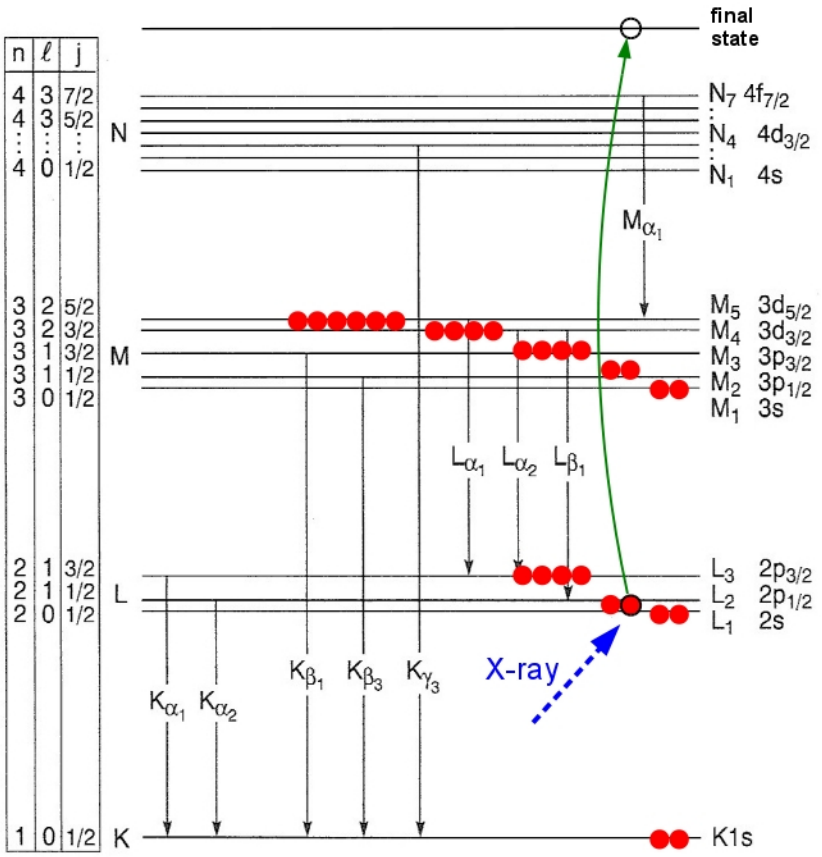

Figure 2.21: Schematic illustration of the energetic levels of a copper atom after [Attwood, 2007]. For a dipole transition of an electron the selection rules are $\Delta l = \pm 1$ and $\Delta j = 0, \pm 1$. In X-ray absorption notations the levels are indicated by the shell symbols and a number, with increasing energy from the core levels up to the valence levels: $1s \rightarrow$ K, $2s \rightarrow$ L_1, $2p_{1/2} \rightarrow$ L_2, $2p_{3/2} \rightarrow$ L_3, and so on.

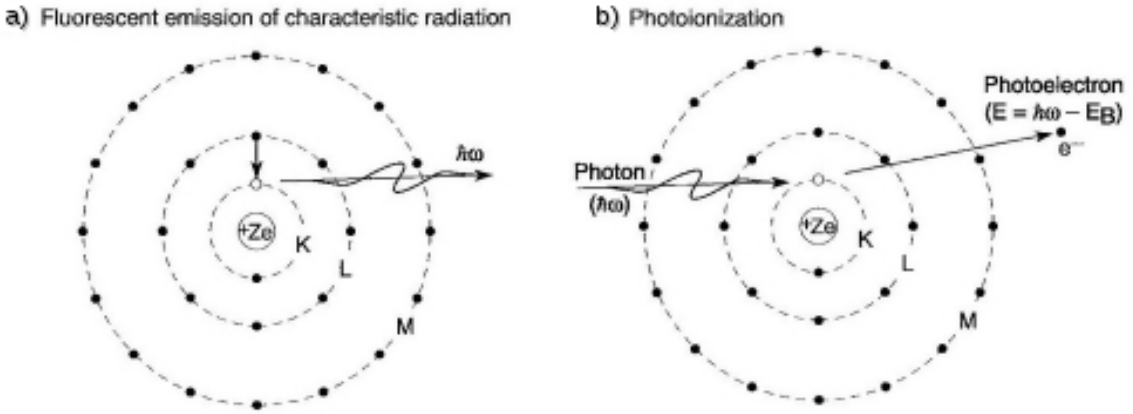

Figure 2.22: Figure a) illustrate a fluorescence process of an atom, after an excitation by a photon. Figure b) illustrates the emission of a photoelectron, excited by photon absorption (after [Attwood, 2007]).

After those processes the atom is in an excited state with a hole in an electronic core level. The atom can relax by filling the hole with an electron of a higher state. The releasing energy is then emitted as

a photon with characteristic energy. The originated hole in the energetic higher shell can be filled by an electron out of an energetic higher shell and so on. Thus the photoemission of a core level electron can cause a cascade of relaxation processes. After those processes, the atom is still electrically neutral (Figure 2.22 a).

If the energy of the incoming photon is equal or larger than the binding energy of an absorbing electron $\hbar\omega > E_B$, the electron can switch into the continuum. This process is called photoionisation and is shown in Figure 2.22 b). The atom is also in an excited state and similar relaxation processes can take place as discussed above. However, in the case of photoionisation, the atom remains in an electrically charged state.

In the following discussion the final state of an excited electron should be an unoccupied state. The probability for the transition from an initial state Ψ_i to another state Ψ_f is connected to the existence of a not vanishing dipole matrix element

$$\begin{aligned}\vec{p} &= q \cdot \vec{d} = -e \cdot <\vec{r}_{if}> \\ &= -\langle \Psi_i \,|\, e\vec{r} \,|\, \Psi_f \rangle = -e \cdot \int \Psi_i^* \, \vec{r} \, \Psi_f \, d\vec{r}\end{aligned} \tag{2.61}$$

which is the quantum mechanical equivalent of a dipole with charge $q = -e$ and the distance $\vec{d}$ between its poles replaced by its expectation value $<\vec{r}_{if}>$. The corresponding frequency is given by $\omega_{if} = (E_f - E_i)/\hbar$.

The insertion of the wave function $\Psi_{n,l,m_l} = (1/\sqrt{2\pi}) \cdot R_{n,l}(r)\Theta_m^l(\theta)e^{im\phi}$ for the states $\Psi_{n_i,l_i,m_{l_i}}$ and $\Psi_{n_f,l_f,m_{l_f}}$ in equation (2.61) where $\Theta_m^l(\theta)$ are the Legendre polynomial and $R_{n,l}(r)$ the Laguerre polynomial, yields a function $\exp\left(i(m_{l_f} - m_{l_i})\varphi\right)$ for the z and $\exp\left(i(m_{l_f} - m_{l_i} - 1)\varphi\right)$ for the x and y components. Thus one condition to become the integral unequal zero is $\Delta m = 0$ for the z component and $\Delta m = \pm 1$ for the x and y components. Additional calculations for the $\Theta_m^l(\theta)$ functions exhibit that the second condition for not vanishing integral is that $\Delta l = l_i - l_f = \pm 1$. The excitation of a dipole transition is thus only permitted for $\Delta l = \pm 1$.

The selection rule for the total spin angular momentum s is given by $\Delta s = s_i - s_f$ if the spin orbit coupling is weak and the wave function can be written as a product of the spin wave function and the space wave function. This is motivated by the transition of an electron in a single electron atom like H. The total value of the spin for a one electron system is $\sqrt{3/4}\hbar$. The total value has to be constant in the case of an excitation or a relaxation of the electron. Thus Δs has to be zero, also in many electron systems. In heavy atoms, where spin orbit interaction is strong, this selection rule is not valid anymore. It also has to be considered that, while the total value of the spin is constant, its direction can change.

The total angular momentum $\vec{j} = \vec{s} + \vec{l}$ thus can only change by $\Delta j = 0, \pm 1$, with one exception: A transition with state $j_i = 0 \rightarrow j_f = 0$ is not permitted. To conclude, the excitation of an electron from a core level with energy E_i into an unoccupied valence level with energy E_f by a photon with energy $\hbar\omega$ is possible, if the following selection rules are fulfilled[15]:

$\hbar\omega \geq E_f - E_i$
$\Delta n \geq 1$
$\Delta j = 0, \pm 1$
$\Delta l = \pm 1$

2.4.2 X-ray Absorption Near Edge Structure (XANES) spectroscopy

In the previous section the condition were discussed, under which the excitation of a core electron is possible. In this section it will be discussed, what information can be delivered by an experiment where a core electron is excited into an unoccupied state.

[15] These are the selection rules for a dipole transition. A quadrupole transition allows $\Delta l = 0, \pm 2$. But because they are about 100 times weaker, they can be neglected [de Groot and Kotani, 2008].

A powerful experiment which yields information about atomic levels, structure and chemical state is the X-ray Absorption Near Edge Structure spectroscopy, often just called XANES. Here an X-ray photon is absorbed by a core level electron and excited into an unoccupied state. Because the probed electron is a core level electron, its energy is well defined and can be matched to a specific element. The final state, however, is determined by the valence electrons and is thus strongly influenced by the chemical state of the atom. Further, in the case of a cluster or a solid, the wavelength of the quantum mechanical wave function of the photoelectron is of the same magnitude like the atom distances. This can cause interferences because the absorption probability of the photoelectron modulates with the wavelength of the photon and the next-neighbour distances of the atom.

Fine structure oscillations

The interaction of X-ray light with matter can be described with Beer-Lambert law (similar to (2.57))

$$I(z) = I_0 \exp\left(-z \cdot \mu(Z, E)\right) \ , \tag{2.62}$$

where I_0 is the intensity of the incident X-ray beam, z the thickness of the sample and μ the absorption coefficient. μ itself depends on the atomic number Z and the energy E of the X-rays. The absorption coefficient is $\mu \propto Z^4 \cdot E^{-3}$ with energy E and the atomic number Z [Demtröder, 2005].

This with increasing energy decreasing cross section, increases instantly if the energy of the impinging radiation fulfils $\hbar\omega = E_f - E_i$ (Figure 2.23). Herein E_i is the energy of an occupied core level and E_f the energy of an unoccupied valence level.

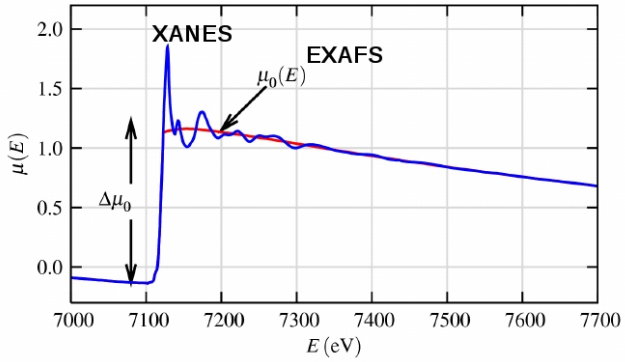

Figure 2.23: XAFS spectrum of FeO [Newville, 2004]

While equation (2.61) yields information about the existence of a dipole transition, the transition rate, which is proportional to the absorption cross section μ, must be calculated in time depending perturbation theory. In first order, this leads to Fermi's golden rule

$$\mu \propto \sum_f |\langle \Psi_i \,|\, H \,|\, \Psi_f \rangle|^2 \, \delta(\hbar\omega - (E_f - E_i)) \ . \tag{2.63}$$

where H is the Hamilton operator and δ the Dirac delta distribution.

In an approach from SAYERS et al., the oscillations in the absorption spectra, as function of wave vector k, caused by scattering of the photoelectron by the surrounding atoms, was calculated for a system of point scatterers arranged around the absorbing atom [Sayers et al., 1971, Rehr and Albers, 2000]

$$\chi(k) = \sum_R S_0^2 N_R \frac{|f(k)|}{kR^2} \sin(2kR + 2\delta_c + \Phi) \exp\left(-2R/\lambda(k)\right) \exp\left(-2\sigma^2 k^2\right) \ . \tag{2.64}$$

Herein R are the interatomic distances, N_R the corresponding coordination numbers and σ the root mean square of the temperature depending fluctuations in bond length. The backscattering amplitude is given by $f(k) = |f(k)|e^{i\Phi(k)}$ with the phase shift $\Phi(k)$. δ_c is the central atom partial-wave phase shift and $\lambda(k)$ is the mean free path. This so called EXAFS (Extended X-ray Absorption Fine Structure) equation is often used to describe and fit the oscillations in the absorption spectrum in the region of about 50 eV - 200 eV above the absorption edge. Thus the whole X-ray Absorption Fine Structure (XAFS) can be divided in the XANES spectrum ($\sim 0\,\text{eV} - 50\,\text{eV}$ behind the absorption edge) and the EXAFS spectrum ($\sim 50\,\text{eV} - 200\,\text{eV}$ behind the absorption edge). However, there is still no theory to describe the oscillations narrow behind the absorption edge quantitatively and analytically. The absorption coefficient is then given by

$$\mu(E) = \mu_0(E)(1 + \chi(E)) \tag{2.65}$$

where $\mu_0(E) = \left|\left\langle \Psi_i \middle| H \middle| \Psi_f^0 \right\rangle\right|$ is the absorption coefficient of the single absorbing atom without any other interactions. A good description of the XAFS is given by NEWVILLE [Newville, 2004].

Fluorescence detection mode

The description above assumes a single electron process where an electron is excited into an unoccupied state due to X-ray absorption. Those experiments can be carried out in transmission mode where a thin, homogeneous sample is illuminated by an X-ray beam and its energy depending intensity is measured before and behind the sample. μ can then be calculated by (2.62). But those transmission experiments are not performable at thick and inhomogeneous samples investigated in the present thesis. In such cases another method of measurement, the fluorescence yield, enables good results of the XANES.

Here the photoelectron is excited from its initial state Ψ_i into an excited state Ψ_n with lifetime Δt. The resulting core hole is then filled by another electron of an outer shell which leads to the final state Ψ_f (Figure 2.24). The intensity of the resulting fluorescence radiation is, under certain circumstances,

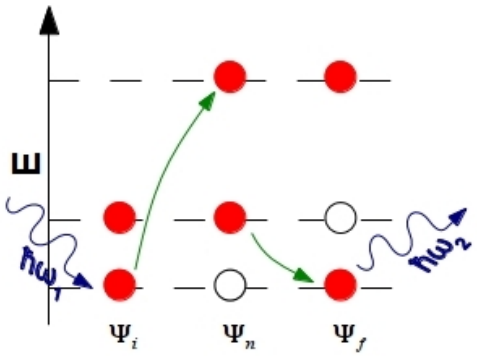

Figure 2.24: Schematic illustration of the two electron excitation process. An impinging X-ray photon with energy $\hbar\omega_1$ is absorbed by an atom in the initial state Ψ_i. The resulting photo electron is excited from a core level into an unoccupied state. The atom is in the unstable state Ψ_n. After the core hole is filled by an electron of a higher shell, the atom is in the final state Ψ_f.

proportional to the absorbed impinging radiation. The most general case of such an experiment are Resonant inelastic X-ray scattering (RIXS) experiments. Here the energy of the imping X-ray radiation is tuned from energy below to energy above the absorption edge and the fluorescence radiation is detected energy-dispersively. When using an energy-dispersive detector, XANES experiments can be performed by adjusting the detector to a fixed, strong fluorescence line of the absorbing atom

(investigated material). Thus the background radiation can be suppressed very effectively. The probability to detect an absorption process is now a function of the probability that a photon is absorbed by an electron and the probability that the resulting core hole is filled by an electron of a specific shell, resulting in the emission of a photon with energy $\hbar\omega_2$. Those measurements are known as partial fluorescence yield (PFY) measurements.

Further it has to be considered that the resulting spectrum is convoluted with a Lorentzian because of the finite lifetime of the core hole. "This Lorentzian broadening is due to the finite lifetime of the core hole, leading to an uncertainty in its energy according to Heisenberg's principle." [de Groot and Kotani, 2008] The broadening of the energy spectrum is less distinct for weakly bound excited electrons than for tight bound electrons. Therefore the lifetime of the final state $|\Psi_f\rangle$ is longer than that of the intermediate state $|\Psi_n\rangle$. So, the resolution of the recorded XANES spectrum depends on the detected fluorescence line.

An additional point is the intensity of the fluorescence lines. Sometimes, especially when dealing with X-ray beams with weak intensities, it is necessary to detect more than one emission line to get a strong fluorescence signal. This so called total fluorescence yield (TFY) can be calculated integrating $\int \mathrm{PFY} d\omega_2$ in the Region Of Interest (ROI). In most cases the resulting resolution is less narrow than that of the PFY measurements. Further it must be considered that the ROI should not include the energetically region of the tuned incident beam. The spectra recorded in TFY are more similar to spectra of measurements recorded in absorption measurements than PFY spectra are.

Self-absorption

Despite the advantages of measurements in fluorescence compared with the transmission mode, not all samples can be measured in fluorescence mode with accurate resolution. For some kinds of samples, self-absorption occurs and must be regarded especially for EXAFS experiments by corrections of the recorded spectra [Tröger et al., 1992]. A good qualitative introduction to this problem is given by RAVEL[16] and BUNKER [Bunker, 2010]. A sample with total thickness z_s consists of the element

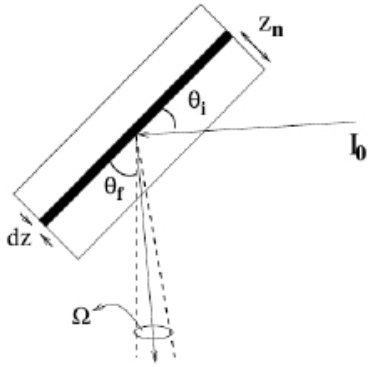

Figure 2.25: Illustration of a XANES experiment in fluorescence mode, from RAVEL

of interest, with absorption coefficient μ_e, and other elements, for example embedding materials with absorption coefficient μ_b. The total absorption coefficient μ_t is a superposition of μ_e and μ_b. With the energy of the fluorescence radiation E_f and the probability of a fluorescence process ϵ_f, the intensity of the fluorescence radiation caused by a layer n with thickness dz_n is given by

$$I_f(z_n)dz_n = I_0 \cdot \exp\left(-\mu_t(E) z_n / \sin(\theta_i)\right) \cdot \epsilon_f(E)\mu_e(E) \frac{dz}{\sin(\theta_i)} \cdot \exp\left(-\mu_t(E_f) z_n / \sin(\theta_f)\right) \cdot \frac{\Omega}{4\pi} \ . \quad (2.66)$$

[16] Bruce Ravel, Understanding self-absorption in fluorescence XAS, https://speakerdeck.com/bruceravel/understanding-self-absorption-in-fluorescence-xas

It can be shown that after integration of equation (2.66) $\int_0^{z_s} I_f(z_n)dz_n$ the total fluorescence signal $I_f(E)$ of the sample which is detected, is given by

$$I_f(E) = I_0 \cdot \frac{\Omega}{4\pi} \left(\frac{\mu_e(E)}{\mu_e(E) + \mu_b(E) + \mu_t(E)\frac{\sin(\theta_i)}{\sin(\theta_f)}} \right) . \tag{2.67}$$

The problem is that the fluorescence signal of interest, caused by the absorption cross section μ_e, is normalised by itself if $\mu_e > \mu_b(E) + \mu_t(E)\sin(\theta_i)/\sin(\theta_f)$. This leads to incorrect peak sizes and less distinct fine structure in XANES and EXAFS signal. The effect of an iron EXAFS signal was investigated and illustrated by RAVEL in Figure 2.26.

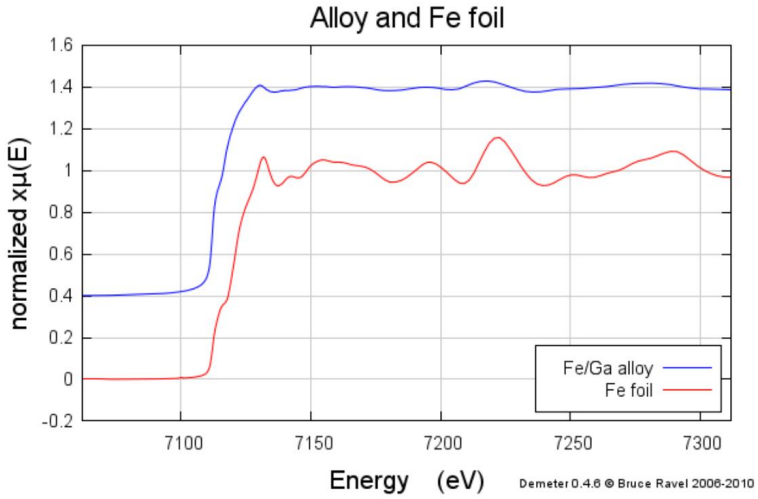

Figure 2.26: EXAFS Fe K edge signal of a thin Fe foil (red line) and a Fe/Ga alloy ($Fe_{72.74}$ $Ga_{27.26}$) with self-absorption effect (blue line), obtained by RAVEL.

This problem can be avoided by several points. If possible, transmission XANES experiments should be performed at the same sample. Also if the transmission experiments yield no perfect results they can be combined with the fluorescence measurements (including self-absorption) to get suitable results. If measurements in transmission mode are not achievable, the sample concentration can be diluted. This is already fulfilled for the samples investigated and discussed in the present thesis. Then μ_b in (2.67) becomes dominant in the denominator and the contribution of μ_e can be neglected. A similar effect can be achieved by changing the photon exit angle θ_f thus $\sin(\theta_f)$ becomes small which causes a domination of μ_t in the denominator of (2.67). The last and most smart solution to avoid self-absorption is making the samples thin. If the thickness of the sample is small compared with the absorption length, (2.66) does not be integrated and thus does not yield (2.67). Also this is fulfilled for the investigated samples and also for the Ag bulk reference sample (100 nm thick Ag film).

Influence of oxidation to the final state of Ag L XANES

A lot of information about the chemical environment of the absorbing atom can be extracted from the final state of the photoelectron. Because the photoelectrons can only switch into unoccupied states which fulfil the selection rules, the intensity and the position of the absorption edge yields information about states of the valence electrons in the absorbing atom.

This will be discussed on the example of silver oxide Ag_2O. Here, four Ag atoms react with one O_2 molecule to form two Ag_2O molecules: $4\,Ag + O_2 \rightarrow 2\,Ag_2O$. Thus the Ag atoms are singly positively charged and the O atoms twofold negatively charged. An excited photoelectron from an Ag atom feels a more attractive effective potential than in a single Ag atom. As a consequence the energetic position

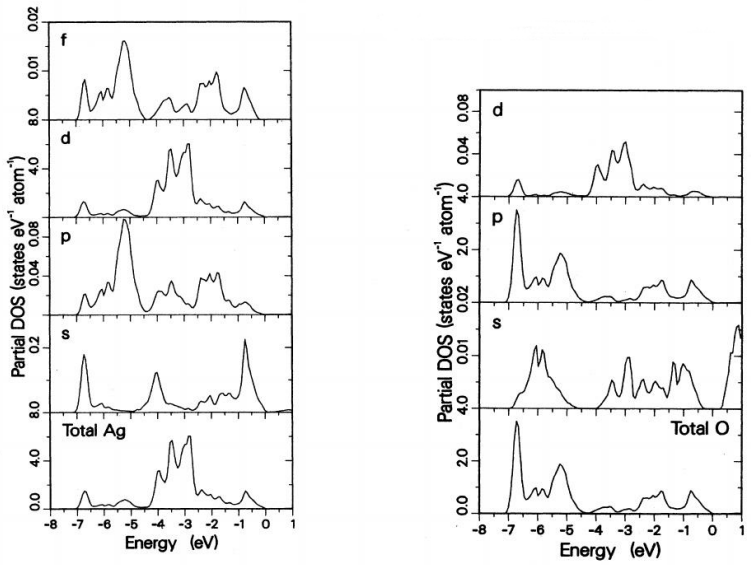

Figure 2.27: Density of states of the Ag site (left) and the O site (right) of Ag_2O [Czyyk et al., 1989].

of the Ag absorption edge shifts to higher energies. The intensity of this shift is a measurand for the ionic character of the chemical reaction.

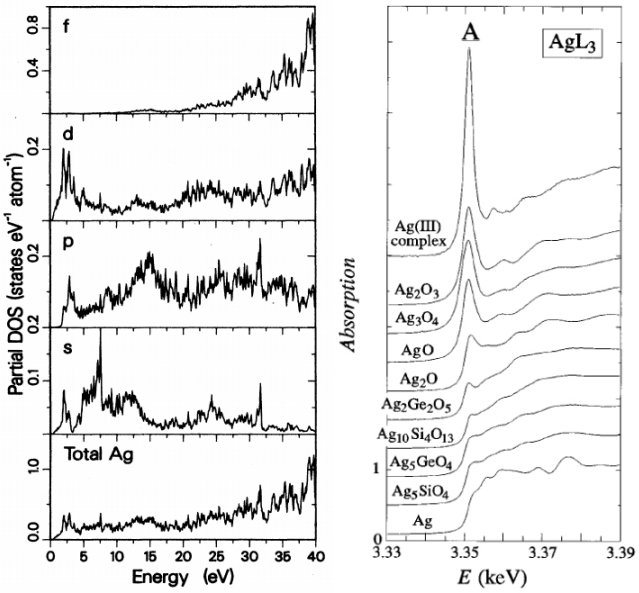

Figure 2.28: The unoccupied density of states of the Ag site in an Ag_2O molecule. The strongest amount to the uDOS close to the Fermi level is given by the d states (left) [Czyyk et al., 1989]. The Ag L_3 absorption edge of several Ag oxides. The white line increases with increasing oxidation state (right) [Behrens et al., 1999].

However, the interpretation is not as easy as described above. Before the shift of the absorption edge can be analysed, the change of the spectrum caused by changes in the valence band final states has to be considered. In Ag_2O the Ag-O bonding causes a break of the closed Ag 4d structure. The valence bands are built by hybridisation, especially out of Ag 4d and O 2p states (Figure 2.27) [Czyyk et al., 1989]. The resulting conduction band structure is dominated by contributions of the 4d orbitals at the Ag side and the 2p orbitals at the O side [Czyyk et al., 1989].

The corresponding unoccupied densities of states are shown for the Ag side in Figure 2.28 left. The Ag 4d shell is filled up to about 90 %. Nevertheless, unoccupied 4d states are present at the bottom of the conduction band. These states are the reason for an increase of the height of the absorption edge with increasing oxidation state. This increase is often called white line[17].

For example the Ag L_3 absorption edge of Ag^{3+} is very intense, which can be ascribed to the presence of two holes in the 4d band [Behrens, 1992]. This is shown in Figure 2.28 right. It should be considered that these effects are not observable for the Ag L_1 edge because a dipole transition to the d states is not permitted for an electron out of the 2s orbital.

Summary of the theoretical considerations for XANES experiments

The most important information about XANES experiments should be summarised at the end of this section:

- The atomic structure of a many electron system splits into energy levels, indicated by K, L, M, N, ... The subshells are numbered consecutively with increasing energy, starting with the tightest bound electrons K, L_1, L_2, L_3, M_1,... .
- The excitation of electrons from lower to higher states is only possible if the following selection rules are fulfilled: $\hbar\omega \geq E_f - E_i$, $\Delta j = 0, \pm 1$, $\Delta n \geq 1$, $\Delta l = \pm 1$ for dipole and $\Delta l = \pm 2$ for quadrupole transitions. Typically dipole transition dominates quadrupole transition by a factor of about 100.
- The excited state can relax by emitting characteristic fluorescence radiation.[18]
- The absorption of X-ray radiation in matter is $\propto \frac{Z^4}{E^3}$.
- Interferences of the photoelectron with neighbour atoms causes modulations of the absorption structure which leads to an X-ray absorption fine structure (XAFS).
- These XAFS can be measured in transmission and fluorescence mode. The fluorescence mode is used for measurements on thick inhomogeneous samples and can be performed in TFY and PFY detection modes. The structure of these spectra are influenced by the lifetime of the excited state.
- The investigated samples should be as thin as possible and/or diluted to prevent self-absorption in fluorescence measurements.
- Chemical reactions of the investigated element can change the final state orbitals of an excited electron. This leads to a change of the structure of the uDOS and thus a change of the absorption spectrum.

[17] In early XAS experiments the X-ray radiation was detected by photo-chemical films. A strong signal caused an overexposure of the film which results in a white line at the films.

[18] An Auger electron can be emitted, too. The probability, which effect takes place, is a function of the atomic number and the energetic level of the core hole.

3 Experimental implementation

In this chapter the experimental setups and the implementations of the experiments will be introduced. This includes the embedding materials and the THErmal CLuster Apparatus (THECLA), which is used to deposit the clusters into the materials. It was designed by HÖVEL to produce a high intense cluster beam with narrow size distribution. Here only a short overview about the apparatus, the cluster production process and the used experimental parameters will be given. A detailed discussion is given by HÖVEL and HOFFMANN [Hövel, 1995, Hoffmann, 2012]. The discussion of THECLA includes the optical setups to perform in-situ UV-Vis measurements. Also the setups for the ex-situ experiments at the beamlines BL8 at Dortmunder ELekTronenspeicherring Anlage (DELTA) and the beamline ID26 at European Synchrotron Radiation Facility (ESRF) where XANES experiments were carried out, will be presented in this chapter.

3.1 Embedding materials

In the present thesis, Ag clusters were deposited into three kinds of different embedding materials: polymers, aerogels and room temperature ionic liquids. The main aim is always to deposit as much clusters as possible into these materials without risking coalescence or aggregation.

The properties of clusters differ from that of bulk material and can be tuned by different methods. Because of their small volume they can only be investigated with a lot of effort. For example for XANES experiments synchrotron radiation with high brilliance is necessary to get a good signal to noise ratio. A good signal to noise ratio can also be achieved when the mass of the investigated material is increased. The problem is to stabilise the clusters to maintain their special properties. Hereto the properties of clusters in different kinds of matrices are investigated. These systems will be described in the present section.

3.1.1 Polydimethylsiloxane (PDMS)

Polydimethylsiloxane (PDMS) is an organic polymer on silica base with the molecular formula $(C_2H_6OSi)_n$ (inset Figure 3.1). PDMS provides properties which are of substantial importance for the realised experiments. It is transparent for light in the visible region up the low energetic UV region (Figure 3.1). This enables the implementation of UV-Vis measurements. Its dielectric constant is $\varepsilon_1(100\,\mathrm{Hz}) = 2.72$, $\varepsilon_1(100\,\mathrm{kHz}) = 2.68$ [Corning, 2014] and $\varepsilon_1(589\,\mathrm{nm}) = 1.89 - 1.97$ [Kuo, 2009]. Further its flexible structure permits the deposition of clusters several ten nanometers into the material (Figure 3.2).

With the deposition into the volume, instead only on the surface, it is possible to deposit higher amounts of clusters before a closed film is formed.

RAVAGNAN et al. [Ravagnan et al., 2009] deposited palladium clusters with a super sonic expansion ($v > 10^3\,\mathrm{m/s}$) at Poly(methyl methacrylate) (PMMA) and observed a penetration of the clusters into the volume of the PMMA. For the deposition of gold clusters into PDMS a larger penetration depth was observed (Figure 3.2) [Corbelli et al., 2011]. The reason is the softer structure of PDMS compared with PMMA. A higher penetration depth correlates with a bigger volume for the same amount of clusters and thus lower densities and larger next neighbour distances.

The PDMS films, used in this thesis, were produced from a silicone oil (PDMS) and a curing agent. For this "`Sylgard®184 Silicone Elastomer Kit`" was purchased from `Dow Corning`. The silicone oil and the curing agent were mixed in a ratio of 10 : 1, respectively. After mixing it was placed for about 15 min in a desiccator for degassing. Then the fluid was brought up on a silica glass substrate

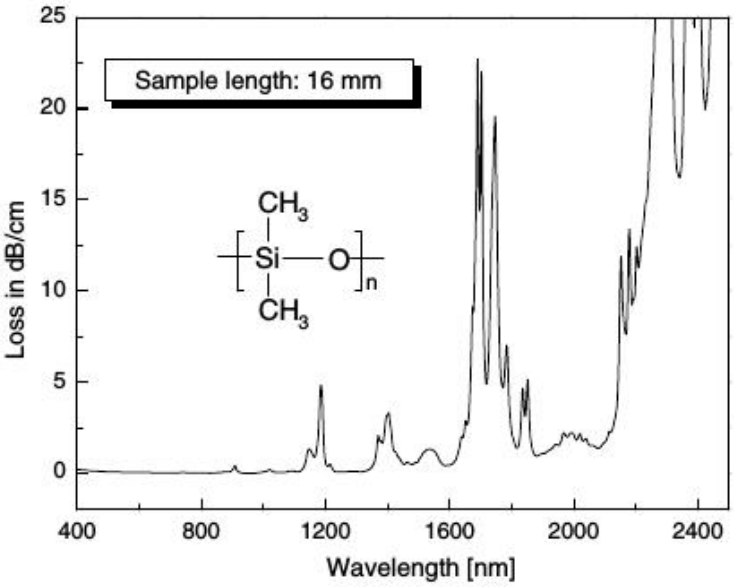

Figure 3.1: Absorption spectrum of a 16 mm thick PDMS film in dB/cm [Cai et al., 2008]. The molecular structure of PDMS monomer unit $(C_2H_6OSi)_n$ is shown in the inset.

with a stainless steel applicator. By these technique films with a thickness of 30 µm, 60 µm, 90 µm and 120 µm can be produced. Finally the sample was heated for 3 hours at 100 °C.

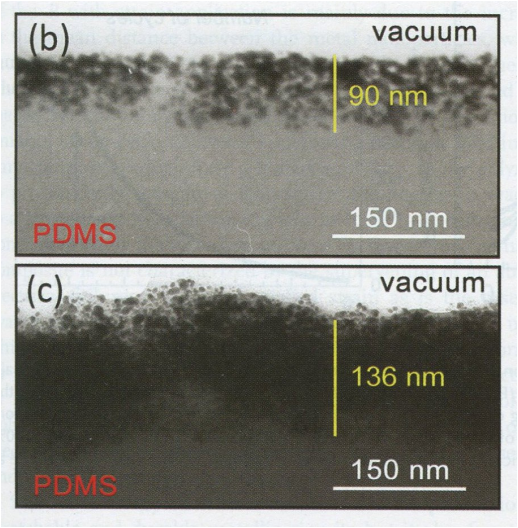

Figure 3.2: TEM image of the cross section of a PDMS sample with deposited gold clusters. The deposition of various effective cluster thicknesses cause various penetration depths. The higher the effective cluster thickness the larger the penetration depth [Corbelli et al., 2011].

3.1.2 Silica (SiO_2) aerogel

Aerogels are highly porous networks of molecules with inter molecular distances of several nanometers. A broad field of investigations on aerogels took place in the 1980s. Silica aerogel is produced in a complicated process from a sol-gel by a supercritical drying. A good overview about history, production, properties and area of application is given by FRICKE [Fricke and Tillotson, 1997]. Their most interesting property is their ultra low density. This leads to additional properties like low heat conductivity [Scheuerpflug et al., 1992], a low sound velocity [Gross and Fricke, 1992] and the necessity

of an effective medium model for a full description of their optical properties due the the high amount of air in the network [Hornfeck et al., 1992].

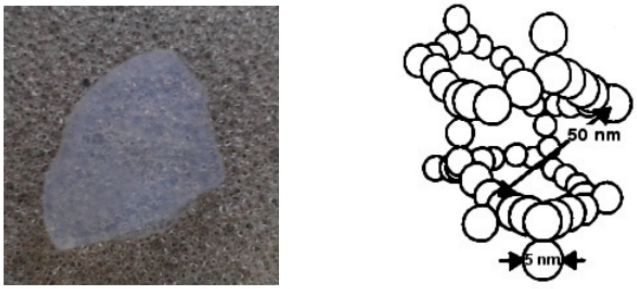

Figure 3.3: Picture of a silica aerogel sample (left). Schematic structure of silica aerogel (right) [Hövel, 1995].

Silica aerogel consists of SiO_2 particles. Its pores have a mean diameter of about 20 nm but have a size distribution which includes pores with more than 40 nm and also less than 2 nm. The size of the SiO_2 particles is about $2\,\text{nm} - 5\,\text{nm}$. The percentage of the SiO_2 on the whole volume is about 5 %, corresponding to 95 % empty space. This enables an internal surface area of about $600\,\text{m}^2/\text{g} - 1000\,\text{m}^2/\text{g}$. The density is about $0.1\,\text{g/cm}^3$, but can vary from $0.003\,\text{g/cm}^3 - 0.35\,\text{g/cm}^3$ [Lawrence-Berkeley-Laboratories, 2014]. These various special properties of silica aerogel fulfil a number of requirements which are desirable for deposition experiments. Also ex-situ experiments, performed after deposition, are benefited by these properties.

The first remarkable property is the possibility of soft landing. Due to the small mass of the weakly bound SiO_2 particles, compared with the mass of the clusters, a landing cluster can fulfil several collisions with the SiO_2 particles before its initial energy is absorbed. These effect was utilised by the NASA to capture microscopic cosmic particles [Tsou, 1995].

Also silica aerogel is optically transparent in the visible region. Like explained before this is necessary for UV-Vis measurements. The transmission spectrum of SiO_2 aerogel is shown in Figure 3.4 [Lawrence-Berkeley-Laboratories, 2014]. The good transmission behaviour is due to the good optical transmission of fused silica. However, silica aerogel has an extinction in the UV region which is caused by Rayleigh scattering at the SiO_2 particles.

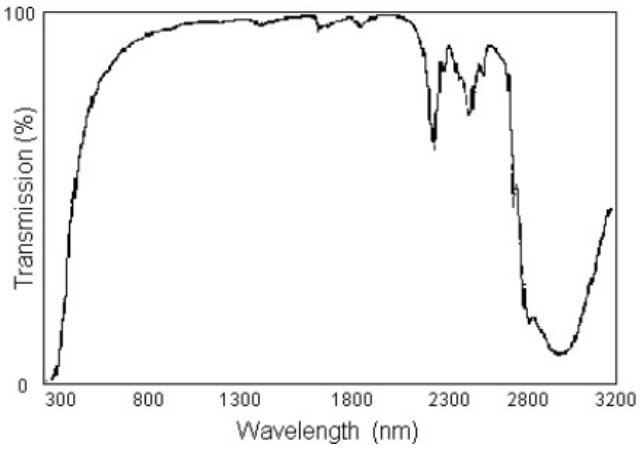

Figure 3.4: Optical transmission of silica aerogel from UV to IR region. The cut off at a wavelength of about $\lambda \leq 300\,\text{nm}$ is a consequence of Rayleigh scattering [Lawrence-Berkeley-Laboratories, 2014].

Another advantage of silica aerogel, versus for example fused silica, is its rough surface. The more

rough a surface is, the more clusters can be deposited before risking coalescence. The factor of microscopic surface (the surface which could be occupied by clusters) S per macroscopic surface (the geometric surface of the sample in which clusters should be deposited) A is given by

$$\frac{S}{A} = \tilde{\rho}_S \cdot \rho \cdot h \ .$$

Herein $\tilde{\rho}_S \approx 600\,\mathrm{m}^2/\mathrm{g}$ is the assumed internal surface area, $\rho \approx 10^5\,\mathrm{g/m}^3$ the density of the aerogel and h the mean penetration depth (on a smooth surface this is 1 ML). For fused silica it is $S/A = 1$. It follows by this that for separated clusters on fused silica, the deposition maximum is limited to 1 ML. To prevent coalescence or electromagnetic, the effective deposition amounts for Ag clusters (diameter $\approx 2\,\mathrm{nm}$) on fused silica are limited to about 1/10 ML [Hövel, 1995]. Similar changes for coverages above 0.1 ML on flat SiO_2 substrate occur above ~ 1 ML for clusters in SiO_2 aerogel. So, the possible deposition amount before risking coalescence is about a factor 10 larger. From this it follows that the maximum coverage (corresponding to 1 ML at fused silica) is limited by $S/A \approx 10$ for silica aerogel. With these simply assumptions the mean penetration depth is of the order of $h_{\mathrm{SiO_2\ aerogel}} \approx 10^1\,\mathrm{nm} - 10^2\,\mathrm{nm}$.

These porous network also permits the exchange of gases and thus experiments where the focus is on cluster-environment (chemical, gaseous) interaction can be performed effectively.

3.1.3 1-Butyl-3-methylimidazolium hexafluorophosphate (BMIM PF_6)

The last sample system investigated in this thesis are clusters in 1-butyl-3-methylimidazolium hexafluorophosphate (BMIM PF_6)[1]. In contrast to the other sample systems, BMIM PF_6 is a liquid, more precisely a Room Temperature Ionic Liquid (RTIL). RTILs are salts, which are in the liquid phase at room temperature . Because they are actually intensively investigated, they are often just called ionic liquids.

BMIM PF_6 is an imidazolium-based ionic liquid. This means it consists of a large asymmetric 1-butyl-3-methylimidazolium cation, an imidazole molecule with hydrocarbon chains, and a small inorganic hexafluorophosphate anion. Its structure is shown in Figure 3.5. The asymmetry in at least one of the ions is the reason that keeps away the system from building a solid. In classical salts the ionic interaction would cause a crystallisation of the system. On the other hand, in the solid state, ionic arrangement caused by hydrogen bonds leads to an extended cooperative network of cations and anions [Dupont, 2011].

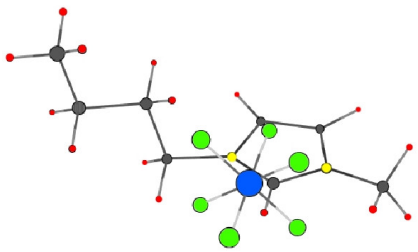

Figure 3.5: BMIM PF_6 after [Paulechka et al., 2003]. The dots represent the atoms and the colour the kind of the atom: hydrogen (red), carbon (grey), nitrogen (yellow), phosphate (blue), fluorine (green)

BMIM PF_6 is one of the best known and most investigated RTILs. One of its outstanding properties is its disappearing vapour pressure of about $\sim 10^{-13}$ mbar [Kabo et al., 2004]. This is a special property of RTILs which make them interesting for vacuum science and technologies. In the present case of

[1] BMIM PF_6 is also known as BMI PF_6 and C_4MIM PF_6.

cluster deposition into RTILs, the moderate electrical conductivity of BMIM PF_6 is an advantage because it enables the deposition of electrically charged clusters without risking charging of the liquid.

Computer simulations exhibited the presence of polar and also nonpolar regions in the ionic liquids. These characteristics change with the length of the cation side chains. The nonpolar domains form a dispersive microphase for C_2mim PF_6 and a continuous microphase for C_6mim PF_6 and molecules with longer side chains. Thus C_4mim PF_6 (BMIM PF_6) marks the onset of a transition from one phase to the other. The nonpolar regions form a 3D network with length scales of 12 Å in the case of BMIM PF_6 [Canongia Lopes and Pádua, 2006]. This is shown in Figure 3.6

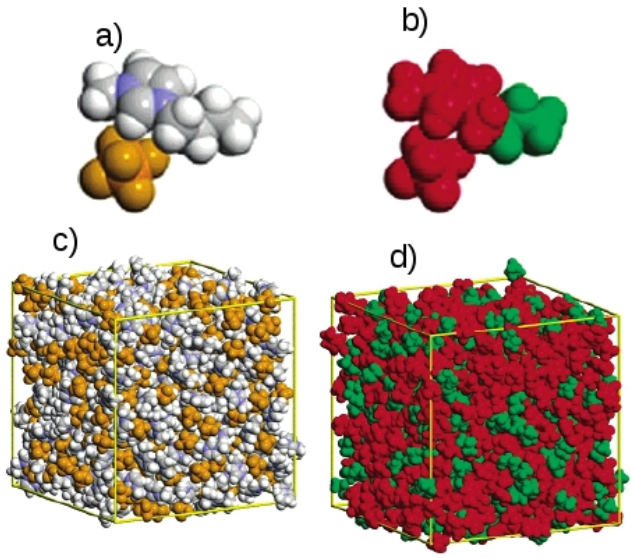

Figure 3.6: a) Structure of the BMIM PF_6 molecules in CPK colouring: hydrogen (white), carbon (black), nitrogen (dark blue), phosphate (orange), fluorine (green). b) Polar regions (red) of the methylimidazolium ring and the PF_6 anion. The butyl side chains are nonpolar (green). c) Arrangement of the ions in the liquid state (CPK colours). d) Polar (red) and nonpolar (green) microstructers in the liquid state [Canongia Lopes and Pádua, 2006].

RTILs, amongst others also BMIM PF_6, are used as solvents in the wet chemistry production of synthesised nanoparticles (NPs). The stability of these particles is still a field of research where no generalised statements can be made. While a number of groups reported the stability of the produced NPs, other groups had to add stabilisation agents to the system. An extensive review about the properties of NPs in RTILs is given by DUPONT and SCHOLTEN [Dupont and Scholten, 2010].

The negligible vapour pressure of the RTILs opened another manufacturing technique in the preparation of NPs. In several experiments a sputter source was placed above a RTIL. The sputtered target atoms moved into the RTIL where nucleation growth started. The size and size distribution of the resulting NP depended on the kind of the RTIL [Hatakeyama et al., 2009], the surface composition of the RTIL and the source parameters like the sputtering current [Wender et al., 2010].

3.2 THECLA

The clusters are produced in the THErmal CLuster Apparatus (THECLA), illustrated in Figure 3.7. It consists of a cluster source, a cryogenic pumping stage and an experimental chamber. The source chamber is connected with a pumping stage which enables the adjustment of the source pressure. The pressure of the source chamber is about $p_{\text{source}} = 1 \cdot 10^{-3}\,\text{mbar}$ when source is down and about $p_{\text{source}} = 3 \cdot 10^{-1}\,\text{mbar}$ when source is running. The pressure in the experimental chamber is about $p_{\text{exp.}} = 10^{-7}\,\text{mbar}$ and $p_{\text{exp.}} = 10^{-4}\,\text{mbar}$, respectively.

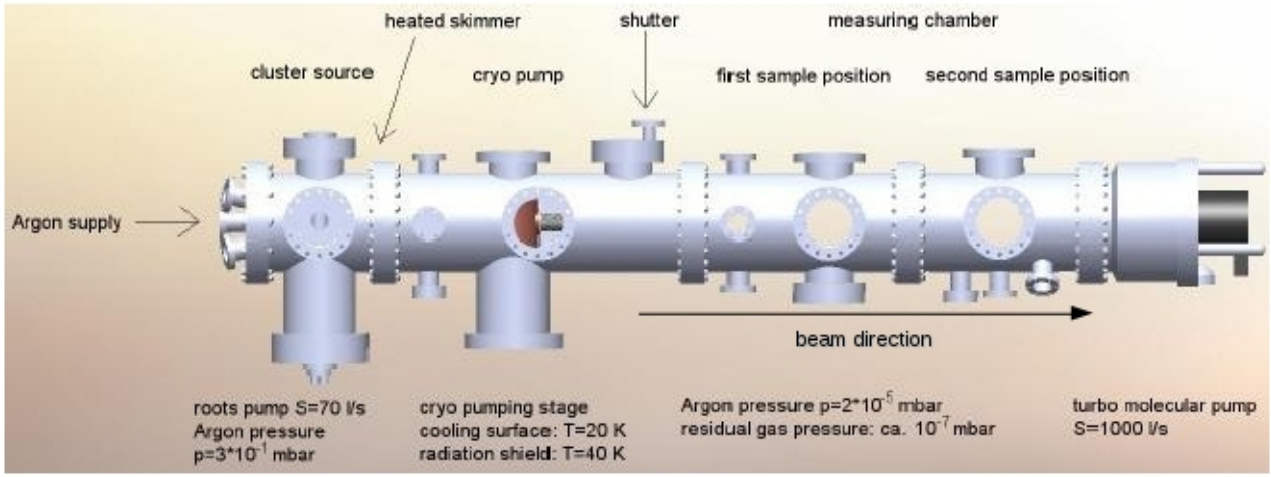

Figure 3.7: Illustration of the THErmal CLuster Apparatus THECLA [Hoffmann, 2012]. Silver is vaporised in the source and expands with the carrier gas argon through a super sonic nozzle into the evacuated experimental chamber. Thus deposition rates up to 9 nm/s can be reached.

3.2.1 Cluster source

The source basically consists of a heater and a vaporisation chamber with a supersonic nozzle, illustrated in Figure 3.8. The tantalum heater foil is heated by an electrical current with a power of about 2 kW. This leads to temperatures of about 2300 K[2]. Under these conditions silver has a saturated vapour pressure of about 400 mbar. The argon pressure is adjusted to 4.5 bar. The expansion of a gas through a heated nozzle into a vacuum has interesting properties.

By choosing a not too small nozzle radius, the mean free path of the atoms is small compared with the nozzle due to the high pressure. The atoms in the nozzle can then be accelerated by collisions up to super sonic speed. Using the conservation of energy and the conservation of mass, the properties of the gas in the nozzle can be calculated as a function of the normalised velocity of the atom $M = v/a$, where v is the velocity of the atoms, a is the local velocity of sound[3] and M is called Mach number. If the parameters in the vaporisation chamber are given by T_0 (temperature), p_0 (pressure) and ρ_0

[2]The temperature can be theoretically calculated by the Stefan-Boltzmann-law for a black body radiator with $W = c \cdot T^4$. Because of radiation shields and a weaker emittance, the constant c is a factor 7 smaller in experiment than theoretically expected.

[3]For an ideal gas with atom mass m the velocity of sound is given by $a = \sqrt{\frac{k_B T \gamma}{m}}$, where k_B is the Boltzmann constant and $\gamma = c_p/c_V$ with the specific heat capacities c_p and c_V at constant pressure and volume.

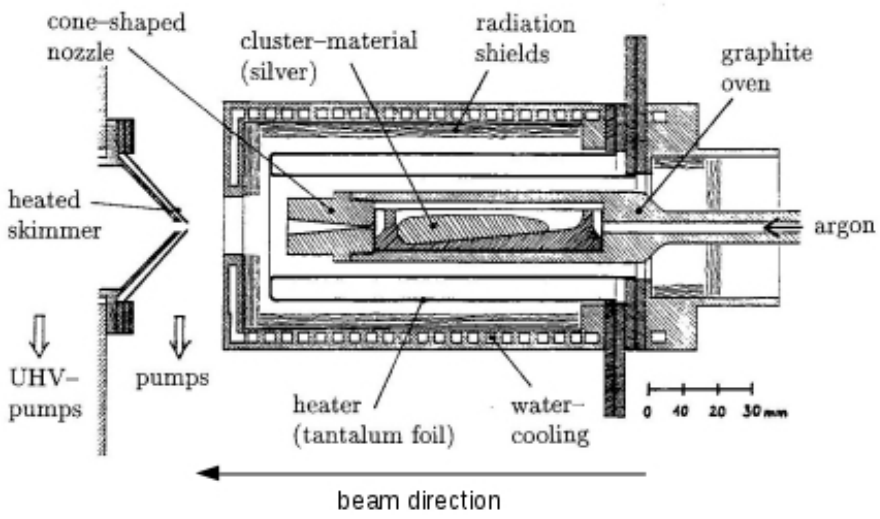

Figure 3.8: Illustration of the cluster source [Hövel, 1995]. The silver powder is localised in a tub like shuttle made of carbon. This shuttle is inserted in the middle of the source, which is a tube made of carbon with an argon inlet on the one and a supersonic nozzle on the other side. The whole source is surrounded by a tantalum heater and the heater is surrounded by a water chilling. The first orifice to extract the cluster beam is a heatable skimmer.

(density), the relative parameters in the nozzle are

$$\frac{T}{T_0} = \left(1 + \frac{1}{2}(\gamma - 1)M^2\right)^{-1} \tag{3.1}$$

$$\frac{p}{p_0} = \left(1 + \frac{1}{2}(\gamma - 1)M^2\right)^{-\gamma/(\gamma-1)} \tag{3.2}$$

$$\frac{\rho}{\rho_0} = \left(1 + \frac{1}{2}(\gamma - 1)M^2\right)^{-1/(\gamma-1)} \tag{3.3}$$

with $\gamma = c_p/c_V$ the fraction of specific heat capacity at constant pressure c_p and volume c_V. For an ideal gas it is $\gamma = 5/3$. This is plotted in Figure 3.9 a). Different Mach numbers for one nozzle under defined conditions can be realised by choosing a cone like nozzle. Now the conservation of mass can be used once again for a nozzle with changing cross section area A:

$$\frac{A}{A^*} = \frac{\rho^* v^*}{\rho v} = \frac{\rho^* a^*}{\rho M a} = \frac{\rho^*}{M\rho}\left(\frac{T^*}{T}\right)^{1/2} = \frac{1}{M}\left(\frac{1 + \frac{1}{2}(\gamma - 1)}{1 + \frac{1}{2}(\gamma - 1)M^2}\right)^{-1/(\gamma-1)-1/2} = \frac{r^2}{r^{*2}} \tag{3.4}$$

The "*" indicates the position in the nozzle with $M = 1$. Further the velocity in the nozzle as a function of the Mach number can be calculated by

$$v = Ma = Ma_0\left(\frac{T}{T_0}\right)^{1/2} = Ma_0\left(1 + \frac{1}{2}(\gamma - 1)M^2\right)^{-1/2} , \tag{3.5}$$

with the limit velocity for an ideal gas

$$\lim_{M\to\infty} v(M) = v_\infty = a_0\sqrt{\frac{2}{\gamma - 1}} \approx 2.24 \cdot \sqrt{T_0 \cdot \frac{k_B}{m}} . \tag{3.6}$$

The relative radius and the relative velocity as a function of the Mach number are plotted in Figure 3.9 b). Now it is possible to find a Mach number for which the partial pressure in the nozzle at a

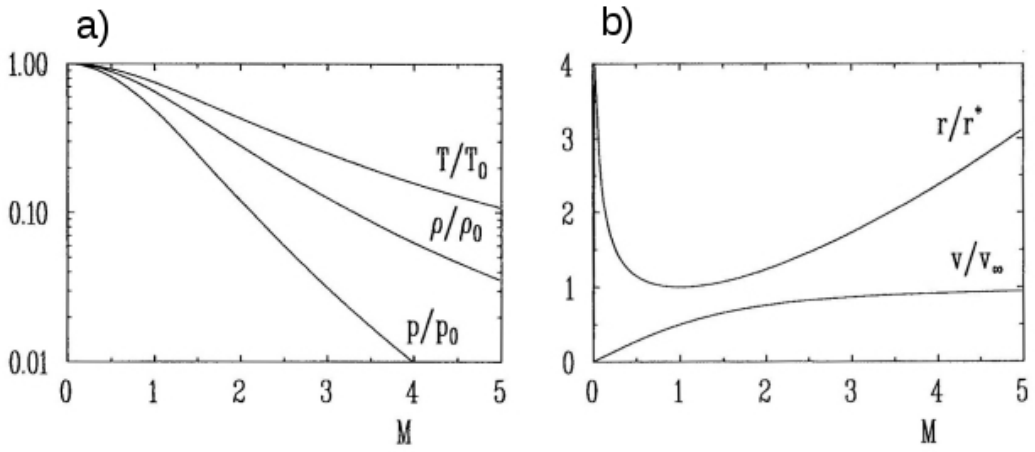

Figure 3.9: a) Temperature, density and pressure of the particles in the beam, normalised to the condensation in the source, at different Mach numbers in the nozzle. b) Radius of the nozzle in dependence of the Mach number, normalised to the radius where $M = 1$ is fulfilled (top curve). At the smallest position of the nozzle the velocity of the beam is equal the speed of sound. Velocity of the beam normalised to the maximum velocity is shown in the bottom curve. The velocity approximates to the maximum velocity and does not increase significantly with increasing Mach number for $M > 2$. [Hövel, 1995]

given temperature is higher than the saturated vapour pressure of the Ag vapour. This means that condensation can take place, especially because the saturated vapour pressure of Ag increases much faster with temperature than the partial pressure in the nozzle does.

HÖVEL calculated some parameters for the represented source. For $M = 0$ the temperature in the nozzle is equal to the temperature in the heater and the partial pressure p_p is equal to the vapour pressure $p_v = p_p$. But if the Mach number increases, the temperature and thus the pressures decreases. The vapour pressure p_v decreases much faster than the partial pressure p_p. Thus the parameter in the nozzle for $M = 1$ are: $T = 1725\,\mathrm{K}$, $p_p = 208\,\mathrm{mbar}$, $p_v = 4.5\,\mathrm{mbar}$ [Hövel, 1995].

To summarise, the expansion of a heated gas through a heated supersonic nozzle leads to a decrease of the unordered motion of the particles. However, the ordered motion, emerging as super sonic expansion, increases which leads to a decrease of temperature, density and pressure. Because the decrease of partial pressure is much weaker than the decrease of the corresponding vapour pressure (depending on the temperature), aggregation can take place. These aggregation leads to a cluster growth in the nozzle. The clusters formed by this process have a narrow size distribution of about $2R = (2.0 \pm 0.6)\,\mathrm{nm}$ and a cluster beam velocity of about $v = 1500\,\mathrm{m/s}$. Thus the clusters consist of about 250 atoms and have a kinetic energy of about 300 eV/cluster. The maximal reachable deposition rate of the cluster beam is of about 9 nm/s.

3.2.2 Skimmer and cryogenic pumping stage

The use of electrical lenses is not possible because the majority of the clusters are electrical neutral. Only a negligible amount of the clusters are charged. The first orifice behind the source is the so-called skimmer. This skimmer cuts off the diffuse edge regions of the beam. This prevents interactions of the atoms and clusters in the centre of the beam with atoms of the outer regions of the beam. Because the skimmer cuts off unnecessary gas, the pressure in the experimental chamber is decreased. The skimmer is made of tantalum and heated up to about 2300 K. This is necessary to prevent the silver from aggregation on the skimmer which would lead to a closing of the orifice.

The skimmer is connected by a teflon isolation with a double-stage cryogenic pumping stage. The

first stage cools a hollow copper block down to about 40 K. This copper block is used as radiation shield and screens the first cooling stage from the heat radiation of the environment. The second cooling stage reaches a temperature of about 10 K. It is connected with a copper tube which surrounds the cluster beam. Gas that encounters with this copper tube is frozen out. Thus most of the argon carriers gas will be hold back by the cryogenic stage.

3.2.3 Mass selection

The latest implementation into THECLA are devices which enable a mass selection to decrease the width of the mass distribution of the source. The first part of the mass selection is an ionisation device, shown in Figure 3.10. The tungsten filament is heated up to temperatures where electrons

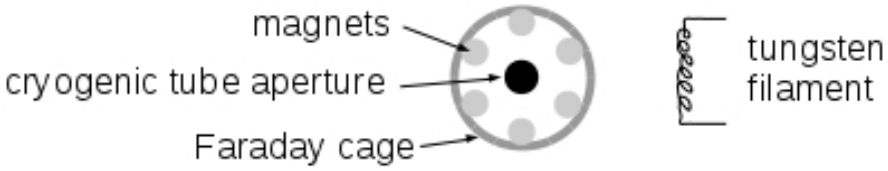

Figure 3.10: Ionisation device of the mass selection. The filament emits electrons which are accelerated from the filament towards the Faraday cage. In the cage the electrons are trapped by the magnetic field of the magnets which forces the electrons onto orbits around the cluster beam. The clusters then can be ionised by electron impact ionisation.

are emitted. A voltage at the filament accelerates the electrons in the direction of the Faraday cage. The Faraday cage cuts off the electric field lines of the filament but allows the electrons to enter the centre of the cage. Here the electrons are trapped by the magnetic field lines onto cyclotron orbits. The clusters leaving the aperture of the cryogenic tube can then be ionised by electron impact. The acceleration voltage is about $U = 100\,\mathrm{V}$ and electron currents of the magnitude mA can be reached. The design is based on the mass selection presented by GOLDBY [Goldby et al., 1997].

The ionised part of the cluster beam can be fanned out by a homogeneous electric field in the middle of the apparatus, generated by two parallel electrodes with a gap of about 2 cm. This field causes an acceleration of the clusters perpendicular to their flight direction. Because the velocity distribution of the clusters is very narrow [Hagena, 1991, Hagena et al., 1991], the deflection at a distinct point behind the electrodes is proportional to the mass of the clusters.

The current of the ionised clusters at different positions (perpendicular to flight direction, at a distinct deposition position) can be measured with a moveable Faraday cup. The Faraday cup is connected with a pico-amperemeter and can be floated to positive and negative potentials.

3.2.4 Deposition

Two kinds of depositions are possible with THECLA:

1. Deposition of clusters on solid samples or into solid matrices. Those experiments are typically performed at sample position 1 (Figure 3.7).

2. Deposition of clusters into liquids with negligible vapour pressure and normal up to high viscosity. Those experiments are typically performed at sample position 2 (Figure 3.7).

The deposition can be controlled by a shutter with a wedge-shaped aperture. The function of the shutter is illustrated and explained in Figure 3.11. By using the shutter to control the deposition it is possible to generate a deposition on a solid sample with a gradient of deposition amount. The samples themselves are mounted at a standard vacuum chamber manipulator. Thus the samples can be moved in the chamber in three directions and also the angle between the sample surface normal

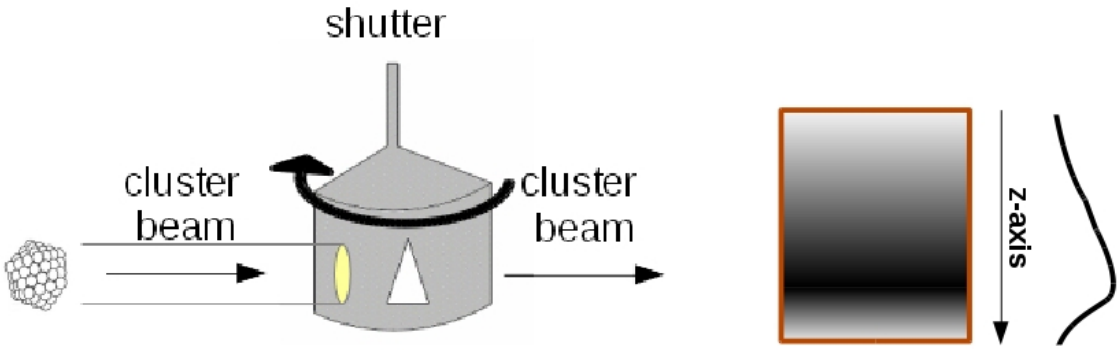

Figure 3.11: The shutter motion is powered by a step motor, controlled by a computer program. While moving the aperture through the cluster beam, the shutter is longer opened where the wedge-shaped aperture is broader. Thus at this position more clusters can reach the sample which leads to a higher deposition amount. The deposition amount decreases with decreasing width of the wedge-shaped aperture. It is also possible to move the shutter completely out of the beam.

and the cluster beam can be adjusted. It is also possible to move the sample out of the beam. This is necessary when the cluster rate should be controlled by a crystal oscillator (see below).

For deposition into liquids two special mixers were designed for these experiments. The latest version (mixer-2) is shown in Figure 3.12 and described in the following. This mixer consists of a tub and a roller which is mounted on an axis which is connected with a crown wheel. The crown wheel grips into a gearwheel which is mounted rotatable below the tub. This gearwheel can be connected in the experimental chamber with a magnetic rod manipulator which is connected with a step motor outside the vacuum chamber. The slits at the edges of the tub are used to fix the tub inside the experimental chamber. By this construction the motion of the step motor can be transferred to the roller which then turns in the tub. Also the position (height) of the mixer can be controlled by the manipulator.

The tub can be filled with a liquid with negligible vapour pressure. If the viscosity is not to small, the surface of the roller gets moistened by turning the roller. When driving the mixer into the cluster beam, the clusters get deposited into the liquid on the surface of the roller. These clusters then are mixed into the liquid at the bottom of the tub. The velocity of this mixing process is controlled by the control electronic of the step motor.

Two fused silica windows are mounted at the bottom of the tub, one at each head of the tub. Further the crown wheel has notches at the height of this windows. This enables optical measurements through the liquid of the bottom of the tube during the deposition process.

The tub, the roller, the axis and the window holder are made of stainless steel. To minimise the weight, the roller is hollow inside. It has four holes to enable a fast evacuation. The crown wheel and the gear wheel are made of aluminium. The axle bearing are made of bronze. At every point of construction several things were considered. The weight of the mixer should be small because of the limited force of the magnetic rod manipulator. Further, all used materials had to be high vacuum suitable. Finally, all materials which are in connection with the liquid had to be chemical resistant.

The tub, with mounted roller, was designed to contain a volume of approximately 15 ml. The volume should be large enough to enable macroscopic investigations like UV-Vis measurements (the volume of a cuvette is 3 ml).

First experiments were performed with the first build mixer (mixer-1) shown in Figure 3.13. Its function is the same as described before with some exceptions. Mixer-1 was made of aluminium to

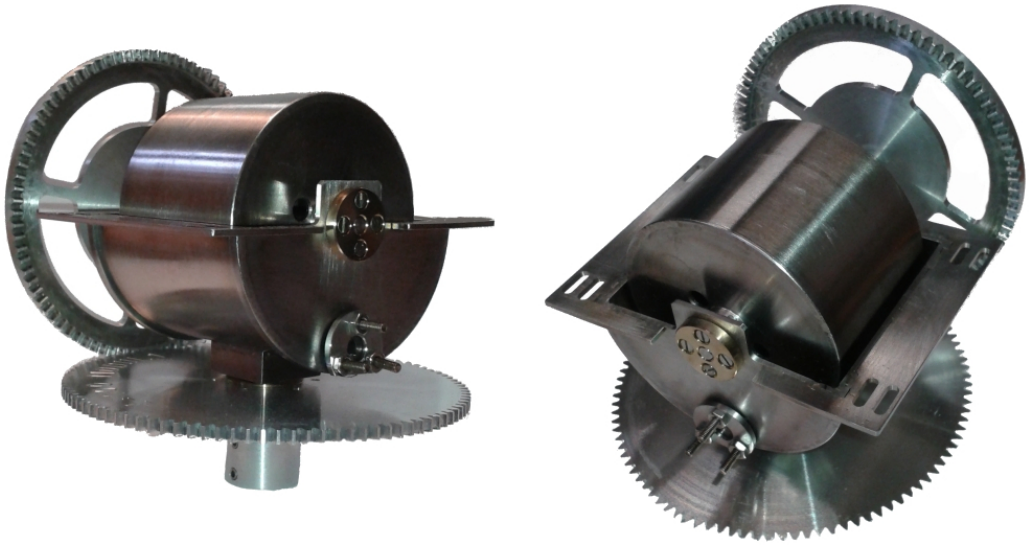

Figure 3.12: Mixer-2: volume ≈ 15 ml, material stainless steel, fused silica windows for in-situ measurements

minimise the weight. Later the roller and the inside of the tub were vaporised with gold[4]. The next difference to mixer-2 is its size. Because at the beginning of the first experiments on liquid systems one did not know how much liquid is used for the experiments after the deposition (XANES, UV-Vis, etc.), the tub was designed to contain a volume of approximately 20 ml. Finally mixer-1 was also designed without a window for in-situ measurements.

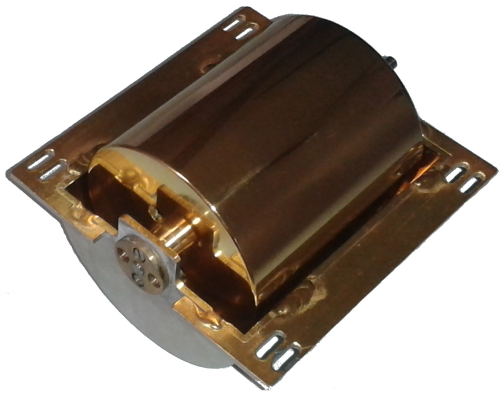

Figure 3.13: Mixer-1: volume ≈ 20 ml, material aluminium (vaporised with gold)

It should be noticed that because mixer-2 was completed approximately simultaneously with the gold-plating of mixer-1, no experiments in the present thesis had been performed with the glided version of mixer-1.

3.2.5 Other devices

In Figure 3.7 **windows** at the first and the second sample position are indicated. These windows consist of fused silica thus UV-Vis measurements can be performed in-situ.

The THECLA is also connected with a **quadrupole mass spectrometer** which enables the determination of residual gas particles up to a mass of 100 atomic mass units.

[4]To exclude the possibility of contaminations of the sample system by influences of the tub or the roller, the mixer-1 was vaporised with gold and mixer-2 was designed of stainless steel.

The experimental chamber can be separated from the cryogenic stage and the source by a **UHV gate valve**. This enables the removal of the sample while cryogenic stage is still running[5].

At the end of the chamber a **crystal oscillator** is mounted which can be used to measure the deposition rate of the source. However, the cluster current of the source is not stable over time and cannot be controlled during the deposition of clusters on a sample. Therefore, the cluster deposition rate before and after deposition is checked and its mean value (approximation of a linear decrease in time) is used to determine the amounts of deposited clusters. It should be noticed that this method has a limited accuracy. However, optical spectroscopy and XANES data can be used to cross-check the clusters coverage.

[5]Because the valve separates the source from the turbo molecular pump, it is not recommended to close the valve while the argon flow of the source is not stopped.

3.3 Optical experiments

In this section an insight in the setup and methods of measurements for the UV-Vis experiments should be given.

3.3.1 Optical setup

Reaction cell

Measurements on clusters in sulphur rich atmosphere cannot be performed in-situ in the vacuum chamber. A part of the sulphur would remain in the vacuum chamber and react with new produced clusters. These reactions would change or completely suppress the optical extinction signal. As a result no cluster characterising measurements in the vacuum would be possible. Therefore an old decommissioned X-ray sample cell was converted for UV-Vis measurements. The sample is shown in Figure 3.14. In the centre of the sample the solid samples with deposited clusters can be fixed. The kapton windows were replaced by thin polyethene foil[6]. Finally the sample cell can be placed on a mechanical Hubert table thus the sample can be measured at different positions. It is possible to use an inlet at the top of the lid to fill the cell with a distinct gas. The cell is also large enough to place an Erlenmeyer flask next to the sample.

Figure 3.14: Sample cell for ex-situ UV-Vis measurements at chemical reacted clusters in matrices.

Polariser

In the case of polarisation measurements, a polariser is used for s- or p- polarisation of the light. This polariser is placed between the focus lens and the sample.

Cuvette holder

The cuvette holder is used for optical measurements at liquid systems. The liquid can be filled into a cuvette with high transmittance in the UV-Vis region. The holder possesses integrated lenses, with also high transmittance in the UV-Vis region, which can be aligned by the user. The cuvette is fixed in the holder at a defined position which enables a good reproducibility of the measurements. To suppress influences of diffuse light in the laboratory the cuvette holder can be covered.

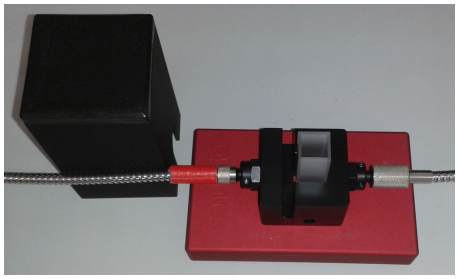

Figure 3.15: Utilised cuvette holder for optical measurements at clusters in liquids.

Lamp and spectrometer

The optical measurements were performed with an Avantes AvaLight-DH-S-BAL light source. This combined light source consists of a deep ultra violet deuterium lamp and a balanced halogen lamp and covers a wavelength range of $\lambda = 190\,\text{nm} - 2500\,\text{nm}$. For spectroscopy of solid samples the light is guided by a fibre optic cable and is focused on the sample by a silica lens. Behind the sample there is a second fused silica lens which collects the transmitted light and focuses it to the

[6] It was observed that simple clingfilm on the basis of polyethene has a good UV-Vis transmittance.

entrance of another fibre optic cable which is connected with a spectrometer [Hövel, 1995, Hoffmann, 2012]. The spectra are recorded using an Avantes AvaSpec-2048x14 spectrometer with a detectable spectral range from $\lambda = 200\,\text{nm}$ to $\lambda = 1100\,\text{nm}$ and a resolution of $\Delta\lambda = 1.4\,\text{nm}$.

3.3.2 Measurements

This section provides an overview about the optical measurements. Most measurements were performed like described here. Individual deviations will be discussed in their respective experimental section.

Before measuring the extinction of the clusters, the extinction of the embedding sample has to be measured, thus UV-Vis measurements are performed at the empty sample. After that, the clusters are deposited and the sample is measured at the same positions z.

The measurements are performed in transmission mode. This means the recorded spectra are normalised to a previously recorded reference spectrum. This reference should be updated regularly because the spectrum of the lamp can change with time[7]. A spectrum, measured through the vacuum chamber or an empty place of a fused silica sample, can be used as reference. This place should always be the same reference position.

With the intensity of the reference I_{ref}, the intensity of the empty sample I_{empty}, the intensity of the diffuse background I_{dark} and the intensity of the sample with the clusters I_{sample}, the transmissions T are given by

$$T_{\text{empty}}(z,E) = \frac{I_{\text{empty}}(z,E) - I_{\text{dark}}}{I_{\text{ref}}(E) - I_{\text{dark}}} \tag{3.7}$$

$$T_{\text{sample}}(z,E) = \frac{I_{\text{sample}}(z,E) - I_{\text{dark}}}{I_{\text{ref}}(E) - I_{\text{dark}}}\ . \tag{3.8}$$

These transmissions correspond to normalised intensities. Thus, with equation 2.59 and $T_{\text{empty}} \leftrightarrow I_0$ and $T_{\text{sample}} \leftrightarrow I_0$, it follows for the cluster transmission T_{cluster} and cluster extinction σ_{cluster}

$$T_{\text{cluster}}(z,E) = \frac{T_{\text{sample}}(z,E)}{T_{\text{empty}}(z,E)} \tag{3.9}$$

$$\sigma_{\text{cluster}}(z,E) = -\lg\left(T_{\text{cluster}}(z,E)\right) \tag{3.10}$$

$$= \lg\left(T_{\text{empty}}(z,E)\right) - \lg\left(T_{\text{sample}}(z,E)\right)\ . \tag{3.11}$$

UV-Vis spectroscopy with polarised light

Measurements with polarised light are carried out by using the polariser described above. The experimental setup is based on Figure 2.19 and similar to that of HILGER [Hilger, 2001]. To measure the plasmon resonances along the c axis, an angle of $\varphi = 90°$ (angle between surface normal and incident light beam) has to be chosen. But this is practically not manageable. Thus an angel of $\varphi = 70°$ is chosen which enables the deposition of clusters and the measurement of their extinction simultaneously.

The extinction of the s-polarised light is given by the extinction cross section along the a axis. But the extinction of the p- polarised light is a superposition of the extinction of the c and $b = a$ axes (for $\varphi = 90°$ the extinction of the p- polarised light would be given only by the extinction cross section of the c axis). Thus the extinction of the p- polarised σ_p light is given by

$$\sigma_p = \sigma_a \cos^2(\varphi) + \sigma_c \sin^2(\varphi) \tag{3.12}$$

[7] The spectrum of the lamp contains characteristic emission lines with high intensities. Small energetic shifts, negligible in the majority of the spectrum, can cause strong signals after normalisation in the vicinity of these characteristic peaks.

while the extinction of the s- polarised light is independent from the angle

$$\sigma_p = \sigma_a \ . \tag{3.13}$$

In-situ UV-Vis spectroscopy at liquid samples

The measurements on cluster-liquid systems during depositing the clusters into the RTIL are performed as following. First the integration time of one measurement has to be much larger than the time of one rotation of the roller. Then with closed shutter, the mixer has to be placed that the cluster beam hits the roller and the light beam the fused silica windows of the tub. Then the lenses have to be aligned so that the intensity is maximal and a reference spectrum has to be recorded[8]. Finally the shutter can be opened and spectra are recorded continuously.

Ex-situ UV-Vis spectroscopy at liquid samples

For clusters deposited into RTILs, the clusters are homogeneously solved in the ionic liquid after deposition. Thus there is no z dependence. A sample of pure RTIL without clusters is used as reference. This reference sample is placed in the experimental chamber during the deposition experiment to enable the same degas process like the RTIL in the tub. The extinction of these samples can be investigated as functions of time.

[8] A first alignment has to be done before the experiment is started.

3.4 XANES experiments

XANES experiments were carried out at third generation synchrotron sources. The Ag L_1 and L_2 absorption edges were investigated at the high brilliance beamline ID26 [Gauthier et al., 1999] at the European Synchrotron Radiation Facility (ESRF) in Grenoble, France. The Ag L_3 absorption edge was investigated at beamline BL8 [Lützenkirchen-Hecht et al., 2009] at the Dortmund Elektronenspeicherring Anlage (DELTA) in Dortmund, Germany. All measurements were performed in fluorescence mode. In this section the setup of the beamlines and the used equipment will be presented. Also an overview to the data preparation will be given.

3.4.1 BL8 @ DELTA

DELTA is a synchrotron radiation source of the third generation. It operates with electrons of an energy up to 1.5 GeV and an electron current up to about 120 mA. The X-ray radiation of beamline BL8 is generated by a superconducting asymmetric wiggler. The energy of the Ag L_3 X-ray absorption edge is $E_{\mathrm{Ag\ L_3}} = 3351.10\,\mathrm{eV}$. This energy can be selected from the X-ray radiation, generated by the wiggler, by using a Si(111) or InSb(111) double-crystal monochromator. After beam collimation by slits, the size of the beam is about $1 \times 5\,\mathrm{mm}^2$ (vertically $\times$ horizontally). The storage ring is directly connected with an UHV vacuum chamber in which the sample and the detectors are located. The absence of Be windows in this setup enables a higher photon flux (up to about $3 \cdot 10^9$ photons per second) especially for low energy experiments. The vacuum chamber has to be pumped for more than 10 hours before the pressure in the chamber is low enough to open a valve, which connects the vacuum chamber with the beamline and the storage ring. In the chamber two Amptek XR-100SDD Silicon Drift Detectors (SDD) with an energy resolution of about $\Delta E = 150\,\mathrm{eV}$ are mounted. Thus the measurements were performed in TFY mode.

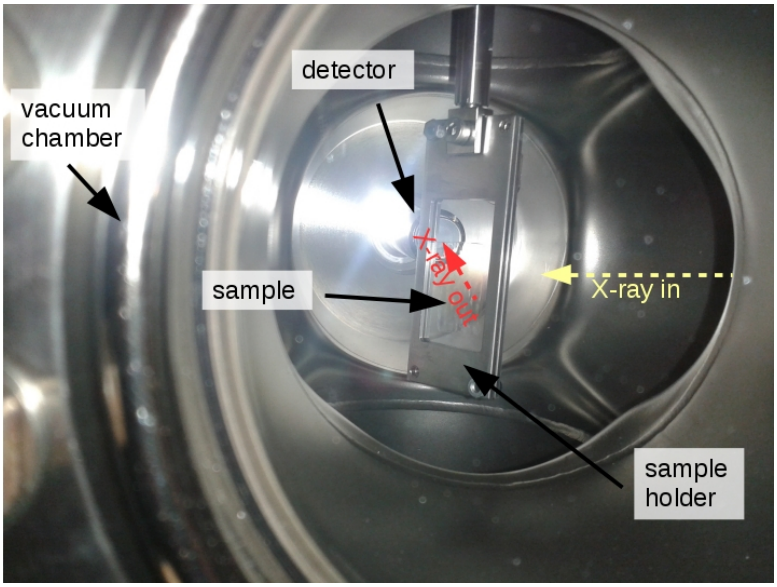

Figure 3.16: Photo of the vacuum chamber at BL8. The sample is mounted with an angle $\varphi = 45°$ of its surface normal to the impinging beam and the detector.

The measurements started 60 eV below and stopped 100 eV above the absorption edge. Due to a better exploitation of beamtime the data points of the measurements were chosen not equidistantly. The data point density in the region 60 eV to 20 eV below the absorption edge was chosen to 1 data point per eV. In the region around the edge, from 20 eV below up to 40 eV above, the data point density was 2 points per eV. Above the edge, in a region from 40 eV to 140 eV above the edge, the data points were chosen to be 1 data point per eV.

The sample holder can be moved in z-direction by controlling a motor driven manipulator. Thus it is possible to measure at different points at the sample with different deposition amounts.

3.4.2 ID26 @ ESRF

The ESRF is a third generation synchrotron which operates at an electron energy of 6 GeV with a maximal current of 200 mA.

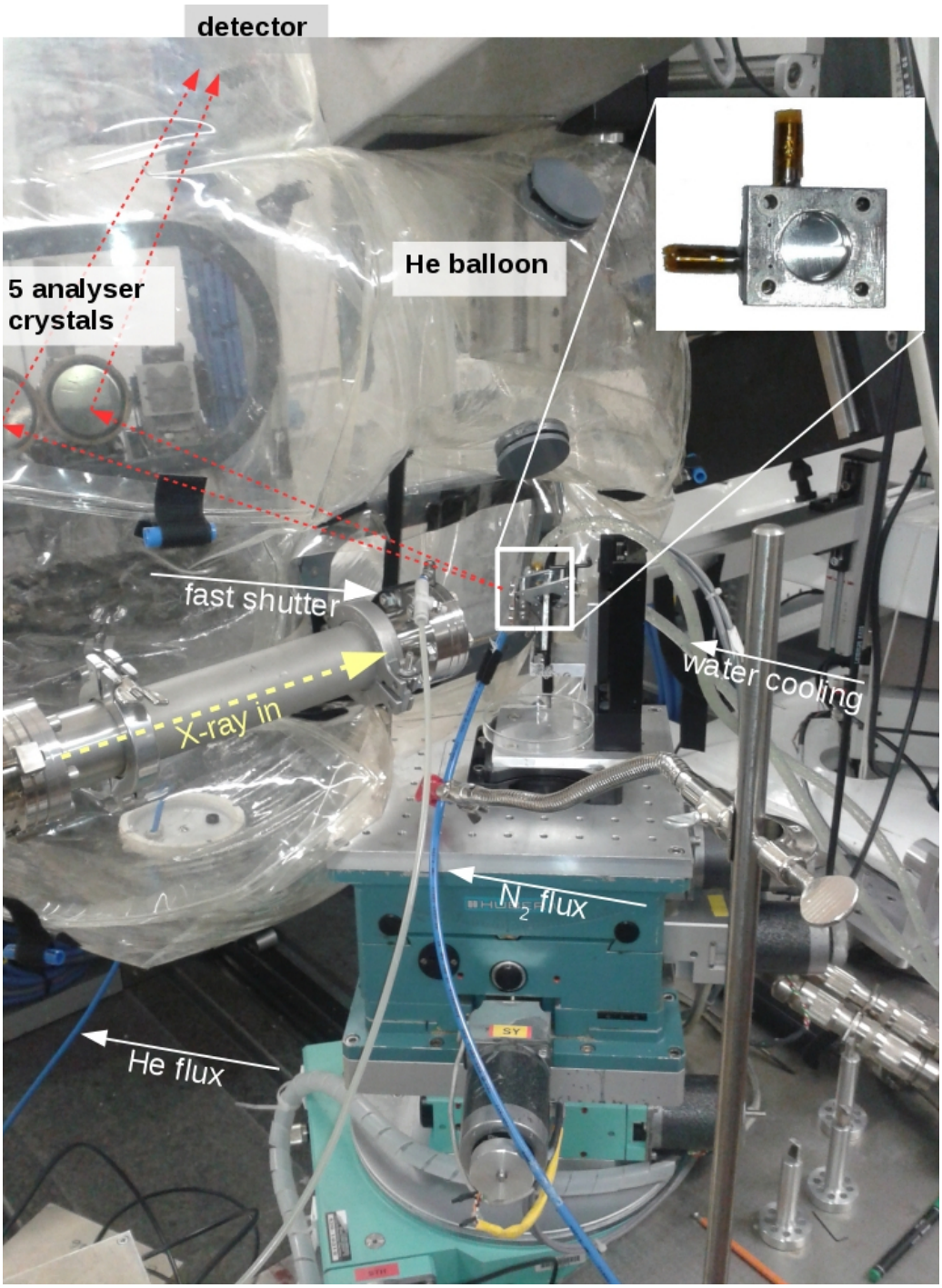

Figure 3.17: ID26 with mounted coolable and heatable cell for liquid samples (see text).

The beamline ID26 at the ESRF is a high brilliance X-ray spectroscopy beamline for X-ray absorption and emission spectroscopy (XAS and XES) experiments. The X-ray radiation is generated by three

mechanically independent undulators[9]. A Si(111) monochromator yields a photon flux of $> 10^{13}$ photons per second. This flux is measured by an ionisation chamber. The experimental setup is shown in Figure 3.17.

The flight path ends with a Be window about 10 cm before the sample. The illumination duration of the sample can be controlled by a fast shutter. The sample is mounted in an angle of about $\varphi = 45°$ between surface normal and impinging X-ray beam. The beam size is $150 \times 600\,\mu\text{m}^2$ (vertically $\times$ horizontally). The emitted fluorescence radiation is collected and focused by five analyser crystals. The reached PFY has an energy resolution of about $\Delta E \approx 0.1\,\text{eV}$. To minimise X-ray absorption, a He balloon is placed between the sample, the analyser crystals and the detector. The energies of the Ag L_2 and Ag L_1 X-ray absorption edges are $E_{\text{Ag L}_2} = 3523.70\,\text{eV}$ and $E_{\text{Ag L}_1} = 3805.80\,\text{eV}$.

Figure 3.17 shows the setup for experiments at clusters in RTILs. The cell can be cooled and heated by a water chiller. To prevent the window of the cell from water aggregation, a continuous flow of nitrogen is adjusted in front of the cell window.

Figure 3.18 shows the setup for experiments at clusters embedded in solid matrices. In former experiments, radiation damages (oxidation of the Ag clusters) could be observed during measurements [Hoffmann, 2012]. Therefore a vacuum chamber was installed. On the one hand this prevents the Ag clusters from oxidation when the cell is evacuated. On the other hand also the aimed investigation of the oxidation process of Ag clusters is possible. The pressure in the cell can be controlled by a vacuum gauge and is about $p \approx 2\,\text{mbar}$ when the cell is completely evacuated. The pressure in the cell can also be varied by partly opening the vent valve while a pump is running and the pump-valve is open.

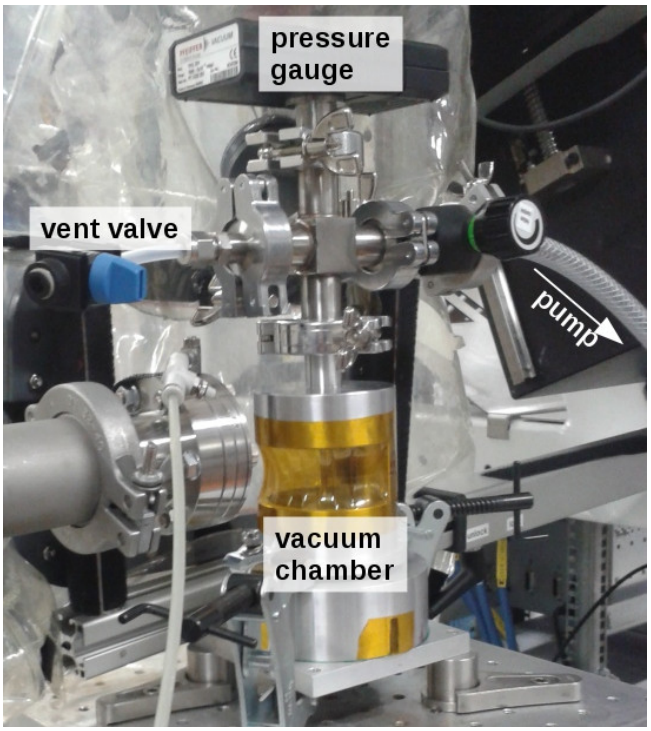

Figure 3.18: ID26 with mounted vacuum cell for solid samples (see text).

3.4.3 Data preparation

The first step in the preparation of the recorded data is the reduction of the spectra from influences of the monochromator and the intensity of the electron beam in the storage ring. This is done by normalising the intensity of every recorded fluorescence spectrum $I^{(i)}(E)$ to the intensity of the

[9] http://www.esrf.eu/UsersAndScience/Experiments/ElectStructMagn/ID26/Characteristics

impinging beam $I_0^{(i)}(E)$

$$\tilde{y}^{(i)}(E) = \frac{I^{(i)}(E)}{I_0^{(i)}(E)} \ . \tag{3.14}$$

The errors of the intensities are given by $\sqrt{I}$ and $\sqrt{I_0}$[10] because the detected counts follow the Poisson distribution. The error of $\tilde{y}^{(i)}(E)$ is indicated with $\tilde{y}e^{(i)}(E)$.

For a better observation of changes of the sample, for example due to beam damages, the measuring time of the single spectra is chosen to be preferably small[11]. Thus the spectra, which were recorded under the same conditions and for which no changes could be observed, have to be add up. The weighted sum $\tilde{y}(E)$ and its error $\tilde{y}e^{(i)}$ follow by[12]

$$\tilde{y}(E) = \sum_i \left(\frac{\tilde{y}^{(i)}(E)}{\tilde{y}e^{(i)^2}(E)} \right) \Bigg/ \sum_i \frac{1}{\tilde{y}e^{(i)^2}(E)} \tag{3.15}$$

$$\tilde{y}e(E) = 1 \Bigg/ \sqrt{\sum_i \frac{1}{\tilde{y}e^{(i)^2}(E)}} \ . \tag{3.16}$$

To get the XANES signal which is only produced by the Ag clusters, the background in each spectrum has to be subtracted. The background is a result of the Z^4/E^3 depending X-ray absorption behaviour of matter. Thus the background is not constant but decreases with E^3 with increasing E. As typical in XANES data preparation E^3 is fitted by a linear function. This is a good approximation because the investigated energetical region at the near edge region is only small compared with the absolute energy of the absorption edge. Thus for subtracting the background, the spectrum is fitted in the pre-edge region with a linear function. In this region only the background should cause any signal. This fit is extrapolated to the complete spectrum and after that subtracted from the spectrum.

For a better comparison, the spectra are normalised to an integral of each spectrum in a distinct energetic range, to have equal intensities. Finally the spectra are smoothed to suppress statistical noise.

[10] Because $I_0 \gg I$, the error of I_0 can be neglected in an error propagation.

[11] If the sample would change its properties during a long measurement, the energetically lower part of the spectrum would be recorded from the sample in its initial state. The middle part of the spectrum would attributed to an intermediate state. And the energetically higher region of the spectrum would be recorded from the sample in its final state.

[12] $X = \left(\sum_i g^{(i)} X^{(i)} \right) / \sum_i g^{(i)}$ where the weighting coefficient is given by $g^{(i)} = \frac{1}{Xe^{(i)^2}}$.

4 Results of experiments on Ag clusters in PDMS

Polydimethylsiloxane (PDMS) is of great interest in optical and electrical technologies. This is reasoned by especially two points of its numerous properties: PDMS is transparent in the visible optical region and it is very stretchable. These properties in composition with its acquisition and manufacturing costs make it to an attractive polymer for example in the use as wave-guides [Cai et al., 2008].

Another area of application for PDMS is investigated by the group of MILANI. Here stretchable, reflective, optical gratings are produced by supersonic cluster beam implantation into PDMS [Ghisleri et al., 2013]. To tune the optical properties of those nanocomposite devices, investigations on clusters in PDMS have to be done. While the group of MILANI deal with large deposition amounts of Ag and Au clusters resulting in conductive films, our group is interested in the single particle properties of clusters in PDMS. This was discussed by HOFFMANN [Hoffmann, 2012]. Here Ag clusters with a mean diameter of about 2 nm were deposited with THECLA (section 3.2) into (0.5 ± 0.2) µm and (1.2 ± 0.2) µm thick PDMS films on fused silica produced by spin casting [Salmen, 2011]. Among others, a double peak structure in the plasmon resonance spectra was observed for the 0.5 µm thick sample but not for the 1.2 µm thick sample. One possible explanation was the coalescence of clusters which were able to pass through the PDMS film and started nucleation in the interlayer between the fused silica and the PDMS. Not at least this observation is a motivation for further investigations of the optical and electronic properties of Ag clusters deposited into PDMS.

4.1 Investigation using UV-Vis spectroscopy

The sample in this experiment was produced by bringing the PDMS in the liquid phase onto fused silica glass by a stainless steel applicator. This causes a 30 µm thick PDMS film. The PDMS then was processed further like described in section 3.1.1. On this sample three deposition spots were placed with 0.05 ML, 0.33 ML and 1.09 ML (illustrated in Figure 4.1). The integrated extinctions of the plasmons in an energetic range from $1.601 - 4.002$ eV are shown in Figure 4.2.

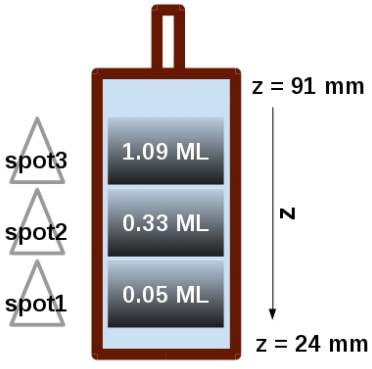

Figure 4.1: Illustration of the deposition profile of the PDMS sample investigated with UV-Vis. The position information and the illustrated deposition spots serve only for illustration and must not correspond with the real geometry of the sample. The deposition amounts were measured with the crystal oscillator and correspond to the mean deposition amount.

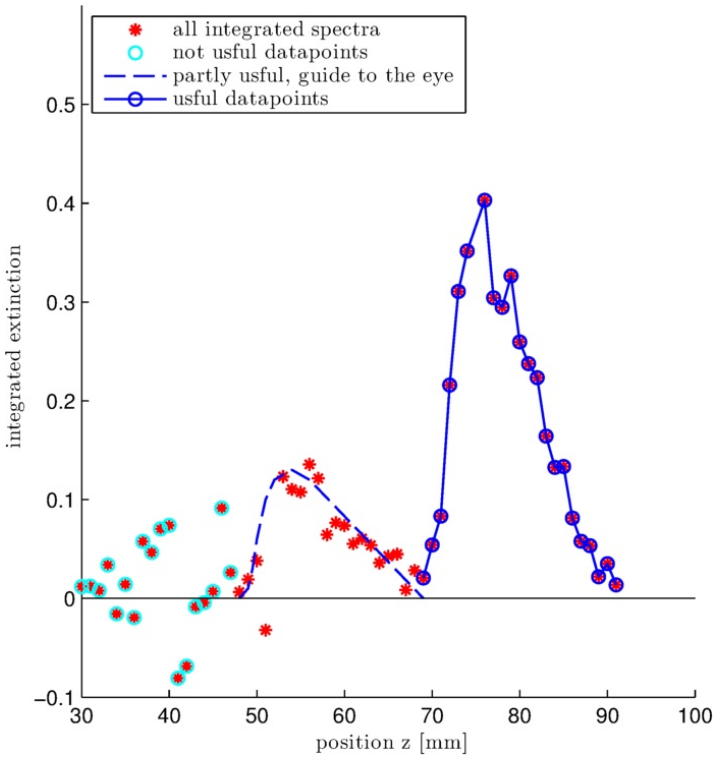

Figure 4.2: Deposition profile of integrated extinctions in an energetic range from $1.601 - 4.002\,\mathrm{eV}$. Because of the low deposition amounts of the first deposition spot, most of the cluster plasmons are not intensive enough to differentiate them from the background signals (despite background subtraction). Therefore only the 1.09 ML coverage can be identified (solid line). The deposition spot with a coverage of 0.33 ML can only partly identified. The problem is that the deposition gradient does not increase monotonously. Thus a "guide to the eye" line (dashed line) must be used to determine the deposition amounts. The 0.05 ML coverage cannot be identified at all.

This also illustrates the problem with the handling of the reference measurements. If the alignment of the sample before the deposition of the clusters (reference measurements) differs only slightly from the alignment after the deposition (cluster extinction measurements), the spectra are influenced by the structure of the PDMS. The extinction spectra can then be dominated by effects of the PDMS, especially for low cluster depositions. A detailed discussion of this effect and how it can be handled is given in the appendix (section 8.3). An example of this effect is given in Figure 4.2 where the integral of the plasmons is negative for some measurements on clusters with low deposition amounts.

4.1.1 Polarisation measurements

For a better investigation of the shape of the clusters in PDMS, cluster plasmon resonance measurements were performed with polarised light. The light was polarised and focused on the surface of the sample with an angle of $\varphi = 70°$ between the surface normal and the light beam. Because these measurements are very sensitive to this angle, the alignment of the sample and the optics was not changed during the reference measurements and the cluster plasmon resonance measurements. Only the alignment of the polariser had to be changed between s- and p-polarisation between reference measurements and cluster extinction measurements. The disadvantage of this method is that for each measurement a new deposition spot had to be placed on the sample. Thus only three deposition amounts were investigated by measurements using polarised light. The results are shown in Figure 4.3. The peak positions and the FWHM of the cluster plasmons with different deposition amounts

are listed in Table 4.1. It has to be mentioned that the optical measurements were not performed at precisely that position on the sample, where the mean deposition amounts were determined. Thus the stated coverages can differ slightly from the actual ones. The FWHM were calculated by the double distance between the position of the peak and the position where the low-energetic flank of the spectrum has half the height of the maximum intensity. This method prevents influences to the FWHM by the onset of interband transitions on the high energetic flank.

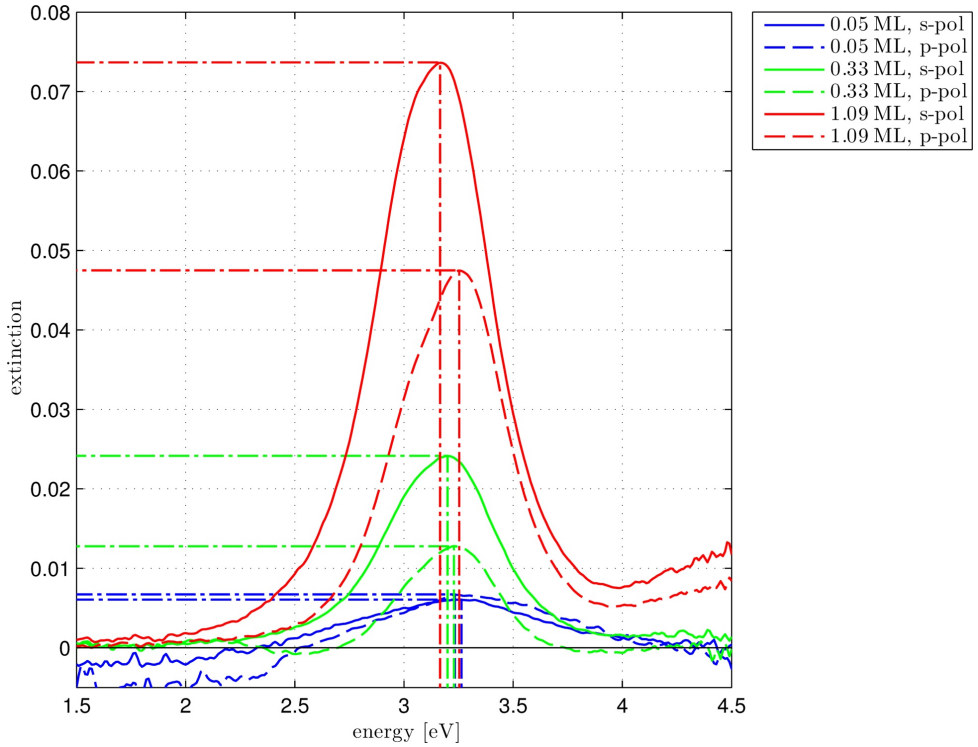

Figure 4.3: Cluster plasmon resonances of Ag clusters deposited into PDMS, measured in vacuum with polarised light and an angle of 70° between surface normal and light beam direction.

deposition	peak position [eV]		FWHM [eV]		peak height	
amount [ML]	s-pol	p-pol	s-pol	p-pol	s-pol	p-pol
0.05	3.26	3.23	1.08	0.74	0.006	0.007
0.33	3.20	3.23	0.66	0.52	0.024	0.013
1.09	3.17	3.25	0.68	0.66	0.074	0.048

Table 4.1: Peak positions and FWHM of the cluster plasmon resonances along the short (p-polarisation) and the long (s-polarisation) clusters axes of deposited clusters with different deposition amounts.

The energetic position of the clusters with a deposition amount of about 0.05 ML are 3.26 eV for the measurement with p-polarised light and 3.23 eV for the measurement with s-polarised light. Such a behaviour would indicate a prolate structure of the clusters which is not expected. Instead, this is attributed to an experimental error due to the low intensity of the plasmon resonances of the clusters, caused by the extremely low deposition amount, compared with the thickness of the sample. Thus for further discussions only the deposition spots with mean deposition amounts of 0.33 ML and 1.09 ML are used.

It can be recognised from Figure 4.3 that the shift between the peaks of the long $a-$axis (measured

by s-polarised light) and the short $c-$axis (measured by p-polarised light[1]) increases with increasing deposition amounts. This is an indication for the beginning of electromagnetic coupling or coalescence.

The fraction of the heights of the plasmon resonance peaks of the measurements in s-polarisation and p-polarisation are $h_{\text{s-pol}}^{0.33\,\text{ML}}/h_{\text{p-pol}}^{0.33\,\text{ML}} = 1.892$ and $h_{\text{s-pol}}^{1.09\,\text{ML}}/h_{\text{p-pol}}^{1.09\,\text{ML}} = 1.551$.

These measurements are compared with simulated spectra presented in Figure 4.4 and Figure 4.5 for uncoupled, separated clusters with a diameter of 2 nm. The chosen damping constant A, the axial ratio $u = c/a \leq 1$ and a normalisation constant G are listed in Table 4.2. The parameters u and A were chosen to reproduce the peak positions/shift and the width of the peaks. The normalisation constant was chosen so that the simulated and measured spectra with s-polarised light have the same peak height (see section 2.3.6). The permittivity of the PDMS was chosen to be $\varepsilon_m = 1.9$ (see section 3.1.1) for all simulations.

Using (2.60) in connection with the determined normalisation constant G, the mean deposition amounts d_{eff} can be cross checked. The results are also listed Table 4.2. These are unexpected good matches because the heights of the simulated and measured plasmons were compared using s-polarised light. A comparison by using p-polarised light would lead to worse matches. Also the positions where the plasmons were measured and where the deposition amounts were measured did not match precisely. It is possible that some of these influences compensated each other.

	0.33 ML	1.09 ML
A	0.78	0.82
u	0.94	0.91
G	24.56 nm^2	7.78 nm^2
d_{eff}	0.32 ML	1.02 ML

Table 4.2: Chosen parameters for the simulated plasmon resonances of Ag clusters in PDMS, which were measured in vacuum with polarised light.

	experiment	simulation
s-pol	3.20 eV	3.17 eV
p-pol	3.23 eV	3.23 eV

Table 4.3: Peak positions of the spectra shown in Figure 4.4

It is remarkable that the widths of the measured spectra of the cluster with 0.33 ML and 1.09 ML coverage are relatively narrow. To simulate these widths, a damping constant A smaller than 1 had to be chosen in both cases.

For 0.33 ML cluster coverage, the ratio of the heights of the peaks cannot be modelled by the simulations. While the peaks of the simulated spectra have nearly the same heights, the peak heights of the measured spectra differ approximately by a factor 2. One reason can be an error which occurred during the measurement with p-polarised light. In the region of about 2.5 eV and 4 eV the extinction is smaller than zero. This can be caused by an alignment error of the polariser: The references have to be measured in both polarisation modes. Thus between the first reference measurement and the last cluster extinction measurement the adjustment of the polariser is changed. An uncertainty at restoring the adjustment would cause these deviations.

The energetic positions of the simulated peaks are shifted slightly to lower energies. This can be described by a small amount of vacuum permittivity to the permittivity of the embedding material $\varepsilon_m = P \cdot \varepsilon_{PDMS} + (1 - P) \cdot \varepsilon_{vacuum}$. If P would be chosen to be about $P = 0.95$, the energetic positions of the plasmon peaks of the measured and simulated spectra would agree. But in that case

[1] also about 10 % of the long $b-$axis is excited

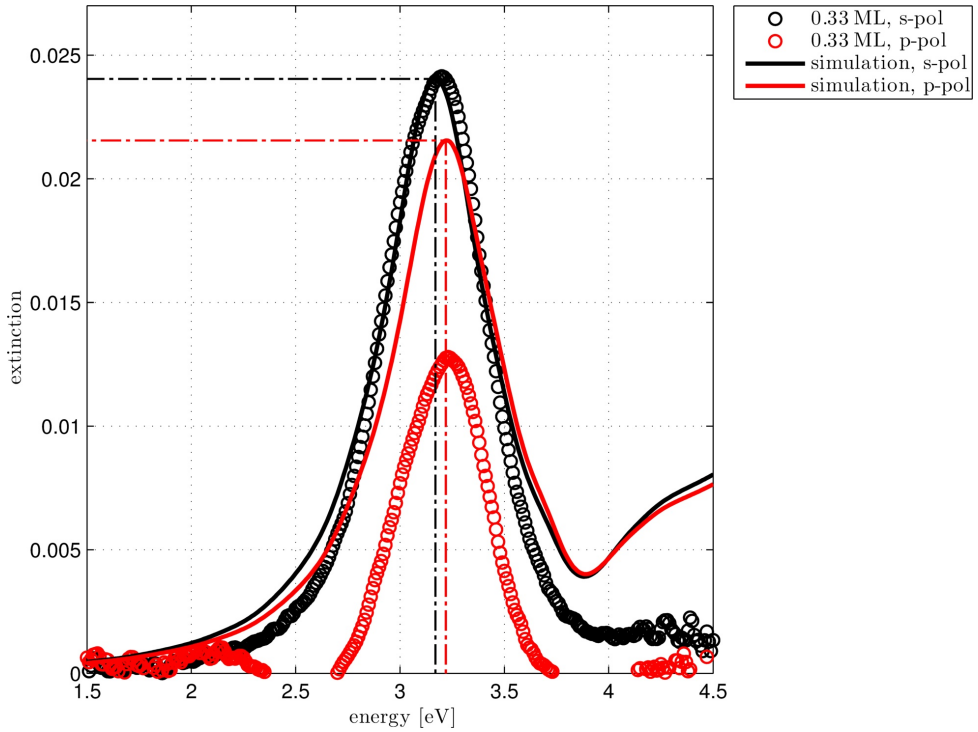

Figure 4.4: Measured and simulated cluster plasmon resonance spectra of Ag clusters deposited into PDMS (deposition amount ≈ 0.33 ML), measured in vacuum with s- and p- polarised light with an angle of $\varphi = 70°$.

the positions of the flanks of the measured and simulated spectra would disagree. This may be an uncertainty in the determination of ε_m as well (see section 3.1.1).

For 0.33 ML cluster coverage, the different peak positions of the measured spectra in s- and p-polarisation correspond to an axial ratio of about $u = c/a \approx 0.94$ in the spheroidal cluster model. While depositing Ag clusters onto fused silica, a deformation of abut $u = 0.84$ was observed by HÖVEL [Hövel, 1995]. By this, two statements can be made: First, the clusters are relatively soft landed as indicated by the value of u close to 1. Furthermore, the amount of clusters which can be deposited without strong coalescence or electromagnetic coupling is larger than on a fused silica surface. This indicates that the clusters penetrate into the PDMS like it was expected. Secondly, the clusters do not form oblate islands at this point of deposition amounts.

	experiment	simulation
s-pol	3.17 eV	3.16 eV
p-pol	3.25 eV	3.24 eV

Table 4.4: Peak positions of the spectra shown in Figure 4.5.

The plasmon resonance spectra of Ag clusters in PDMS with a mean deposition amount of about 1.09 ML are shown in Figure 4.5. In contrast to the spectra in Figure 4.4, a misalignment of the polariser was prevented. However, the ratios of the cluster plasmon peak heights of the simulated spectra do not coincide with those of the measured spectra.

As compared with the spectra of clusters with a deposition amount of 0.33 ML, the FWHM of the spectra with coverages of 1.09 ML, increased (Table 4.1). This can also be observed by an increase of the damping constant used for the simulated spectra. The increase of the FWHM and the damping constatn A can be explained by the emerge of a broader size distribution of the clusters in the PDMS which is caused by small amounts of coalesced clusters. However, most clusters are still separated.

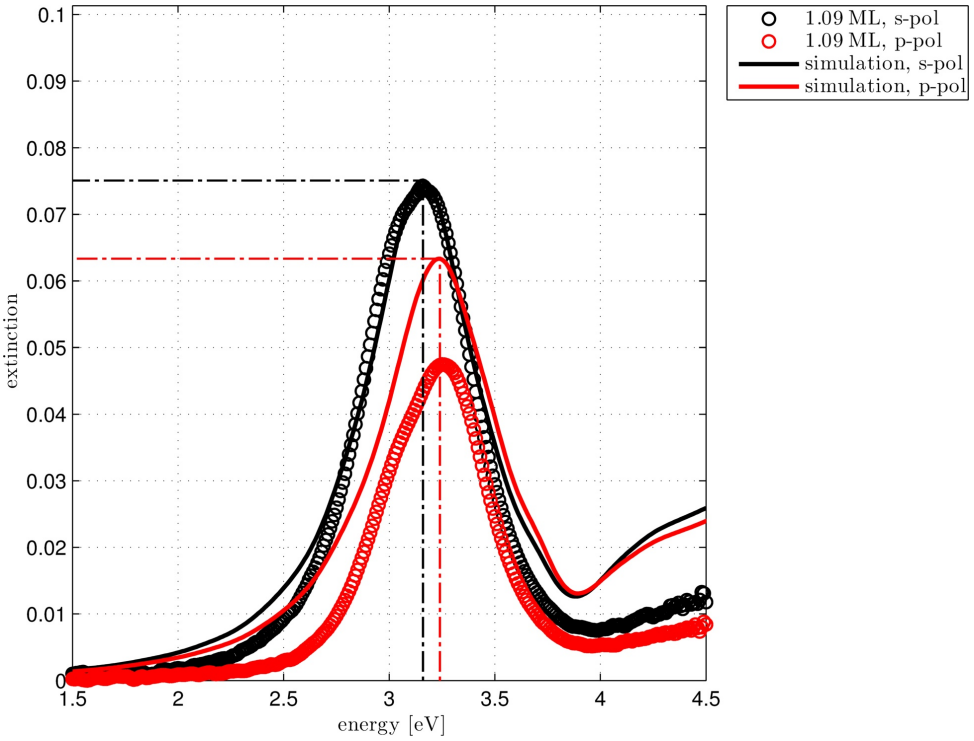

Figure 4.5: Measured and simulated cluster plasmon resonance spectra of Ag clusters deposited into PDMS (deposition amount $\approx 1.09\,\mathrm{ML}$), measured in vacuum with s- and p- polarised light with an angle of $\varphi = 70°$.

The difference between the peak positions of the measured spectra in s- and p-polarisation increased for the higher deposition amount. The axial ratio decreased to $u = 0.91$.

The most remarkable observation in the measured spectra is the appearing of a shoulder between about 3 eV and 3.1 eV. This coincides with the observations made by HOFFMANN [Hoffmann, 2012]. The double peak structure cannot be explained by the simulated spectra. Because it also appears in the spectra recorded with s-polarised light, where only the a axis of the cluster is excited, a geometrical effect of single clusters can be excluded.

It is more likely that the clusters started electromagnetic coupling which results in an anisotropy in the interaction with light. QUINTEN calculated the cluster plasmon resonance signals for an ensemble of 64 statistically deposited Ag clusters with a mean diameter of about 6 nm on a substrate with the refraction index $n = 1.71$. These data were digitalised and plotted in Figure 4.6.

In the left plot of Figure 4.6 the cluster extinctions isolated clusters (red circles) and interacting clusters in s- and p-polarisation (green and blue circles, respectively) are plotted. The angle between the surface normal and the light beam is 0°. The electromagnetic interaction of the clusters does not change the shape of the spectra significantly but causes a shift of the plasmon resonance to lower energies. The spectrum of isolated clusters is compared to the spectrum of a spherical cluster in dipole approximation (red line). This spectrum was calculated for a spherical Ag cluster (equation 2.38) with a diameter of 6 nm. For a comparison the other parameters had to become $A = 0.8$ and $\varepsilon_m^{eff} = 2.85$. This matches approximately with the permittivity used by QUINTEN $\varepsilon_m = n^2 = 2.92$.

When changing the angle between the surface normal and the light beam to become 60°, the spectrum of the isolated clusters does not change but the spectra of the interacting clusters split up. This is shown in the right plot of Figure 4.6 (circles). However, a similar behaviour can be observed for isolated spheroidal clusters and is shown by the solid lines. Using the parameters determined above ($A = 0.8$ and $\varepsilon_m^{eff} = 2.85$), an axial ratio of $u = 0.75$ had to be chosen to generate a good match of

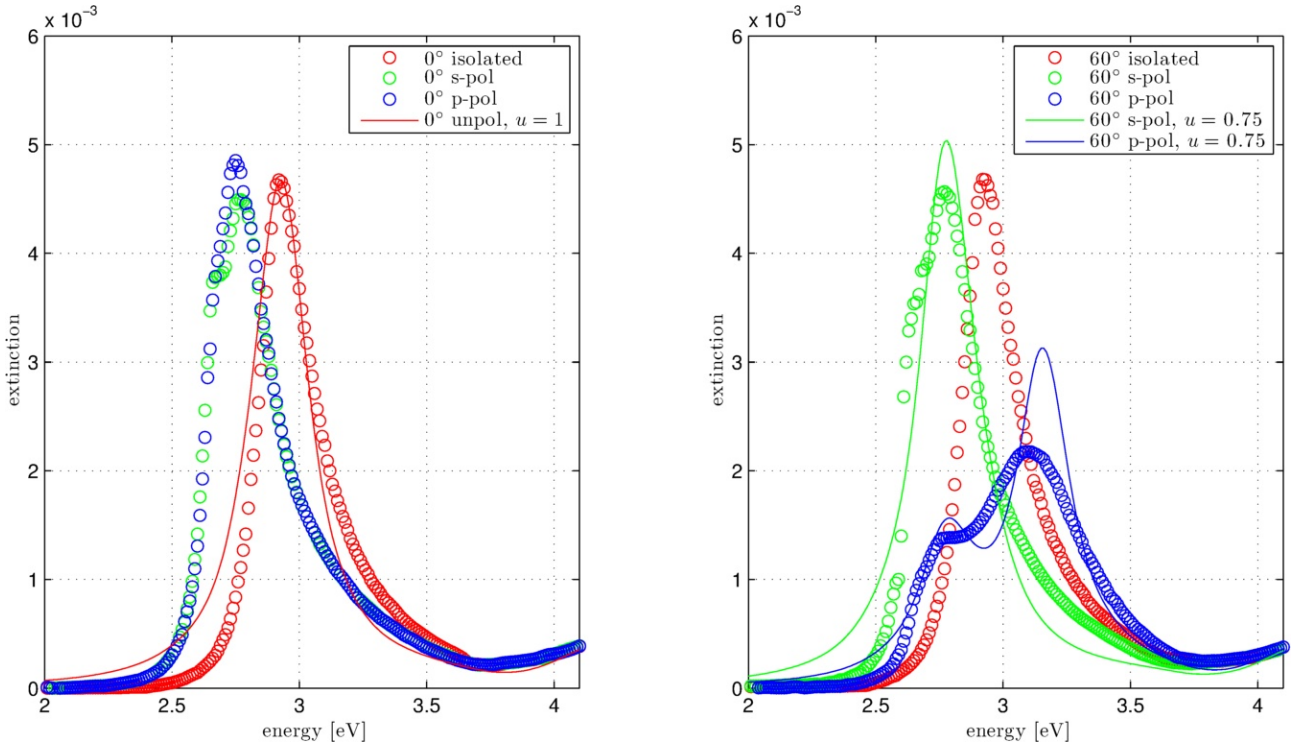

Figure 4.6: Simulation of the cluster plasmon resonance spectra of 64 statistically deposited Ag clusters on a substrate ($\varepsilon_m = n^2 \approx 2.92$) with a mean diameter of 6 nm. The red, green and blue coloured circles are data taken from QUINTEN [Quinten, 2010]. In the left plot the simulation for an angle of 0° between the surface normal and the light beam are shown. In the right plot the angel is 60°. The data of QUINTEN are compared to simulated extinction spectra of non interacting spheroidal Ag clusters (solid lines, see text).

the s-polarised spectrum with the simulations of QUINTEN.

Both simulations display an anisotropy effect. The spectrum of p-polarised light and an angle of 60° exhibits a clearly visible double peak structure for spherical interacting clusters and for isolated spheroidal clusters. So, the anisotropic effect caused by electromagnetic coupling can be simulated, up to a certain point of correctness, by using the model for distorted clusters.

Finally, it seems to be the most appropriate assumption that the double peak structure observed in the spectra of clusters in PDMS should be attributed to the starting of electromagnetic coupling of the clusters in the material. The occurrence of a double peak structure in s-polarisation, different to the cluster extinction spectra of clusters on fused silica, can then be attributed to the possible interaction in three dimensions for PDMS instead only two dimensions for fused silica. While the clusters on fused silica are located in one plane, the clusters in PDMS can form different layers due to different cluster implantation depths. Thus the plasmon resonance spectra of clusters in PDMS is dominated, up to a certain deposition amount, by the electromagnetic interactions. At a point of high deposition amounts (> 1 ML), the coalescence effects begin to dominate the coupling effects. For this see also Figure 2.20.

4.1.2 Influence of air

The cluster extinction spectra measured with unpolarised light ($\varphi = 0°$) after subtracting the background of clusters in PDMS at a fused silica substrate are shown in Figure 4.7a and Figure 4.7b. The spectra in Figure 4.7a are from clusters in vacuum and in Figure 4.7b from clusters in vacuum after

exposure the clusters for about one hour to air[2]. The maxima of the spectra are indicated by dots and FWHM with bars. Despite a careful selection of the analysed spectra and a detailed background sub-

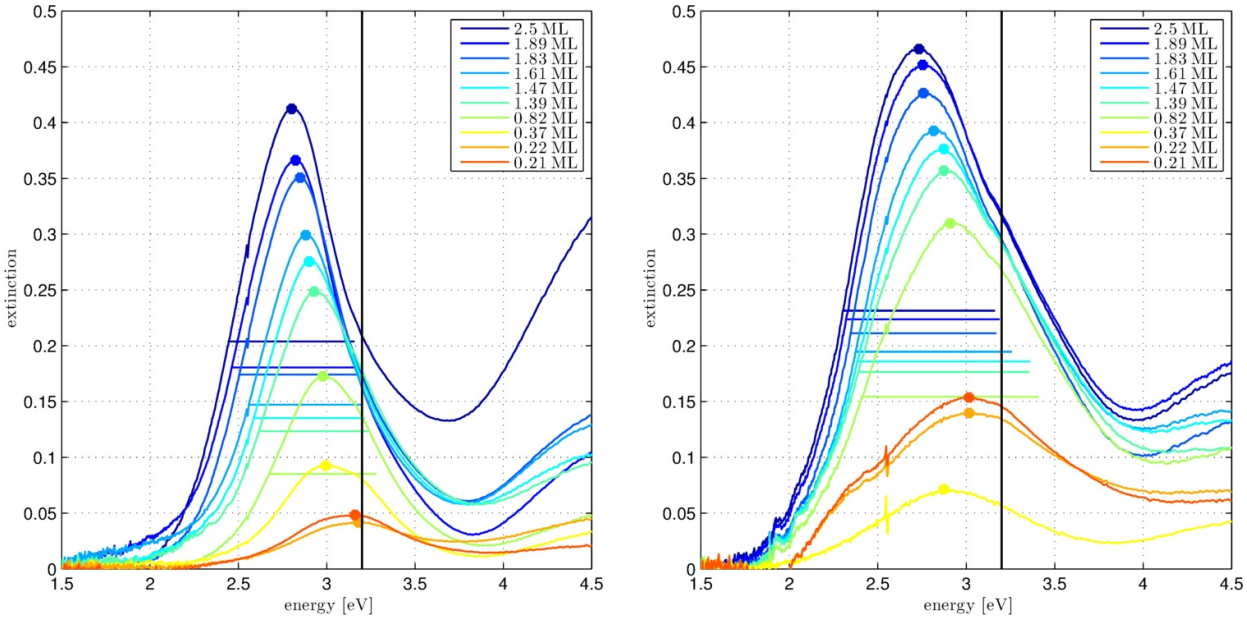

(a) after deposition, before exposing the clusters air

(b) after exposing the clusters for one hour to air

Figure 4.7: Cluster plasmon resonance spectra of Ag clusters deposited into PDMS, measured in vacuum using unpolarised light and an angle of $\varphi = 0°$. The peak positions are indicated by dots and the FWHM by bars.

traction, the shape of the spectra are slightly distorted. However, a qualitative discussion is possible with the help of simulations and earlier experiments [Hoffmann, 2012].

The shift of the maxima caused by electromagnetic coupling and coalescence is of about $\Delta E \approx 0.4\,\text{eV}$ from the lowest coverage $\sim 0.2\,\text{ML}$ to the highest coverage $\sim 2.5\,\text{ML}$. This result confirms the observations made by HOFFMANN at clusters in 0.5 µm and 1.2 µm thick PDMS films. This suggests the assumption that the thickness d of the sample with $d \geq 0.5\,\mu\text{m}$ does not influence the efficiency of the separation process.

Also double peak structures are observed. The secondary peaks are localised at about $E_{2nd\ max} \approx 3.2\,\text{eV}$ (black vertical line) and seem to be independent of the deposition amounts. This is in contrast to the observations made by HOFFMANN where the second peak is only stable for deposition amounts up to about 0.25 ML and then shifts to lower energies with increasing deposition amounts.

In former experiments these double peak structure was observed for clusters in a 0.5 µm thick PDMS film but not for clusters in a 1.2 µm thick PDMS film. The fact that the double peak structure is now observed at clusters in a PDMS film with a thickness of about 30 µm contradicts the assumption that a part of the clusters are localised at the layer between the SiO_2 substrate and the PDMS. In such a case the double peak structures would also be observed at samples with a PDMS film thickness of 1.2 µm.

The cluster plasmon resonance spectra after exposing the sample to air are shown in Figure 4.7b and the changes of the peak positions and FWHM after exposing the sample to air are shown in Figure 4.8. The peak positions shifted to lower energies with a larger shift for the coverages with amounts less than 1 ML.

The physisorption of molecules from the air at the surface of the clusters is the reason for these changes of the cluster extinction spectra (see section 4.2). The fact that the peak shifts seem to be

[2] After exposing the clusters to air, the extinctions of the coverages with 0.21 ML, 0.22 ML and 0.37 ML changed their order. This could be due to general background problems. Thus the FWHM of these spectra is not analysed.

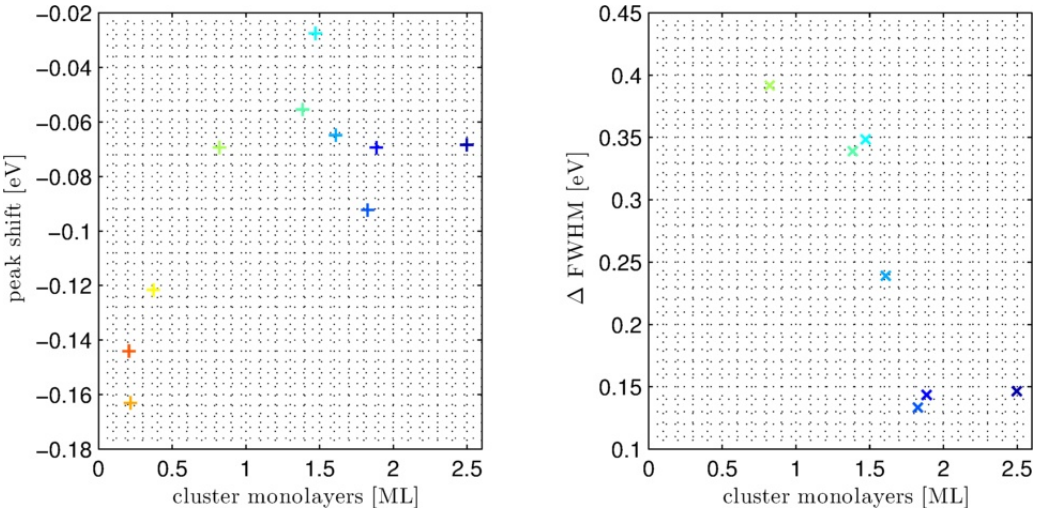

Figure 4.8: Changes of the peak positions and the FWHM of the in PDMS deposited clusters after exposing the sample for about one hour to air.

constant for deposition amounts with more than about 0.8 ML, leads to the assumption that these cluster extinction spectra are strongly influenced by the coalescence of single clusters to bigger clusters. This is in agreement with the observations made by experiments with polarised light for coverages of 1.09 ML.[3]

The FWHM for coverages < 1 ML are not evaluable. The increase of the FWHM after exposing the clusters with coverages > 1 ML to air, is weaker for higher coverages. This can be explained by the smaller surface to volume ratio of coalesced clusters. The smaller the surface the less strong is the influence of the environment. However, the broadening of the FWHM may be caused by background problems as well.

Further it is remarkable that the clusters are not protected by the PDMS against the influence of gases in the environment. This is enables experiments on the reactivity of Ag clusters in matrices, discussed in the following section at the influence of sulphur to the Ag cluster plasmons.

4.1.3 Influence of sulphur

While the Ag clusters produced and deposited in THECLA do not react with the oxygen or nitrogen (see section 4.2) of the air, they react very effectively with sulphur. The reaction of silver with sulphur can be observed at the tarnishing of silverware. To investigate the changes in the plasmon resonance spectra of clusters in PDMS after the reaction with sulphur, the clusters were measured by UV-Vis spectroscopy before reaction with sulphur, after 20 s and after 300 s in sulphurous atmosphere. The sulphurous atmosphere was produced by $2H_3PO_4 + 3Na_2S \rightarrow 2Na_3PO_4 + 3H_2S$. The experiments were performed ex-situ using the reaction cell presented in section 3.3.1. The H_2S reacts with the Ag clusters to build an Ag_2S shell around the Ag core.

The changes in the spectra for different deposition amounts are shown in the Figures 4.9a, 4.9b and 4.9c. Already after short sulfidation times the cluster plasmons, especially for small deposition amounts, exhibit a strong damping. Thus the identification of the cluster plasmon peak position and the FWHM is not clearly possible. This observations agree with the theoretical considerations presented in section 2.3.5. After the sample was exposed for about 20 s to the H_2S rich atmosphere, the cluster plasmon shapes of the spectra changed clearly visible. It is remarkable that the damping

[3]The deviating statements, of weakly coalesced clusters for coverages of 1.09 ML in the measurements with polarised light and strongly coalesced clusters for coverages of about ≥ 0.8 ML in the measurements with unpolarised light, can be referred to the imprecisely determined coverages in the case of the measurements with polarised light as explained previously (see section 4.1.1).

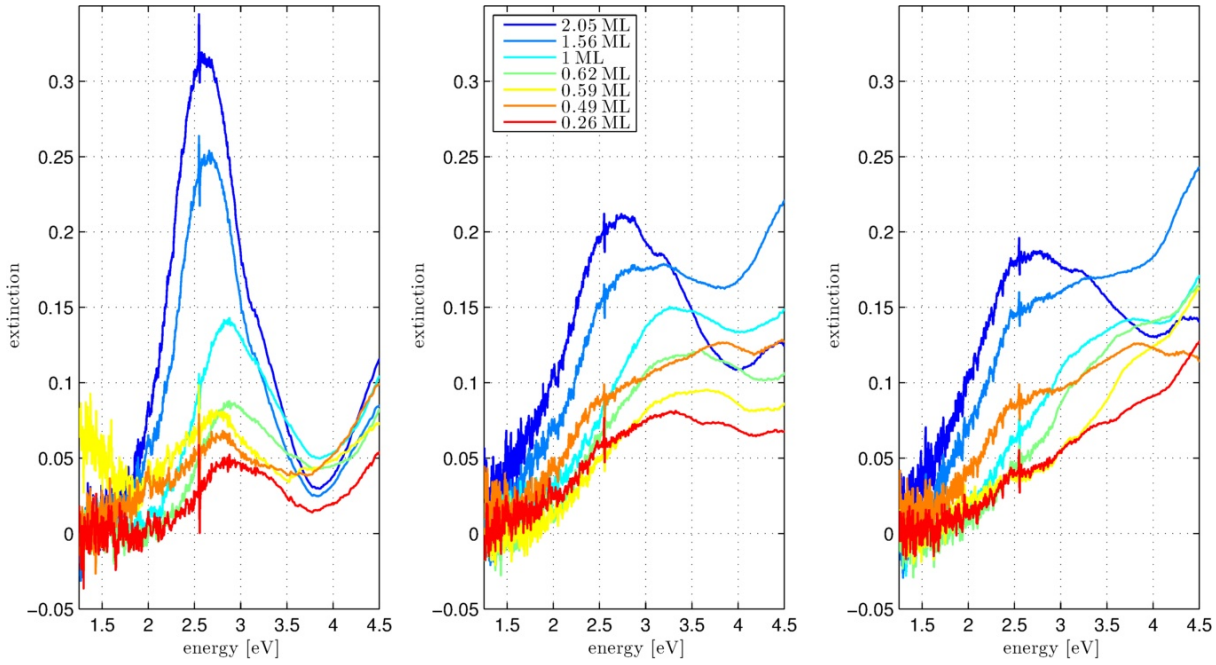

(a) under normal conditions (b) 20 s in H_2S rich atmosphere (c) 320 s in H_2S rich atmosphere

Figure 4.9: Plasmon resonance spectra of Ag clusters in PDMS.

of the shell for deposition amounts of less than 1 ML is as strong that neither the peak position nor the FWHM can be determined clearly. Nevertheless the plasmon peak position of the clusters with a deposition amount of about 2.05 ML does not change its energetic position significantly due to the sulfidation. The spectra changed once again after the second sulfidation step. The sample was additionally exposed to a H_2S rich atmosphere for about 300 s. The cluster plasmon spectra recorded after the sample was exposed for about the whole 320 s to a sulphur rich atmosphere are shown in Figure 4.9c. Only the highest deposition amount with about 2 ML still exhibits a cluster plasmon structure. This can be explained by the coalescence of single clusters to bigger clusters which leads to a lower surface to volume ratio. A more detailed investigation of the sulfidation process was tried by comparing the measured plasmon spectra of cluster depositions with about 0.26 ML, 0.62 ML, 1.00 ML, 1.56 ML and 2.05 ML to the simulations of cluster plasmon resonances in an ellipsoidal core-shell model in Figure 4.10.

For the simulation of clusters in PDMS with a deposition amount of about 0.26 ML, a cluster distortion of $u = 0.95$ was assumed. For clusters with deposition amounts of about 0.62 ML, 1.00 ML and 1.56 ML a distortion of $u = 0.90$ was used. However, for cluster depositions amounts of about 2.05 ML, a distortion of $u = 0.535$ had to be chosen. This is in agreement with the assumption of bigger particles with ellipsoidal shape, formed by the coalescence of clusters for high deposition amounts.

The permittivity of the PDMS was set to be $\varepsilon_m = 1.9$ (according to the simulations made in section 4.1.1). With this assumption the cluster plasmon spectra for Ag-core-Ag_2S-shell clusters could be simulated relatively well, but not for pure Ag clusters. For the measured spectra of these clusters, the plasmon resonances were energetic to low. This is due to the shift of the cluster spectra after contact to air as shown in section 4.1.2. Thus a correcting permittivity at the surface of the clusters had to be introduced for these clusters. This was realised by using an Ag-core-Ag_2O-shell cluster model for the clusters, measured by UV-Vis before sulfidation. It should be noticed that this is just needed for modelling this shift and no proof for the presence of oxidised clusters. Oxidation of clusters under normal conditions is excluded by XANES experiments, presented in the following section.

The simulation parameters used are listed in Table 4.5. A is the damping constant and P the relative reaction of the original clusters in %. The diameter of the clusters in the simulation was

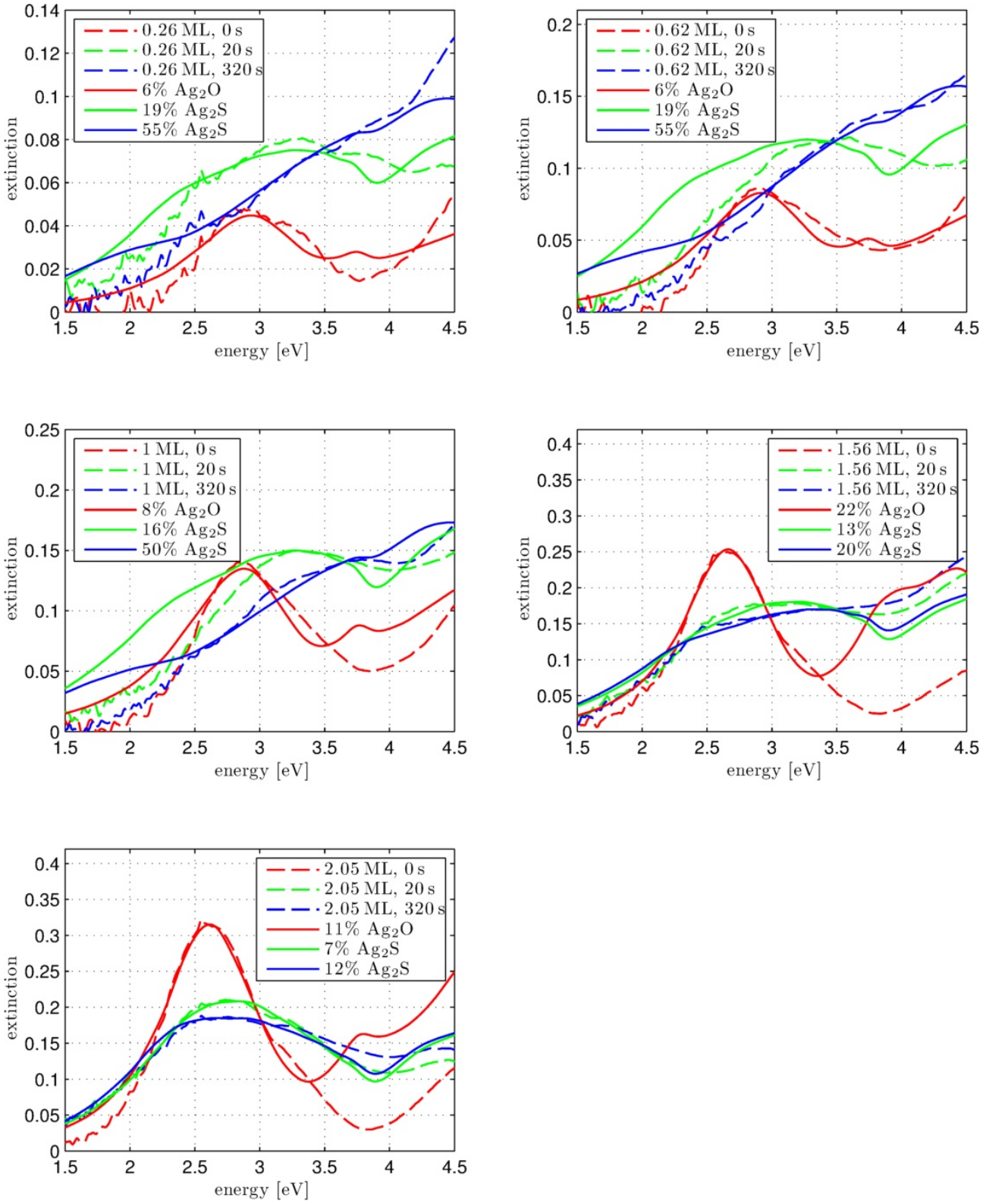

Figure 4.10: Measured and simulated cluster plasmon resonance spectra of clusters in PDMS before and after 20 s or 320 s in sulphur rich atmosphere. The dashed lines indicate the measurements. The solid lines indicate the simulations of single cluster extinctions where x % of the original Ag cluster reacted to Ag_2O (red lines) or Ag_2S (green and blue lines).

sulfidation	0.26 ML		0.62 ML		1.00 ML		1.56 ML		2.05 ML	
time	A	P	A	P	A	P	A	P	A	P
0 s	1.6	6 %	1.6	6 %	1.6	8 %	1.05	22 %	1.1	11 %
20 s	1.6	19 %	1.6	19 %	2.0	16 %	1.8	13 %	1.5	7 %
320 s	1.6	55 %	2.0	55 %	2.0	50 %	1.7	20 %	1.4	12 %

Table 4.5: Simulation parameters for Ag clusters in PDMS before and after sulfidation.

set constant to $2R = 2\,\text{nm}$.[4] For the sulfidation time 0 s an Ag_2O shell was used for the simulations and for 20 s and 320 s sulfidation times an Ag_2S shell was assumed. For a better comparability the simulated spectra were multiplied with a normalisation constant.

Before discussing the results of the simulations, it should be mentioned that the simulation parameters are determined by a qualitative conformity of the measured and the simulated spectra. Numerical fits were not performable.

Without considering the intensities of the optical cluster extinctions, the cluster plasmon spectra of the deposition amounts 0.26 ML and 0.62 ML could be simulated with approximately the same relative reaction of 19 % and 55 % after 20 s and 320 s sulfidation time, respectively. This corroborates the assumption that the clusters do not coalesce to larger islands up to deposition amounts of about 1 ML. Changes in the spectra of clusters with deposition amounts below 1 ML can then be attributed to electromagnetic coupling.

At a deposition amount of about 1 ML, the relative reaction after 20 s and 320 s sulfidation time decreased to 16 % and 50 %, respectively. But this is in the range of possible inaccuracies by the only qualitative comparability between measured and simulated spectra. Especially for relative sulfidations of $P > 40\,\%$ a plasmon resonance maximum cannot be identified. In such a case it is difficult to find appropriate parameters for the simulations. However, the decrease of relative sulfidation after each sulfidation step, compared with lower deposition amounts, is compatible with the assumption that first bigger particles are build at depositions larger than 1 ML for Ag cluster in PDMS. Bigger particles have a lower surface to volume ratio and thus a lower relative reactivity is expected.

The comparison between the measured and simulated spectra for deposition amounts larger than 1.5 ML supports this assumption: The relative reaction after 20 s sulfidation time decreases further to 13% and 7% for deposition amounts of 1.56 ML and 2.05 ML, respectively.

This becomes visible especially for long sulfidation times (320 s). The plasmon resonance maxima are still observable. The relative sulfidation in the simulated spectrum for the highest deposition amounts is lower than the relative sulfidation of the spectrum for the lowest deposition amounts after just 20 s sulfidation time. Further, for the simulations of the cluster plasmon spectra with a deposition amount of 2.05 ML, a distortion of $u = 55$ had to be chosen. Summarising, for deposition amounts larger than two cluster monolayers in PDMS, the plasmon resonance spectra are dominated by coalesced particles and the amounts of separated single clusters can be neglected.

Finally, the changes of the relative reactivity are remarkable. While the single clusters were reacted up to about 20 % after 20 s, an additional sulfidation time of further 300 s caused only an additional reaction of about 35 %. Thus, while the time was increased of a factor 15, the relative reaction increased only by factor of less than 3.

The clusters with a deposition amount of 2.05 ML exhibit a similar behaviour. After 20 s suflidation time the clusters reacted to about 7 %. 300 s additional sulfidation time caused only an increase to about 13 % reacted clusters. Thus a factor 15 longer sulfidation time yields only a doubling of reacted atoms.

From this it follows that small amounts of reacted atoms in a cluster decreases the reactivity of the cluster significantly. This is also observable for coalesced clusters, where a high number of unreacted atoms ($> 90\,\%$) are still present.

[4] $\varepsilon_{cluster} = \varepsilon_{cluster}(A/R)$

4.2 Ag L_3 XANES spectroscopy

Beside the investigations obtained by using UV-Vis, also XANES was used to complete the information about the electronic and chemical properties of Ag clusters in a 30 µm thick PDMS film. Here the Ag L_3 absorption edge was investigated using synchrotron radiation. This experiment was performed at the beamline BL8 at DELTA. It should be noticed that an alignment problem occurred to the monitor signal, which influenced the measured intensity of the impinging beam during the measurements. Because the cluster fluorescence signal is normalised to this signal, the spectra appear deformed. That is the reason for the strong background signal in the measurement of clusters in PDMS. This background cannot be subtracted by standard methods because this would cause a tilt of the spectrum due to the slope of the signal in the pre-edge region. However the Ag L_3 absorption spectrum of the clusters can be compared qualitatively to the recorded reference spectrum of an about 100 nm thick Ag reference film and to the spectra recorded by BEHRENS in Figure 2.28 (right). For a better comparability the cluster spectrum was multiplied by a constant factor ($6 \cdot 10^6$).

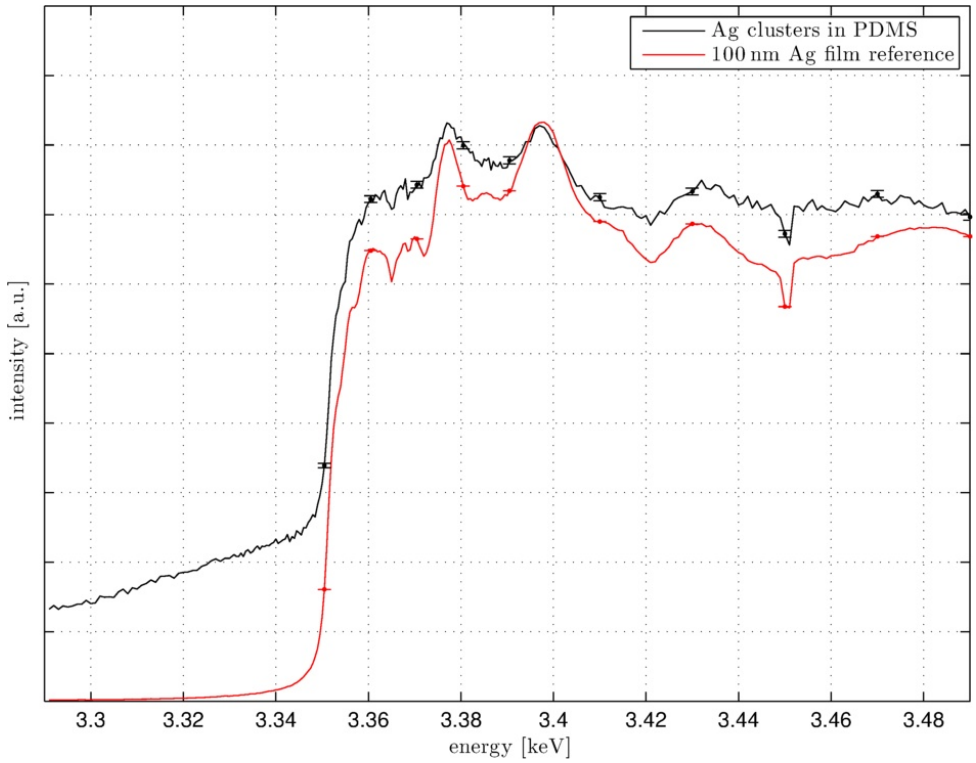

Figure 4.11: Ag L_3 XANES spectrum of Ag clusters ($\sim$ 0.3 ML) in PDMS compared with the spectrum of a 100 nm Ag film.

The main statement, which can be made from the recorded spectra, is that the presence of a white line can be excluded. This corresponds to the absence of an oxidised state like discussed for the Ag L_3 and L_2 data of Ag clusters in thin PDMS films by HOFFMANN [Hoffmann, 2012]. Thus the changes of the UV-Vis spectra have to be ascribed to the adhesion (i. e. physisorption) of nitrogen, oxygen or water molecules to the Ag clusters surfaces or the PDMS and not the building of an Ag_2O shell around the Ag core of the clusters.

4.3 Summary and discussion of Ag clusters deposited into PDMS

In this section the results of the experiments on Ag clusters deposited into PDMS by a supersonic nozzle expansion will be summarised.

First, it could be observed that the thickness and manufacturing of the PDMS is of significant influence to the optical measurements. Especially for the investigation of small deposition amounts of clusters, thin homogeneous PDMS films have to be produced to handle background problems.

However, in agreement with the cluster penetration depth in the experiments of MILANI et al. [Corbelli et al., 2011], the separation properties of PDMS in the present experiments are not influenced by the thickness d of the film for $d > 500\,\text{nm}$.

The double peak structure observed in previous experiments, performed by HOFFMANN [Hoffmann, 2012], could be reproduced in the present thesis. In contrast to former assumptions, a PDMS film thickness dependence of the double peak structure could be refuted.

Measurements with polarised light showed that for coverages $< 1\,\text{ML}$ the mean distortion is at the order $u = 0.90$ and the distortion is therefore smaller than for deposited clusters with coverages $< 1\,\text{ML}$ on fused silica ($u = 0.86$). This result is expected for a soft impact and a distribution in a depth of about 100 nm in PDMS. A double peak structure was also observed in the spectra recorded with polarised light, and could not be simulated by an ensemble of distorted clusters with distortion of about $u = 0.9 \pm 0.05$ (Figure 4.4 and Figure 4.5). By comparing the spectra recorded with polarised light with calculations made by QUINTEN [Quinten, 2010], it is most probably that the double peak structure is caused by the interaction of clusters due to electromagnetic coupling (4.6).

The clusters are not protected by the PDMS against the gaseous environment. The presence of air changes the structure of the plasmon signal and the presence of sulphur causes a chemical reaction. For the plasmon signal changes, in the case of air in the environment, a chemical reaction can be excluded by XANES experiments (Figure 4.11). It is conceivable, that the contact with air changes the PDMS dielectric function. An increase of the dielectric function would cause a shift of the cluster plasmon resonances to lower energies (Figure 4.7a, 4.7b and Figure 4.8). These effects are may be caused by a modification of the overall dielectric function of the PDMS or only by a local modification of the environment of the clusters.

From the experiments at clusters exposed to a sulphur rich atmosphere it can be extracted, that the clusters deposited into PDMS stay separated up to deposition amount of about 1 ML. At about 1.5 ML coalescence effects could be observed. For deposition amounts of about two cluster monolayers, most clusters were coalesced to bigger particles (Figure 4.10).

The reactivity of the clusters decreases significantly after first atoms of the clusters reacted with sulphur to Ag_2S. This seems to be independent on the the clusters size i. e., number of unreacted atoms in the clusters (Figures 4.9a, 4.9b and 4.9c).

5 Results of experiments on Ag clusters in SiO_2 aerogel

As described in section 3.1.2, silica aerogel is a highly porous network with an extremely rough surface. Therefore its structure is highly fragile and its surface is easily damaged. To produce a new surface with intact nano pores, the cylindrical aerogel drops were cleaved parallel to their surfaces. Using intact aerogel surfaces enables the deposition of higher amounts of clusters before risking coalescence. One of the cleaved drops is shown in Figure 5.1. Especially the red framed region exhibits an intact surface area. This is indicated by the high transparency of this region compared with the rest of the surface. The disadvantage of suchlike produced samples is the strong refraction of light caused by macroscopic irregularities of the surface. This, and the thickness of the aerogel drop ($\sim 5\,\mathrm{mm}$), complicate optical measurements at Ag clusters deposited into the aerogel.

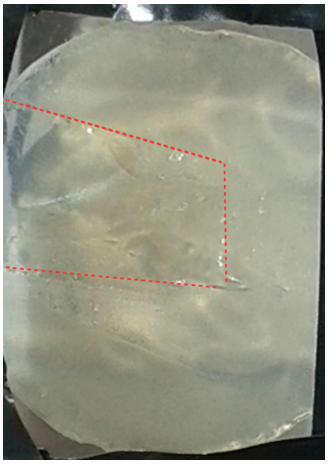

Figure 5.1: Picture of a cleaved silica aerogel sample with deposited clusters. The red frame indicates a region of the sample with fresh, undamaged aerogel. The slightly yellow colour of the sample is a consequence of the Ag cluster extinction.

The samples with clusters deposited into those transparent surfaces of cleaved silica aerogel were investigated and the results are discussed in this section. Especially the possibility to deposit high amounts of clusters into silica aerogel improves the practicability of XANES experiments, where high amounts of sample material are required to enable a good signal to noise ratio.

5.1 Investigation using UV-Vis spectroscopy

The Ag cluster plasmon resonance spectra of clusters in three different aerogel drops with different deposition amounts are presented in Figure 5.2. The aerogel drops were mounted at a sample holder onto a fused silica substrate and coated with clusters in one experimental run. Drop 1 was coated with a moderate mean deposition amount of about 1.7 ML (Figure 5.2 c)). For drop 2 a high mean deposition amount of about 5.7 ML (Figure 5.2 d)) was chosen. Drop 3 was coated with a low mean deposition amount of about 0.4 ML (Figure 5.2 b)). Ag clusters with a deposition amount of about 0.4 ML were also placed at the silica substrate. For comparison the cluster extinction spectra of this deposition is also shown in Figure 5.2 a).

Because the surfaces of the cleaved aerogel drops are very inhomogeneous and have a strong refraction of light, even if the refraction index of aerogel is close to 1, a cluster extinction measurement at position z has to be subtracted by a reference measurement at precisely the same position z. This is, as explained in section 8.3, only possible up to a limited accuracy, so that there are still small amounts of background signal in the cluster extinction spectra.[1] The spectra were smoothed using a Gauss convolution with a FWHM of 0.05 eV.

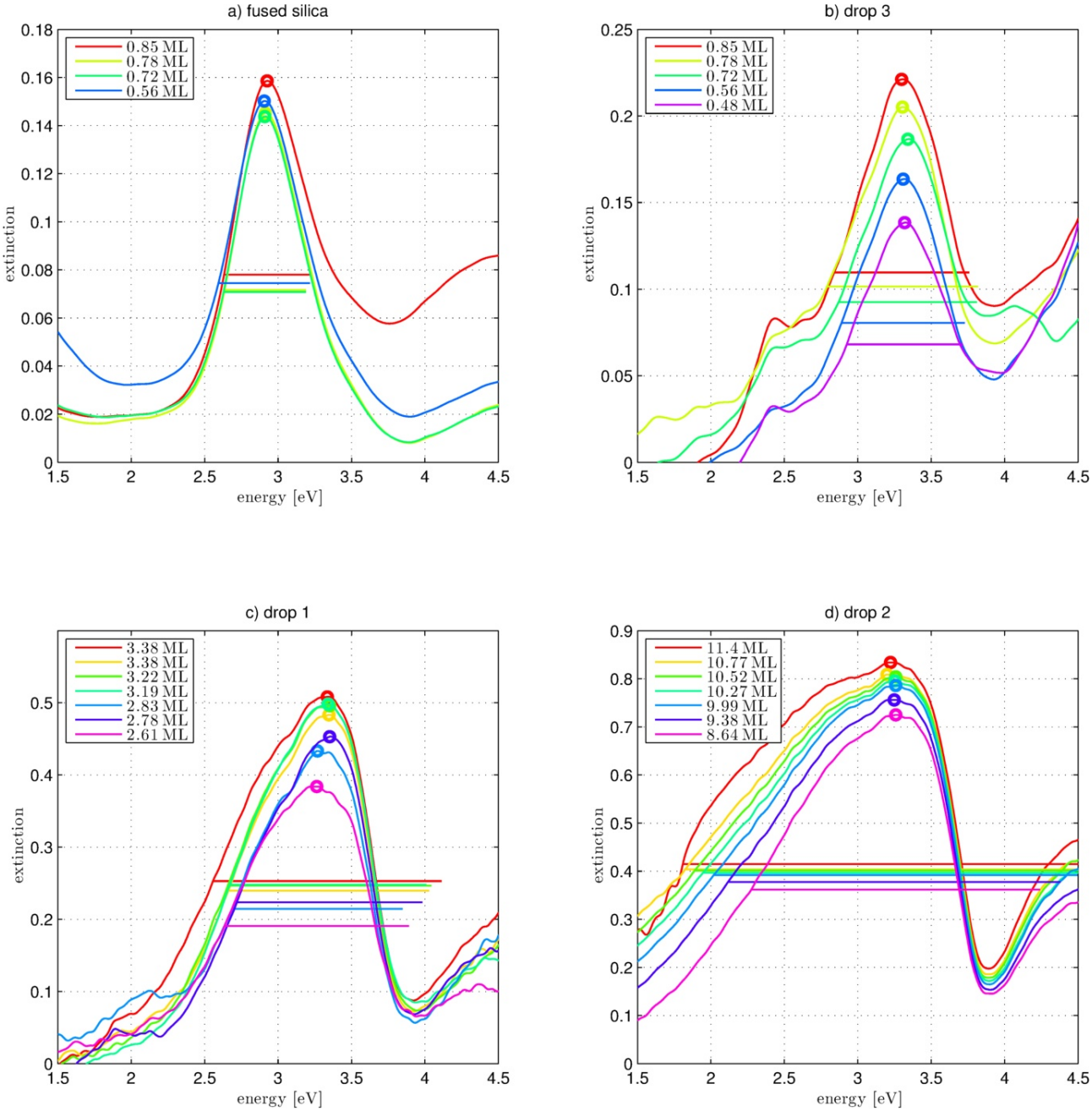

Figure 5.2: Extinction spectra of Ag clusters deposited on fused silica substrate a) and on cleaved silica aerogel b) - d), measured in vacuum before exposure to air. The peak positions are indicated by dots and the FWHM by horizontal lines.

The cluster plasmon extinction spectra of Ag clusters in silica aerogel are shown in Figure 5.2. Their maxima are indicated by dots and their FWHM by horizontal lines. For a first discussion the spectra

[1] The cluster extinction spectra of clusters in silica substrate were not subtracted by a reference measurement. The background signal of the fused silica substrate can be neglected at deposition amounts > 0.5 ML.

of clusters in aerogel with small deposition amounts (Figure 5.2 b)) can be compared with those on fused silica (Figure 5.2 a)).

Their peak positions in aerogel are at about 3.3 eV and thus about 0.4 eV higher than for the clusters on silica substrate. This can be attributed to the nanostructure of the aerogel: Not every cluster has the same contact with the substrate. Some clusters are more influenced by the dielectric function of the vacuum $\varepsilon_m = 1$ and some by the dielectric function of the silica material $\varepsilon_m = 1.48$ [Hövel, 1995]. Thus the peak position $E_{\text{peak}}^{\text{aerogel}}$ is located between the peak positions of clusters in vacuum $E_{\text{peak}}^{\text{vacuum}} = 3.65\,\text{eV}$ and of clusters on fused silica $E_{\text{peak}}^{\text{SiO}_2} \approx 2.9\,\text{eV}$. It has to be recognised that the peak position of separated clusters on fused silica is at about 3.2 eV. But due to coalescence and electromagnetic coupling for deposition amounts of more than 0.16 ML on an even surface like fused silica, the peak shifts to lower energies. The effect of the uneven surface is also indicated by the width of the plasmon resonances. The different dielectric functions of the environment $1 \leq \varepsilon_m \leq 1.48$ can cause a superposition of different cluster plasmon peaks which results in a broadening of the plasmon FWHM.

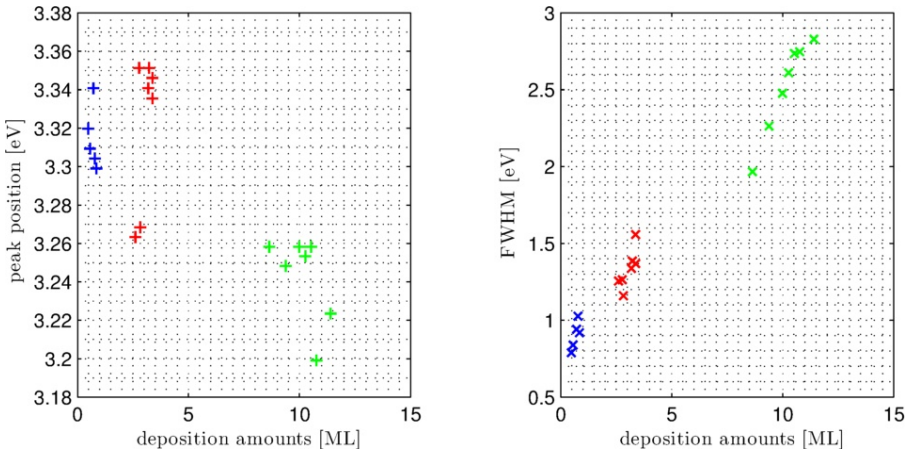

Figure 5.3: Extinction maxima (left) and FWHM (right) of Ag clusters in three drops of cleaved silica aerogel before exposure to air. The drops are indicated by colours: blue for drop 3 with a mean deposition amount of about 0.4 ML, red for drop 2 with a mean deposition amount of about 1.7 ML and green for drop 3 with a mean deposition amount of about 5.7 ML.

For clusters in aerogel their extinction maxima stay nearly stable with increasing deposition amounts. This is shown in Figure 5.3. The extinction maxima of the clusters in drop 3 (blue) are localised with one exception, between 3.30 eV and 3.32 eV. The maxima for clusters in drop 1 (red), without two exceptions, between about 3.33 eV and 3.35 eV. And the maxima of clusters in drop 2 (green), without two exceptions, are localised between about 3.23 eV and 3.24 eV. Thus the variance of the peak positions is very small for each drop and can be neglected. The variance of the peak positions between different drops may be assigned to influences of the surface structures of each drop.

In contrast to the peak positions, the FWHM of the cluster plasmon resonances increases with increasing deposition amounts. This is similar to emerging double peak like structures in the spectra with increasing deposition amounts in PDMS (Figure 4.6).

It can be assumed that the clusters start electromagnetic coupling with increasing deposition amounts. Also the presence of coalesced particles can cause the broadening of the cluster plasmon resonances. But because the resonance maxima are nearly stable up to deposition amounts larger than 10 ML, the amount of separated, spherical particles with diameters of about 2 nm seems to dominate the structure of the extinction spectra.

The cluster plasmon resonances, after exposure the sample for about one hour to air, are shown in Figure 5.4.

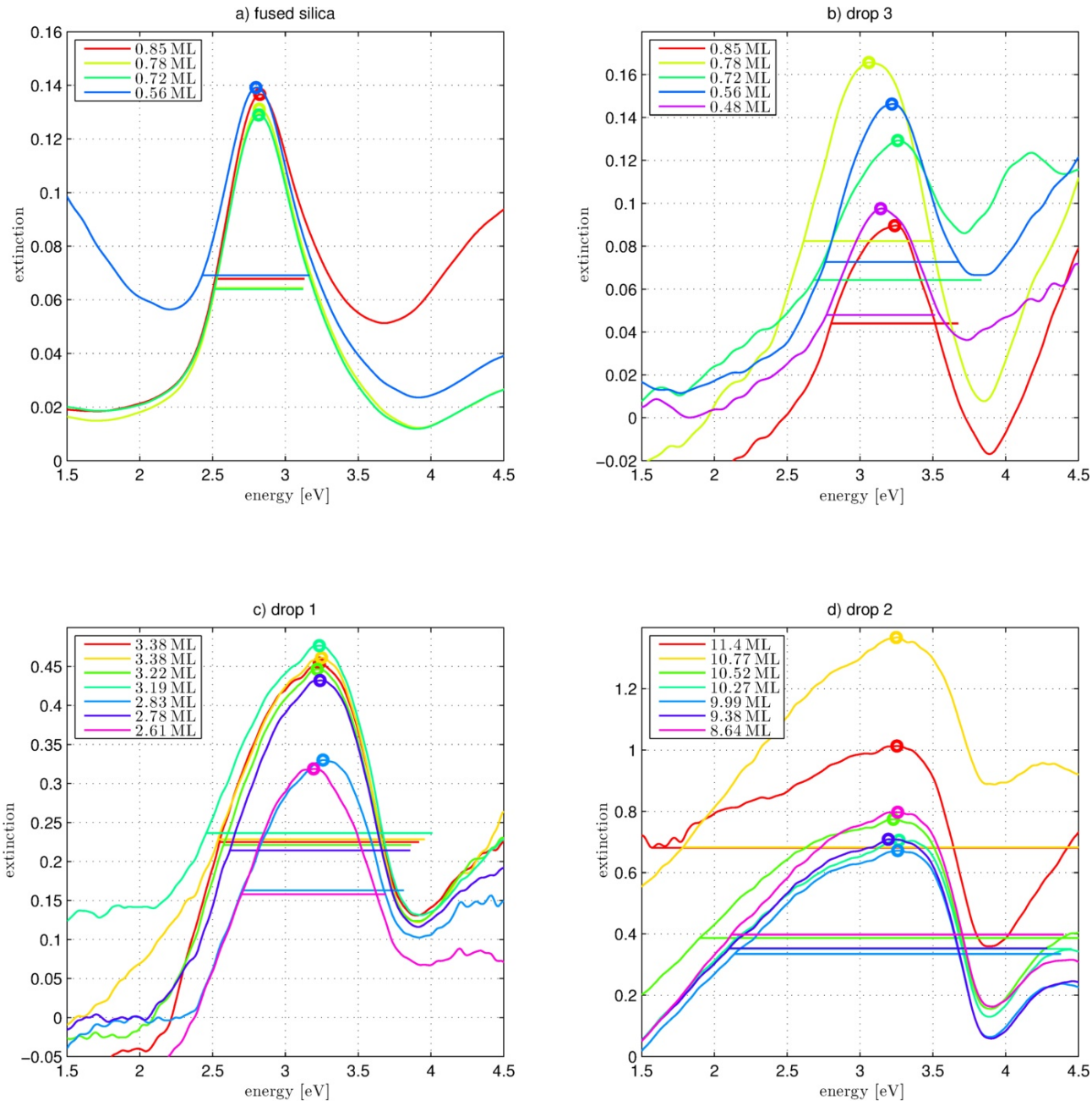

Figure 5.4: Extinction spectra of Ag clusters deposited on fused silica substrate a) and on cleaved silica aerogel b) - d), measured in vacuum after exposure to air. The peak positions are indicated by dots and the FWHM by horizontal lines.

The cluster plasmon resonances, after exposure the sample for about one hour to air, are shown in Figure 5.4. Unfortunately, a misalignment seems to be occurred between the reference measurements and the cluster plasmon measurements in vacuum and the measurements after exposing the sample to air. Thus some spectra have an unusual background signal which causes a higher variance of the extinction maxima as expected. The FWHM exhibits an increase with increasing deposition amounts, similar to the behaviour observed before exposing the sample with cluster in PDMS to air. The positions of the extinction maxima and its FWHM are shown in Figure 5.5. Their changes due to the venting effect are plotted in Figure 5.6.

The changes of the energetic positions of the extinction maxima and even more the FWHM data, are influenced by the misalignment of the sample or the optics. Therefore significant scatter exists. However, at least for drop 3 and 1 with low to moderate coverage $< 3.5\,\mathrm{ML}$ the peak shift after

contact to air is comparable to the clusters in PDMS for low coverages. Thus, for less than 3.5 ML the assumption of the presence of mainly separated spherical clusters with changes caused by the adhesion of air molecules at the Ag cluster surfaces is made. For a coverage $\geq$ 10 ML coalescence to larger islands seems to occur. These is, amongst others, verified in the next section by XANES experiments.

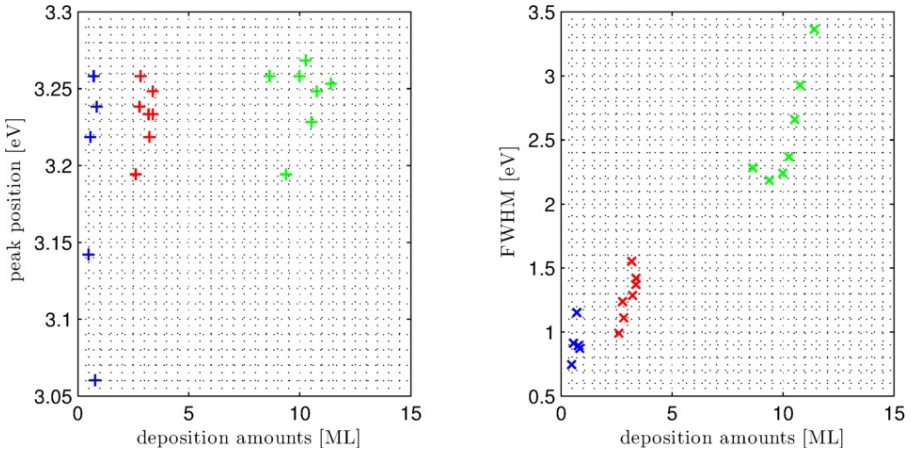

Figure 5.5: Extinction maxima (left) and FWHM (right) of Ag clusters in three drops of cleaved silica aerogel after exposure to air, measured in vacuum. The drops are indicated by colours: blue for drop 3 with a mean deposition amount of about 0.4 ML, red for drop 2 with a mean deposition amount of about 1.7 ML and green for drop 3 with a mean deposition amount of about 5.7 ML.

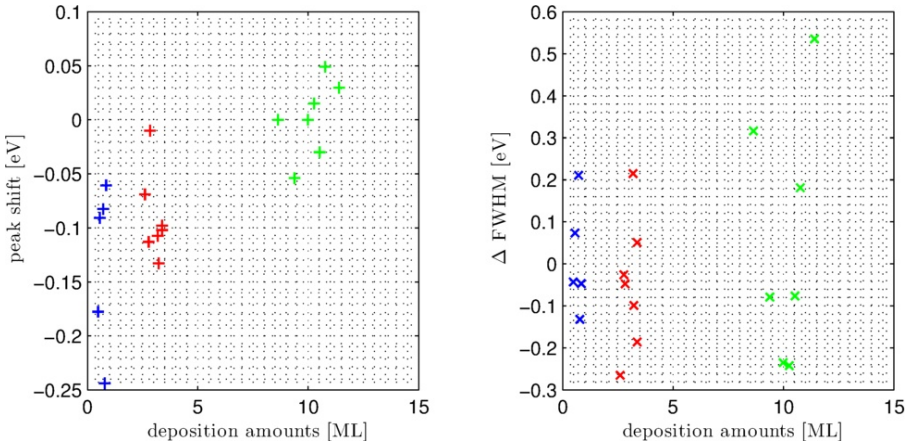

Figure 5.6: Changes of the energetic positions of the plasmon resonance maxima (left) and their FWHM (right) after exposure the sample for about one hour to air, measured in vacuum.

5.2 Electronic, chemical and structural properties of Ag clusters, investigated using Ag L_1 and L_2 XANES spectroscopy

This section presents and discusses the results of XANES experiments on Ag clusters in silica aerogel. Altogether five aerogel samples with different deposition amounts were investigated. The section starts with the investigations on the Ag L_1 edge followed by the investigations of the Ag L_2 edge. For each absorption edge, the spectra of the samples with deposited Ag clusters with different coverages are presented after the spectra of the measured reference samples were presented. The chemical properties of the clusters were investigated in oxidation and sulfidation experiments on the Ag L_2 absorption edge. These experiments can also yield information about the electronic and geometric structure of the clusters. All measurements presented in this section were performed at beamline ID26 at the ESRF in Grenoble. All spectra in this section were smoothed using a Gauss convolution with a FWHM of 1 eV.

5.2.1 Ag L_1 absorption edge of Ag clusters in vacuum

The Ag L_1 absorption spectra of various reference samples are shown in Figure 5.7. The Ag reference is a 100 nm thick evaporated silver film on fused silica. The AgO, Ag_2O and Ag_2S samples were made of powder as pellets. The spectra were recorded in vacuum with a pressure of about $p \approx 2$ mbar.

The influence of the different chemical states can be obtained from the structure of the spectra and the energetic position of the absorption edge. Especially the edge position is an indication for the effective potential of the X-ray photon absorbing atom. With increasing oxidation state the effective potential is more positive and the edge shifts to higher energies. In contrast to the Ag L_2 and Ag L_3 absorption edges, the edge is not superimposed by a white line. The peak at about 3.81 keV is attributed to a 2s→4d transition. This transition in not prohibited because the 5p orbital, which has a peak in the density of states (DOS) in this region, builds a hybridisation with the 4d orbital [Sham, 1985].

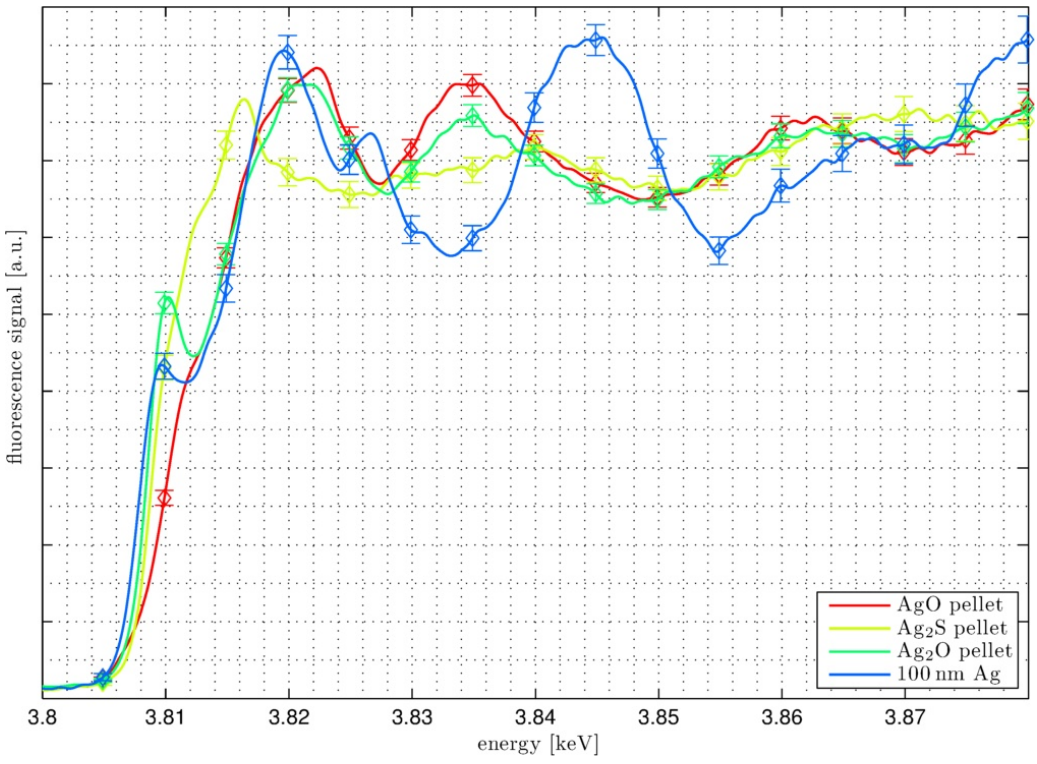

Figure 5.7: Ag L_1 XANES spectra of bulk Ag, AgO, Ag_2O and Ag_2S reference samples.

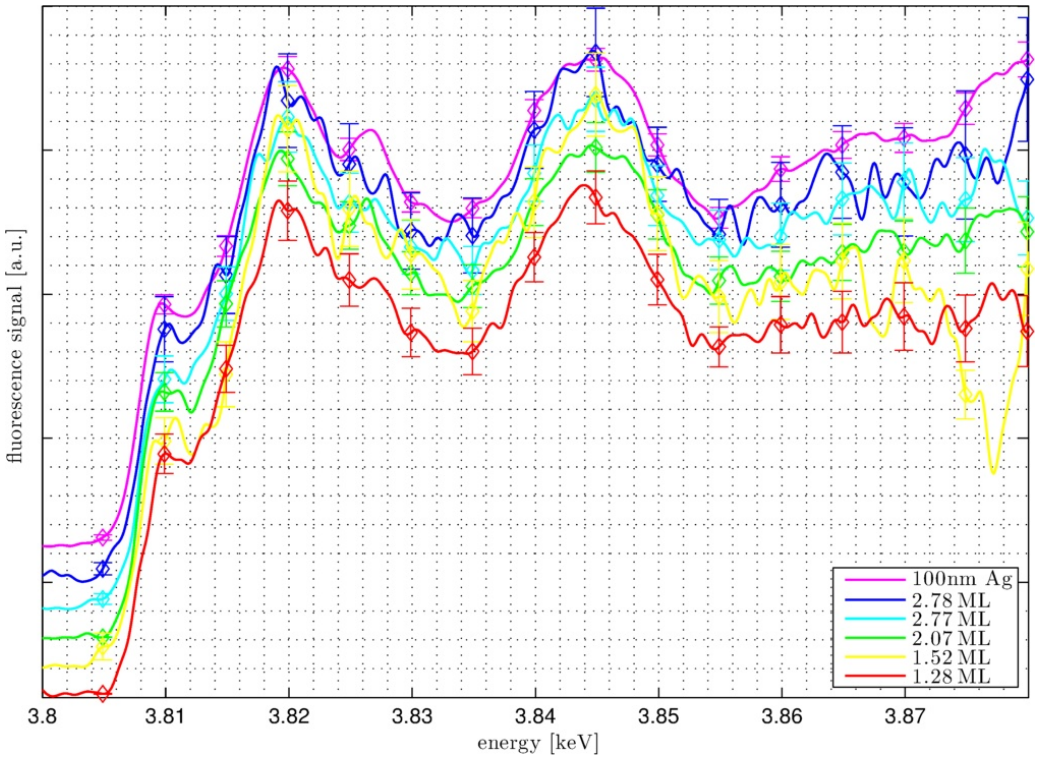

Figure 5.8: Ag L_1 XANES spectra of Ag clusters with different deposition amounts.

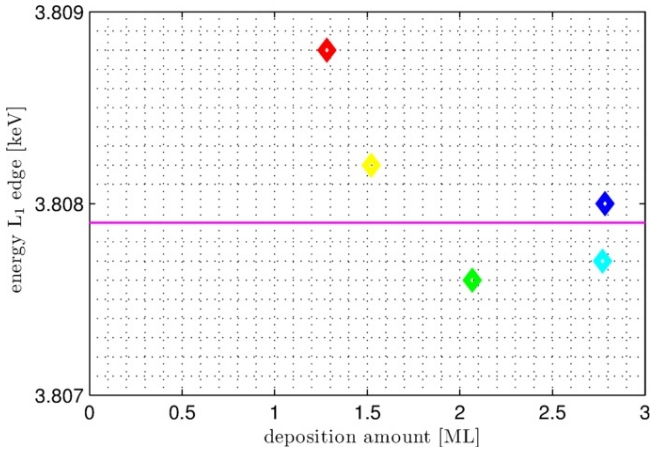

Figure 5.9: Energetic positions of the Ag L_1 XANES absorption edge calculated from the maxima of the deviations of the spectra.

The L_1 XANES spectra of clusters in silica aerogel are shown in Figure 5.8. The spectra of clusters with different deposition amounts exhibit strong similarities to the reference spectrum of a 100 nm thick Ag film, independent on the deposition amounts. The clusters in aerogel with deposition amounts of about 3 ML can be assumed to be separated clusters (compare section 5.1 and section 5.2.2) with mean diameters of about $2R = 2$ nm. Thus the final state, the 5p orbital, does not change its unoccupied density of states (uDOS) with increasing size of the system and the rearrangement from cluster structure to bulk structure. This leads to the statement that the 5p band of a the investigated clusters has a similar electronic structure like that of bulk material.

The effect of the increasing deposition amounts to the position of the absorption edge are shown in Figure 5.9. The edge position of the 100 nm reference film is indicated with a horizontal line. However, there are no systematic changes observable. Thus the changes of the energetic position of the absorption edge (inflection point where the first deviation is maximal) have to be ascribed to

statistical effects (low statistic and Gauss convolution smooth). The low statistic is a consequence of the few electrons in the 2s initial state and the lower fluorescence yield ($E_{L_1M_3}$ = 3.2344 keV, rate = 0.01450) compared with the Ag L_2 absorption edge ($E_{L_2M_4}$ = 3.1509 keV, rate = 0.21605) (data extracted from database of the software *PyMca* [Solé et al., 2007]).[2]

5.2.2 Ag L_2 absorption edge of Ag clusters in vacuum

The spectra of various reference samples are shown in Figure 5.10. The reference spectra of a 100 nm thick Ag film was measured in vacuum for 10 minutes (red line), then at p = 500 mbar for 10 minutes(orange line) and again in vacuum for 60 minutes (pale green line). These spectra do not differ from each other, thus the emergence of beam damages caused by oxidation can by excluded for measurements on bulk silver (if measurement time is not to high).

Further an Ag solid with a thickness of the magnitude mm was measured two times. The first time without prepared surface (green line, indicated by sheet dirty) and once again after scraping away the topmost layers of the surface (cyan line, indicated by sheet clean). These spectra do not differ from those of the 100 nm thick Ag film. From this it follows that self-absorption can be neglected in the present experiments, especially for the cluster samples with effective "thicknesses" of some nm.

The topmost spectra in Figure 5.10 were recorded at Ag_2O, Ag_2S and AgO pellets. The shift of the position of the absorption edge is clearly visible. In the case of Ag_2O and AgO the shift of the absorption edge to higher binding energies is superimposed by a white line which results in a shift of the onset to lower energies. In the case of Ag_2S, where no white line emerges, the shift of the absorption edge goes to higher binding energies in the same order of magnitude as observed at the L_1 absorption edge.

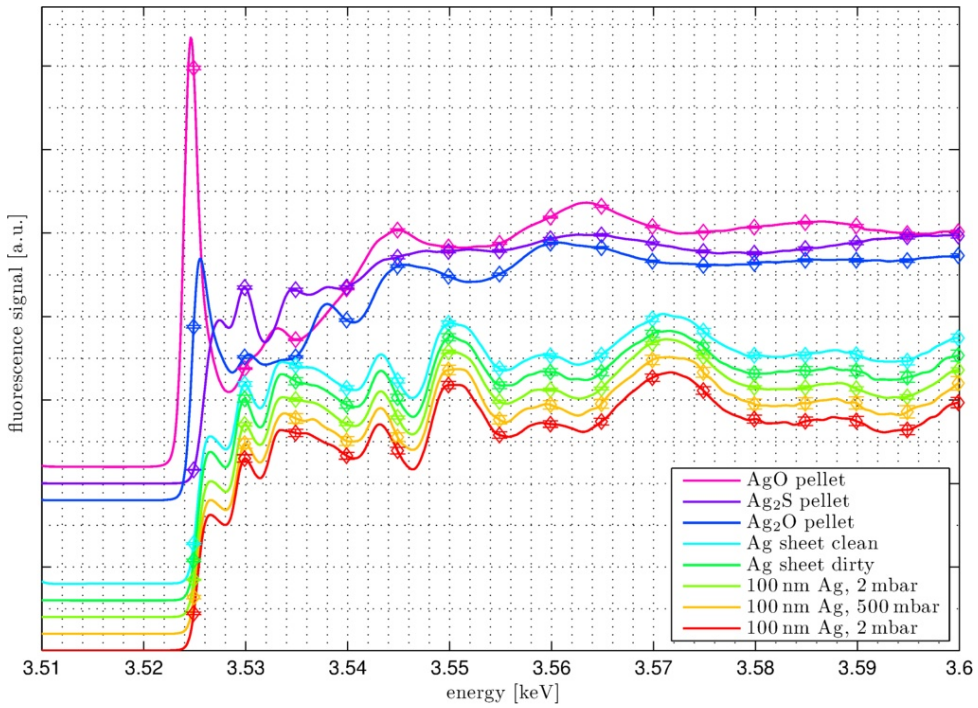

Figure 5.10: Ag L_2 XANES spectra of bulk Ag, AgO, Ag_2O and Ag_2S reference samples.

[2]The fluorescence yield is given by the rate which is the quotient of a specific fluorescence yield, for example from M_4 state into L_2, and the sum over all fluorescence yields of all possible relaxation processes into the L core level.

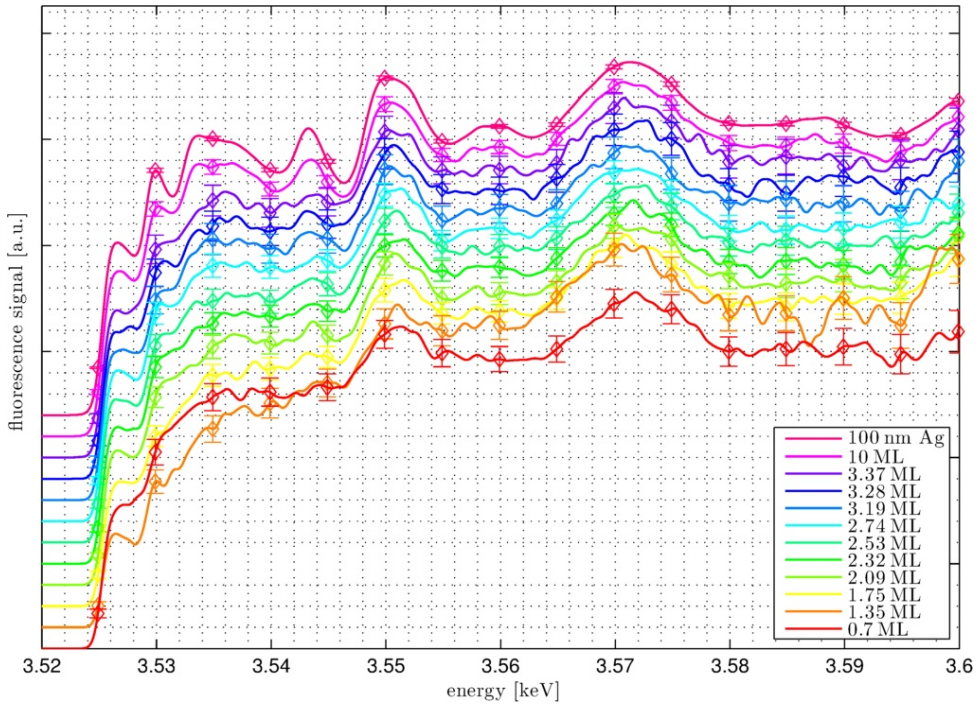

Figure 5.11: Ag L_2 XANES spectra of Ag clusters deposited into silica aerogel.

The spectra of unreacted Ag clusters with different deposition amounts are shown in Figure 5.11.[3] The position of their absorption edges are plotted in Figure 5.12 as a function of the deposition amount. Also here, like at the L_1 edge, no systematic shift with increasing deposition amount can be observed. The absorption edges of the clusters have almost the same energetic positions like that of the 100 nm Ag film reference, indicated as a horizontal line.

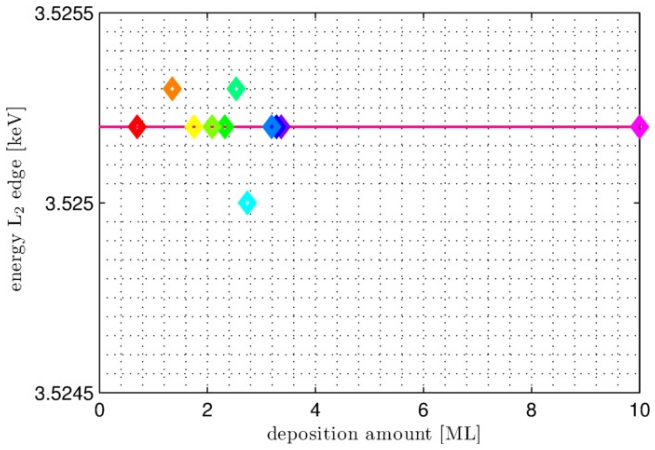

Figure 5.12: Ag L_2 absorption edge positions of Ag clusters deposited into silica aerogel for different deposition amounts. The absorption edge positions of the bulk reference is indicated as a horizontal line.

The spectra with deposition amounts less than about 4 ML exhibit the same structural features but differ from the spectrum of clusters with a deposition amount of about 10 ML which has the same features like the 100 ML Ag film reference.

[3] It should be noticed that the spectra of clusters with deposition amounts between 1.35 ML and 3.37 ML were recorded at one drop. The spectra of clusters with deposition amounts of 0.7 ML and 10 ML were recorded at a second and third drop, thus the comparison between these amounts has to be done carefully.

From the optical measurements in section 5.1 it was inferred that for deposition amounts of about 1 ML and less, the Ag clusters produced and deposited into silica aerogel by THECLA stay separated without electromagnetic coupling. By this it follows that also the XANES spectrum of clusters with deposition amounts of 0.7 ML represents the structure of separated clusters. With increasing deposition amounts the structure seems to be unchanged up to a deposition amount of about 4 ML. This can explain the assumptions that the clusters are still separated up to deposition amounts less than 4 ML. However, for deposition amounts of about 10 ML coalescence to larger particles occurred due to the bulk like XANES signal. These coverage dependent changes agree with the results by optical spectroscopy in section 5.1. It is important to note that in contrast to the optical spectroscopy, the XANES data approach bulk features only for coverages larger then 4 ML because they are not influenced by the electromagnetic coupling of still separated clusters.

The differences between the bulk and cluster XANES signal will be discussed in the following.
The structure of the XANES signals in Figure 5.11 can be divided into three sections. The first is from the pre-edge region up to an energy of about 3.530 keV. The second from 3.530 keV to 3.546 keV and the third region is above 3.546 keV. The first and the third region have the same characteristics for clusters like for bulk material. But in the second region there are significant differences.

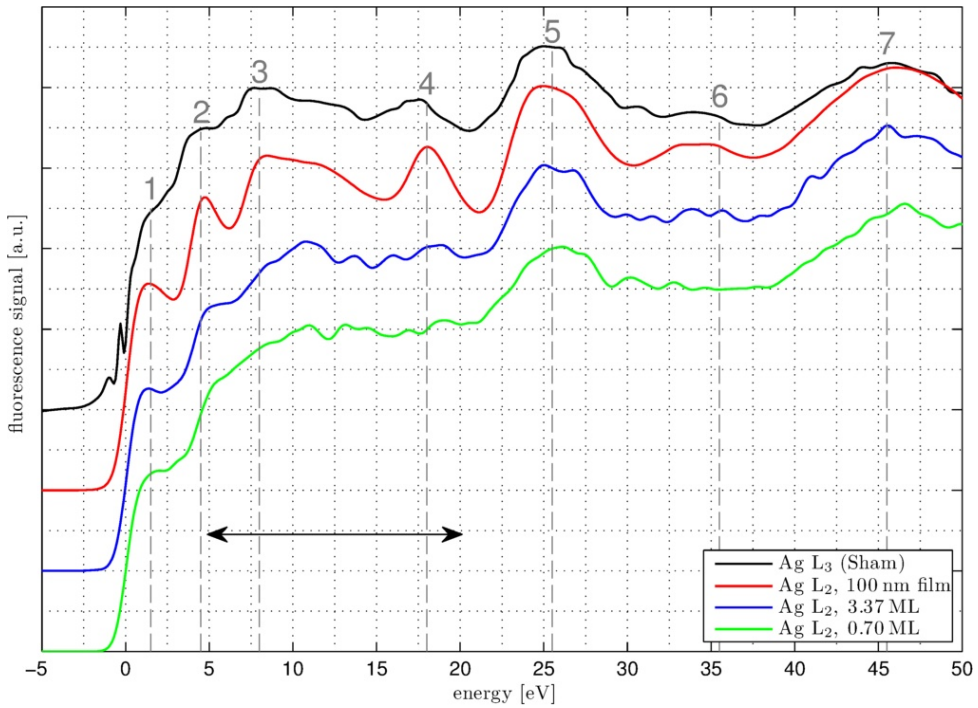

Figure 5.13: Ag L XANES spectra normalised to the absorption edges. The black line is an Ag L_3 XANES spectra, digitalised from SHAM [Sham, 1985]. The red line is of an Ag L_2 XANES spectra of a 100 nm Ag film. The blue and green lines are of the L_2 XANES spectra of deposited clusters with coverage densities of 3.37 ML and 0.70 ML, respectively. The region where the clusters XANES spectra differ from the bulk XANES spectrum are marked with a double arrow. The peaks marked with numbers between 1 and 7 correspond to final states listed in table 5.1, taken over from [Sham, 1985].

SHAM [Sham, 1985] investigated the Ag $L_{1,2,3}$ XANES spectra of Rh, Pd and Ag and found a correlation between final states during L edge absorption processes and peaks in the resulting XANES spectra. The data of the Ag L_3 XANES signal, measured by SHAM, were digitalised and plotted in Figure 5.13 (black line). The energy axis was shifted thus the absorption edge is at 0 eV. The results of our measurements on the Ag L_2 absorption edge of the 100 nm Ag film (red line) and the clusters

with deposition amounts of 3.37 ML and 0.7 ML (blue and green lines, respectively) were added to this plot. The peaks of the Ag L_3 XANES signal are numbered from 1 to 7.

Because the L_3 and L_2 XANES have the same final states, the spectra of the bulk samples nearly have the same structure.[4] SHAM assigned the different peaks to the occupation of the photoelectron to different bands/orbits in the final state. Thus, for example, the peak marked with 1 is assigned to a $2p_{3/2} \rightarrow 5s$ transition. The assignment of the peaks due to the corresponding final states is listed in table 5.1. A comparison between the L_3 and L_2 XANES leads to good agreements thus the

Peak #	Assignment
1	s
2	pd
3	pd
4	pd
5	df
6	f
7	df

Table 5.1: Electronic final states [Sham, 1985]

assignments for the L_3 transitions can be transferred to the L_2 transitions. The second region (3.530 keV to 3.546 keV in Figure 5.12, marked with a double arrow in Figure 5.13), where the XANES signal of the clusters differs from the XANES signal of the bulk, exhibits no peaks at the positions 3 or 4. Also the peak 2 is only very weak. These peaks are assigned to final states with pd-hybridisations.

This leads to two possible assumptions:

- The proportion of the p orbital to the pd-hybrid orbital is higher for clusters than for bulk material. A higher amount of the p orbital corresponds to a higher amount of forbidden dipole transitions from the 2p initial state and thus to a decrease in the XANES signal in this region. Nevertheless, the Ag L_1 XANES spectra showed no significant differences of the uDOS of the 5p orbitals between bulk and clusters.

- The amount of free states in the d region (caused by the hybridisation) is decreased in clusters in comparison to a bulk system.

Both assumptions speak for a attenuation of the pd-hybridisation in clusters. This effect is in qualitative agreement with the theoretical expectations for an increasing system from a single atoms system to a bulk. However, the observation of such quantum size effects would be remarkable for clusters consisting of about 250 atom.

[4] It should be noticed that differences in the spectra can occur due to the different alignments of the setups. For example the experiments of SHAM were carried out at the Stanford Synchrotron Radiation Laboratory (SSRL) in transmission mode (i.e. TFY) while the experiments presented in this thesis were carried out at the ESRF in fluorescence detection mode with high energy resolution (i. e. PFY).

5.2.3 Oxide effect on Ag clusters, investigated using Ag L_2 XANES spectroscopy

The effect of oxide to the Ag clusters is discussed in the present section. In section 4.2 and in [Hoffmann, 2012] it was shown that Ag clusters with a mean diameter of about 2 nm do not oxidise under normal conditions of room temperature and atmospheric pressure within time scales of weeks. However, the reaction of Ag clusters with oxide can be initiated by exposing the cluster sample to a highly intense X-ray beam (like at ID26, ESRF). By controlling the pressure of the environment and the duration of the beam shining, those experiments can also yield information about the chemical properties of the clusters.

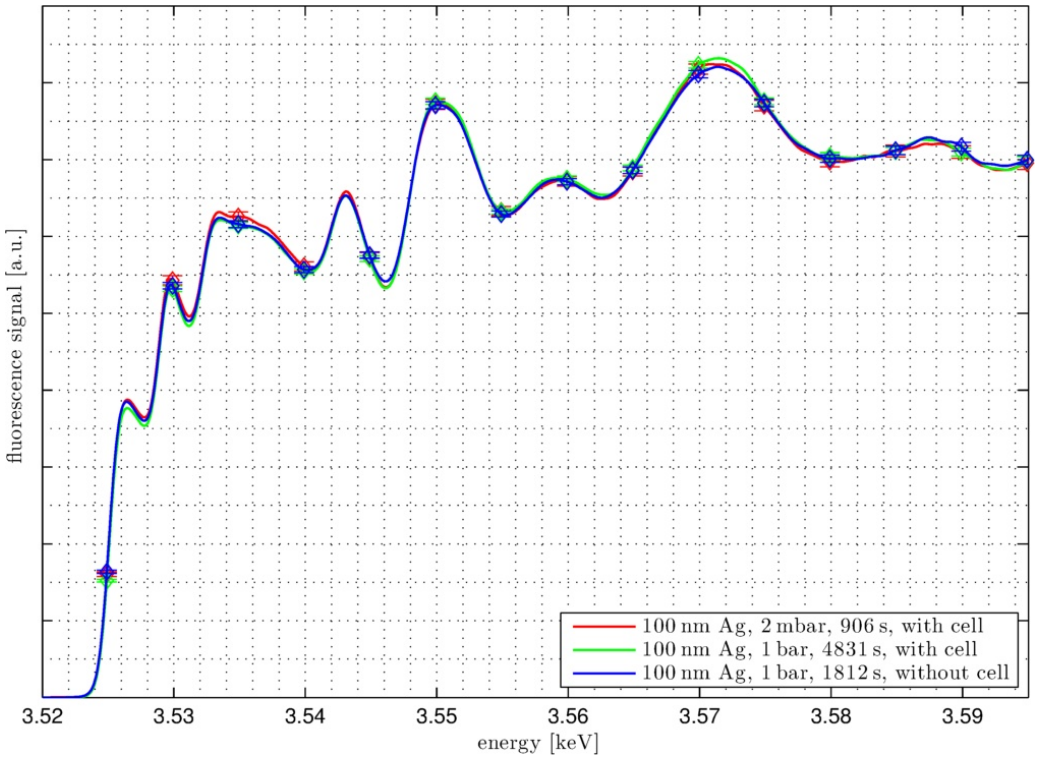

Figure 5.14: Ag L_2 XANES spectra of a 100 nm Ag film measured at atmospheric pressure and in vacuum.

At first spectra of the 100 nm Ag film reference in air (with and without vacuum cell) and in vacuum were recorded. The results are shown in Figure 5.14. The blue line represents a measurement on the sample under normal conditions without using the vacuum cell, where the green line represents a measurement under the same conditions but with the sample covered by the vacuum cell. So, a kapton window was in front of the incoming beam and the outgoing fluorescence radiation during this measurement. The spectrum is similar to the spectrum recorded without the vacuum cell. This confirms, that the cell did not influence the spectral shape. Only the measurement time had to be increased due to the decreased beam intensity. The red line represents the spectrum of the sample under vacuum conditions ($p \approx 2$ mbar). Here the measurement time could be decreased due to the lower X-ray scattering by air. Also this spectrum does not differ from the spectra recorded with the sample in air (atmospheric pressure). Thus the X-ray beam does not cause detectable beam damages at the 100 nm Ag film of up to measurement times of about 5000 s if the sample is in the vented vacuum cell.

The spectra of clusters with deposition amounts of about 10 ML measured in vacuum and at a pressure of $p \approx 500$ mbar are shown in Figure 5.15. The first two lines (from top to bottom) are the spectra of the reference samples, an Ag_2O pellet and a 100 nm Ag film.

The cyan coloured line is the spectrum of clusters with a deposition amount of about 10 ML measured

in vacuum. This spectrum is similar to the Ag film reference spectrum which indicates that the clusters are coalesced to big particles with bulk like structure. After exposing the sample to air and starting

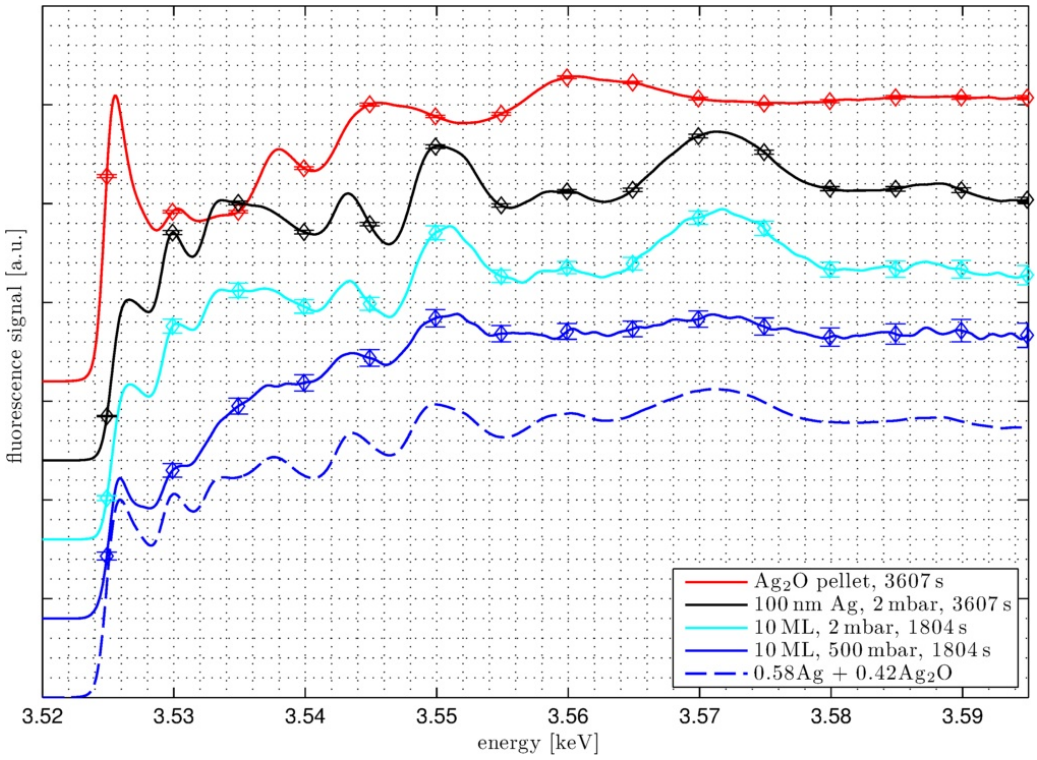

Figure 5.15: Ag L_2 XANES spectra of coalesced Ag clusters in silica aerogel in vacuum and oxidised at air ($p = 500\,\text{mbar}$) by X-ray radiation.

measurements again, the spectrum changes its shape (solid blue line). The distinct peaks at about 3.530 keV, 3.534 keV, 3.550 keV and 3.572 keV decrease. Also the relative height of the absorption edge increases. These are indications for a chemical reaction. However, while the spectrum of the unoxidised clusters was similar to that of the Ag film reference, the spectrum of the oxidised clusters does not match completely with the Ag_2O pellet reference.

The bottommost spectrum (dashed blue line) is constructed by a superimposition of the Ag film and Ag_2O pellet reference spectra: $p{\cdot}\text{Ag}+(1-p){\cdot}\text{Ag}_2\text{O}$. The factor p was calculated by a last square fit between this superimposed spectrum and the spectrum of the oxidised clusters. This leads to the assumption that the clusters were partly oxidised, thus about 42 % of the clusters were oxidised and about 58 % unoxidised.

Nevertheless also this constructed spectrum does not match optimally with the spectrum of the oxidised clusters. Thus it is sensible to have a closer look to the recorded single spectra of the oxidised clusters[5] This is shown in Figure 5.16. The black line in every plot is the spectrum of the first single measurement on the sample. The red ones are those which were recorded subsequently. Despite the low statistics, a good agreement can be observed between the first and second recorded spectra. After the forth measurement $\Delta t = 721\,\text{s}$, a shift of the onset of the absorption edge can be observed. After the fifth measurement a decrease of the peak intensities can be noticed. After about $\Delta t = 1263\,\text{s}$ measurement time the spectrum does not have typical features of a pure Ag sample anymore. Also the following spectra do not change any further.

This is also illustrated in Figure 5.17. Here the region around the absorption edge is plotted in detail for each measurement. The spectra were smoothed with a Gauss convolution with a FWHM

[5]It should be noticed that the spectra above were averaged over several single measurement spectra like explained in section 3.4.3. Here a single measurement had a duration of 180 seconds.

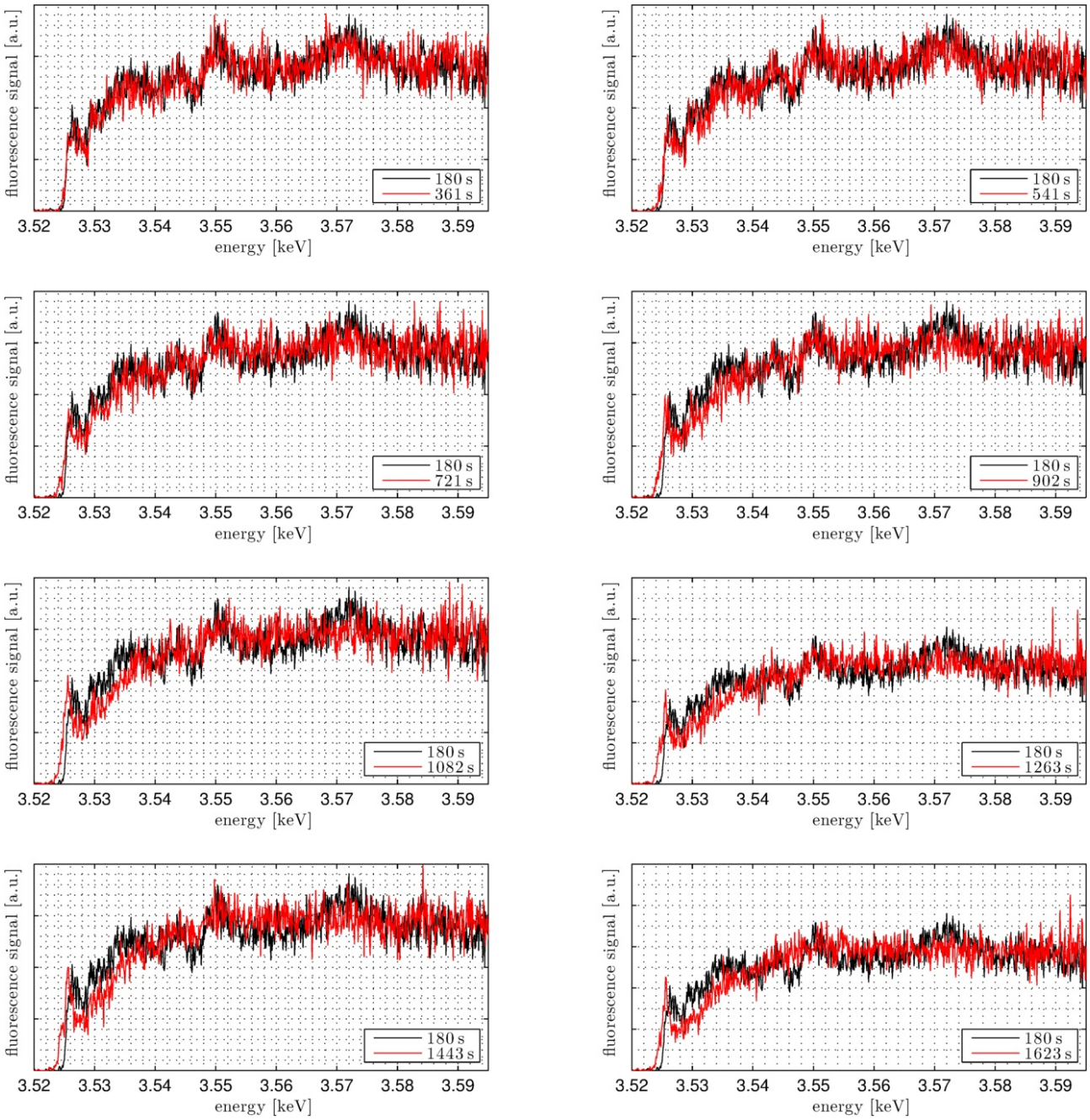

Figure 5.16: Single spectra of oxidation experiments ($p = 500$ mbar) on Ag clusters in a silica aerogel sample with a mean deposition amount of about 10 ML.

of 0.3 eV. The peak positions of the absorption edges are indicated by diamonds. First the height of the absorption edge decreases. Then the shift to lower energies starts due to the emergence of free d orbitals caused by Ag 4d orbital - O 2p orbital - hybridisation [Czyyk et al., 1989]. Also the onset itself shifts to lower energies. After about $\Delta t = 721$ s the appearance of the white line starts [Behrens et al., 1999]. After about $\Delta t = 1263$ s no systematic changes of the structure can be observed in the following recorded spectra. However, for completely oxidised clusters a more pronounced white line would be expected. Thus further experiments on separated clusters were carried out and are discussed in following.

In this experiment a sample with deposition amounts of 1.01 ML and 1.53 ML was placed in the vacuum chamber. The Ag L_2 XANES spectra are shown in Figure 5.18. The first measurements were

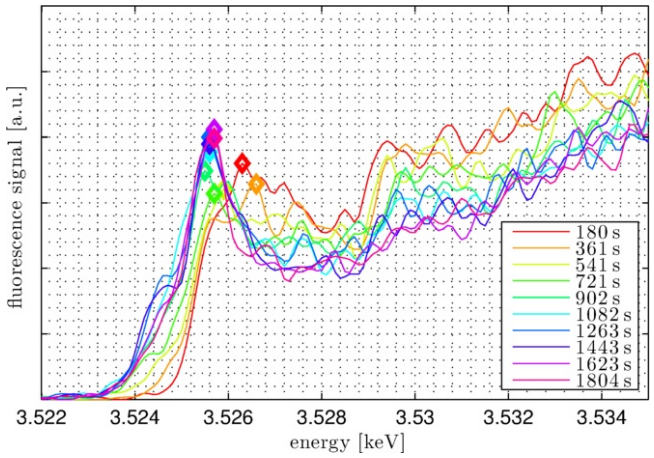

Figure 5.17: Near edge single spectra of the oxidation experiments ($p = 500\,\text{mbar}$) on Ag clusters in a silica aerogel sample with a mean deposition amount of about 10 ML, smoothed with FWHM of 0.3 eV. The peak positions are indicated by diamonds.

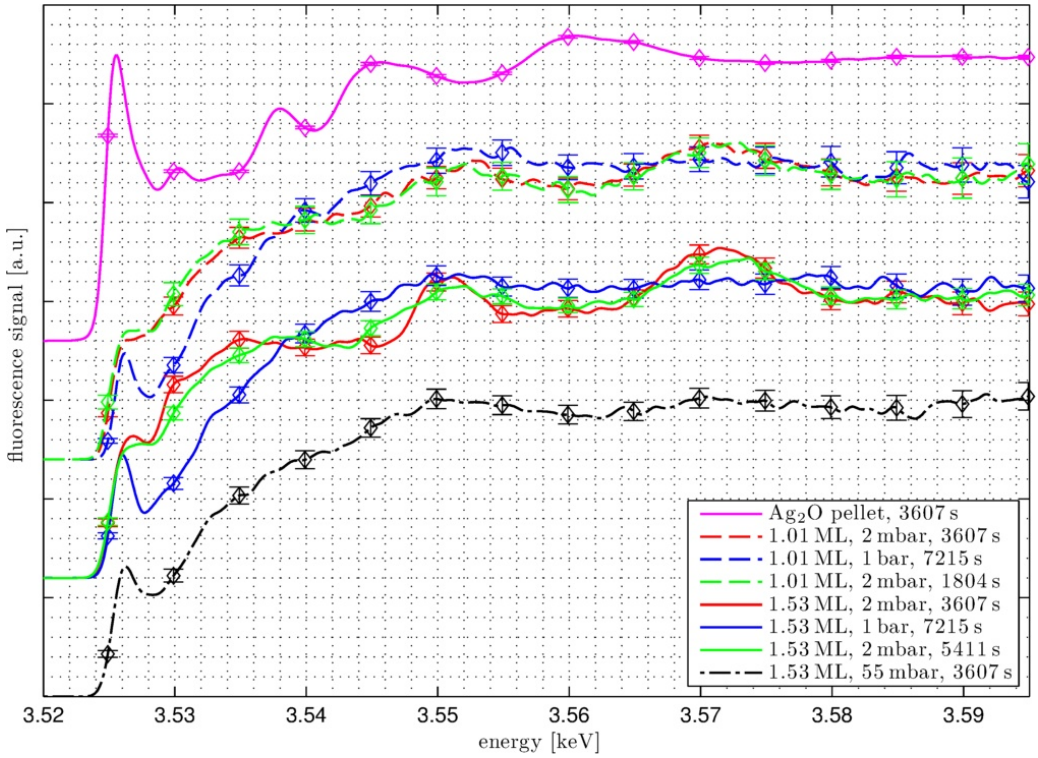

Figure 5.18: Ag L_2 XANES spectra of Ag clusters in silica aerogel with deposition amounts of 1.01 ML and 1.53 ML. Each position was measured first in vacuum, then in air and at last in vacuum again. Here the emergence and the disappearance of an oxidation state can be observed.

performed on Ag clusters with deposition amounts of about 1.01 ML in vacuum (dashed red line). The structure of the XANES spectrum indicates that the clusters are well separated. After increasing the pressure in the vacuum cell up to 1 bar and starting the measurements again, the emergence of an oxidation state is clearly visible (dashed blue line). However, also after 2 hours of measurement, typically features of an Ag_2O sample, like the peaks at 3.538 keV, 3.544 and 3.560 keV, are still not observable. Further, when decreasing the pressure in the sample cell down to 2 mbar (vacuum), the

chemical bonding between the Ag and O atoms is broken up and the XANES signal (dashed green line) is again similar to the signal of the sample, measured at the beginning.

These measurements were repeated on Ag clusters with a deposition amount of about 1.53 ML. It is remarkable that the XANES signal of these clusters has a more bulk like structure[6]. Thus it seems that some clusters started to coalesce and formed bigger particles. However, the spectrum still differs clearly from those of bulk material. The changes of the spectra caused by the increase and decrease of the pressure in the sample are similar to that observed before. It stands out, that despite the differences between the spectra of the pure Ag clusters with 1.53 ML and 1.01 ML, the spectra of the oxidised clusters are effectively equal (dashed and solid blue lines). After evacuating the cell again the spectra changes to become a pure Ag clusters XANES signal again. Nevertheless, the spectrum is a little bit smoothed. The peaks are less high but more broadly. This is an indication for still existing Ag_2O bondings.

It was also tried to create an equilibrium between the oxidation of the clusters and the breaking of the Ag_2O bonds. For this the pressure in the cell was increased from vacuum to about $p = 55$ mbar. The recorded XANES spectrum is indicated in Figure 5.18 by the dashed black line. The spectrum indicates a similar oxidation state like observed in the experiment before (solid blue line). Thus also at a low pressure with about 55 mbar the chemical process is shifted the bonding side and not to the breaking side. To exclude the measurement of mixed states caused by averaging the recorded spectra, the first four recorded single spectra of each measurement were checked individually. Though the statistics for these individual measurements are low, no time dependent changes could be observed, in contrast to the larger islands produced with a deposition amount of 10 ML.[7] This leads to the assumption that those clusters were oxidised very fast after the cell was filled with air and the beam shutter was opened. Also the disappearance of the oxidised state seems to be occurred on time scales which could not be detected.

[6] The 1.53 ML seems to be a lower limit of the deposition because at these deposition amounts a change in the spectrum is not expected.

[7] See appendix 8.4

5.2.4 Effect of sulphur on Ag clusters, investigated using Ag L_2 XANES spectroscopy

Additional to the experiments on oxidised Ag clusters, also XANES experiments on sulfidised Ag clusters were performed. Here Ag clusters in silica aerogel were placed for different time steps in a sulphur rich atmosphere by holding the samples above a conical flask inside a fume hood. This atmosphere was produced, like described before, by the reaction $2H_3PO_4 + 3Na_2S \rightarrow 2Na_3PO_4 + 3H_2S$. The produced H_2S then can react with silver $H_2S + 2Ag \rightarrow Ag_2S + H_2$.

Two samples with different deposition amounts were investigated. The first one had a relative high deposition amount of about 2.5 ML. Because the spectra of this sample have some similarities with the bulk reference spectrum, it is assumed that the clusters started coalescence. The second sample had a deposition amount of about 0.7 ML and can be assumed to consist of separated clusters.

The XANES measurements were performed in the vacuum chamber to prevent the sample from changing the sulfidised state into an oxidised state. It was observed that also the chemical bonding between the Ag and S atoms can be broken by X-ray radiation. To get a better knowledge of this process, the measurement position on the sample was systematically changed[8] in most cases to perform XANES measurements at positions where the X-ray beam did not incident before.[9] Also after each sulfidation step several of these measurements were performed to improve the possibility to observe the changes in the spectrum.

The recorded spectra are shown below. In each plot the bottommost spectrum is the sum of the single spectra in the first measurement sequence. The measurement time for each measurement sequence is indicated in the legend. The parameters for the measurements are listed in Table 5.2, Table 5.3 and Table 5.4. The letter in the first column indicates the sulfidation step (A for the first, B for the second and so on) and the following number denoted the number of the measurement sequence (first measurement sequence, second measurement sequence and so on). The time, the sample was exposed to sulphur rich atmosphere is listed in the second column. In the third column the number of measurements of each measurement sequence are listed and the times of each single spectrum in a sequence are listed in the last column. The fourth column presents information about the measurement position: macro means that the measurement position was changed after each single measurement of the height of the X-ray beam.[10]

Optical measurements were performed after each sulfidation step to get qualitative information about the reaction progress. Before sulfidation, a dip occurred in the sample transmission at the energetic position of the cluster plasmon. After the first sulfidation step this dip was much weaker. For the following sulfidation steps, a dip was not visible anymore. These measurements were performed ex-situ without the use of standard equipment and without information about the background scattering/absorption of the silica aerogel substrate. Thus a quantitative analysis of these measurements is not possible.

Coalesced sulfidised Ag clusters

The first sulfidation experiments were performed on a sample with coalesced Ag clusters in silica aerogel. The mean deposition amount of the clusters was about 2.5 ML. This sample was cut into four pieces. The spectrum of the unsulfidised piece is shown in Figure 5.19. The second piece of this cut sample was exposed for about 20 s to sulphur rich atmosphere. The corresponding spectra are shown in Figure 5.20 and the corresponding parameters are listed in Table 5.2. The third piece of the cut

[8] A macro procedure relocates the position of the beam at the sample after each single measurement of the height of the beam (300 μm). It has to be noticed, that after a macro has finished once, every position at the sample was illuminated once by the X-ray beam. If a macro was started another time, the same procedure was done in backward/opposite direction with an offset of 150 μm (half height of the beam).

[9] Because the positions on the sample correlate with the deposition amounts, the effective deposition amounts can vary slightly from measurement to measurement.

[10] It should be noted that after the macro did run the first time, the X-ray beam illuminated every position on the sample one time.

sample was sulfidised for longer times (300 s-3000 s). The corresponding spectra of the measurement sequences after each suflidation step are shown in Figure 5.21, Figure 5.22 and Figure 5.23. The parameters are listed in Table 5.3.

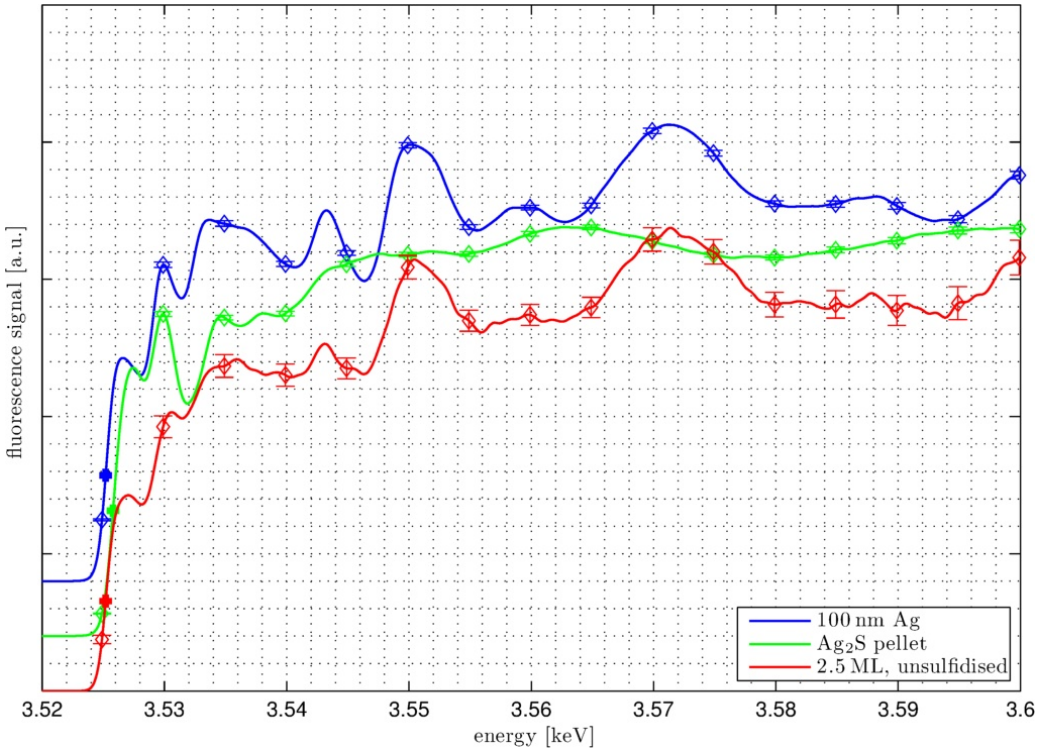

Figure 5.19: Ag L_2 XANES spectrum of a sample with about 2.5 ML Ag clusters in silica aerogel before sulfidation, measured in vacuum compared with the spectra of a 100 nm Ag film and an Ag_2S pellet reference sample.

The spectrum of the first piece of the unsulfidised cut sample in Figure 5.19 shows strong similarities between the spectrum of the Ag clusters in silica aerogel and the 100 nm Ag film. This indicates the presence of large silver particles with bulk like structures. Also no chemical reaction can be detected. Only the less pronounced peaks at about 3.530 keV and 3.534 keV suggest that the structure is not completely bulk like.

measurement	sulfidation time	measurements	position	time/spectrum
A1	20 s	10	same position	180 s
A2	20 s	17	macro	120 s
A3	20 s	18	macro	120 s
A4	20 s	6	macro	120 s

Table 5.2: Parameters of the measurements on partly sulfidised, coalesced Ag clusters in silica aerogel. The parameters belong to the second piece (see text) and correspond to Figure 5.20

The second piece was exposed to a sulphur rich atmosphere for about 20 s. The XANES spectra of four measurement sequences are shown in Figure 5.20. The spectrum of the first measurement sequence (red curve) consists of 10 single measurements at the same position (see Table 5.2). Each single spectrum was measured for 180 s. The resulting spectrum has the same features like the spectrum of unsulfidised Ag clusters in Figure 5.19. Here two possible explanations exist.

The first explanation is that the time of 20 s in the sulphur rich atmosphere was not long enough to cause a detectable chemical reaction. In this case the model of the optical measurements has to be

corrected. The changes in the spectra then have to be explained by damping effects of single foreign atoms or molecules in the cluster and not by a closed shell with a specific thickness.

The second explanation is that the illumination of the sample by the X-ray beam causes a break of the Ag-S-bonding so that no Ag_2S state can be observed. To check this, an additional measurement sequence was performed at the same sample, but the measurement time of the single spectra was decreased to 120 s and the sample position was relocated after each single measurement. Nevertheless, the resulting spectrum (yellow curve) does not differ significantly from the spectrum of the first measurement sequence and also no Ag_2S like characteristics can be observed. This procedure was repeated two additional times (green and cyan curves) but the resulting spectra are also similar to the ones recorded before.

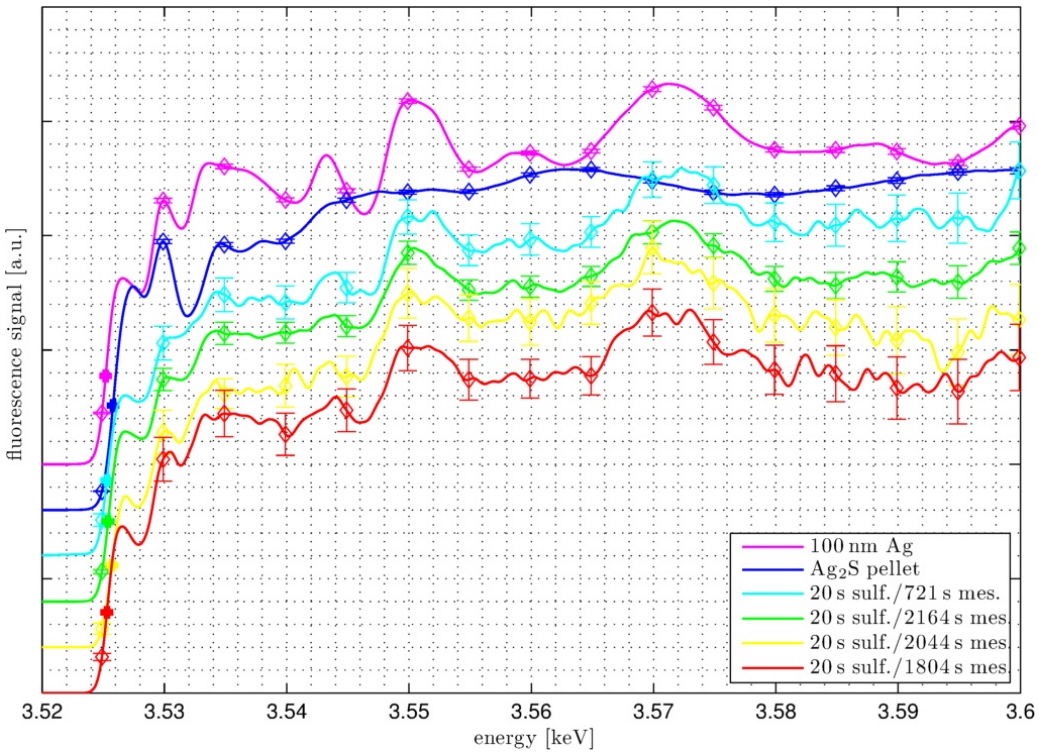

Figure 5.20: Ag L_2 XANES spectra of a sample with about 2.5 ML Ag clusters in silica aerogel after exposing the sample for about 20 s to sulphur rich atmosphere, measured by four sequences in vacuum compared with the spectra of a 100 nm Ag film and an Ag_2S pellet reference sample. The order from bottom to top corresponds to the chronological order of the measurement sequences.

The third piece was first sulfidised for about 300 s. The corresponding spectra are shown in Figure 5.21. Two measurement sequences were performed after the sulfidation step. The first (red curve) at the same position and the second (green curve) at different positions using a macro. However, the spectra are similar to the spectra in Figure 5.20. Thus no Ag_2S state can be observed.

For the second sulfidation step the third piece was placed again for additional 900 s in sulphur rich atmosphere. The resulting spectrum is shown in Figure 5.22 (red curve). Here differences between the 100 nm reference (and thus also from the unsulfidised cluster sample) and the spectrum of the sulfidised clusters sample are clearly visible. The peak at about 3.526 keV shifts almost 2 eV to about 3.528 keV, corresponding to the position of the peak of the Ag_2S reference spectrum at this position. Also the dip at about 3.532 keV is more pronounced while the structure between 3.536 keV and 3.55 keV loses Ag bulk characteristics. The structure above this energy is still present but essentially less pronounced. This can be explained by the presence of Ag and Ag_2S atoms/molecules in the clusters.

An additional sulfidation step of exposing the sample to sulphur rich atmosphere for additional

measurement	sulfidation time	measurements	position	time/spectrum
A1	300 s	20	same position	180 s
A2	300 s	25	macro	180 s
B1	300 s + 900 s = 1200 s	17	macro	120 s
C1	300 s + 900 s + 2 · 900 s = 3000 s	9	macro	120 s
C2	300 s + 900 s + 2 · 900 s = 3000 s	17	macro	120 s
C3	300 s + 900 s + 2 · 900 s = 3000 s	10	same position	120 s
C4	300 s + 900 s + 2 · 900 s = 3000 s	5	same position	120 s

Table 5.3: Parameters of the measurements on partly sulfidised, coalesced Ag clusters in silica aerogel.

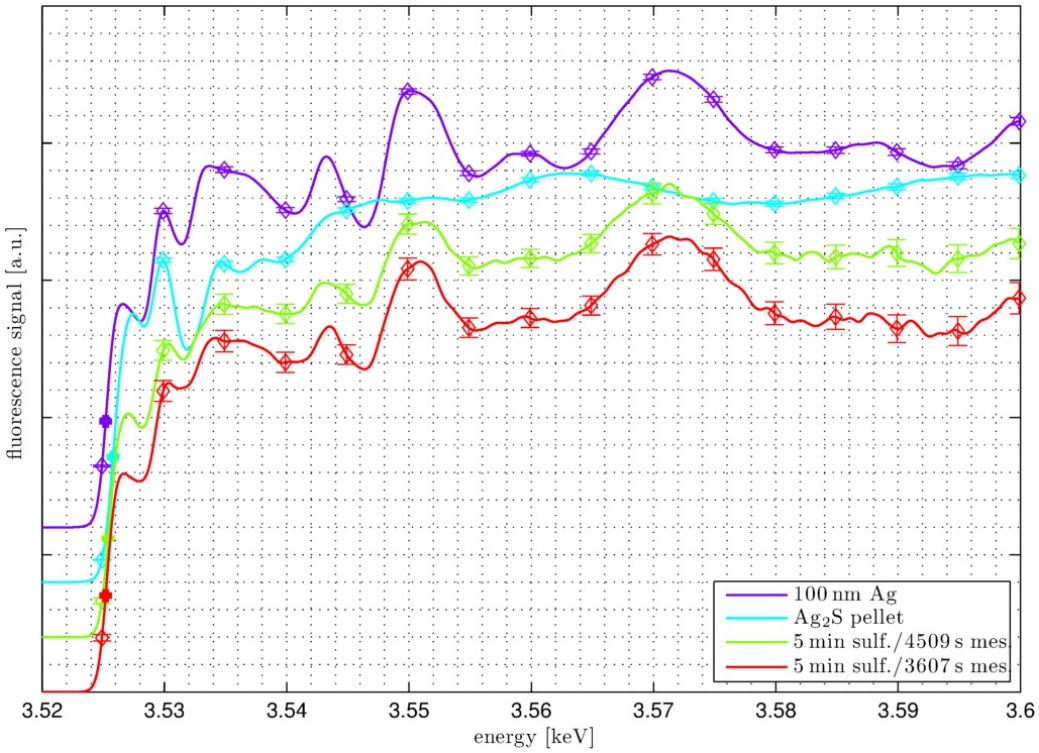

Figure 5.21: Ag L_2 XANES spectra of a sample with about 2.5 ML Ag clusters in silica aerogel after exposing the sample for about 300 s to sulphur rich atmosphere, measured by two sequences in vacuum compared with the spectra of a 100 nm Ag film and an Ag_2S pellet reference sample. The order from bottom to top corresponds to the chronological order of the measurement sequences.

1800 s causes a change in the structure of the XANES spectrum which corresponds to completely sulfidised silver. This is shown in Figure 5.23 by the red curve. In this measurement sequence a macro was used to reduce the influence of the X-ray beam to the chemical state during recording the spectra. The spectrum has the same structure like the Ag_2S reference spectrum. Small deviations can be explained by the low statistics of the spectrum which is a result of the short measurement time of 1082 s. This time was chosen to prevent/minimize beam damages. In the following measurement sequence, the single spectra were recorded at always the same position with a measurement time of 2044 s. The resulting spectrum (yellow curve) still exhibits characteristics of the Ag_2S structure. However, the structure changed after a third (green spectrum) and a fourth (cyan spectrum) measurement sequence, corresponding to additional 1804 s and 902 s measurement time, respectively. This is a result of the Ag-S-bond breaking, caused by the highly intense X-ray beam.

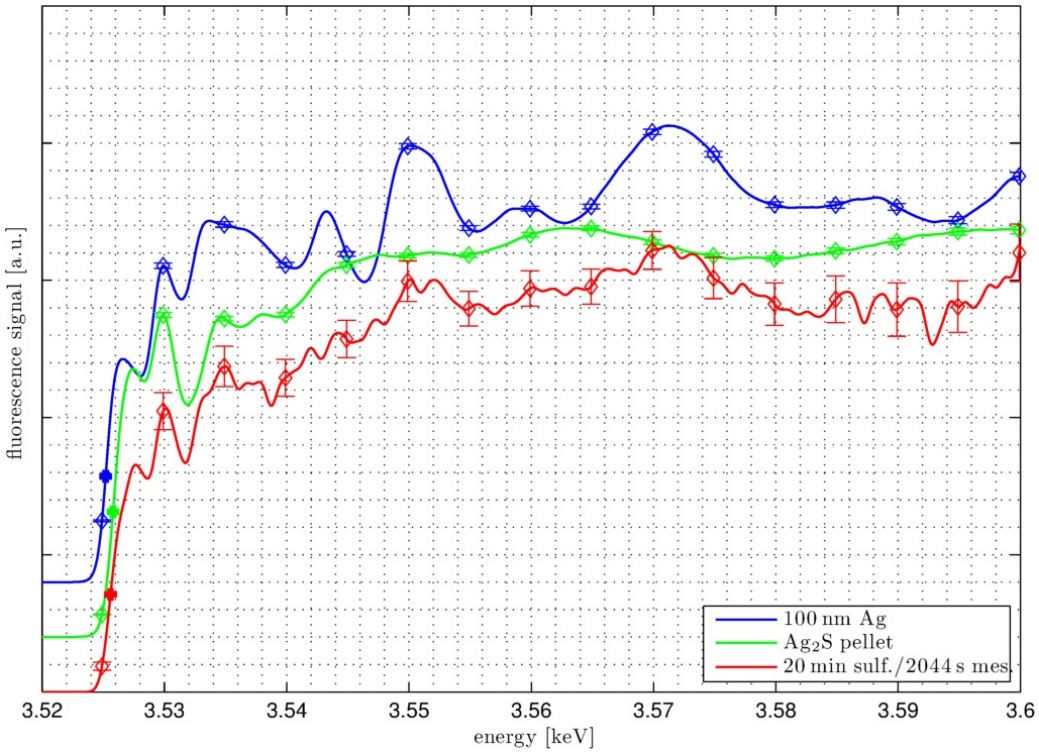

Figure 5.22: Ag L_2 XANES spectra of a sample with about 2.5 ML Ag clusters in silica aerogel after exposing the sample for about 1200 s to sulphur rich atmosphere, measured by one sequence in vacuum compared with the spectra of a 100 nm Ag film and an Ag_2S pellet reference sample.

To get a better insight to the processes which take place during the illumination of a sulfidised sample by the X-ray beam, it is of benefit to have a closer look to the spectra of the single measurements. However, the statistic is in that case not sufficient to extract information from the single spectra. Thus in the following the measurement sequences were divided into blocks of up to five single measurements. These (maximum) five single measurements were added up and smoothed by a Gauss convolution with a FWHM of 0.3 eV. The results are shown in Figure 5.24. The spectra were not normalised and an offset was not extrapolated or subtracted.

The partly summarised spectra of coalesced Ag clusters in silica aerogel after exposing for about 20 s to sulphur rich atmosphere are shown in the topmost row of Figure 5.24. Corresponding to the observations made in Figure 5.20, also in the present spectra no Ag_2S state can be observed. Further changes in the spectra due to the beam incident can not be observed. The spectra of the second measurement sequence exhibits more noise signals than the spectra of the other measurement sequences which is explained by a decrease of the total intensity of the X-ray beam (probably caused by a low storage ring current).

In the spectra of the first measurement sequence after exposing a sample for about 300 s to sulphur rich atmosphere, also no significant differences from the spectrum of the unsulfidised sample can be observed. However, these spectra were always recorded at the same position. In the second measurement sequence, a macro was used and the position was relocated. Here it seems, that the summarised spectrum of the first five single spectra differs from the following spectra due to the less pronounced structural characteristics. Nevertheless, a structural effect cannot be confirmed because also the following spectra were recorded by running the macro at unirradiated positions and would have to exhibit the same effect.

While the cluster spectrum in Figure 5.21 exhibits characteristics of an Ag_2S reference sample, this is not clearly observable in the corresponding summarised single spectra in Figure 5.24 (plot in the

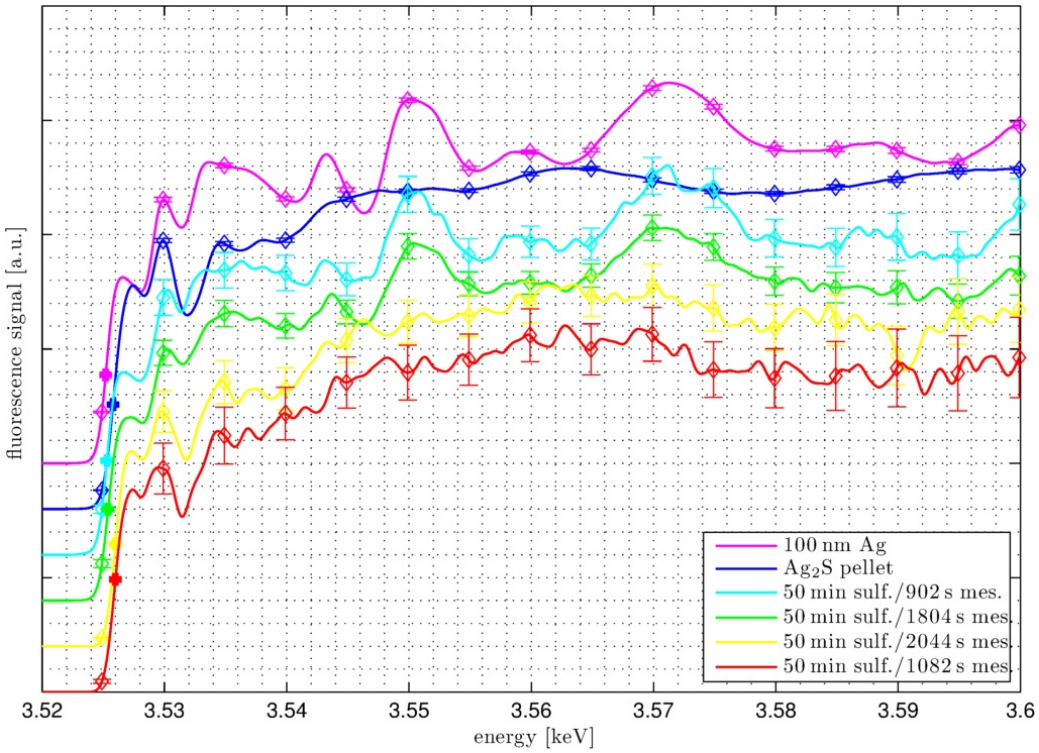

Figure 5.23: Ag L_2 XANES spectra of a sample with about 2.5 ML Ag clusters in silica aerogel after exposing the sample for about 3000 s to sulphur rich atmosphere, measured by four sequences in vacuum compared with the spectra of a 100 nm Ag film and an Ag_2S pellet reference sample. The order from bottom to top corresponds to the chronological order of the measurement sequences.

third row), due to the lower statistics. However, the strong peak at about 3.530 keV in connection with the strong dip at about 3.532 keV in the spectra suggests the presence of Ag_2S in the clusters.

After the last suflidation step (altogether about 3000 s in sulphur rich atmosphere), the first measurement sequence was recorded using a macro. The first five summarised single spectra exhibit clear Ag_2S characteristics indicated by the peak and the dip at about 3.530 keV and 3.532 keV, respectively, and the absence of the pronounced peaks at about 3.550 keV and 3.572 keV. The same characteristics can be observed in the summarised single spectra of the second measurement sequence, where also a macro was used to record the spectra. In the third measurement sequence all spectra were recorded at the same position. Already the spectrum of the first five summarised single spectra looks more similar to the spectrum of a silver sample than that of a silver-sulphur sample. The sum of the following recorded spectra confirms the assumption that the Ag_2S bonding was broken up by the incident beam.

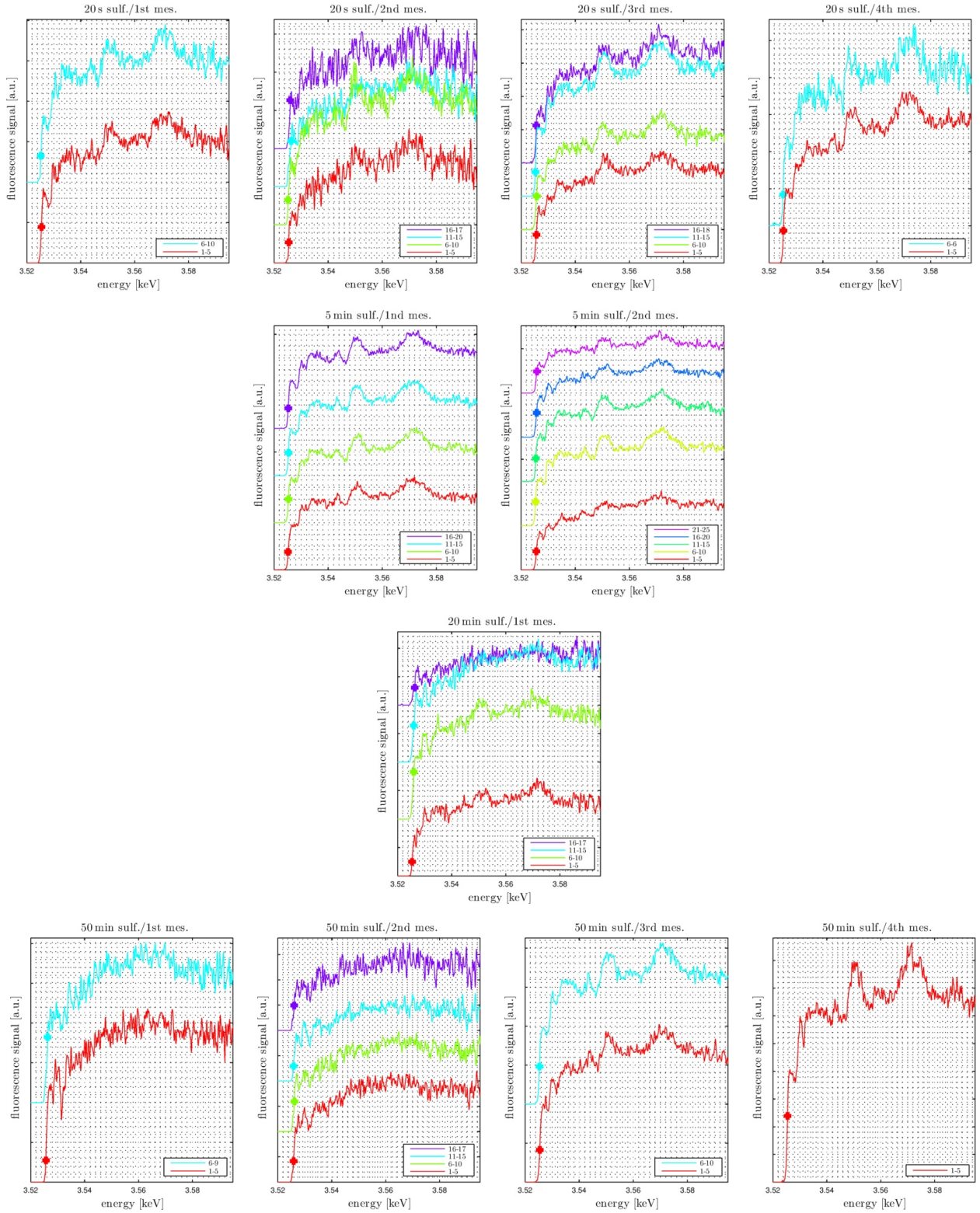

Figure 5.24: For a better insight on changes of the sample indicated by the Ag L_2 XANES spectra of partly sulfidised clusters in silica aerogel, every measurement sequence was divided into blocks of maximum five single spectra. These spectra were added up and smoothed by a Gauss convolution with a FWHM of 0.3 eV. The rows from top to bottom represent the first to the forth sulfidation steps, respectively.

Separated sulfidised Ag clusters

The measurements discussed above were repeated at isolated Ag clusters in silica aerogel with a mean deposition amount of about 0.7 ML. The parameters of the experiments are listed in Table 5.4. Because during the experiments for 2.5 ML, a fast decay of the Ag-S bonding due to X-ray beam exposition was observed, for every measurement sequence a macro which relocates the beam position after each single measurement was used for spectra recording.

measurement	sulfidation time	measurements	position	time/spectrum
A1	20 s	17	macro	120 s
A2	20 s	17	macro	120 s
A3	20 s	17	macro	120 s
A4	20 s	20	vert. reloc. + macro	120 s
A5	20 s	20	macro	120 s
B1	20 s + 60 s = 80 s	23	macro	120 s
B2	20 s + 60 s = 80 s	23	macro	120 s
C1	20 s + 60 s + 600 s = 680 s	23	macro	120 s
C2	20 s + 60 s + 600 s = 680 s	23	macro	120 s

Table 5.4: Parameters of the measurements on partly sulfidised, separated Ag clusters in silica aerogel.

Before starting the sulfidation experiments, two spectra at the unsulfidised sample were recorded at a distance of $\Delta = 300\,\mu m$, the height of the X-ray beam. The resulting spectra are shown in Figure 5.25. The absence of the peaks at about 3.530 keV, 3.534 keV and 3.543 keV confirms that the clusters are separated in the aerogel.

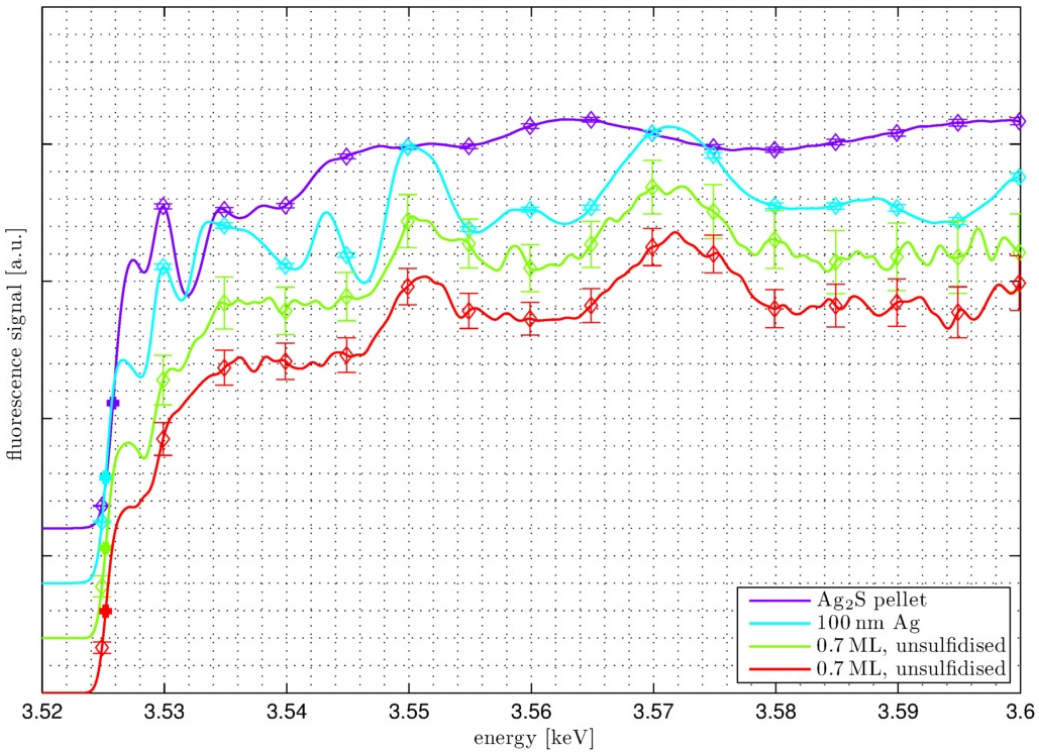

Figure 5.25: Ag L_2 XANES spectra of a sample with about 0.7 ML Ag clusters in silica aerogel before sulfidation, measured in vacuum compared with the spectra of a 100 nm Ag film and an Ag_2S pellet reference sample.

After the sample was exposed for about 20 *s* to sulphur rich atmosphere, the spectra (Figure 5.26)

differ from the spectra of the unsulfidised sample. The low statistics complicate a more detailed analysis because the observed changes are in the magnitude of the error bars. However, the missing pronounced peaks at about 3.550 keV and 3.572 keV in the first recorded spectra leads to the assumption that the clusters were at least partly sulfidised. The reappearance of those peaks in the following two spectra with decreasing amount of Ag-S bondings (due to beam damages), is in agreement with the observations made previously at the sample with coalesced clusters. The fourth measurement sequence confirms this assumption. After the sample was measured three times using a macro, the sample was relocated vertically thus the following measurements were performed at positions where the sample was not illuminated by the X-ray beam before. The fifth measurement has still similarities with the fourth but the emergence of Ag L_2 XANES peaks at 3.550 keV and 3.572 keV can be observed.

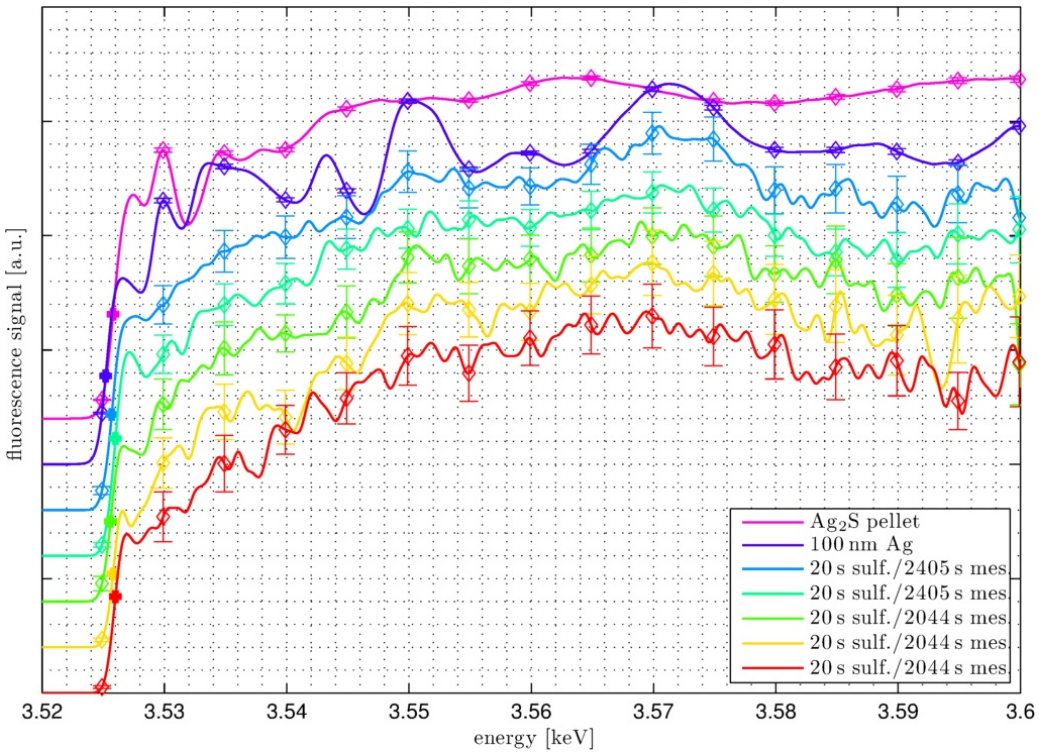

Figure 5.26: Ag L_2 XANES spectra of a sample with about 0.7 ML Ag clusters in silica aerogel after exposing the sample for about 20 s to sulphur rich atmosphere, measured by five sequences in vacuum compared with the spectra of a 100 nm Ag film and an Ag_2S pellet reference sample. The order from bottom to top corresponds to the chronological order of the measurement sequences.

In the second sulfidation step the sample was exposed for additional 60 s to the sulphur rich atmosphere. The following spectra, shown in Figure 5.27, look quite similar to those of the unsulfidised sample. This cannot be explained by an influence of the setup or the alignment. An explanation is difficult. The spectra look similar to the spectra of the 2nd, 3rd and 5th measurement after 20 s sulfidation. These are the measurements on sulfidised Ag clusters which were illuminated at least one time by the X-ray beam. Thus after the last measurement sequence on the 20 s sulfidised sample, most Ag_2S bonds were broken. In the case, the Ag clusters did not react well with the sulphur in the H_2S atmosphere in the following (60 s) sulfidation step, the subsequently recorded spectra would have similarities to those spectra recorded after 20 s sulfidation. This could be the explanation for the less pronounced Ag_2S structure after altogether 80 s in the sulphur rich atmosphere.

The spectrum of the first measurement sequence after the last sulfidation step (exposure of the sample to H_2S atmosphere for additional ten minutes) is similar to the previously observed spectra of

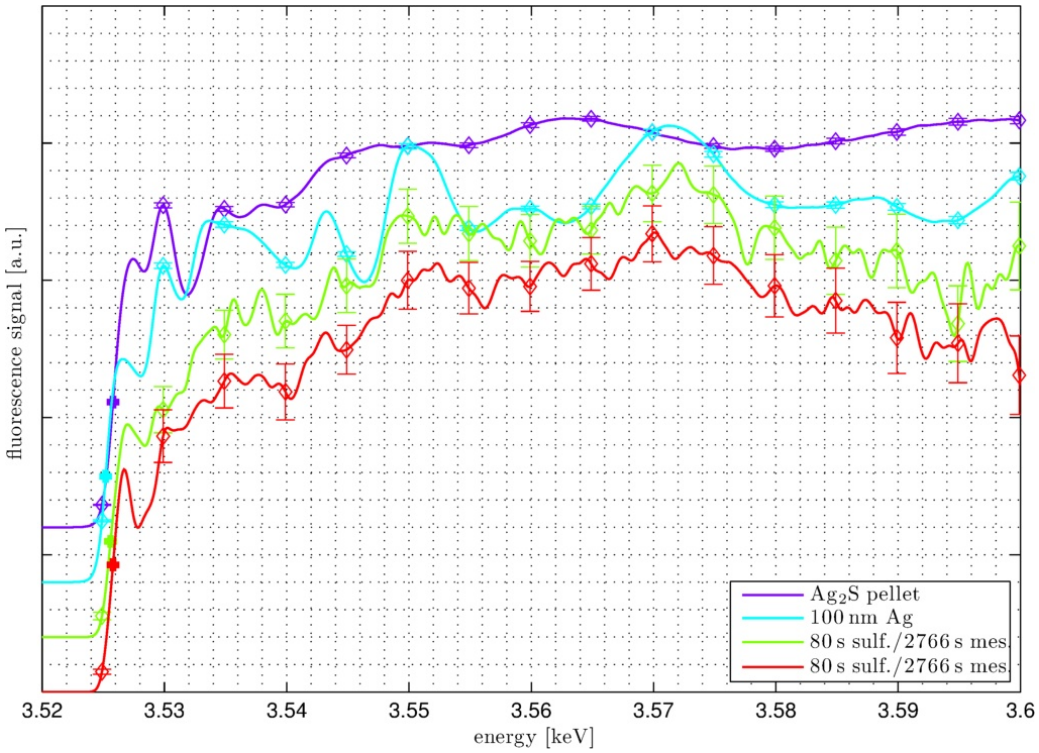

Figure 5.27: Ag L_2 XANES spectra of a sample with about 0.7 ML Ag clusters in silica aerogel after exposing the sample for about 80 s to sulphur rich atmosphere, measured by two sequences in vacuum compared with the spectra of a 100 nm Ag film and an Ag_2S pellet reference sample. The order from bottom to top corresponds to the chronological order of the measurement sequences.

sulfidised, separated clusters. This confirms the assumption that reactivity of the Ag clusters decreases quickly with the amount of reacted atoms. A second measurement sequence than again destroys a distinct amount of the Ag-S bondings, which is indicated by the Ag bulk like peaks of the green curve in Figure 5.28 at 3.550 keV and 3.572 keV.

The overall influence of sulphur on the separated Ag clusters will be discussed in following. A comparison between different single spectra or partly summarised single spectra is not useful here. Because at the sample with separated clusters, the beam position was relocated after each single measurement. Thus influences by the X-ray beam are only expected for different measurement sequences.

The spectra discussed previously are collected in Figure 5.29. The corresponding positions of the absorption edges are plotted in Figure 5.30.[11]

In contrast to the oxidation of silver, the Ag L_2 XANES spectrum of Ag_2S is not superimposed by a white line. Thus the progress of the chemical reaction can be observed by the shift of the absorption edge to higher energies with increasing amounts of Ag_2S.[12] The incidence of the X-ray beam can break the Ag-S bonding. Thus the amount of the Ag_2S like XANES signal decreases while the amount of the Ag like XANES signal increases.

In Figure 5.30 the Ag L_2 absorption edge position for pure separated Ag clusters is indicated by the measurements 1 and 2 at 3.5251 keV. After the first sulfidation (20 s in sulphur rich atmosphere) the edge shifted to an energy of 3.5259 keV.

[11] The assignment from measurement 1 to 13 in the x-axis of Figure 5.30 corresponds to the spectra listed in the legend in Figure 5.29 from bottom to top.

[12] The effective binding energy of an electron in an Ag atom is higher for Ag_2S (and also Ag_2O) than for pure Ag because the Ag atom is positively charged in this bounding.

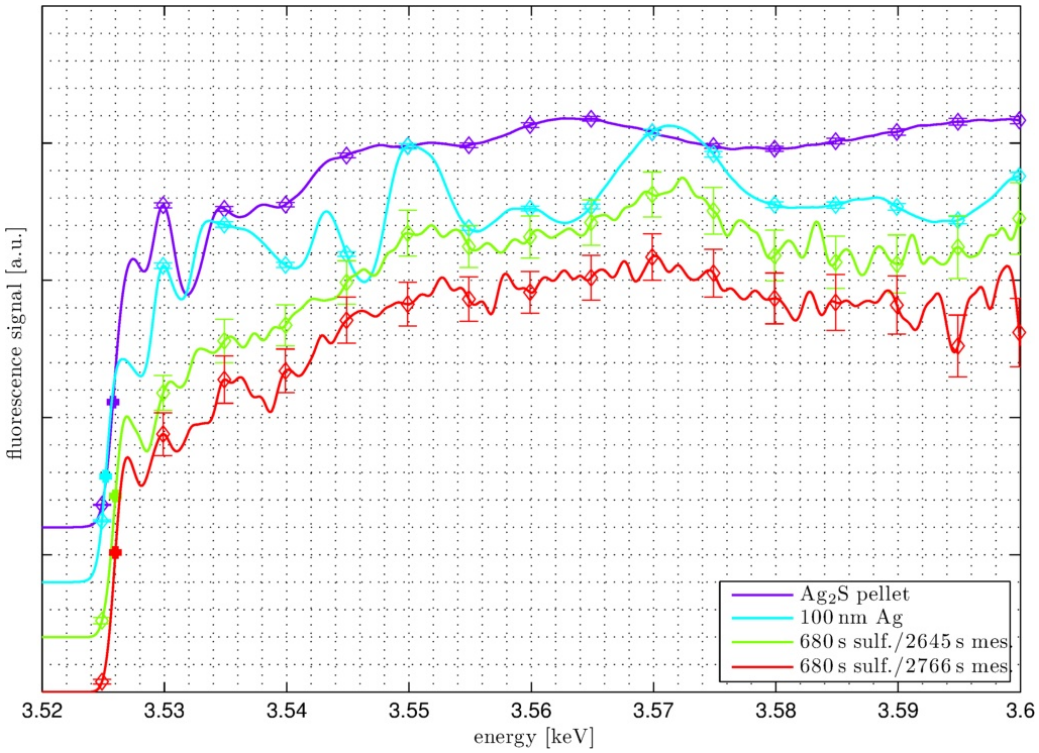

Figure 5.28: Ag L_2 XANES spectra of a sample with about 0.7 ML Ag clusters in silica aerogel after exposing the sample for about 680 s to sulphur rich atmosphere, measured by two sequences in vacuum compared with the spectra of a 100 nm Ag film and an Ag_2S pellet reference sample. The order from bottom to top corresponds to the chronological order of the measurement sequences.

The next measurements (numbers 4 and 5) caused a decrease of the existing Ag_2S and thus a shift back to lower energies. For measurement 6 the sample was relocated vertically thus the X-ray beam illuminated unaltered sulfidised Ag clusters again. This is confirmed by an absorption edge position of 3.5259 keV. The following measurement (number 7) was performed at the same position like measurement 6. Thus a part of the Ag-S bonds broke and the edge shifted to an energy of 3.5256 keV.

The absorption edge position of the measurements 8 and 9 confirm the assumption of an incomplete reaction between the Ag clusters and the H_2S. Also here the illumination caused a shift to lower energies.

After the sample was exposed to H_2S for about additional 600 s, the edge position again was at 3.5259 keV, like after 20 s sulfidation. This leads to the assumption that this is a final value for the absorption edge energy of sulfidised Ag clusters with a diameter of about 2 nm. It is striking that this energy is 0.2 eV above the energy of the Ag L_2 absorption edge of bulk Ag_2S. However, because the position of the absorption edge of the cluster samples investigated in section 5.2.2 was at 3.5252 keV, an error of $\Delta E = \pm 0.1$ eV should be considered. After another measurement the peak position is stable at 3.5259 keV. Similarities between the spectra of long time sulfidised clusters and the spectra of pure Ag clusters, lead to the assumption that also after ten minutes reaction time not all Ag atoms in the clusters reacted with S atoms.

This can be explained by a model where the Ag clusters first react quickly to an Ag-core Ag_2S-shell cluster. For further reactions S atoms or Ag_2S molecules have to diffuse to the core of cluster. This process is slow and occurs on long time scales.

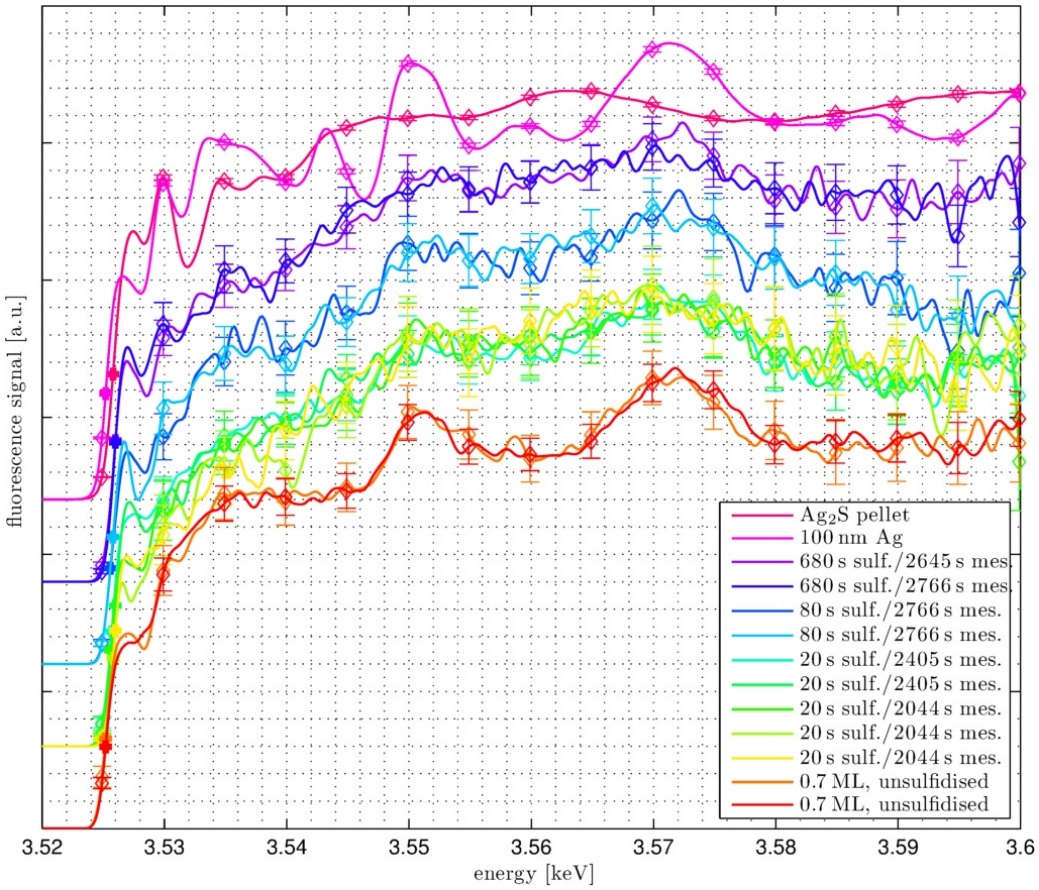

Figure 5.29: Summary of the Ag L_2 XANES spectra of (un-)sulfidised Ag clusters in silica aerogel, measured in vacuum.

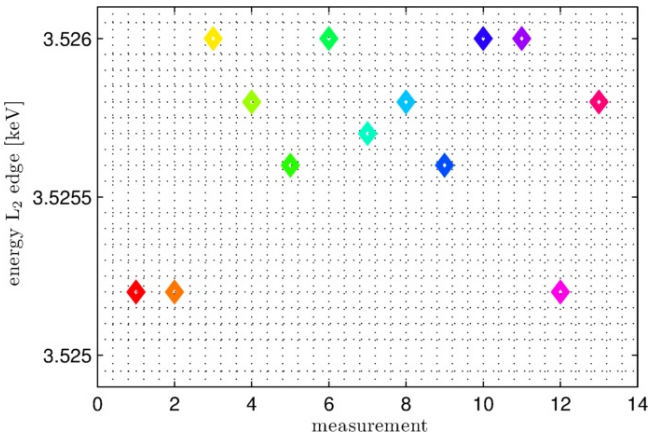

Figure 5.30: Positions of the Ag L_2 absorption edge of separated Ag clusters in silica aerogel after different times exposed to sulphur rich atmosphere. The corrsponding spectra of the edge positions indicated by measurement $1-13$ are shown in Figure 5.29 from bottom to top.

5.3 Summary and discussion of Ag clusters deposited into SiO_2 aerogel

From Ag L_2 XANES spectra of separated Ag clusters with a mean diameter of about 2 nm it was observed that the uDOS of pd hybrid band final states is lower than for bulk material. In contrast the uDOS of the p band final states for an Ag L_1 excitation of Ag clusters is similar to that of Ag bulk. Accordingly, it must be assumed that the uDOS of the d band of the investigated Ag clusters is lower than for bulk material.

The experiments on oxidised Ag clusters confirm this observations. For the Ag_2O pellet reference, the white line had about the height of the maximum of the spectra. For coalesced clusters (Figure 5.15) the height of the white line is of about 45 % of the height of the maximum of the spectra. And for separated clusters with deposition amounts of about 1.53 ML and 1.01 ML the ratios of the heights of the white lines to the maxima are 40 % and 35 %, respectively. Thus with decreasing clusters size, also the height of the white line decreases. This may be explained as following:
In Ag_2O, the transitions from the Ag 2p state to the d state dominate the transitions into the s state by an order of magnitude [Šipr et al., 1999]. Further the height of the white line correlates with the degree of covalent bonding [Behrens, 1992]. Theses covalent bondings cause a decrease in the occupation of the d states on the Ag site of the Ag_2O [Czyyk et al., 1989]. A decrease of the white line for a given oxidation state thus indicates a decrease of the de-occupation of the d states [Behrens et al., 1999] or a weaker contribution of the d electrons to the Ag_2O bonding.

Here the question is, if this would correlate with an overlap of the valence bands. A smaller overlap would result in a lower DOS (and uDOS) in the region above the white line and thus could yield an explanation for the more pronounced dip at 3.528 keV in Figure 5.18 for separated clusters than for coalesced clusters (Figure 5.15).

Oxidised Ag clusters were produced by exposing the samples with deposited clusters to the X-ray beam at a pressure of 1000 mbar. The fast oxidation process observed at separated clusters can be regarded to their high surface to volume ratio. A more stable oxygen bonding for those clusters is unlikely because after decreasing the pressure of the atmosphere to a few mbar the oxidation signal disappeared as quickly as it emerged (Figure 8.5). For comparison, no changes in the spectra of an Ag bulk reference could be observed under similar conditions. It is remarkable that after 1 hour XANES measurements at a pressure of about 55 mbar, a silver-oxide signal was detected (Figure 5.18).

From the Ag L_2 XANES measurements at coalesced Ag clusters at air ($p = 500$ mbar) the emergence of an oxidation state can be well observed at the position and the height of the absorption edge (Figure 5.17). However, the Ag L_2 XANES signal after 30 minutes measuring at air does still differ from the Ag_2O reference signal (Figure 5.15).

Ex-situ experiments on partly sulfidised clusters are difficult to perform because the intense X-ray beam breaks up the bondings between sulphur and silver. A sulphur-silver bonding is indicated by the shift of the Ag L_2 absorption edge to higher binding energies (Figure 5.30).

The Ag L_2 XANES spectra of long time sulfidised coalesced clusters are similar to the spectrum of an Ag_2S pellet reference. It is possible that incorporations of H_2S in the SiO_2 aerogel network (after long sulfidation times) stabilised the measurement of an Ag_2S XANES signal (Figure 5.23).

The peak and the dip at about 3.530 keV and 3.532 keV, respectively, in the Ag L_2 spectrum of the Ag_2S reference appeared also for the sample with long time sulfidised (20 min and 50 min) coalesced clusters (Figure 5.22 and Figure 5.23). However these structures were not observed for the 10 min sulfidised sample with separated clusters (Figure 5.28). This could be due to the shorter sulfidation time or to the absence of these electronic structures for those separated clusters .

6 Results of experiments on Ag clusters in BMIM PF_6

The last investigated system in this thesis are Ag clusters deposited into room temperature ionic liquids. In contrast to the deposition of clusters onto surfaces, the deposition of clusters into a liquid can enable the deposition of higher amounts of clusters before risking coalescence/aggregation. However, this requires the transfer of the clusters from the surface of the liquid into the volume of the liquid or the transfer of liquid from the volume to the surface, to prevent the formation of a closed Ag layer on the surface of the liquid.

A disadvantage in the use of liquid systems compared to solid samples, is the probability of aggregation processes for also low deposition amounts. On solid samples, aggregation takes part for very smooth surfaces which interact only weakly with the deposited clusters [Goldby et al., 1996]. For clusters on those surfaces it was observed that cooling the system can decrease and stop these aggregation processes [Engemann, 2011, Miroslawski, 2014].

Clusters in RTILs are a currently intensively investigated sample system. Because RTILs are produced since several years industrially and can be purchased by adequate prices, many research groups use RTILs for different experiments, also for cluster production. Especially because the RTILs are known as green solvents, chemists use them for the synthetic production of clusters by reduction of metallic precursors in ionic liquid solvents [Zhang et al., 2004, Redel et al., 2008].

Beside the usage of RTILs as solvents in wet chemical production of clusters, also further properties of the RTILs are used for cluster production. In sputter deposition experiments their extremely low vapour pressure is used to spark a plasma discharge between a metal target and the surface of the RTIL [Torimoto et al., 2006]. Atoms and clusters are sputtered out of the target and travel to the surface of the liquid where a first growth phase occurs. A second growth phase occurs in the volume of the liquid [Kuwabata et al., 2010]. With these method also the production of Au-Ag core-shell nanoparticles (NPs) could be realised [ichi Okazaki et al., 2008]. It was observed by the investigation of small angle X-ray scattering that the size and size distribution of those produced NPs is influenced by the kind of the ionic liquid, especially by the length of the side chains in the case of imidazolium based ionic liquids [Hatakeyama et al., 2009]. Also the experimental parameters of the sputtering process have significant influences of the size of the NPs. While the size of the NPs is independent from the sputtering time, the sputtering discharge current influences the size of the produced NPs [Wender et al., 2010].

However, there are also disadvantages of the above described NP producing processes. Thus the size of the produced NPs depends on the used RTIL. Further in the wet chemical production the precursors and reduction chemicals have to be removed after the NP were formed from the liquid system. The presence of those impurities can, in some circumstances, lead to unwanted side effects.

In the present thesis, first experiments for depositing Ag clusters with a mean diameter of about 2 nm and a narrow size distribution into a RTIL were performed. These experiments enable a new approach to the tuning of cluster functionalization. For example the clusters might be mass selected before depositing them into the liquid.

Also fundamental investigations of the properties of the Ag clusters in the ionic liquid could be made. For example, while OKAZAKI et al. observed the stability of Au, Ag and Au-Ag alloy clusters in BMIM PF_6 produced by sputter deposition without the addition of stabilisation agents [ichi Okazaki et al., 2008], in our experiments we observed an aggregation of the Ag clusters after deposition into the RTIL.

In the experiments of the present thesis, a structure in the UV-Vis spectra of clusters in BMIM PF_6 was observed between an energy of 4 eV and 4.5 eV. It is supposed that this could be caused by different amounts of water in the sample with deposited Ag clusters and the corresponding reference samples. Although the optical absorption of water is very low in the region between 200 nm and 400 nm (corresponding to energies of 6.2 eV and 3.1 eV), it increases from 3.1 eV and 6.2 eV of about two orders of magnitude [Hale and Querry, 1973]. Further the intensity of the lamp spectra decreases in the energetic range between 4 eV and 4.5 eV. This is illustrated in Figure 6.1. The transmission of

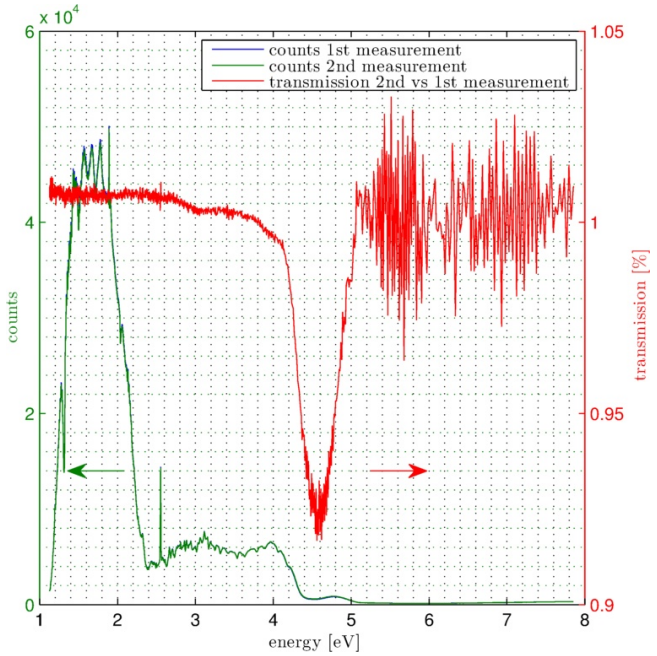

Figure 6.1: Raw spectrum of a BMIM PF_6 sample measured two times (blue and green curve). The blue curve is nearly completely covered by the green one. The transmission of the second measurement referred to the first is shown by the red curve. The rough spectra (blue and green curve) are referred to the left axis and the transmission spectrum is referred to the right axis. The spectra were recorded with a temporal distance of a few minutes under equal conditions.

the UV-Vis light through the RTIL in a cuvette was measured twice with a temporal distance of a few minutes. The used BMIM PF_6 was purchased from Sigma Aldrich, Fluka Analytical, purity $\geq 98.5\,\%$. It was degassed in the vacuum chamber for about 5 hours and measured after about 1 hour at air. The first measured blue spectrum is almost completely covered by the second measured green spectrum. Differences can be made visible by using the first spectrum as a reference for the second one. If both spectra were equal, the resulting red curve should be a constant line with an intensity of 100 %. A dip can be observed at an energy of about 4.3 eV. Thus peak like structures in the UV-Vis extinction spectra on Ag cluster in BMIM PF_6 in the region between 4 eV and 4.5 eV should be considered to effects in the liquid, that are not connected to the deposited Ag clusters.

6.1 Time depending aggregation process of deposited Ag clusters into BMIM PF_6

In first deposition experiments the aggregation process of the clusters in the ionic liquid could be observed optically. While the colour of the liquid is typically light yellowish, after cluster deposition it was strongly yellow, caused by the extinction of the Ag cluster plasmon resonance. With increasing time after deposition, the clusters aggregated and the colour switched into a transparent yellow-grey. After these observations, the experiment was repeated and this process was documented by taking pictures using a webcam. In an additional experiments this process was controlled by performing UV-Vis measurements.

6.1.1 Optical observations of aggregation

The room temperature ionic liquid 1-Butyl-3-methylimidazolium hexafluorophosphate was purchased from Carl Roth GmbH + Co. KG (batch nr. 20896717, with a purity $\geq 99\,\%$) and placed into the mixer (section 3.2.4) under vacuum conditions over night. To enable a better degassing process the mixer ran over night with an appropriate small velocity. It could be observed that the pressure in the experimental chamber increased when the mixer was started. In a later experiment this process was controlled using a quadrupole mass spectrometer at another BMIM PF_6 sample[1] The results of the quadrupole measurements with stopped and running mixer are shown in Figure 6.2. The blue bars

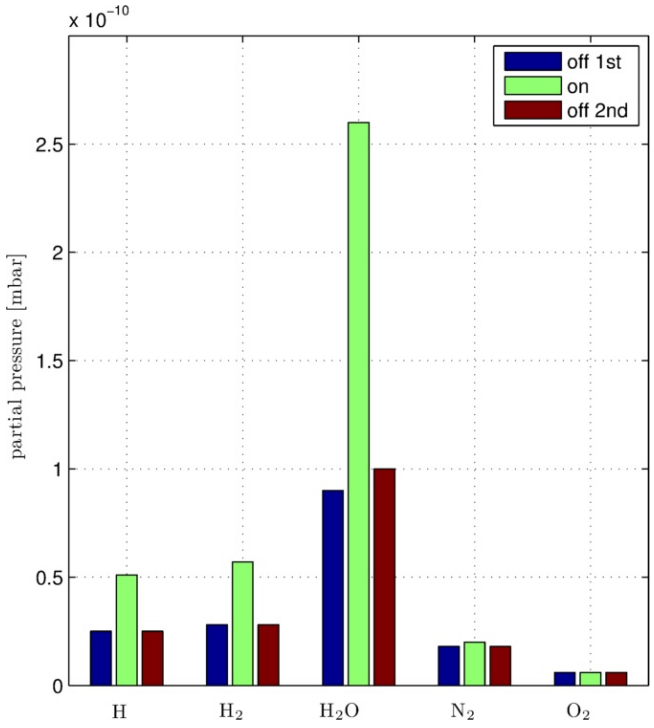

Figure 6.2: Quadrupole mass spectra indicate the partial pressure in the experimental chamber with RTIL. The blue bars indicate the partial pressures with mixer off. The the green bars indicate the partial pressures while the mixer is running. After that, the mixer was switched off again. The corresponding partial pressures are indicated by the red bars.

in Figure 6.2 show the mass spectra while the liquid is in the mixer under vacuum conditions and the mixer is turned off. After the mixer is turned on, especially the partial pressure signal of water increases (Figure 6.2, green bars). After the mixer was turned off again, also the signals of the mass

[1] This liquid was also purchased by Carl Roth GmbH + Co. KG but of the batch nr. 323203553, with a purity $\geq 99\,\%$.

spectra decreased to their origin values (Figure 6.2, red bars). Thus most impurities can be assigned to water incorporations which can be removed by storing the RTIL for several hours (best over night) under vacuum conditions and turning the mixer on.[2]

After drying the RTIL in the mixer under vacuum conditions, Ag clusters were deposited into the liquid ($m_{\mathrm{IL}} = 29.71\,\mathrm{g}$, $\rho_{\mathrm{IL}} \approx 1.38\,\mathrm{g/ml}$, $V_{\mathrm{IL}} = 21.53\,\mathrm{ml}$) for about 150 s with a deposition rate of about 0.35 nm/s. Thus the total deposition amount was $h_{eff} = 52.5\,\mathrm{nm} = 43.4\,\mathrm{ML}$. The radius of the roller of the mixer is 30 mm and the diameter of the cluster beam is about 36 mm so that the beam strikes the height of the upper half of the mixer completely. Thus the effective deposition area is about $A_{\mathrm{Ag}} = \pi \cdot 15^2\,\mathrm{mm}^2 = 706\mathrm{mm}^2$ and the volume of the deposited clusters $V_{\mathrm{Ag}} = A_{\mathrm{Ag}} \cdot h_{eff} \approx 37.1 \cdot 10^{-6}\,\mathrm{cm}^3$. This corresponds ($\rho_{\mathrm{Ag}} = 10.49\,\mathrm{g/cm}^3$) to a deposited mass of $m_{\mathrm{Ag}} = 389\,\mu\mathrm{g}$. Pictures of the prepared

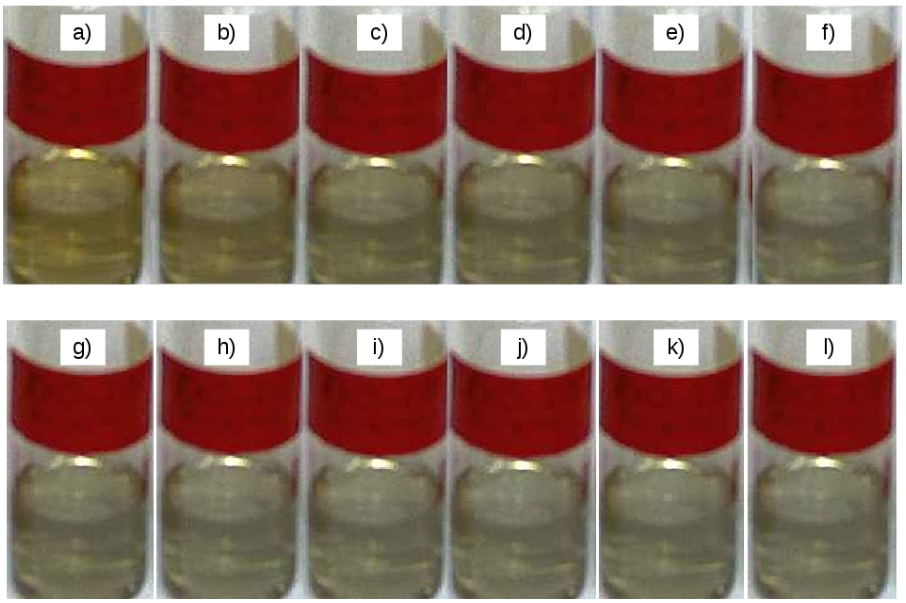

Figure 6.3: Pictures of a sample with Ag clusters in BMIM PF_6, taken at different times (hh:mm) after preparation: a) 05:03, b) 06:20, c) 08:19, d) 09:34, e) 10:20, f) 12:48, g) 13:23, h) 17:47, i) 19:07, j) 19:08, k) 20:58, l) 21:45. The pictures i) and j) were taken at about the same time. Because they look similar, influences by the camera can be excluded.

sample, taken at different time steps after deposition, are shown in Figure 6.3. A clear shift of the colour of the sample can be observed from strong yellow to a transparent like yellow-grey. Also it is observable that this shift takes part in the first hours after deposition. The last pictures in these series do not differ noticeable which indicates that most clusters in the sample already seem to be aggregated.

[2] Another often used method is heating the liquid up to temperatures of about 100 °C for several hours under vacuum conditions. For the experiments presented here, this method is not very practicable because the RTIL does incorporate H_2O again from the air by transferring the liquid from the vacuum oven to THECLA.

6.1.2 UV-Vis measurements after deposition process

After these first experiments, the tub of the mixer was filled in a following experiment with about 21 ml of the same RTIL. In opposite to the previously performed experiments it was not possible to put the liquid into the vacuum over night. This sample was only able to degas for about 7 hours. The deposition took 150 s with a mean cluster beam rate of about 0.11 nm/s. Thus the deposition mass was about $m_{Ag} = 123\,\mu g$. The sample was stored and measured at room temperature. The UV-Vis measurements were performed without using the cuvette holder presented in section 3.3.1. Thus the calibration of the optical setup was something failure-prone and the resulting extinction spectra have to be analysed carefully. This will be shortly discussed at Figure 6.4.

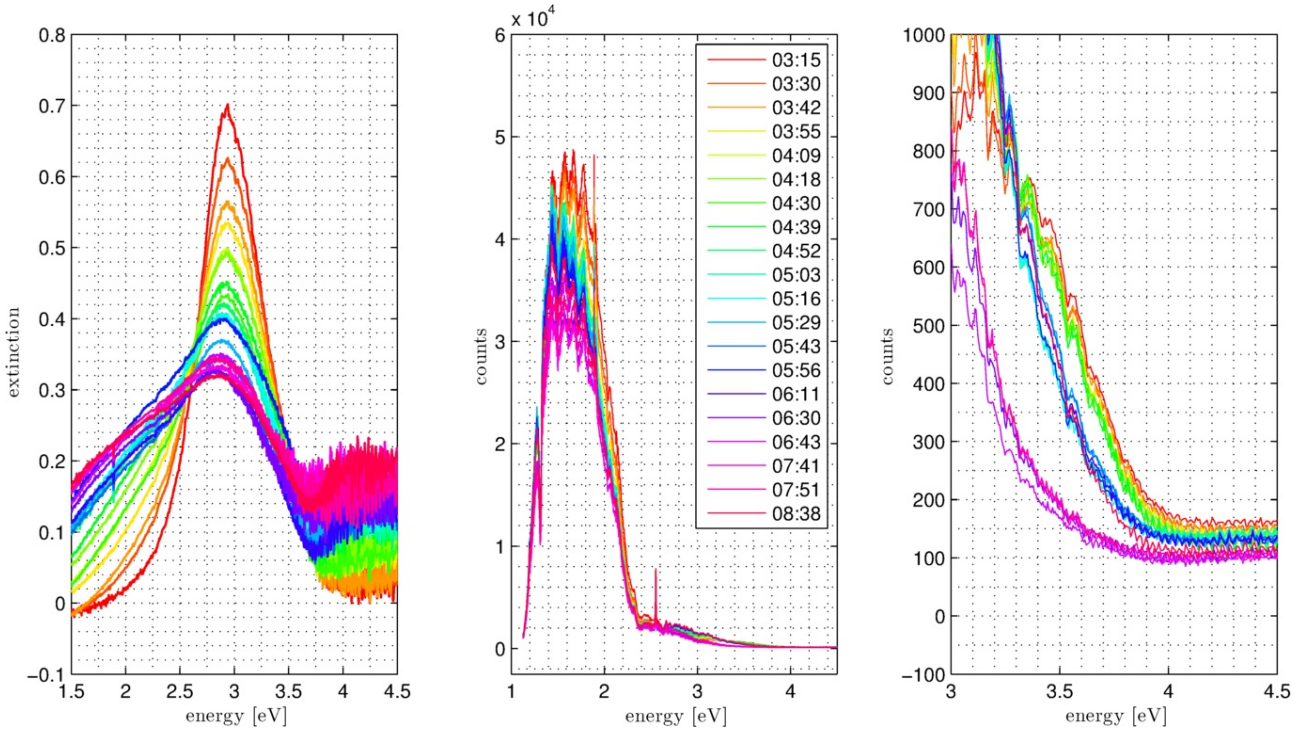

Figure 6.4: Left: Optical extinction spectra of Ag clusters deposited in BMIM PF_6 for different times after deposition. Middle: Measured raw counts of the performed extinction measurements after subtracting the dark counts. The legend corresponds to all three plots. Right: Zoom into the region where the intensities in the middle plot are low.

In Figure 6.4 (left plot) all measured extinctions are shown, in the middle plot the raw measured counts after subtracting the dark signal[3] and in the right plot a zoom into the middle plot. It can be seen, that the signal is only analytical for energies below about 3.6 eV. Above this energy the intensity is very low and the transmission and extinction should be considered cautiously.

Nevertheless, the extinctions measured by cluster sample and reference sample with high intensity and also those with weak intensity correspond to typical cluster extinction spectra. Changes in the spectra for different time steps do not only appear for the low intensity region but also for the region with high intensity (1.5 eV-2.6 eV, middle plot). Thus the shapes of the cluster plasmon resonance spectra are not influenced by the low optical signal for energies below about 3.6 eV.

There is a clear decrease of the height of the cluster plasmon observable for spectra recorded less than 5.5 hours after deposition which can be attributed to aggregation processes of the clusters in the RTIL.

For a better depiction, some chosen spectra of Figure 6.4 are plotted in Figure 6.5 (left). The decrease

[3] the signal which is present also when the UV-Vis lamps are switched off

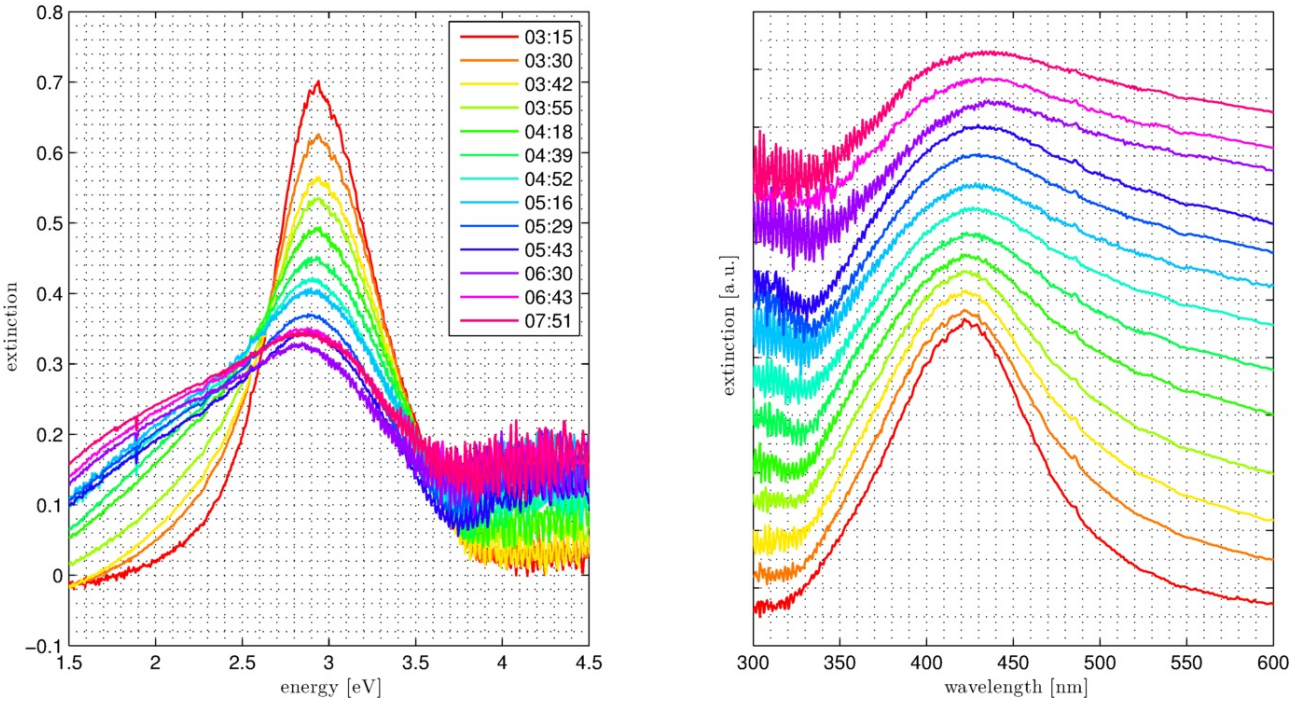

Figure 6.5: In the left plot a range of Ag cluster extinction spectra from Figure 6.4 are shown for a better depiction. The same spectra as functions of wavelength, normalised to the area under each curve between 350 nm and 500 nm are plotted with an increasing offset in the right figure.

of the height of the extinctions with increasing time after deposition is visible. Also the increase of the FWHM is visible. The peak stays stable at about the same position while the extinction in the energetic region below the peak increases. This behaviour seems to be describable by the forming of chain like structures, consisting of agglomerated clusters. This behaviour was described in section 2.3.6 by simulations from QUINTEN.

For comparison the same spectra as functions of wavelength, normalised to the area under each curve between 350 nm and 500 nm are plotted with an increasing offset (waterfall plot) in Figure 6.5 (right). The comparison with Figure 2.20 leads to the assumption that only few (< 4) clusters were coupled and that there were still single clusters. A quantitative comparison is not possible because the ε_m and also the size and size distribution of the clusters differ from the model made by QUINTEN. Furthermore, there are no information about the geometric structures of the formed agglomerates. Similar to Figure 6.3 a change of the sample colour from yellow to grey accompanied the change of the spectra in Figure 6.5. The change was much weaker for a control sample which was kept simultaneously in a refrigerator for most of the time.

6.1.3 UV-Vis in-situ measurements during deposition process

In further experiments using another batch of BMIM PF_6 (Carl Roth GmbH + Co. KG, batch nr. 323203553, with a purity $\geq 99\,\%$) also strong aggregations and precipitation of silver during the deposition process was observed. To get a better insight in this process an additional mixer was constructed which enables optical in-situ measurements of the RTIL during the deposition process(see Figure 3.12).

15 ml of the RTIL were given into the tub of mixer-2 and stored in vacuum for one night. The cluster beam rate at the beginning of the experiment was 0.04 nm/s and at the end 0.005 nm/s. For the calculation of the deposition amounts a linear decrease of this rate was assumed. The resulting extinction spectra are shown in Figure 6.6. At an energy of about 4.1 eV there is a cut-off due to absorptions the RTIL and the mixer. The transmittance decreases for energies above 4.0 eV virtually to zero. The spectrum of the raw counts for pure BMIM PF_6 in the mixer is attached in Figure 6.12.

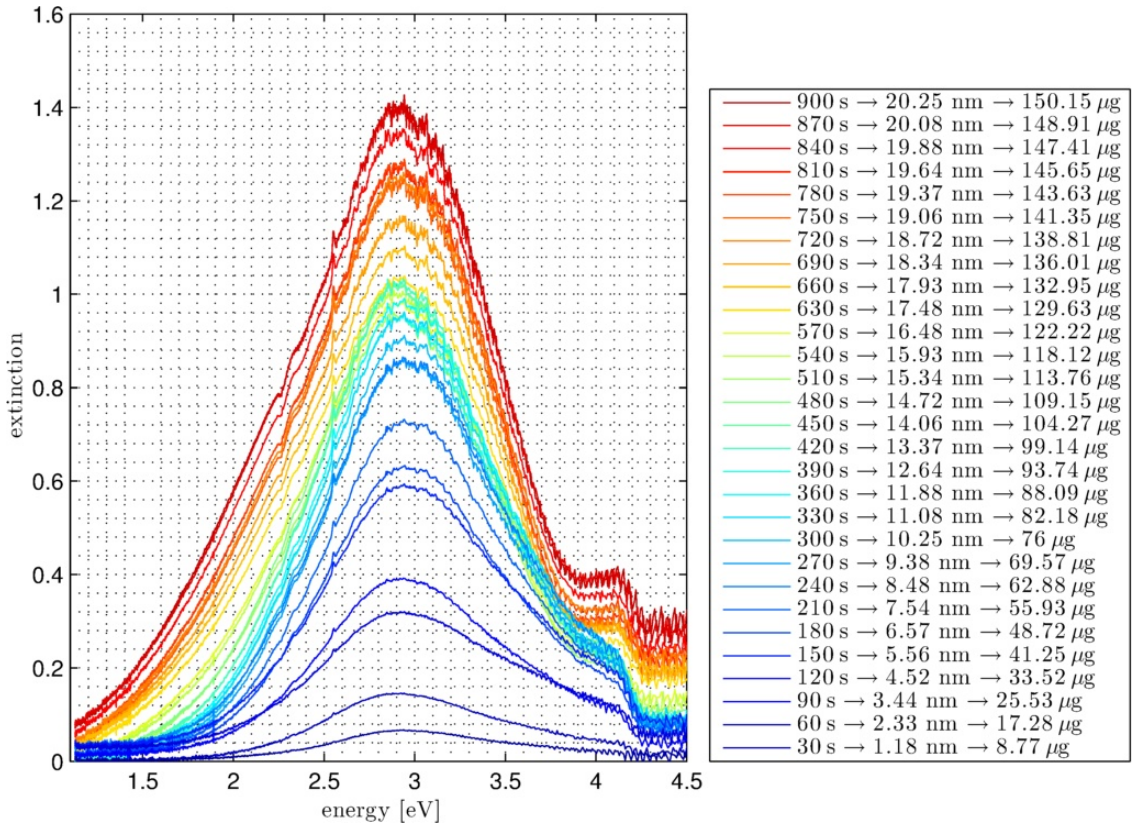

Figure 6.6: Measured cluster plasmon resonances of Ag clusters in BMIM PF_6.

In th extinction spectra, recorded at the beginning of the deposition, the extinction increases relatively fast due to the relative high cluster beam rate at the beginning of the experiment. After about 5 minutes the increase of the heights of the maximum extinction stopped and stayed quite stable up to about 10 minutes. Then the height and width increase with increasing deposition time. This is also illustrated in Figure 6.8. The corresponding deposition amounts are between about 76 µg and 126 µg. The amounts of deposited clusters is theoretically proportional to the area below the extinction spectrum. This dependency is plotted in Figure 6.9. However, the area below the spectra is not a (ideal) linear function of the approximated deposition amounts. This leads to the assumption that the cluster current rate did not decrease linearly or that a misalignment of the optics occurred during the cluster deposition (at about $t = 500\,\mathrm{s}$).

A similar behaviour can be observed at the FWHM of the spectra which are plotted in Figure 6.10. Up to about 5 minutes the FWHM increases with significant scatter. Up to a deposition time of about

8 minutes the FWHM of the spectra are relatively stable. Above this time, the FWHM of the spectra increase with time and with the estimated deposition amount.

While the energetic peak position of the extinction is approximately stable (Figure 6.7 dots in the right plot) it is observable that the flanks of the spectra shift to lower energies with increasing deposition time/amounts. This is shown in Figure 6.7 in the left plot by normalising the spectra to an integral of each spectrum between 1.2 eV-4.0 eV.

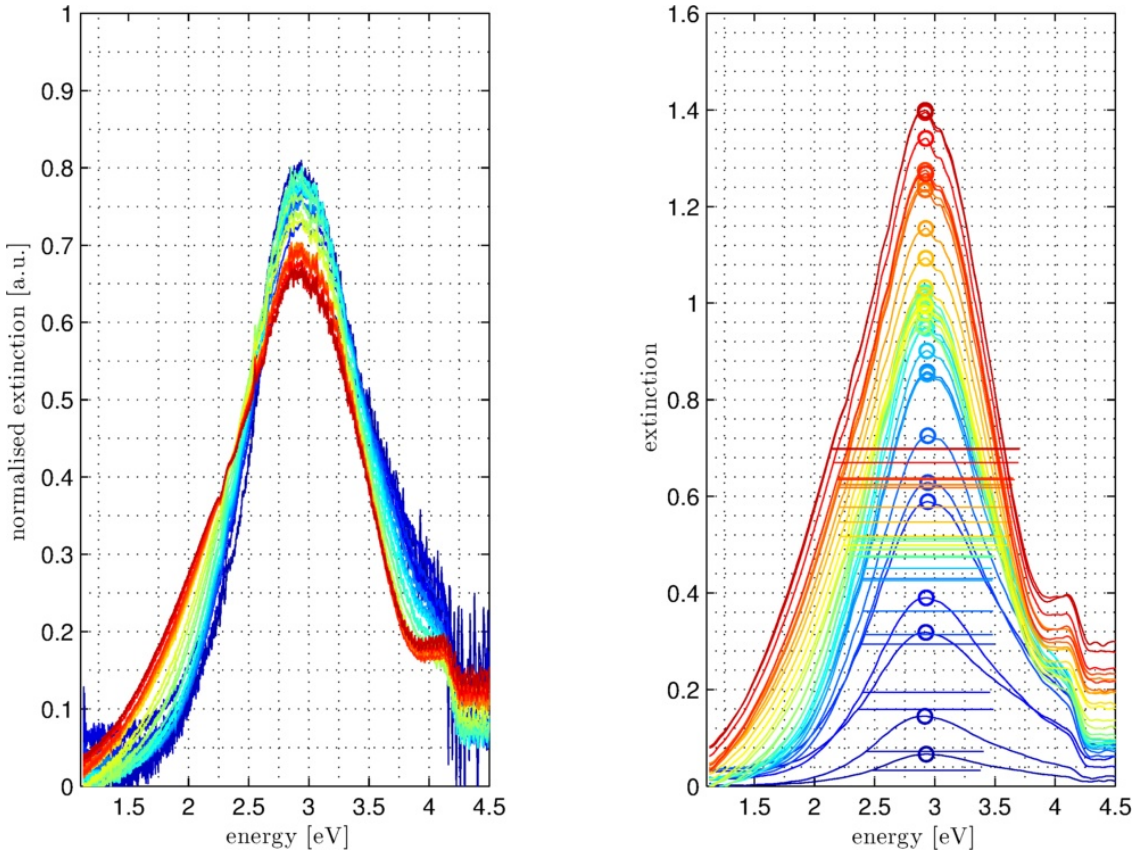

Figure 6.7: Measured cluster plasmon resonances of Ag clusters in BMIM PF_6, normalised to an integral between 4.0 eV-1.2 eV (left) and smoothed by a Gauss convolution with a FWHM maximum of 0.05 eV (right). The dots and the bars in the right plot mark the peaks and the FWHM of the extinction spectra. The colours and order correspond to the legend in Figure 6.6.

Summarising, the clusters seem to be mostly separated during the deposition. The peak position does not shift with increasing deposition amounts. This effect normally takes place when electromagnetic coupling starts. However, the increase of the FWHM and the flank shift for higher deposition amounts indicate a change of the structure of the clusters. This, in comparison with the observed aggregation process of clusters after deposition, indicates that first clusters begin to form chain like structures.

After the deposition also UV-Vis measurements were performed ex-situ using cuvettes and a cuvette holder. The resulting cluster plasmon extinctions are shown in Figure 6.11. The structure of the spectra is more complicated. The peak position is still at about the same energy ($\approx$ 2.9 eV) like during the deposition, also several days after the deposition. The overall extinction drops fast on time scales shortly after deposition and slowly on time scales of days after deposition. Below an energy of about 1.8 eV a second peak can be observed. This peak shifts with increasing time to lower energies and its relative height (height compared to the height of the main peak) increases with time.

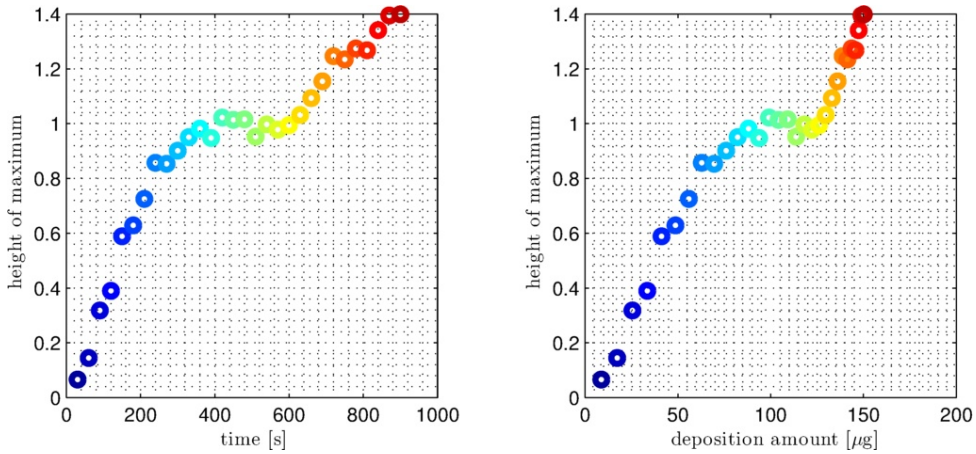

Figure 6.8: Maximum heights of the smoothed extinction spectra of Ag clusters in BMIM PF_6, plotted as function of deposition time (left) and estimated deposition amounts (right).

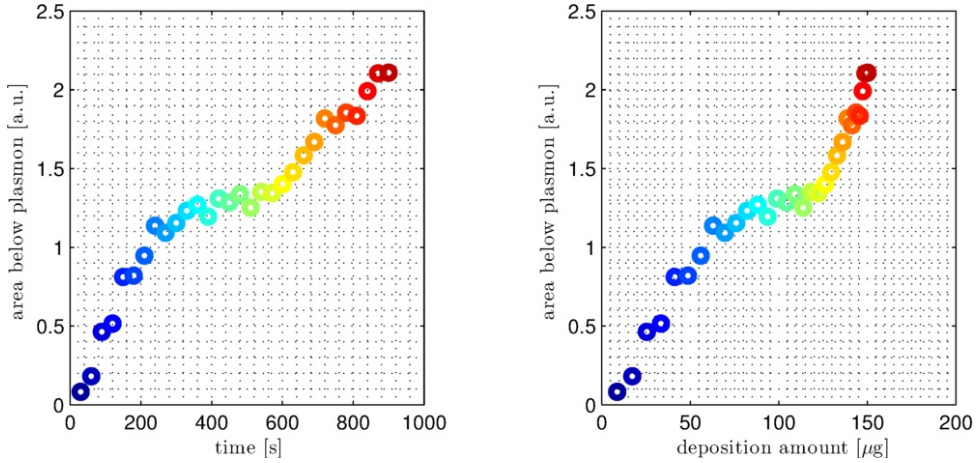

Figure 6.9: Areas below the curves of the extinction spectra (between 1.2 eV and 4.0 eV) of Ag clusters in BMIM PF_6, plotted as function of deposition time (left) and estimated deposition amounts (right).

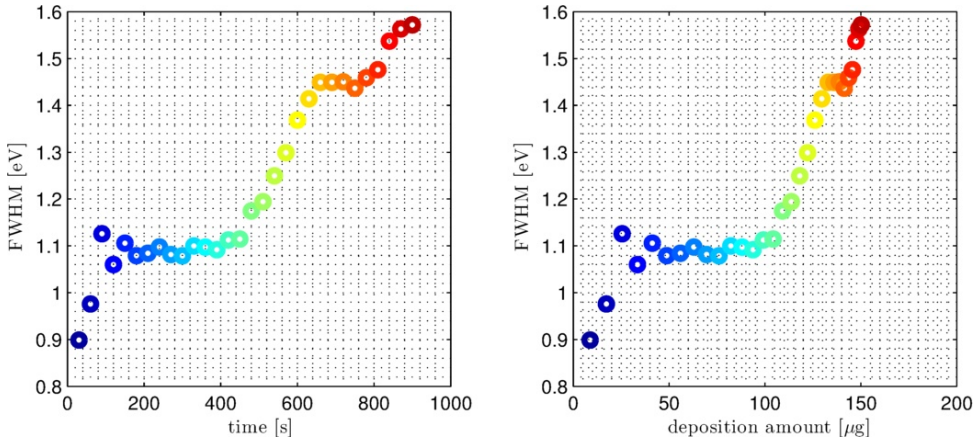

Figure 6.10: FWHM of the smoothed extinction spectra of Ag clusters in BMIM PF_6, plotted as function of deposition time (left) and estimated deposition amounts (right).

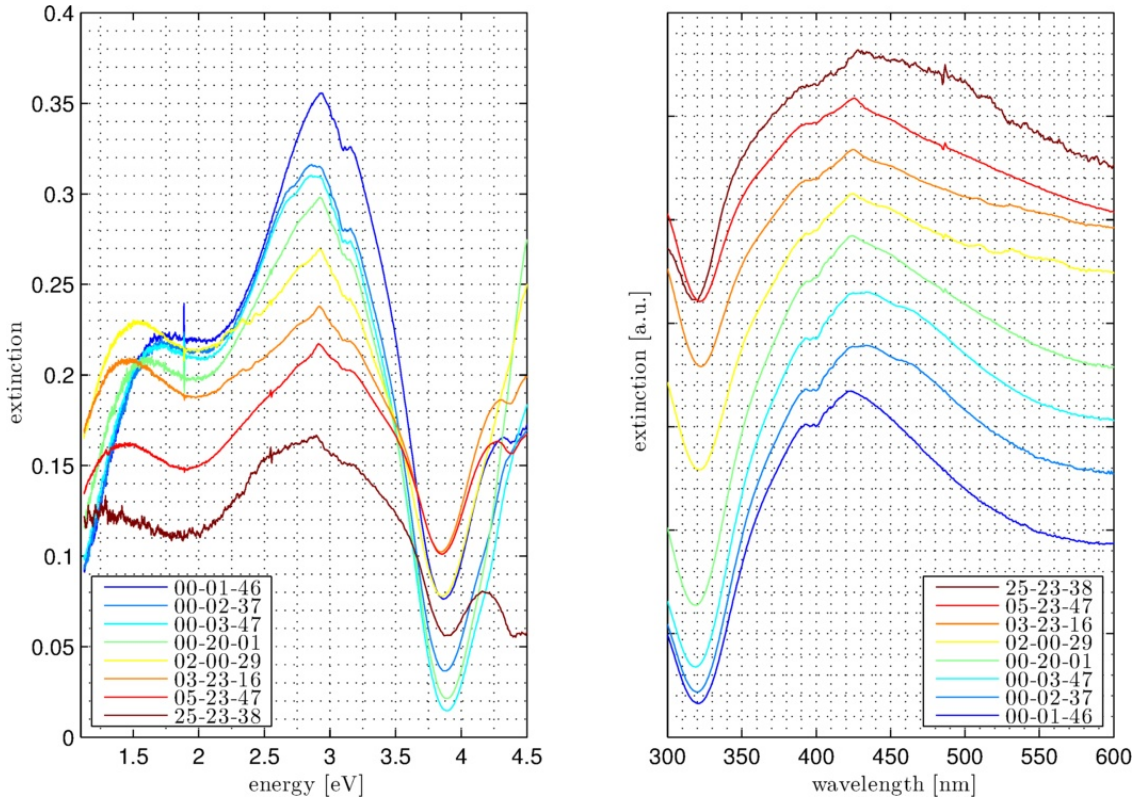

Figure 6.11: Left: Cluster plasmon resonance spectra of Ag clusters in BMIM PF_6 at different time steps after deposition, labelled by dd-hh-mm. Right: The same spectra as functions of wavelength, normalised to the area under each curve between 350 nm and 500 nm and plotted with an increasing offset.

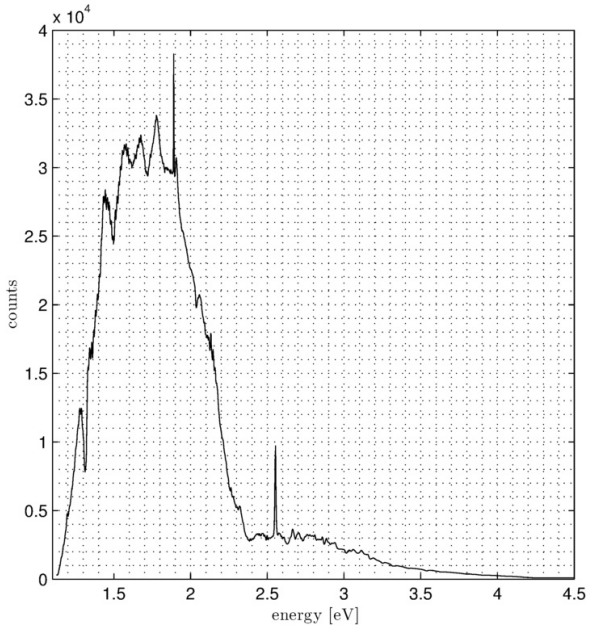

Figure 6.12: Spectrum of the raw counts of BMIM PF_6 in the mixer before deposition was started.

6.1.4 Influence of the purity of BMIM PF_6 on the Ag cluster plasmon shape

It was observed that the aggregation process of Ag clusters deposited into BMIM PF_6 was influenced by the kind of the purchased batch. In our first experiments (see section 6.1.2, BMIM PF_6 purchased from Carl Roth GmbH + Co. KG, batch nr. 20896717, with a purity $\geq$ 99, in the following called

RTIL 1) a strong cluster plasmon with small FWHM was observed still several hours after deposition. In later experiments (see section 6.1.3, BMIM PF_6 purchased from Carl Roth GmbH + Co. KG, batch nr. 323203553, with a purity ≥ 99, in the following called *RTIL 2*) the FWHM is already larger during the deposition. This is shown in Figure 6.13. The dashed lines represent cluster plasmons of

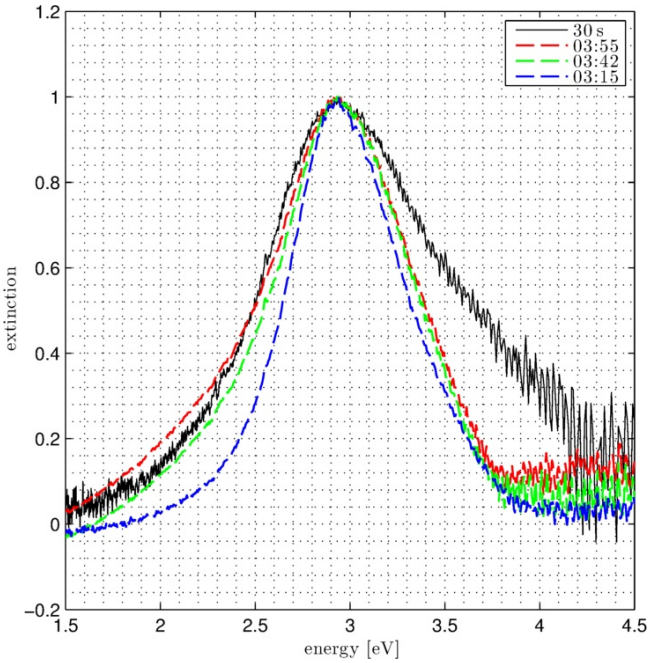

Figure 6.13: Ag cluster plasmon resonances of Ag clusters in RTILs (see text), normalised to 1. The black curve was recorded during the deposition (30 s after the deposition started) of clusters into *RTIL 2*. The dashed curves represent plasmon resonance measurements after the deposition (hh:mm) of clusters into *RTIL 1*.

Ag clusters in *RTIL 1* measured after deposition. The solid black line represents a cluster plasmon of Ag clusters in *RTIL 2* recorded during the deposition process (30 s after the deposition started). The heights of the plasmons were normalised to 1.

About 3 hours after deposition, the FWHM of the plasmon of the Ag clusters in *RTIL 1* is narrower than the FWHM of Ag clusters in *RTIL 2* recorded during deposition. The FWHM in *RTIL 1* for times earlier than 3 hours after deposition is expected to be even narrower. With increasing time the FWHM of the Ag clusters in *RTIL 1* increases which is explained by the ongoing aggregation process of the clusters. About 4 hours after deposition the FWHM in *RTIL 1* approaches that of the clusters measured during deposition in *RTIL 2*. If an aggregation process which starts on a time-scale of seconds in *RTIL 2* is excluded, the different FWHM of the Ag cluster plasmon in both RTILs may be explained by the chemical interface damping [Hövel et al., 1993] which is more intense for *RTIL 2* than for *RTIL 1*.

6.2 Influence of the addition of chemical agents to the Ag clusters in BMIM PF_6

The observed aggregation processes of the Ag clusters in BMIM PF_6 lead to various attempts to stabilise the clusters in the liquid. One was the addition of chemical agents to the RTIL-cluster-sample. It was shown by DASH and SCOTT that the presence of low levels of 1-methylimidazole can stabilise Au nanoparticles which were produced by synthesis in BMIM PF_6 [Dash and Scott, 2009]. This observation can be transferred to Ag nanoparticles due to their similar properties (for example their isoelectric structure) and the experiments of CARTER et al. who reported the adsorption of 1-methylimidazole on Ag surfaces [Carter et al., 1998]. The second stabilisation agent was dodecanethiol. Dodecanethiol was used to stabilise Ag nanoparticles in a synthetic production by digestive ripening [Smetana et al., 2005] and also to stabilise Au nanoparticles produced by sputtering Au atoms into BMIM PF_6 [Khatri et al., 2008][4]. The previous made observations on the strong sulphur-Ag-cluster-interaction lead to the assumption that a chain like hydrocarbon molecule with a sulphur head group exhibits excellent capping properties.

6.2.1 Addition of 1-methylimidazole and dodecanethiol after deposition

In a first experiment the interaction of Ag clusters in BMIM PF_6 with 1-methylimidazole and dodecanethiol was investigated using UV-Vis measurements. The BMIM PF_6 was purchased from Carl Roth GmbH + Co. KG, batch 323203553 with a purity $\geq 99\,\%$. The liquid was dried in a vacuum oven for about 3 hours at 100 °C. 22 ml were placed in the tub of the mixer over night. The deposition lasted for 4 minutes at a mean cluster current rate of about 0.09 nm/s. The deposited mass was 158.4 µg. After the deposition three samples were prepared: One original sample without the addition of any chemical agents. One sample (3 ml) was mixed with 4 µl dodecanethiol and another one (3 ml) with 6 µl 1-methylimidazole. To cause an interaction between the Ag clusters and the stabilisation agents the samples were shaken and put in an ultrasonic bath at room temperature for a few minutes.

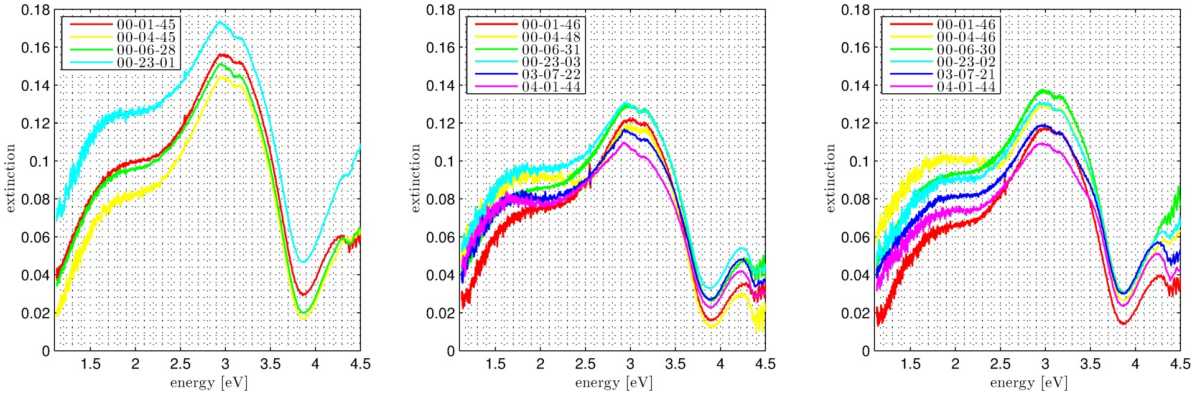

(a) original (b) 1-methylimidazole (c) dodecanethiol

Figure 6.14: UV-Vis spectra of Ag clusters deposited into BMIM PF_6 without and with low levels of different stabilisation agents. The spectra were recorded at different time steps after deposition, labelled by dd-hh-mm.

The results of this experiments are shown in Figure 6.14a for the original sample, in Figure 6.14b for the sample with 1-methylimidazole and in Figure 6.14c for the sample with dodecanethiol. The spectra exhibit the same kind of structure like observed in the experiments discussed above. The structures of the spectra do not differ from each other. The addition of the 1-methylimidazole or dodecanethiol did not cause any changes of the spectra and thus no stabilisation effects. This could

[4] Here BMIM PF_6 was replaced from the Au clusters by dodecanethiol.

be due the extremely low amounts of the chemicals which were added. It was also observed that the most aggregation processes, using this type of BMIM PF_6, took place on time scales below 1 h 45 min (Figure 6.11). Thus it seems to be promising to add the chemical agents to the BMIM PF_6 before starting the deposition. This was tried with dodecanethiol and is discussed in section 6.2.2.

6.2.2 Addition of dodecanethiol before deposition

In this experiment 50 µg dodecanethiol were added to 20 ml BMIM PF_6[5] and filled into the tub of the mixer and put over night into the evacuated experimental chamber. Pure BMIM PF_6 of the same kind was used as a reference sample. The deposition lasted 12 minutes at a mean deposition cluster current of about 0.11 nm/s. The deposited cluster mass was 603.3 µg.

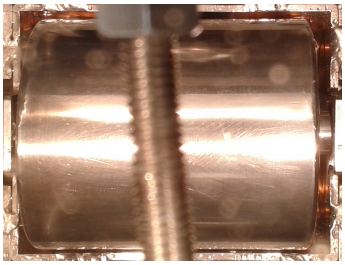

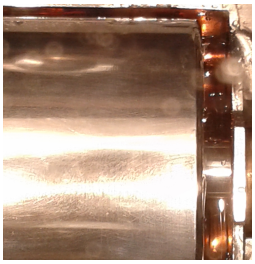

Figure 6.15: Pictures of the mixer during the deposition. The reddish colour of the RTIL with the deposited Ag clusters is clearly visible.

The colour of the liquid changed during deposition from yellowish to reddish. Also the formation of macroscopic black coloured aggregates could be observed. Pictures of the liquid during deposition are shown in Figure 6.15. The reddish colour is a remarkable observation because the typical colour of silver nanoparticles without dodecanethiol in BMIM PF_6 is yellow. The red colour indicates a shift of the cluster plasmon resonance to lower energies. For comparison, the red colour of gold nanoparticles in aqueous solutions can be assigned to a plasmon resonance energy of about 2.42 eV while the corresponding plasmon resonance energy of Ag nanoparticles is at about 3.10 eV [Quinten, 2010]. This shift could be explained by a chemical reaction between the sulphur head group of the dodecanethiol with the surface atoms of the Ag clusters.

After deposition the colour of the sample lost its intensity and differed no longer significantly from the colour of other samples prepared during previous performed experiments. Also a striking yellow colour was not observed. The ex-situ performed cluster extinction measurements are shown Figure 6.16. The peak of the cluster plasmon resonance spectra is between 2.8 eV and 2.9 eV and thus at about the same position like in the previous discussed experiments. The second peak at the low energetic flank is suppressed. However, the width of the plasmon is broader. These observations indicate that the clusters aggregated. It is possible that these aggregated Ag clusters also comprised sulphur atoms which would cause the broadening of the plasmon signal.

[5] purchased from Carl Roth GmbH + Co. KG, batch 323203553 with a purity $\geq 98\,\%$

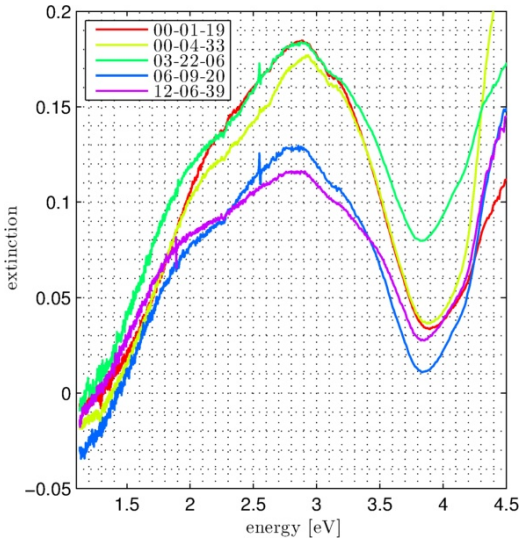

Figure 6.16: UV-Vis spectra of Ag clusters deposited into BMIM PF_6 with low levels of dodecanethiol, added before deposition started. The spectra were recorded at different time steps after deposition, labelled by dd-hh-mm.

6.3 Ag L_2 XANES spectroscopy on Ag clusters in BMIM PF_6

For the investigation of the electronic structure of Ag clusters in BMIM PF_6 also XANES experiments on the Ag L_2 absorption edge were performed at ID26 at the ESRF. The measurements were performed using a sample cell which can be cooled or heated to a fixed temperature between 0 °C and 100 °C.

Two samples were investigated. The first sample consisted of high amounts of clusters which aggregated to crystals with a bulk like structure. The second sample consisted of partly aggregated or agglomerated clusters with a lower amounts of deposited clusters.

6.3.1 Electronic structure of Ag crystals in BMIM PF_6, formed by aggregation of deposited clusters

To get first information about XANES experiments on Ag particles in RTILs, a sample with known electronic structure and an expected relatively strong fluorescence signal was investigated. The sample was produced as following: BMIM PF_6 was purchased from Carl Roth GmbH + Co. KG (batch nr. 20896717, with a purity $\geq 99\,\%$), degassed in a vacuum oven for about 3 hours at about 120 °C and ~ 27 ml stored in the tub of the mixer (section 3.2.4) for about two days under vacuum conditions. The deposition was performed by two steps. First about 1902 µg were deposited by a mean cluster rate of 0.285 nm/s during 15 minutes. In the second step about 1301 µg were deposited by a mean cluster rate of 0.195 nm/s during 15 minutes. Thus about 3.2 mg were deposited. The sample was stored over months under normal conditions. The deposited Ag clusters aggregated to bigger particles with approximately µm length scales. The results of the XANES measurements are shown in Figure 6.17.

A first measurement was performed at a pure sample without any additives (red curve). The second measurement was performed on a sample prepared by adding several volume percent of dodecanethiol. To give the dodecanethiol the possibility of interacting with the silver surface, this sample was shaken and ultrasonic bathed for several minutes before the measurement was started. The motivation was to get information about possible interactions between the silver crystals and the chemical environment and how it influences the XANES spectrum.

The recorded spectra (smoothed using a Gauss convolution with FWHM of 1 eV) look very similar to the reference spectrum of a silver bulk. Every feature observable in the reference spectrum is

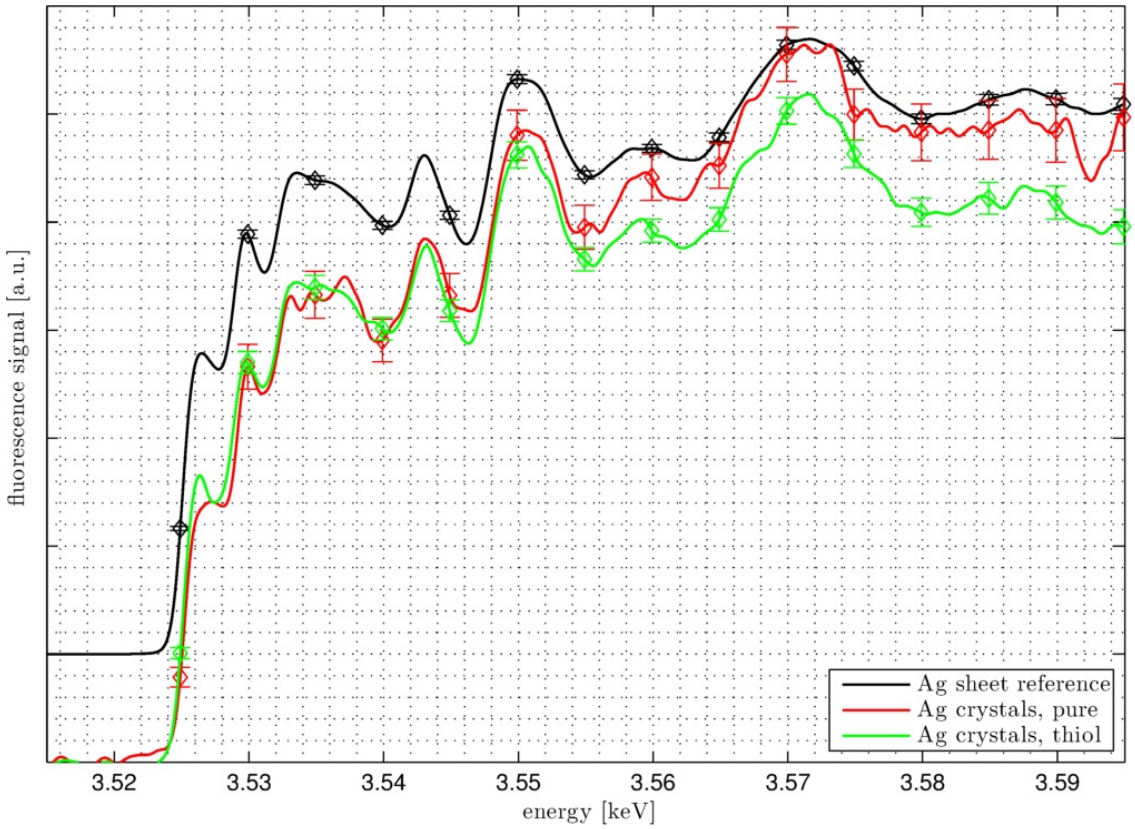

Figure 6.17: Ag L_2 XANES spectra of Ag micro crystals formed by aggregation of Ag clusters in BMIM PF_6 during and after deposition. The addition of dodecanethiol to the sample seems to have no influence to the chemical structure of the Ag clusters.

also present in the Ag crystal spectra. Modulations of the recorded spectra of the Ag crystal can be assigned to statistic effects and lie in the borders of the error bars. The very weak shift of the absorption edge cannot be assigned to a chemical effect. For the interaction of dodecanethiol with Ag, a charge transfer from Ag to the dodecanethiol is expected and thus a shift to higher binding energies. It is possible that effects like charge transfer cannot be detected due to the small surface to volume ratio of those crystals. It should be mentioned that no influence of the ionic liquid to the structure of the formed crystals could be observed by the XANES spectra.

6.3.2 Electronic structure of partly aggregated and agglomerated Ag clusters deposited into BMIM PF_6

The second sample which was produced for the beamtime consisted of partly agglomerated and aggregated Ag clusters deposited with a mean cluster current rate of about 0.077 nm/s for about 14 minutes into 20 ml BMIM PF_6 purchased from Carl Roth GmbH + Co. KG (batch nr. 323203553, with a purity $\geq 99\,\%$). The total deposited mass was 479.6 µg. During the deposition a filament was heated next to the mixer resulting in an electron current of 1 mA from filament to mixer. However, an effect on the stability of the cluster in the RTIL due to ionisation effects could not be observed. The sample was stored between 4 °C and 8 °C to diminish further aggregation processes.

Pre-investigation using UV-Vis

The sample was investigated during the beam time ex-situ at the beamline using the portable laboratory spectrometer described in section 3.3.1. Pure, untreated BMIM PF_6 was used for reference

measurements. The sample with the Ag clusters in BMIM PF_6 was measured twice before starting the XANES measurements and exposing the sample to the X-ray beam. The resulting spectra are shown in Figure 6.18. The shapes of the spectra are similar to the shapes of the spectra discussed above. The

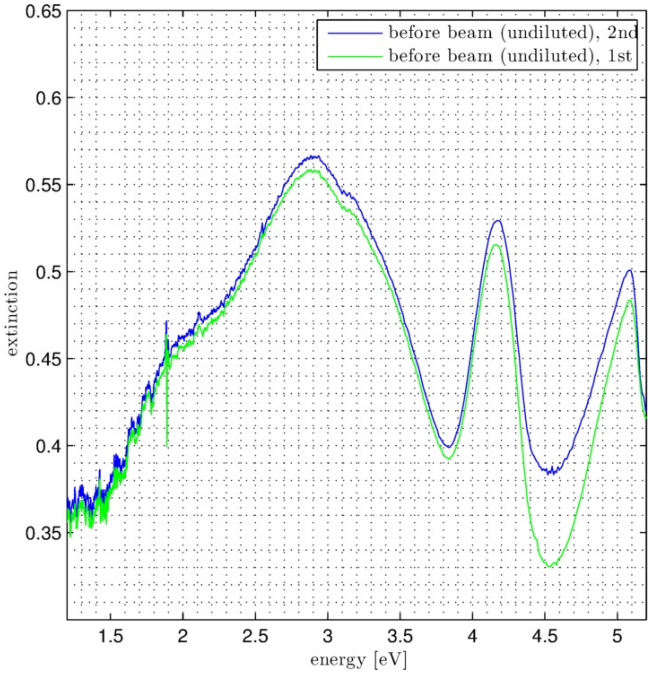

Figure 6.18: UV-Vis extinction spectra of partly aggregated and agglomerated Ag clusters in BMIM PF_6, measured ex-situ before exposing the sample to X-ray radiation. The sample was not diluted thus the overall extinction is relatively high.

peak of the extinction is at about 2.9 eV. The high overall extinction follows from diffuse scattering and absorption of polydisperse big particles in the sample, caused by partially aggregated clusters. This is especially indicated by the extinction of about 0.35 in the infrared range. The "peak" at about 5 eV is caused by a cut-off of the strongly increasing extinction. The peak and the dip between 4 eV and 4.5 eV is caused by differences between the RTIL of the sample and the reference (see Figure 6.1).

Ag L_2 XANES spectroscopy of partly aggregated and agglomerated Ag clusters deposited into BMIM PF_6

The samples cells with the Ag clusters in the RTIL were cooled down to about 4 °C during the measurements to minimize further aggregation processes. The fluorescence yield was very low during the measurements due to the small penetration depth of the X-rays into the RTIL.[6] Thus the scan range was narrowed to the pre-edge region to decrease the measurement time for a single spectrum. However, the measurement time was about 18 hours for the first measurement (red curve). For the second (green curve) and third (blue curve) measurement time was decreased to about 6 and 10 hours, respectively. The measurement of a single spectrum took 10 minutes. The recorded and added up spectra were smoothed by a Gauss convolution with a FWHM of 1 eV and normalised to the integral between 3.520 keV and 3.554 keV. The resulting spectra are shown in Figure 6.19.

The spectrum of the first measurement on the pure sample of Ag clusters in BMIM PF_6 without any additional agent differs clearly from the corresponding bulk reference spectrum. The structure of the spectrum is less pronounced than that of the bulk reference sample. A similar behaviour was also observed for separated clusters deposited into silica aerogel (section 5.2.2). Even though the clusters

[6] For an energy of 3.5 keV the transmission of the X-ray beam through 1 µm BMIM PF_6 is 97.5 %. With increasing depth the transmission decreases drastically: 10 µm → 77.6 %, 100 µm → 7.9 %, 1 mm → 0 %.

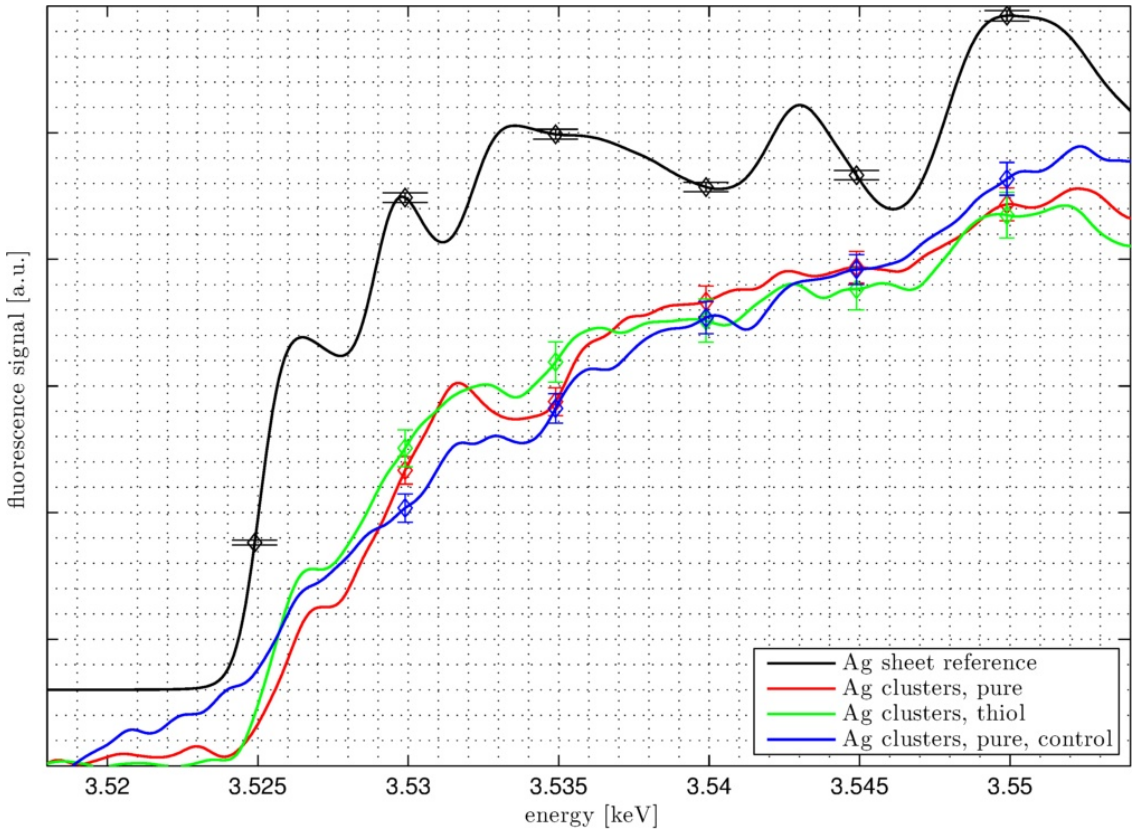

Figure 6.19: Ag L_2 XANES spectra of partly aggregated and agglomerated Ag clusters deposited into BMIM PF_6. After the first measurement (red curve), a few volume percent of dodecanethiol were added to the sample and measured again (green curve). A second measurement on a pure sample was started to check the observations (blue curve).

have the optical properties of aggregated or agglomerated clusters, the XANES spectra obviously indicate separated clusters. Remarkable is the dip at about 3.534 keV which was not observed in the spectra of Ag clusters in silica aerogel.

The spectrum of the same sample after the addition of dodecanethiol is shown by the green curve in Figure 6.19. This curve shows approximately the same characteristics like the spectrum of Ag clusters in pure ionic liquid. However, the relative height of the absorption edge at about 3.5265 keV is increased. PADMOS and ZHANG reported a slight increase of the Ag L_3 white line of dodecanethiol protected Ag clusters [Padmos and Zhang, 2012].[7] Also LÓPEZ-CARTES et al. reported a similar behaviour for the Au L_3 absorption edge of dodecanethiol stabilised Au clusters [López-Cartes et al., 2005]. While the increase of the absorption line in Figure 6.17 was in the borders of the statistical error, an influence of the additionally given dodecanethiol to the height of the absorption edge could now not be fully excluded. Nevertheless, one of the most striking characteristics, a shift of the absorption edge to higher binding energies (as discussed in section 5.2.4) in the case of a chemical reaction between the Ag clusters and sulphur atoms, could not be observed in the present spectrum.

Finally, the reiterated presence of the dip at about 3.534 keV confirms a modification of the electronic structure of the Ag clusters in BMIM PF_6 compared with those in silica aerogel. The control measurement on Ag clusters in pure BMIM PF_6 (blue curve) confirms the observations discussed above. The spectrum seems to contain a significant background signal and no additional information except the reproduction of the dip at about 3.534 keV.

[7] These clusters were produced synthetic, purified, solved into toluene and a drop of this solution was placed for XANES experiments onto an aluminium plate, allowed to dry.

Post-investigation of Ag clusters in BMIM PF_6 after X-ray exposition

After XANES measurements the samples switched their colour from grey to yellow (insets Figure 6.22a and Figure 6.22b). This leads to the question what happened with the samples during the X-ray exposition. Thus the samples were post-investigated by UV-Vis measurements. The results are shown in Figure 6.20a. The red curve is the spectrum of the sample directly after XANES measurements. The

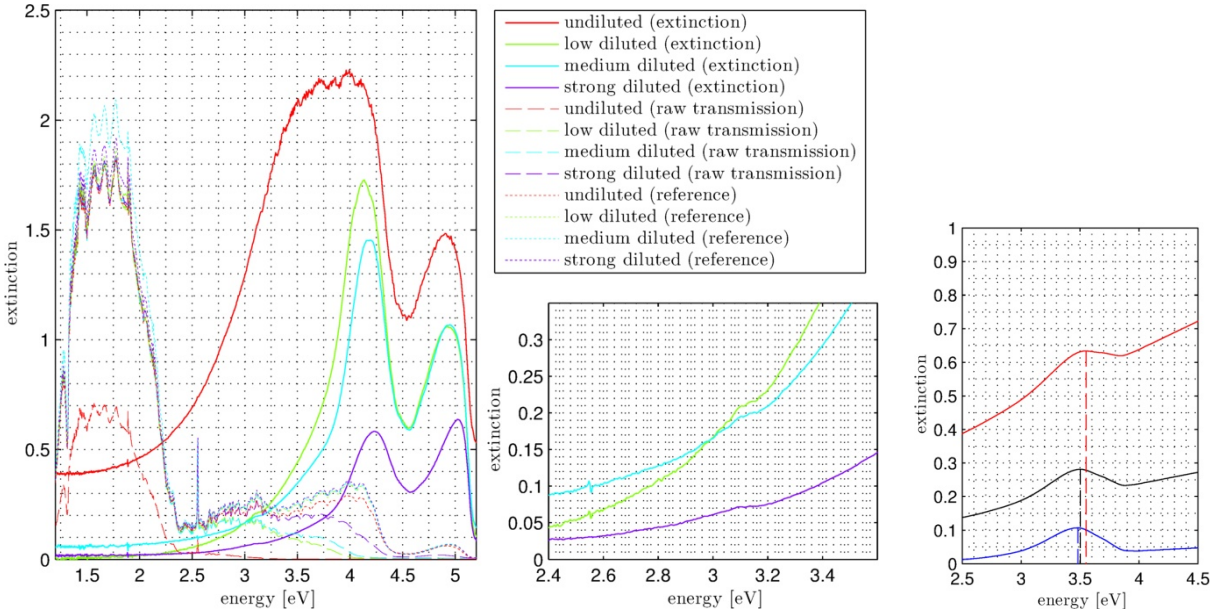

(a) The solid curves show the extinction spectra, the dashed lines the corresponding raw transmission spectra and the dotted lines the corresponding reference signal (both given by counts/$(3 \cdot 10^4)$). A peak is observable at about 3.1 eV (figure on the bottom right).

(b) Illustration of a peak shift (simulated cluster plasmon of an Ag cluster in vacuum) caused by a linear increasing background.

Figure 6.20: UV-Vis spectra of the investigated sample after XANES measurements. The peak at about 3.1 eV could be explained by a shift of the peak in Figure 6.18 caused by the superimposition with an increasing background, shown in (b).

background extinction in the range below 1.5 eV is of the same magnitude as observed before exposing the sample to the X-ray beam. But the extinction increased drastically up to a not detectable limit (extinction > 2), thus the samples had to be diluted with pure BMIM PF_6.

After the dilution a strong peak is observable between 4.0 eV and 4.2 eV. This is at about the same position where a peak also was observed before X-ray exposition. This peak was suggested to be a consequence of different purities of the sample with the Ag clusters and a pure BMIM PF_6 sample used for reference spectrum. However, the high intensity of this peak speaks against the assumption that this extinction could be caused by impurities. This is confirmed by having a look at the raw spectra in Figure 6.20a. The raw intensity (counts) of the undiluted sample decreases to zero above an energy of about 3.25 eV. This cannot be explained by typical impurities of the sample. With increasing dilution this cut-off shifts to higher energies. For a strong dilution this cut-off shifts above an energy of 5 eV. Above this energy the technically possible detection limit is reached and the extinction increases before it falls down to zero.

There is also a small peak at about 3.1 eV. This peak is similar to those peaks observed in the experiments discussed above. The shift from about 2.9 eV to 3.1 eV could be a consequence of the superimposition of the corresponding cluster extinction spectrum with an increasing background. Such a shift is illustrated in Figure 6.20b on the example of an Ag cluster plasmon resonance (Ag cluster

with a diameter of 2 nm in vacuum), superimposed by a linear increasing function. With increasing slope also the maximum position of the peak shifts to higher energies. However the extremely small FWHM of the peak superimposed on the background at 3.1 eV in Figure 6.18 does not fit to a cluster plasmon.

The high extinction and the yellow colour of the sample could be explained by three hypotheses: 1) Changes of the structure of BMIM PF_6 due to X-ray beam exposition. 2) Fragmentation of the Ag clusters or the cluster aggregates/agglomerates in the sample due to X-ray beam exposition. 3) A combination of both. Point 1) and 2) are discussed in following.

1) During the control measurement (blue curve in Figure 6.19) the colour of the sample was checked a couple of times. After about 7 hours of illumination the sample occurred yellowish (Figure 6.21). Such an effect could not be observed at the sample with Ag crystals in BMIM PF_6 after the same illumination time under the same conditions. This leads to the assumption that the changes of the colour and the strong extinction are not caused directly by X-ray beam damages to the RTIL.

Figure 6.21

The decomposition of BMIM PF_6 molecules by photo electrons out of the M, N or O shells of cluster atoms can also be excluded because these effect would also take place in the Ag crystal sample.

In contrast, the decomposition of BMIM PF_6 molecules due to heat which is produced by X-ray cluster heating can not be excluded completely. Here a higher temperature is expected for the clusters than for the crystals because of the lower degrees of freedom in clusters than in crystals. At high temperatures the structure of the RTIL is able to change.

2) Separated, aggregated and agglomerated clusters might be fragmented into smaller nano clusters. This would explain why the recorded XANES spectra look similar to those of separated clusters with deviations to the electronic bulk structure. Corresponding to these observations the intense extinction peak can be explained by the plasmon resonances of Ag clusters consisting out of less than 10 atoms [Harbich et al., 1992, Tiggesbäumker et al., 1993, Liebsch, 1993].

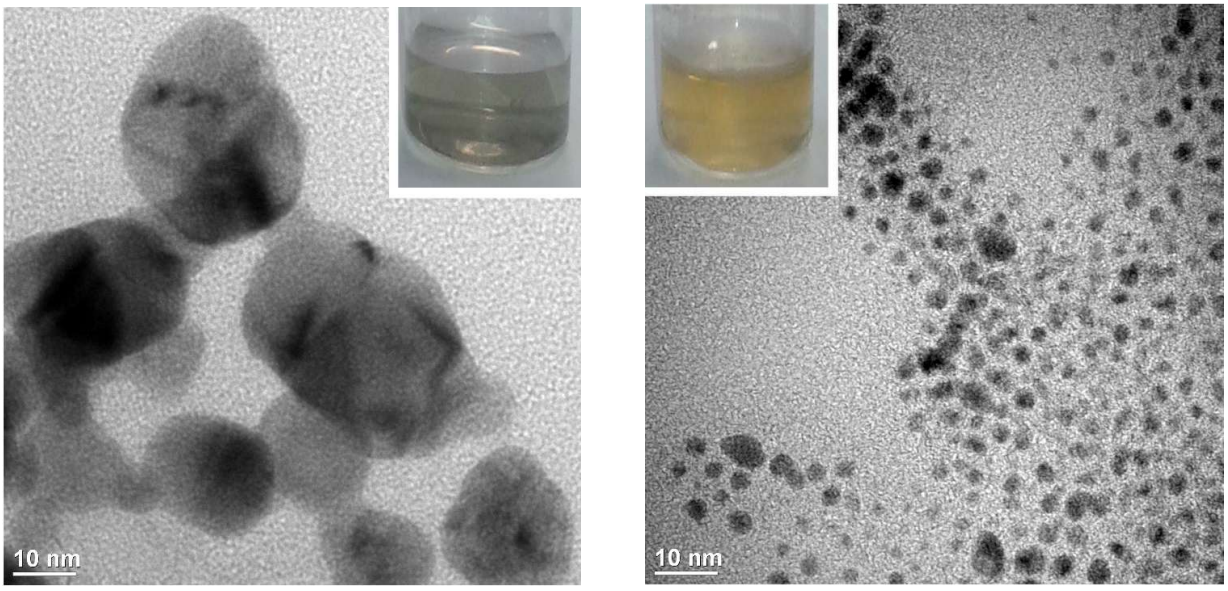

(a) before exposition to X-ray beam

(b) after exposition to X-ray beam

Figure 6.22: TEM images of Ag clusters in BMIM PF_6. Photos of the samples, before and after exposing to X-ray radiation, are shown by the inlets.

To get more information on the processes which could have taken place during the X-ray exposition

also transmission electron microscopy (TEM) images were recorded by M. MEURIS[8]. Two generic TEM images are shown in Figure 6.22. More TEM pictures are shown in the appendix 8.5.

The TEM image of the sample before the exposition to X-ray radiation is shown in Figure 6.22a and after the exposition to X-ray radiation is shown in Figure 6.22b. It should be noticed that the TEM samples were produced by solving the RTIL with the clusters in 2-propanol before placing them on a TEM grid. Thus aggregations, caused by this process, cannot be excluded. The clusters in Figure 6.22a have a typical diameter of several 10 nm. The colour of this sample is shown in the picture of the inlet in Figure 6.22a. In contrast the typical diameters of the clusters in the TEM picture after exposing the sample to the X-ray beam (Figure 6.22b) are below 5 nm. The fragmenting impact of the X-ray beam to the clusters in BMIM PF_6 is therefore clearly revealed.

In an additional experiment the influence of the temperature to colour changing effect was investigated. For that the sample was measured three times for always 1 hour at 24 °C, 40 °C and 60 °C and UV-Vis measured after each XANES sequence. After the total 3 hours of illumination the sample changed its colour into yellow. The spectra of the UV-Vis measurements are shown in Figure 6.23. It

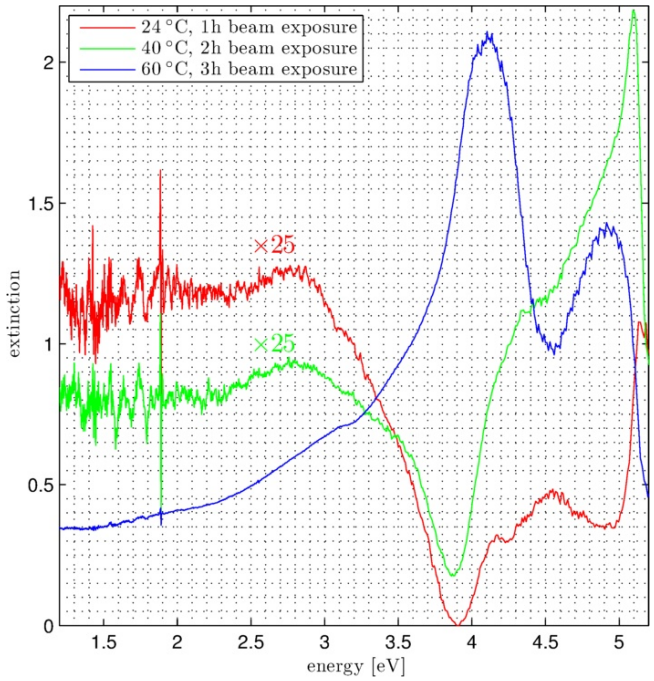

Figure 6.23: UV-Vis extinction spectra of Ag clusters in BMIM PF_6, recorded during XANES measurements (ex-situ). The green (after 1 hour at 24 °C) and the red curve (after an additional hour at 40 °C) were multiplied, for a better comparability with the blue curve (after increasing the temperature to 60 °C for another hour), by a factor of 25.

is observable that the spectra recorded after the first hour at 24 °C differs from those recorded before starting XANES measurements (Figure 6.18). After the second hour at 40 °C the spectrum changed again. However, after an additional hour at 60 °C the spectrum is similar to those recorded after several hours X-ray beam exposition at 4 °C. Thus the effect is accelerated at higher temperatures. This insight supports both thesis:
1) In the case of clusters induced temperature enhancement, which causes structural changes of the RTIL, the lower temperature of 4 °C counteracts the heating of the clusters environment.
2) In the case of cluster fragmentation the higher temperature of the RTIL lowers its surface tension and viscosity. Thus the cluster fragments can diffuse faster in the RTIL and more aggregated/agglomerated clusters can be illuminated by the X-ray beam.

[8] Fakultät Bio– und Chemieingenieurwesen, TU Dortmund. The microscope had a resolution of 0.2 nm.

Finally, to check the influences of the X-ray beam and the sample temperature to the RTIL, a cell was filled with pure BMIM PF_6 and exposed for about 70 minutes to the X-ray beam at 60 °C. Here no changes of the colour of the RTIL could be observed.

6.4 Summary and discussion of Ag clusters deposited into BMIM PF_6

The experiments showed that it is possible to deposit clusters into RTILs. This is of fundamental interest because most experiments in this field of research deal with using RTILs for the production of clusters [Kuwabata et al., 2010, Dupont and Scholten, 2010]. This opens the field to deposit pre-functionalized clusters like mass selected clusters without the use of any additional chemicals.

The stability of Ag clusters deposited into BMIM PF_6 is still a problem. The most promising approach is to use ionic liquids with definite purity. Within the first experiments performed during this work, the clusters started aggregation after several hours (Figure 6.5), in the following experiments aggregation was observed already during the deposition process (Figure 6.7) or shortly ($\sim 1\,\mathrm{h}$) after the deposition stopped (Figure 6.11). Parameters like degassing time, cluster deposition rate and mixer speed did not influence the process noticeably. The batch of the RTIL which was purchased at the first experiments could not be purchased again. This seems to be the most striking difference. Here it should be noticed that the RTILs store water (Figure 6.2) from the environment which may have dramatic effects on the stability of metal clusters in the RTIL.

However, the UV-Vis measurements lead to the assumption that the clusters do not only aggregate. It seems to be more probably that the clusters form agglomerates in the shape of short chains with angles between the clusters. The XANES measurements on those samples confirm this assumption because no bulk structure could be observed (Figure 6.17). Only after the deposition of very high amounts ($\sim 10^2\,\mu\mathrm{g}$) the clusters aggregated to crystals with bulk like electronic structures (Figure 6.17).

It was observed that low temperatures of the RTIL decelerate the aggregation process, probably due to the higher viscosity [Jacquemin et al., 2006] of the RTIL and thus lower mobility of the clusters.

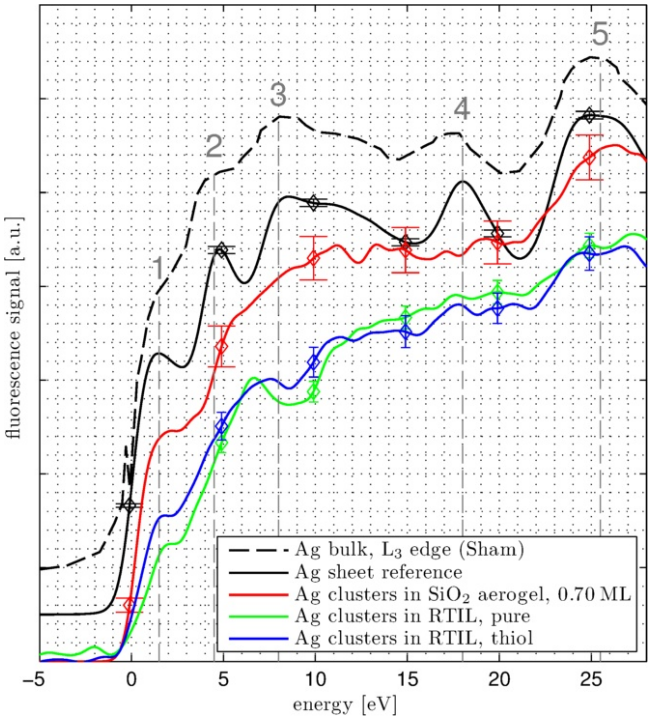

Figure 6.24: Comparison of the Ag L_2 XANES spectra of Ag clusters in BMIM PF_6 and aerogel to the Ag L_2 and L_3 XANES spectra of an Ag bulk references. The spectra were shifted to the absorption edge position of the Ag bulk. The Ag L_3 XANES spectrum was extracted from [Sham, 1985].

The XANES spectra of the Ag clusters in BMIM PF_6 look very similar to those of separated Ag clusters in silica aerogel. Thus it is clear that the measured spectra indicate the uDOS of single

clusters with diameter of about 2 nm or smaller. The absence of the typical bulk structures 2, 3 and 4 (transitions of the photoelectron into pd hybrid orbital) indicate a deviating electronic structure to Ag crystals. Further, there is an additional dip about 9 eV behind the absorption edge (Figure 6.24, blue and green curves). This structure is not present in the spectrum of separated Ag clusters in silica aerogel (Figure 6.24, red curve).

The addition of dodecanethiol does not seem to have a significant influence to the spectra. An expected shift of the absorption edge could not be observed. A small increase of the height of the absorption edge could be observed for Ag crystals and Ag clusters in BMIM PF_6 after adding dodecanethiol.

Finally the fragmentation of the agglomerates or aggregates by X-ray irradiation could be observed. As explained above, the XANES spectra can be assigned to those of separated Ag clusters. The TEM pictures show big structures for the sample which was not exposed to X-ray radiation and small clusters for the sample which was exposed to X-ray radiation. A beam damage on the BMIM PF_6 cannot be excluded. TSUDA et at. reported a process of cluster production where $NaAuCl_4$ was solved in RTILs with different cations and a bis(trifluoromethanesulfonyl)amide (Tf_2N) anion, and then irradiated by an electron beam or γ-rays. It was observed that especially BMIM cations are radiochemically unstable and release radicals relatively easy [Tsuda et al., 2009]. Au nanoparticles produced this way were stable over more than three months. This is in analogy to our observations where the samples kept their yellow coloured appearance over several months, too.

7 Summary and outlook

In the present thesis the chemical, structural, optical and electronic properties of Ag clusters with a mean diameter of about 2 nm were investigated. The cluster were therefore deposited into three different embedding media. The embedding media were 30 µm thick polydimethylsiloxane PDMS (polymer), silica aerogel (highly porous solid) and 1-butyl-3-methylimidazolium hexafluorophosphate BMIM PF_6 (room temperature ionic liquid). The investigations were performed using UV-Vis spectroscopy, XANES spectroscopy and TEM.

7.1 Ag clusters in PDMS

UV-Vis of the plasmon resonances of Ag clusters deposited into PDMS showed that for deposition amounts up to about 1 ML the Ag clusters stayed separated. UV-Vis measurements using polarised light showed that the clusters were weakly distorted after deposition. The axis ratio was about $u = 0.90$. This suggests, that the clusters are relatively soft landed into the PDMS. For deposition amounts of about > 1.5 ML coalescence was observed. The resulting cluster plasmons exhibited a double peak structure. It is possible to explain this by 3D arrangements, produced with the varying penetration depths of the clusters into the PDMS. The spectra could be simulated qualitatively with the model of spheroidal clusters.

In experiments, where the cluster/PDMS sample was exposed to H_2S, it was observed that the clusters reacted with the sulphur. The resulting cluster plasmon resonance spectra could be simulated by a core-shell model with Ag core and Ag_2S shell. It was observed that the reaction is a surface sensitive effect and is weaker for coalesced clusters with lower surface to volume ratios. After a first initial fast reaction of the clusters, a decrease of the reaction speed was observed.

7.2 Ag clusters in SiO_2 aerogel

Using SiO_2 aerogel as embedding material enabled the deposition of high amounts of cluster material before risking coalescence. For deposition amounts of about 1 ML, the clusters were assumed as separated. With increasing deposition amounts up to about 3 ML, weak changes in the Ag L_2 XANES spectra could be observed. With increasing deposition amount the spectra were more similar to an Ag bulk reference. For deposition amounts of about 10 ML the spectrum is similar to that of an Ag bulk.

Comparing the Ag L_2 XANES spectrum of the coalesced clusters (10 ML) with those of the separated clusters, peaks at about 2.527 keV, 2.530 keV and 2.543 keV (2 eV, 5 eV and 18 eV behind the absorption edge, respectively) are absent. These peaks assigned to transitions into the pd-hybrid band. Corresponding Ag L_1 XANES spectra (final state p orbital) exhibited the same structure as an Ag bulk reference. Thus it is assumed that the uDOS of d orbitals in single Ag clusters (2 nm diameter) is changed as compared to bulk material. Experiments on oxidised Ag clusters could be used to confirm these observations. A pronounced dip at about 3.528 keV in the spectra of oxidised Ag clusters provides the hypothesis that the valence bands have a weaker overlap in this energy region, resulting in a weaker DOS and uDOS.

The Ag clusters oxidised within a few minutes at air under X-ray exposition. Comparing the Ag L_2 XANES spectra of oxidised (30 minutes at air during X-ray exposition) coalesced clusters with that of an Ag_2O reference sample, differences between the spectra can be observed, while the spectra before

starting oxidation were similar to a bulk silver reference. This leads to the conclusion that passivation effects takes place on silver, so no complete reaction to Ag_2O takes place. The oxidised states could be destroyed by X-ray exposition under vacuum conditions. The resulting spectrum is similar to the spectrum before oxidation, thus the process is reversible.

A similar behaviour was observed for the sulfidation of Ag clusters. The Ag_2S XANES signal disappeared when measuring the samples in vacuum with X-rays. However, this may be used to design devices which can convert $H_2S + 2Ag \rightarrow Ag_2S + H_2$ by exposing Ag clusters to H_2S and reactivate them by exposing them to X-ray radiation in vacuum.

7.3 Ag clusters in BMIM PF_6

The experiments on Ag clusters in BMIM PF_6 in the present thesis are one of the first experiments where completely formed clusters were deposited into a room temperature ionic liquid. It was shown that it is possible to deposit Ag clusters into BMIM PF_6 and investigate them during and after deposition.

In the performed experiments agglomeration and aggregation of Ag clusters in the RTILs was observed, with a significant variation for different individual batches of RTIL from different manufactures. During the experiments big aggregates precipitated and were not investigated. UV-Vis spectroscopy lead to the assumption that the clusters agglomerated. Ag L_2 XANES spectroscopy on these samples showed that the clusters exhibited an electronic structure similar to those of separated clusters. The XANES spectra are probably also influenced by a fragmentation of the clusters. The fragmentation of the agglomerated clusters was confirmed by TEM measurements. Ag L_2 XANES measurements on big aggregated crystal-like Ag clusters exhibited a bulk-like signal. Fragmentation processes could not be observed at these samples. The fragmentation of the Ag clusters in BMIM PF_6 was accompanied with a change of the sample colour from grey to yellow. UV-Vis spectroscopy showed a strong extinction at about 4.1 eV. The process of the changing colour could be accelerated by increasing the temperature of the sample during X-ray exposition. The yellow colour of the samples exposed to X-ray radiation was stable over months.

Since RTIL itself seems to be stable during X-ray exposition, it would be interesting to produce extremely small Ag clusters by this kind of radiolysis. Ag clusters can be deposited into various species of RTILs using THECLA and illuminated at beamline BL1 of DELTA. The size of the clusters could be tuned by the intensity of the X-ray beam and the illumination time. XANES experiments at those samples would yield further information of the size depending electronic structure of Ag clusters.

Performing in-situ UV-Vis experiments during cluster deposition into various species of RTILs can yield information on the chemical interface damping and also the aggregation/agglomeration processes. Especially for RTILs with large anions a weaker anion-cation interaction and thus a stronger cation-metal-cluster interaction is expected. Those experiments can be extended by the addition of various chemicals which are used as stabilisation agents. Also the influence of water impurities and the viscosity of the RTIL to the deposition process is of interest. This can be checked by heating the mixer before and during the deposition process.

7.4 Free-beam experiments

Currently also free-beam experiments with synchrotron radiation are proposed. THECLA is would be connected to a beamline at PETRA III (DESY in Hamburg) and X-ray experiments performed at free clusters. By comparing those experiments with the experiments presented in this thesis, information on the influence of the embedding medium to the electronic structure of the clusters should be available.

8 Appendix

8.1 Height of a cluster monolayer

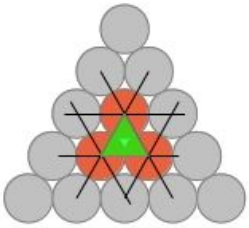

Figure 8.1: Cluster in hexagon dense package.

A cluster monolayer in a hexagon dense package can be derived by the volume of the layer $V = A \cdot h = n \cdot V_c$. This is the volume of n clusters with the cluster volume V_c. The effective layer thickness h is then given by

$$h = \frac{n \cdot V_c}{A} \ .$$

Corresponding to the green triangle in Figure 8.1 the mean surface of $n = 3$ clusters with radii R is given by

$$A = \sqrt{3} \cdot R^2 \ .$$

At last it has to be considered that every of the three atom take only part to the whole volume with a sixth of its own volume. From this it follows:

$$h = \frac{3 \cdot \frac{1}{6}\frac{4}{3}\pi R^3}{\sqrt{3}R^2} \approx 1.21\, R \ .$$

8.2 Construction sketches of the mixers

B-B (1 : 1)

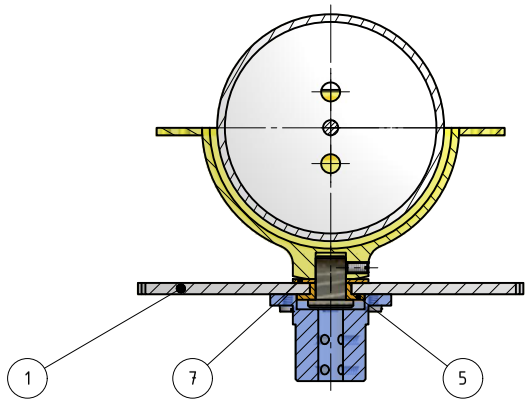

Stirnrad m=1
d0=Ø100
z=100

A-A (1 : 1)

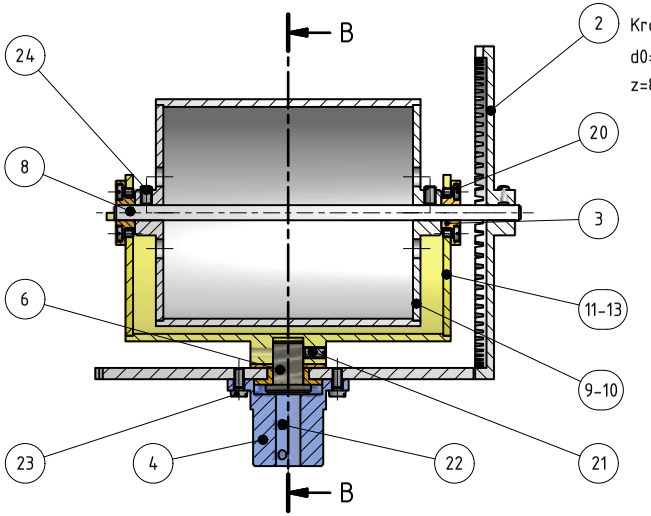

Kronenrad m=1
d0=Ø85
z=85

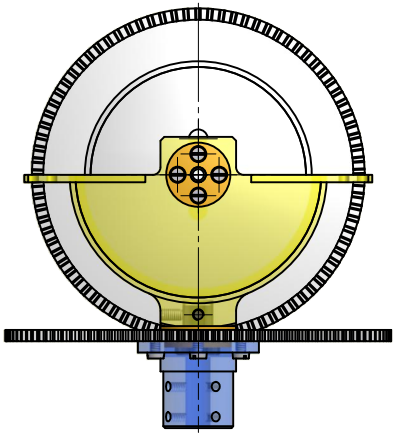

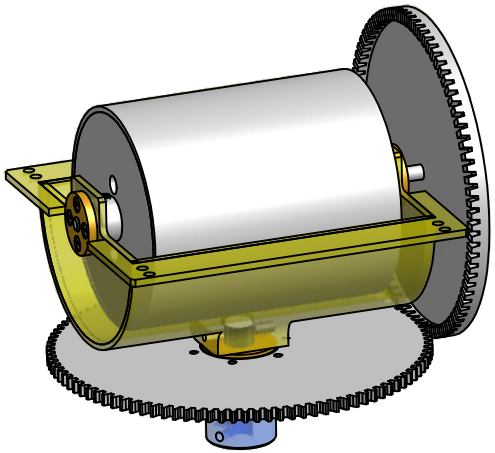

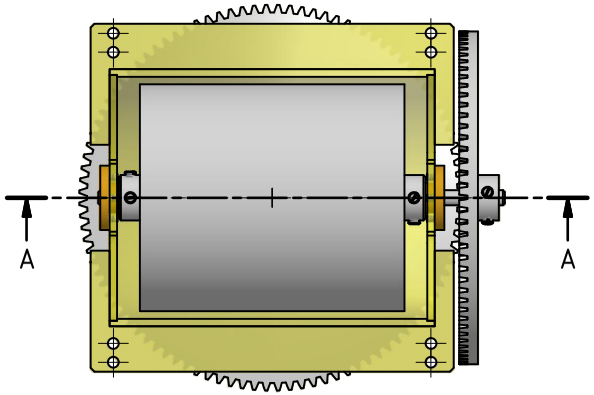

		Werkst./Stoff-Nr.:				Oberflächenschutz:								
		Kanten gebrochen/entgratet				Freimaßtoleranzen: ISO 2768 - m								
		Ra(µm)		0,05	0,1	0,2	0,4	0,8	1,6	3,2	6,3	12,5		
		Rauheitsgrad		N2	N3	N4	N5	N6	N7	N8	N9	N10		
			Datum	Name		technische universität dortmund							fakultät physik	
		Gezeichnet	29.03.12	Beyer										
		Geprüft												
		Maßstab	Benennung									Zchng.-Nr.		
		1:1	Probenpreparations-Cluster									e1.1318.03.12		
Passmaß	Abmaß in µm													

D–D

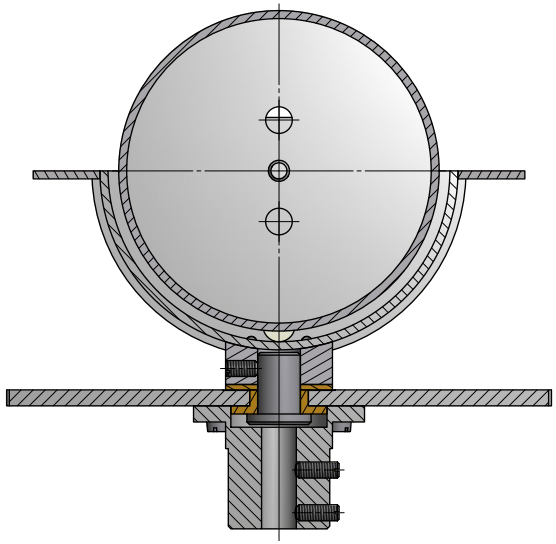

A–A

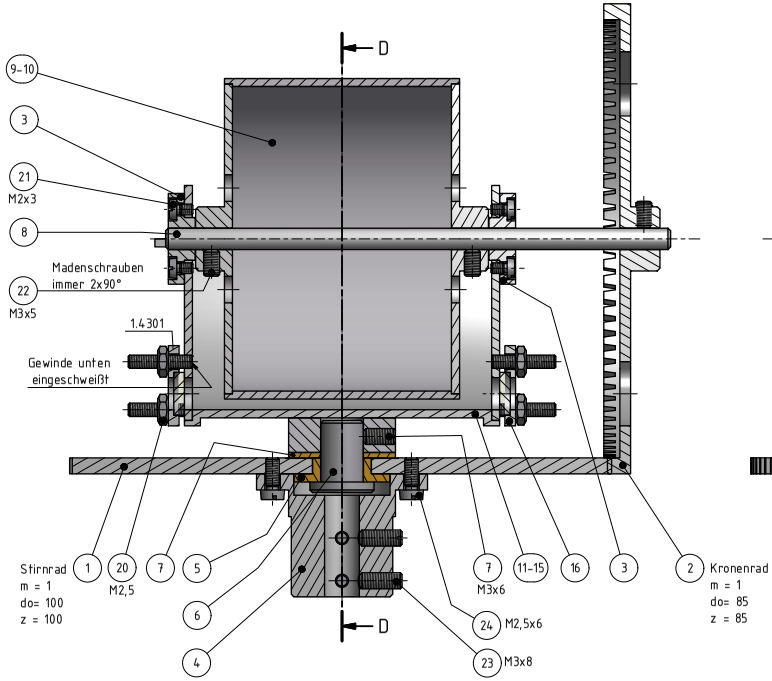

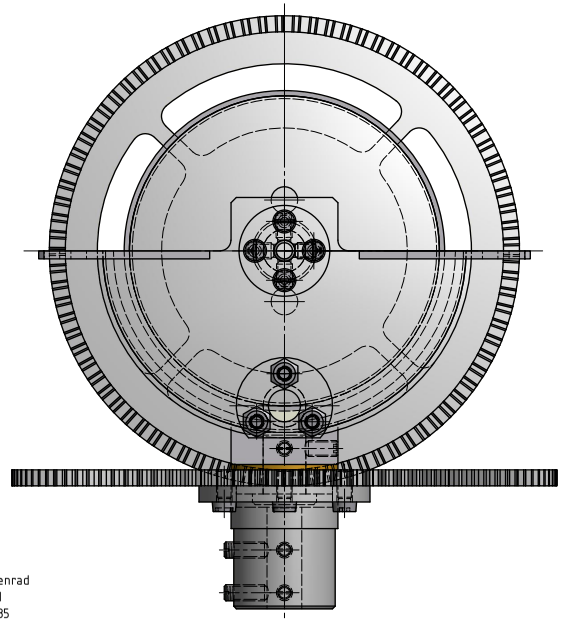

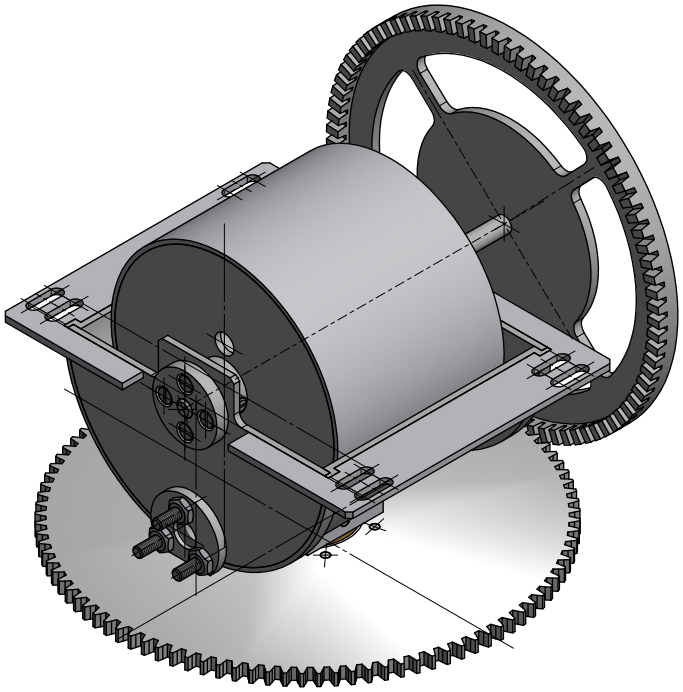

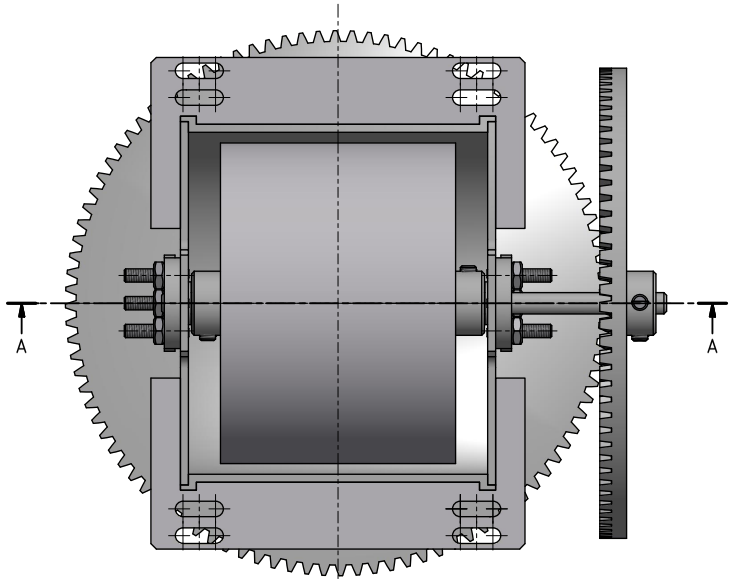

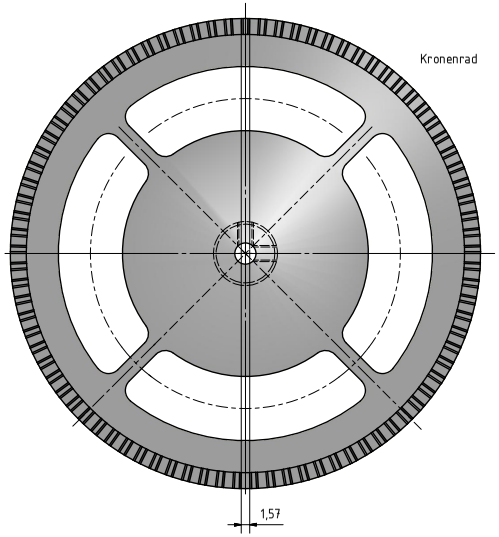

Hohltrommel u. Halbschale Werkst. 1.4301,
alle übrigen wie bei Auftrag: e1.1318.03.12

Verbindungsstellen wasserdicht geschweißt

		Werkst./Stoff-Nr.:			Oberflächenschutz:									
		Kanten gebrochen/entgratet			Freimaßtoleranzen: ISO 2768 – m									
		Rajum		0,05	0,1	0,2	0,4	0,8	1,6	3,2	6,3	12,5		
		Rauheitsgrad		N2	N3	N4	N5	N6	N7	N8	N9	N10		
			Datum	Name	technische universität dortmund								fakultät physik	
		Gezeichnet	25.02.14	Lange										
		Geprüft												
		Maßstab	Benennung		Zchng.-Nr.									
Passmaß	Abmaß in µm	2:1	Probenpräparations-Cluster (schmale Ausführung)		e1.1383.02.14									

8.3 Background effects for clusters in PDMS

Before the experiment started, optical reference measurements on the empty PDMS substrate were performed. These measurements can be used to subtract the background signal from the extinctions of the clusters in PDMS. The technical problem is that between the reference measurements and the cluster extinction measurements the sample has to be moved out of the optical focus. The restoring of the previous alignment is only possible up to a limited accuracy. Thus it can happen that after subtracting the reference signal at position z from the extinction signal at position z, the integrated extinction is mainly influenced by background signals (Figure 4.2). So, also integrated extinctions < 0 can be produced, especially when the extinction of the clusters is of the same magnitude like the extinction and refraction effects of the PDMS. These spectra have to be excluded manually from further analyses. The deposition amounts then are calculated by the maximum of the deposition profile (Figure 4.2) which corresponds to the double mean deposition amount of each deposition spot measured with the crystal oscillator.

The spectra, which were not excluded, are shown in Figure 8.2. In the left haft of the Figure the spectra are presented which follow by the classical method of background subtraction. This means that an extinction spectrum at position z is subtracted by a reference spectrum at position z. Nevertheless there is still a background signal in the spectra especially in the energetic region below the plasmon resonances. To solve this problem a new approach for background subtraction is tested here: The reference measurements are used as a pool of possible background spectra for each cluster extinction measurement. The requirements are, that after subtracting a reference curve from a cluster extinction curve, the signal in the range from 1.2 eV to 1.7 eV should be as small as possible. In this region the transparency of PDMS is very high and not energy depending. Further the deposited Ag clusters have no extinction in this region. The theoretically expected signal in this region is almost zero. Thus from each extinction spectrum every reference spectrum is subtracted. The resulting spectra, for which the requirements above are fulfilled best, is then chosen for further analysis.

The benefit of this method is that it is also practicable in the case, that there are only limited information about the positions and alignments of the measurements. The results are presented in Figure 8.2 b) and d).

To check the efficiency of this method also the background subtraction by using fits of several degrees were performed: It was tried to fit the background signal in an energetic range of about $1.2\,\mathrm{eV} - 1.7\,\mathrm{eV}$. By performing a fit of the order zero (mean value), one (linear fit), two (quadratic) or three (cubic) and subtracting the resulting extrapolated curves should cause a vanishing background. This is done for clusters in PDMS still in vacuum and after air exposure in Figure 8.3. As a result the fits of first, second and third order cause deformations of the spectra. Only the subtraction of a constant value seems to preserve the physical information of the spectra. However the background is reduced less efficient than with the selection of the reference spectra described above.

These considerations yield information about an appropriate background subtraction method and also about the sample system itself. The mentioned double peak structure appears in nearly all spectra independent of the background subtraction method. Thus this is no artefact of an inadequate background subtraction. For the further discussion, the spectra with background subtracted by the above represented method using a pool of reference spectra will be used. It should be noticed that in former experiments, like in the thesis of HOFFMANN, this remnant-background-effect was negligible due to the less thick and the more homogeneous surface of the PDMS samples produced by spin casting. This effect can be assigned to refraction of the impinging light and thus increases with thickness and rawness of the (surface of the) sample.

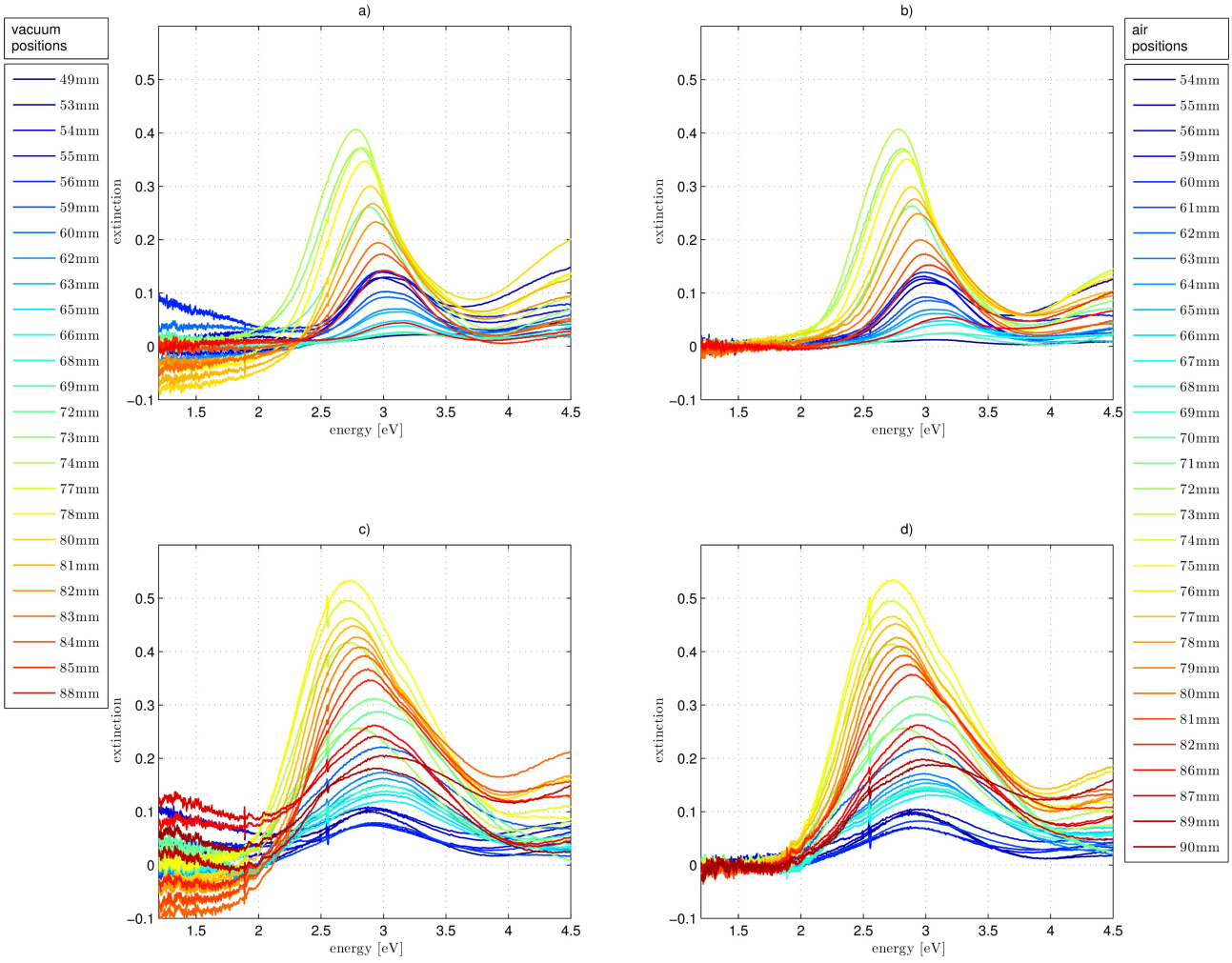

Figure 8.2: The cluster plasmon extinctions of Ag clusters in PDMS in vacuum are shown in the subfigures a) and b) and after exposure to air in the subfigures c) and d). The spectra of the left side were calculated with the classical background subtraction method: extinction spectrum at position z subtracted by the reference spectrum at position z. The spectra at the right side were calculated by using a pool of possible reference spectra for each extinction spectrum.

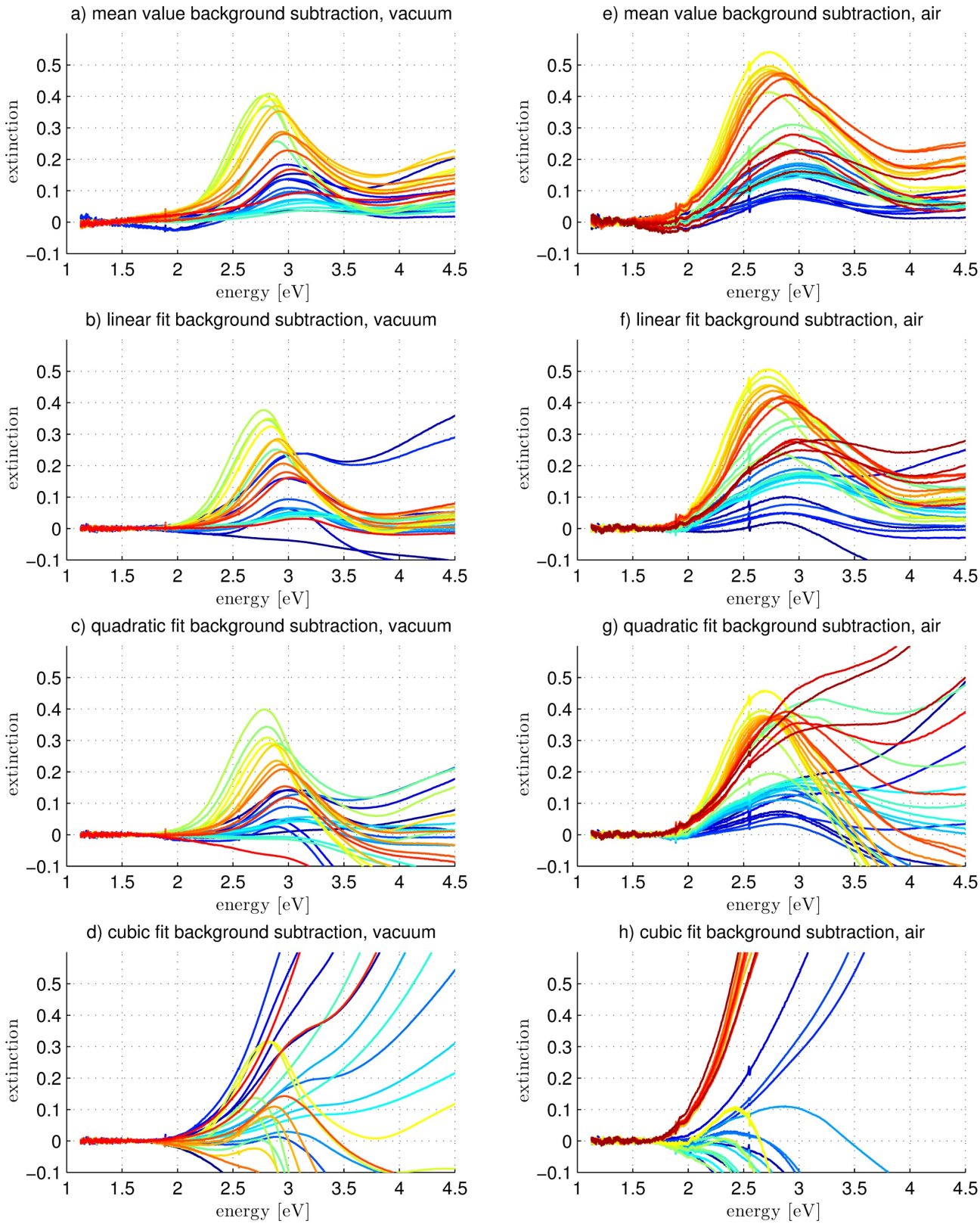

Figure 8.3: Plasmon resonances of Ag clusters in PDMS in vacuum and after air exposure calculated by background subtraction using a fit up to the fourth order.

8.4 Single Ag L_2 XANES spectra of partly oxidised Ag clusters in silica aerogel

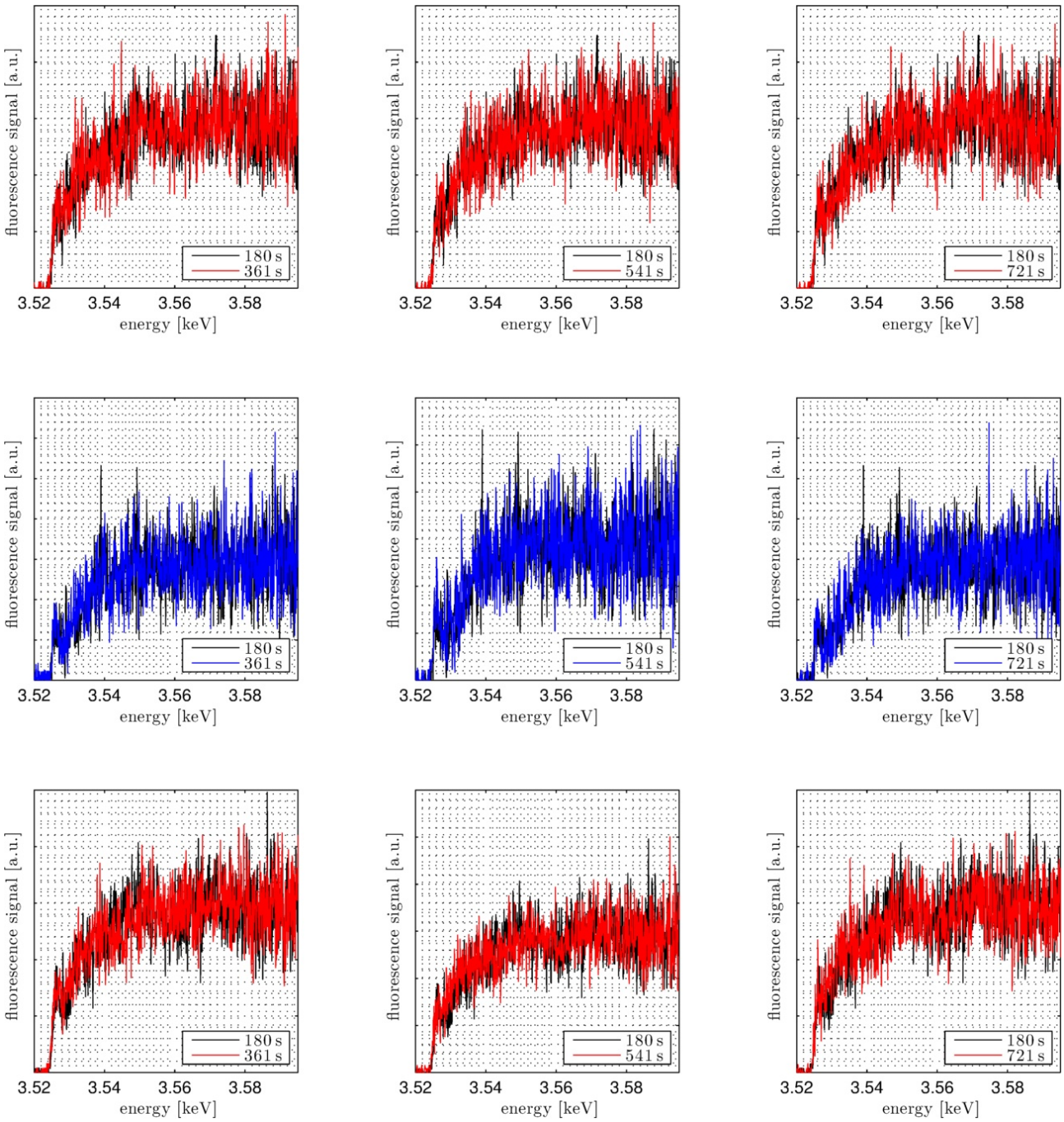

Figure 8.4: Single spectra of oxidation experiments on Ag clusters in a silica aerogel sample with a mean deposition amount of about 1.01 ML. First row → $p = 2$ mbar, second row → $p = 1$ bar, third row → $p = 2$ mbar.

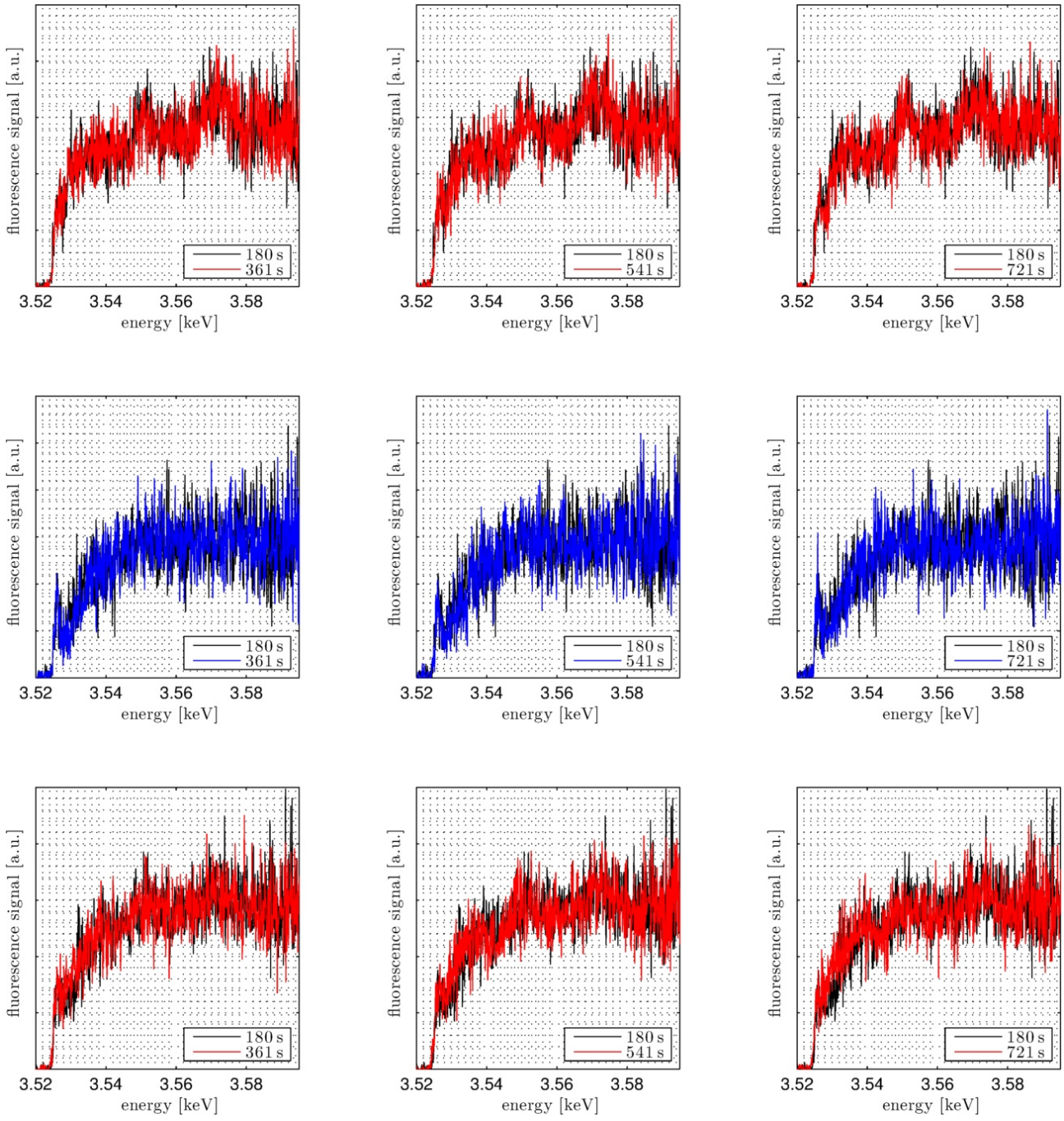

Figure 8.5: Single spectra of oxidation experiments on Ag clusters in a silica aerogel sample with a mean deposition amount of about 1.53 ML. First row → $p = 2$ mbar, second row → $p = 1$ bar, third row → $p = 2$ mbar.

8.5 TEM pictures

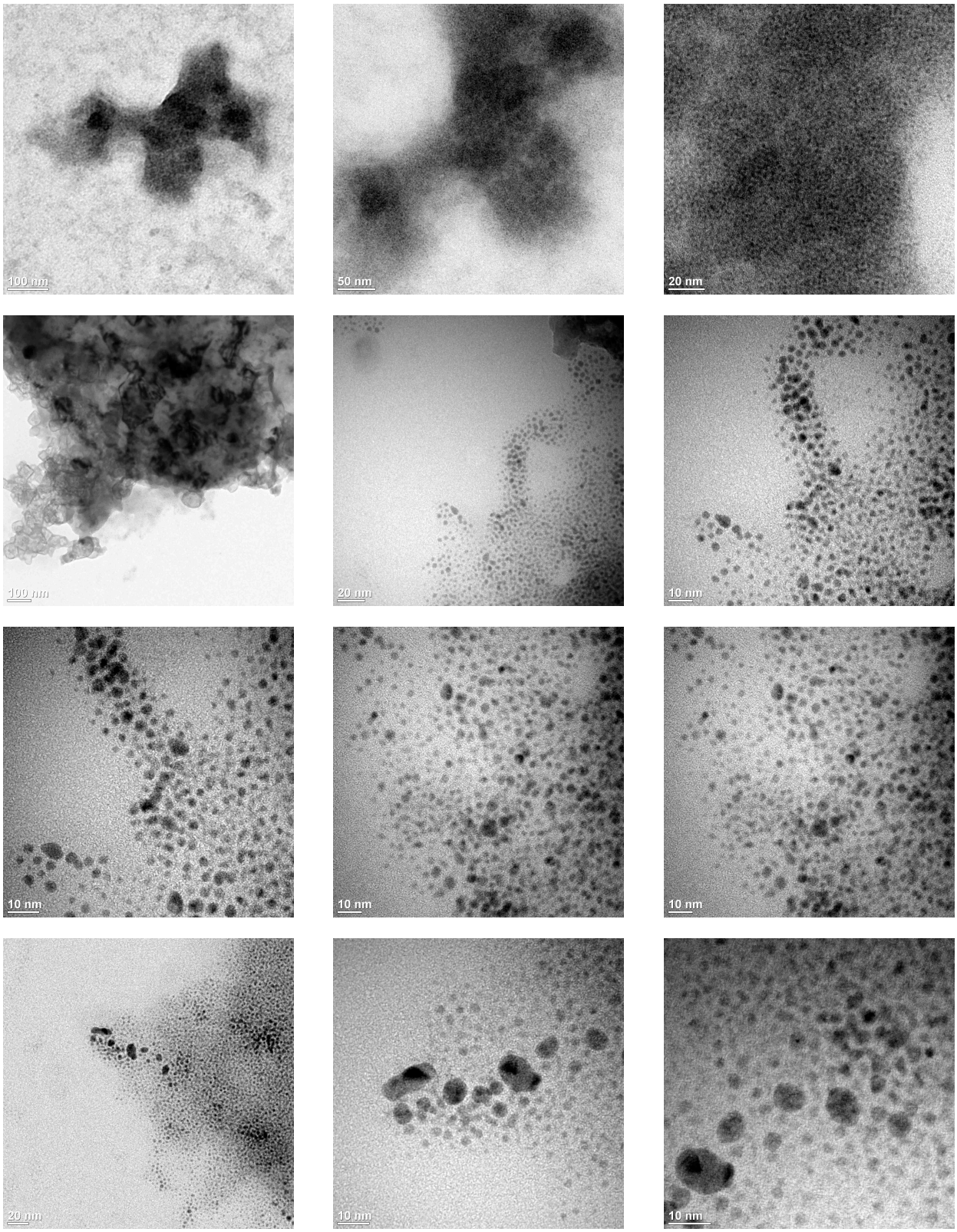

Figure 8.6: TEM pictures of Ag clusters deposited into BMIM PF_6 after X-ray exposition.

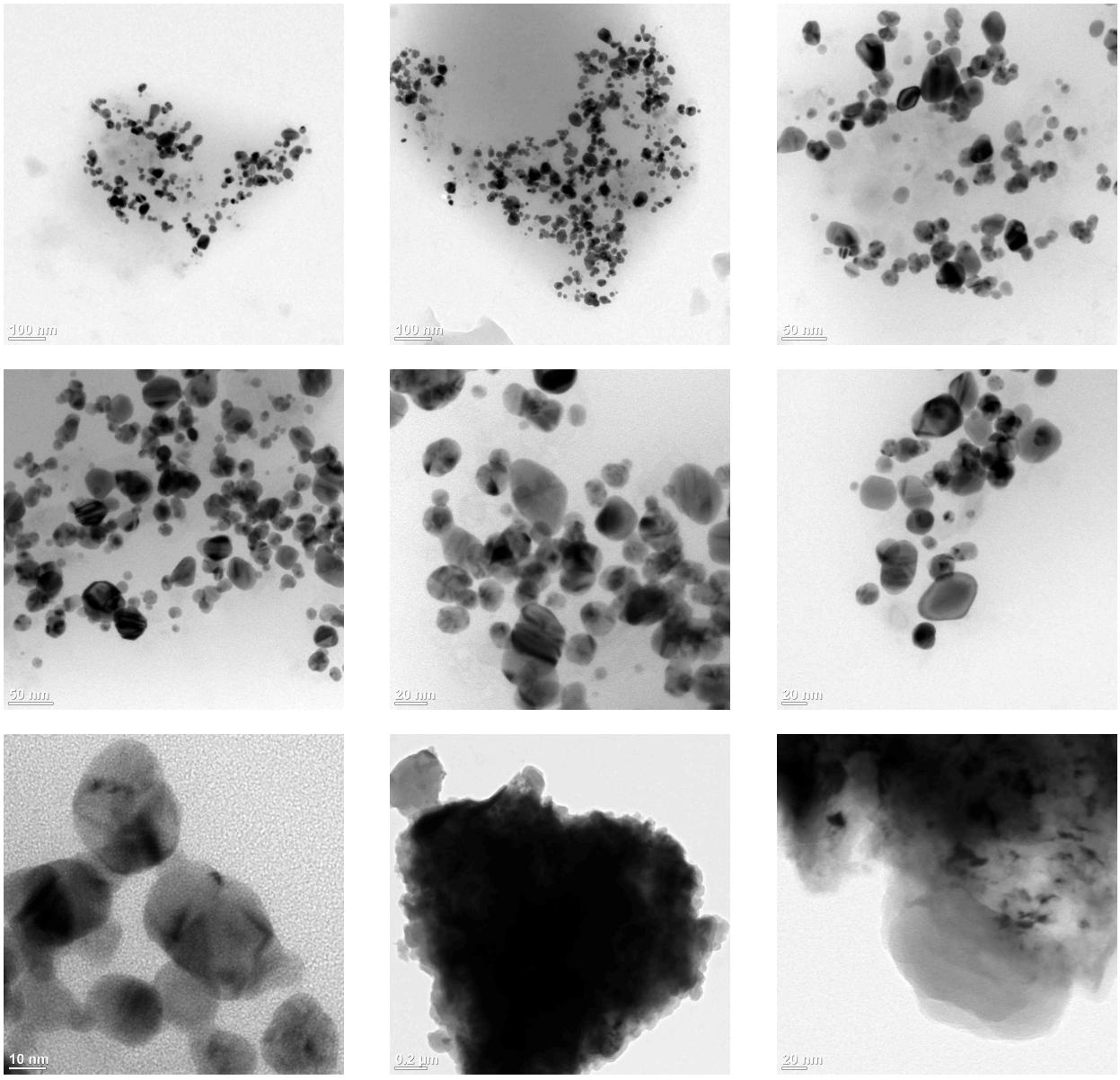

Figure 8.7: TEM pictures of Ag clusters deposited into BMIM PF_6 before X-ray exposition.

Bibliography

[Attwood, 2007] Attwood, D. (2007). *Soft X Rays And Extreme Ultraviolet Radiation*. Cambridge University Press.

[Barke and Hövel, 2003] Barke, I. and Hövel, H. (2003). Confined Shockley Surface States on the (111) Facets of Gold Clusters. *Physical Review Letters*, 90(16):166801.

[Behrens, 1992] Behrens, P. (1992). Bonding in silver-oxygen compounds from Ag L_3 XANES spectroscopy. *Solid State Communications*, 81(3):235–239.

[Behrens et al., 1999] Behrens, P., Assmann, S., Bilow, U., Linke, C., and Jansen, M. (1999). Electronic Structure of Silver Oxides Investigated by Ag L XANES Spectroscopy. *Zeitschrift für anorganische und allgemeine Chemie*, 625(1):111–116.

[Bohren and Huffman, 2004] Bohren, C. F. and Huffman, D. R. (2004). *Absorption and Scattering of Light by Small Particles*. Wiley-VCH Verlag GmbH.

[Bunker, 2010] Bunker, G. (2010). *Introduction to XAFS*. Cambridge University Press.

[Cai et al., 2008] Cai, D. K., Neyer, A., Kuckuk, R., and Heise, H. M. (2008). Optical absorption in transparent PDMS materials applied for multimode waveguides fabrication. *Optical Materials*, 30(7):1157–1161.

[Canongia Lopes and Pádua, 2006] Canongia Lopes, J. N. A. and Pádua, A. A. H. (2006). Nanostructural Organization in Ionic Liquids. *The Journal of Physical Chemistry B*, 110(7):3330–3335.

[Carter et al., 1998] Carter, D. A., Pemberton, J. E., and Woelfel, K. J. (1998). Orientation of 1- and 2-Methylimidazole on Silver Electrodes Determined with Surface-Enhanced Raman Scattering. *The Journal of Physical Chemistry B*, 102(49):9870–9880.

[Clemenger, 1985] Clemenger, K. (1985). Ellipsoidal shell structure in free-electron metal clusters. *Physical Review B*, 32(2):1359–1362.

[Corbelli et al., 2011] Corbelli, G., Ghisleri, C., Marelli, M., Milani, P., and Ravagnan, L. (2011). Highly Deformable Nanostructured Elastomeric Electrodes With Improving Conductivity Upon Cyclical Stretching. *Advanced Materials*, 23(39):4504–4508.

[Corning, 2014] Corning, D. (2014). *SYLGARD® 184 SILICONE ELASTOMER KIT Product Information Electronics*.

[Czyyk et al., 1989] Czyyk, M. T., de Groot, R. A., Dalba, G., Fornasini, P., Kisiel, A., Rocca, F., and Burattini, E. (1989). Ag_2O band structure and x-ray-absorption near-edge spectra. *Physical Review B*, 39(14):9831–9838.

[Dash and Scott, 2009] Dash, P. and Scott, R. W. J. (2009). 1-Methylimidazole stabilization of gold nanoparticles in imidazolium ionic liquids. *Chemical Communications*, (7):812–814.

[de Groot and Kotani, 2008] de Groot, F. and Kotani, A. (2008). *Core Level Spectroscopy of Solids*. CRC Press.

[de Heer, 1993] de Heer, W. A. (1993). The physics of simple metal clusters: experimental aspects and simple models. *Reviews of Modern Physics*, 65(3):611–676.

[Demtröder, 2005] Demtröder, W. (2005). *Experimentalphysik 3 - Atome, Moleküle und Festkörper*. Springer.

[Demtröder, 2013] Demtröder, W. (2013). *Experimentalphysik 2: Elektrizität und Optik*. Springer-Lehrbuch. Springer Berlin Heidelberg, Berlin, Heidelberg, 6., überarb. u. akt. aufl. 2013 edition.

[Dupont, 2011] Dupont, J. (2011). From Molten Salts to Ionic Liquids: A "Nano" Journey. *Accounts of Chemical Research*, 44(11):1223–1231.

[Dupont and Scholten, 2010] Dupont, J. and Scholten, J. D. (2010). On the structural and surface properties of transition-metal nanoparticles in ionic liquids. *Chemical Society Reviews*, 39(5):1780–1804.

[Echt et al., 1981] Echt, O., Sattler, K., and Recknagel, E. (1981). Magic Numbers for Sphere Packings: Experimental Verification in Free Xenon Clusters. *Physical Review Letters*, 47(16):1121–1124.

[Ehrenreich and Philipp, 1962] Ehrenreich, H. and Philipp, H. R. (1962). Optical Properties of Ag and Cu. *Physical Review*, 128(4):1622–1629.

[Engemann, 2011] Engemann, D. (2011). Anwendung und Weiterentwicklung von Photoemission und Rastertunnelmikroskopie zur Untersuchung von massenselektierten Ag und Cu Clustern deponiert auf Oberflächen. Master's thesis.

[Fricke and Tillotson, 1997] Fricke, J. and Tillotson, T. (1997). Aerogels: production, characterization, and applications. *Thin Solid Films*, 297(1–2):212–223.

[Gauthier et al., 1999] Gauthier, C., Solé, V. A., Signorato, R., Goulon, J., and Moguiline, E. (1999). The ESRF beamline ID26: X-ray absorption on ultra dilute sample. *Journal of Synchrotron Radiation*, 6(Pt 3):164–166.

[Ghisleri et al., 2013] Ghisleri, C., Siano, M., Ravagnan, L., Potenza, M. A. C., and Milani, P. (2013). Nanocomposite-based stretchable optics. *Laser & Photonics Reviews*, 7(6):1020–1026.

[Goldby et al., 1996] Goldby, I., Kuipers, L., von Issendorff, B., and Palmer, R. (1996). Diffusion and aggregation of size selected silver clusters on a graphite surface. *Applied Physics Letters*, 69(19):2819–2821.

[Goldby et al., 1997] Goldby, I. M., von Issendorff, B., Kuipers, L., and Palmer, R. E. (1997). Gas condensation source for production and deposition of size-selected metal clusters. *Review of Scientific Instruments*, 68(9):3327–3334.

[Green et al., 2011] Green, I. X., Tang, W., Neurock, M., and Yates, J. T. (2011). Spectroscopic Observation of Dual Catalytic Sites During Oxidation of CO on a Au/TiO_2 Catalyst. *Science*, 333(6043):736–739.

[Grönhagen, 2011] Grönhagen, N. (2011). *Cluster-surface interaction of mass selected Ag clusters with graphite, gold and C_{60} functionalized surfaces*. PhD thesis.

[Gross and Fricke, 1992] Gross, J. and Fricke, J. (1992). Ultrasonic velocity measurements in silica, carbon and organic aerogels. *Journal of Non-Crystalline Solids*, 145:217–222.

[Haberland et al., 2006] Haberland, H., Kleinermanns, K., and Träger, F. (2006). Cluster. In *Bergmann/Schaefer, Lehrbuch der Experimentalphysik*, volume 5. de Gruyter.

[Haes et al., 2004] Haes, A. J., Hall, W. P., Chang, L., Klein, W. L., and Duyne, R. P. V. (2004). A Localized Surface Plasmon Resonance Biosensor: First Steps toward an Assay for Alzheimer's Disease. *Nano Letters*, 4(6):1029–1034.

[Hagena, 1991] Hagena, O. F. (1991). Formation of silver clusters in nozzle expansions. *Zeitschrift für Physik D Atoms, Molecules and Clusters*, 20(1):425–428.

[Hagena et al., 1991] Hagena, O. F., Knop, G., and Ries, R. (1991). Silber-Clusterstrahlen zur Erzeugung dünner Schichten. *KfK- Nachrichten*, 23(2-3).

[Hale and Querry, 1973] Hale, G. M. and Querry, M. R. (1973). Optical Constants of Water in the 200-nm to 200-µm Wavelength Region. *Applied Optics*, 12(3):555–563.

[Harbich et al., 1992] Harbich, W., Fedrigo, S., and Buttet, J. (1992). The optical absorption spectra of small silver clusters (n=5–11) embedded in argon matrices. *Chemical Physics Letters*, 195(5–6):613–617.

[Hatakeyama et al., 2009] Hatakeyama, Y., Okamoto, M., Torimoto, T., Kuwabata, S., and Nishikawa, K. (2009). Small-Angle X-ray Scattering Study of Au Nanoparticles Dispersed in the Ionic Liquids 1-Alkyl-3-methylimidazolium Tetrafluoroborate. *The Journal of Physical Chemistry C*, 113(10):3917–3922.

[Heiz and Schneider, 1999] Heiz, U. and Schneider, W.-D. (1999). Physical Chemistry of Supported Clusters. In *Metal Clusters at Surfaces*, pages 237–273. Springer.

[Hilger, 2001] Hilger, A. (2001). *Grenzflächen-Analyse durch Mie-Plasmon-Spektroskopie an Edelmetallclustern*. PhD thesis, RWTH Aachen, Aachen.

[Hoffmann, 2012] Hoffmann, S. (2012). *Structure and electronic properties of supported noble metal clusters*. PhD thesis, Technischen Universität Dortmund.

[Hornfeck et al., 1992] Hornfeck, M., Theiss, W., and Clasen, R. (1992). IR spectroscopy of porous silica gels. *Journal of Non-Crystalline Solids*, 145:154–158.

[Hövel, 1995] Hövel, H. (1995). *Grenzflächeneigenschaften von Metallclustern*. PhD thesis, RWTH Aachen.

[Hövel et al., 1993] Hövel, H., Fritz, S., Hilger, A., Kreibig, U., and Vollmer, M. (1993). Width of cluster plasmon resonances: Bulk dielectric functions and chemical interface damping. *Physical Review B*, 48(24):18178–18188.

[ichi Okazaki et al., 2008] ichi Okazaki, K., Kiyama, T., Hirahara, K., Tanaka, N., Kuwabata, S., and Torimoto, T. (2008). Single-step synthesis of gold–silver alloy nanoparticles in ionic liquids by a sputter deposition technique. *Chemical Communications*, (6):691–693.

[Jacquemin et al., 2006] Jacquemin, J., Husson, P., Padua, A. A. H., and Majer, V. (2006). Density and viscosity of several pure and water-saturated ionic liquids. *Green Chemistry*, 8(2):172.

[Jahn and Teller, 1937] Jahn, H. A. and Teller, E. (1937). Stability of Polyatomic Molecules in Degenerate Electronic States. I. Orbital Degeneracy. *Proceedings of the Royal Society of London. Series A - Mathematical and Physical Sciences*, 161(905):220–235.

[Johnson and Christy, 1972] Johnson, P. B. and Christy, R. W. (1972). Optical Constants of the Noble Metals. *Physical Review B*, 6(12):4370–4379.

[Kabo et al., 2004] Kabo, G. J., Blokhin, A. V., Paulechka, Y. U., Kabo, A. G., Shymanovich, M. P., and Magee, J. W. (2004). Thermodynamic Properties of 1-Butyl-3-methylimidazolium Hexafluorophosphate in the Condensed State. *Journal of Chemical & Engineering Data*, 49(3):453–461.

[Khatri et al., 2008] Khatri, O. P., Adachi, K., Murase, K., ichi Okazaki, K., Torimoto, T., Tanaka, N., Kuwabata, S., and Sugimura, H. (2008). Self-Assembly of Ionic Liquid (BMI-PF6)-Stabilized Gold Nanoparticles on a Silicon Surface: Chemical and Structural Aspects. *Langmuir*, 24(15):7785–7792.

[Kim et al., 2007] Kim, J. S., Kuk, E., Yu, K. N., Kim, J.-H., Park, S. J., Lee, H. J., Kim, S. H., Park, Y. K., Park, Y. H., Hwang, C.-Y., Kim, Y.-K., Lee, Y.-S., Jeong, D. H., and Cho, M.-H. (2007). Antimicrobial effects of silver nanoparticles. *Nanomedicine: Nanotechnology, Biology and Medicine*, 3(1):95–101.

[Kittel, 1999] Kittel, C. (1999). *Charles Kittel: Einführung in die Festkörperphysik*. R. Oldenbourg Verlag, 12 edition.

[Kreibig and Fragstein, C. V., 1969] Kreibig, U. and Fragstein, C. V. (1969). The Limitation of Electron Mean Free Path in Small Silver Particles. *Zeitschrift für Phyik*, 224:307–323.

[Kreibig and Vollmer, 1995] Kreibig, U. and Vollmer, M. (1995). *Optical Properties of Metal Clusters*. Springer.

[Kuo, 2009] Kuo, A. C. M. (2009). Poly(dimethylsiloxane). In *Polymer Data Handbook 2ed*, pages 411–435. Oxford University Press: New York.

[Kuwabata et al., 2010] Kuwabata, S., Tsuda, T., and Torimoto, T. (2010). Room-Temperature Ionic Liquid. A New Medium for Material Production and Analyses under Vacuum Conditions. *The Journal of Physical Chemistry Letters*, 1(21):3177–3188.

[Lawrence-Berkeley-Laboratories, 2014] Lawrence-Berkeley-Laboratories (2014). Silica Aerogels. *http://www.sps.aero/Key_ComSpace_Articles/TSA-009_White_Paper_Silica_Aerogels.pdf*.

[Liebsch, 1993] Liebsch, A. (1993). Surface-plasmon dispersion and size dependence of Mie resonance: Silver versus simple metals. *Physical Review B*, 48(15):11317–11328.

[López-Cartes et al., 2005] López-Cartes, C., Rojas, T. C., Litrán, R., Martínez-Martínez, D., de la Fuente, J. M., Penadés, S., and Fernández, A. (2005). Gold Nanoparticles with Different Capping Systems: An Electronic and Structural XAS Analysis. *The Journal of Physical Chemistry B*, 109(18):8761–8766.

[Lützenkirchen-Hecht et al., 2009] Lützenkirchen-Hecht, D., Wagner, R., Haake, U., Watenphul, A., and Frahm, R. (2009). The materials science X-ray beamline BL8 at the DELTA storage ring. *Journal of Synchrotron Radiation*, 16(2):264–272.

[Mackay, 1962] Mackay, A. L. (1962). A dense non-crystallographic packing of equal spheres. *Acta Crystallographica*, 15(9):916–918.

[Martin et al., 1991] Martin, T. P., Bergmann, T., Göhlich, H., and Lange, T. (1991). Electronic shells and shells of atoms in metallic clusters. *Zeitschrift für Physik D Atoms, Molecules and Clusters*, 19(4):25–29.

[Mie, 1908] Mie, G. (1908). Beiträge zur Optik trüber Medien, speziell kolloidaler Metallösungen. *Annalen der Physik*, 330(3):377–445.

[Miroslawski, 2014] Miroslawski, N. J. (2014). Ultraviolet photoelectron spectroscopy and scanning tunnelling microscopy of silver and copper clusters on HOPG, noble metals and rare gas layers.

[Newville, 2004] Newville, M. (2004). Fundamentals of XAFS.

[Nilsson, 1955] Nilsson, S. G. (1955). *Binding states of individual nucleons in strongly deformed nuclei.*

[Nolting, 2001] Nolting, W. (2001). *Grundkurs Theoretische Physik 3.* Springer.

[Nour et al., 2014] Nour, M., Berean, K., Chrimes, A., Zoolfakar, A. S., Latham, K., McSweeney, C., Field, M. R., Sriram, S., Kalantar-zadeh, K., and Ou, J. Z. (2014). Silver nanoparticle/PDMS nanocomposite catalytic membranes for H_2S gas removal. *Journal of Membrane Science*, 470:346–355.

[Padmos and Zhang, 2012] Padmos, J. D. and Zhang, P. (2012). Surface Structure of Organosulfur Stabilized Silver Nanoparticles Studied with X-ray Absorption Spectroscopy. *The Journal of Physical Chemistry C*, 116(43):23094–23101.

[Paulechka et al., 2003] Paulechka, Y. U., Kabo, G. J., Blokhin, A. V., Vydrov, O. A., Magee, J. W., and Frenkel, M. (2003). Thermodynamic Properties of 1-Butyl-3-methylimidazolium Hexafluorophosphate in the Ideal Gas State†. *Journal of Chemical & Engineering Data*, 48(3):457–462.

[Pissuwan et al., 2006] Pissuwan, D., Valenzuela, S. M., and Cortie, M. B. (2006). Therapeutic possibilities of plasmonically heated gold nanoparticles. *Trends in Biotechnology*, 24(2):62–67.

[Quinten, 2010] Quinten, M. (2010). *Optical Properties of Nanoparticle Systems: Mie and Beyond.* John Wiley & Sons.

[Ravagnan et al., 2009] Ravagnan, L., Divitini, G., Rebasti, S., Marelli, M., Piseri, P., and Milani, P. (2009). Poly(methyl methacrylate) - Palladium clusters nanocomposite formation by supersonic cluster beam deposition: a method for microstructured metallization of polymer surfaces. *Journal of Physics D: Applied Physics*, 42(8):082002. arXiv:0902.0228 [cond-mat].

[Redel et al., 2008] Redel, E., Thomann, R., and Janiak, C. (2008). First Correlation of Nanoparticle Size-Dependent Formation with the Ionic Liquid Anion Molecular Volume. *Inorganic Chemistry*, 47(1):14–16.

[Rehr and Albers, 2000] Rehr, J. J. and Albers, R. C. (2000). Theoretical approaches to x-ray absorption fine structure. *Reviews of Modern Physics*, 72(3):621–654.

[Salmen, 2011] Salmen, P. (2011). Untersuchung des Polymers Polydimethylsiloxan (PDMS) zur Deposition von Silberclustern.

[Sayers et al., 1971] Sayers, D. E., Stern, E. A., and Lytle, F. W. (1971). New Technique for Investigating Noncrystalline Structures: Fourier Analysis of the Extended X-Ray—Absorption Fine Structure. *Physical Review Letters*, 27(18):1204–1207.

[Scheuerpflug et al., 1992] Scheuerpflug, P., Hauck, M., and Fricke, J. (1992). Thermal properties of silica aerogels between 1.4 and 330 K. *Journal of Non-Crystalline Solids*, 145:196–201.

[Sham, 1985] Sham, T. K. (1985). L-edge x-ray-absorption systematics of the noble metals Rh, Pd, and Ag and the main-group metals In and Sn: A study of the unoccupied density of states in 4d elements. *Physical Review B*, 31(4):1888–1902.

[Smetana et al., 2005] Smetana, A. B., Klabunde, K. J., and Sorensen, C. M. (2005). Synthesis of spherical silver nanoparticles by digestive ripening, stabilization with various agents, and their 3-D and 2-D superlattice formation. *Journal of colloid and interface science*, 284(2):521–526.

[Solé et al., 2007] Solé, V. A., Papillon, E., Cotte, M., Walter, P., and Susini, J. (2007). A multiplatform code for the analysis of energy-dispersive X-ray fluorescence spectra. *Spectrochimica Acta Part B: Atomic Spectroscopy*, 62(1):63–68.

[Tiggesbäumker et al., 1993] Tiggesbäumker, J., Köller, L., Meiwes-Broer, K.-H., and Liebsch, A. (1993). Blue shift of the Mie plasma frequency in Ag clusters and particles. *Physical Review A*, 48(3):R1749–R1752.

[Torimoto et al., 2006] Torimoto, T., ichi Okazaki, K., Kiyama, T., Hirahara, K., Tanaka, N., and Kuwabata, S. (2006). Sputter deposition onto ionic liquids: Simple and clean synthesis of highly dispersed ultrafine metal nanoparticles. *Applied Physics Letters*, 89(24):243117.

[Tröger et al., 1992] Tröger, L., Arvanitis, D., Baberschke, K., Michaelis, H., Grimm, U., and Zschech, E. (1992). Full correction of the self-absorption in soft-fluorescence extended x-ray-absorption fine structure. *Physical Review B*, 46(6):3283–3289.

[Tsou, 1995] Tsou, P. (1995). Silica aerogel captures cosmic dust intact. *Journal of Non-Crystalline Solids*, 186:415–427.

[Tsuda et al., 2009] Tsuda, T., Seino, S., and Kuwabata, S. (2009). Gold nanoparticles prepared with a room-temperature ionic liquid–radiation irradiation method. *Chemical Communications*, (44):6792–6794.

[von Issendorff, 2011] von Issendorff, B. (2011). The Electronic Structure of Alkali and Noble Metal Clusters. In *Handbook of Nanophysics: Clusters and Fullerenes*, Handbook of Nanophysics. CRC Press.

[Šipr et al., 1999] Šipr, O., Rocca, F., and Dalba, G. (1999). Real-space multiple-scattering analysis of Ag L_1 - and L_3 -edge XANES spectra of Ag_2O. *Journal of Synchrotron Radiation*, 6(3):770–772.

[Wender et al., 2010] Wender, H., de Oliveira, L. F., Migowski, P., Feil, A. F., Lissner, E., Prechtl, M. H. G., Teixeira, S. R., and Dupont, J. (2010). Ionic Liquid Surface Composition Controls the Size of Gold Nanoparticles Prepared by Sputtering Deposition. *The Journal of Physical Chemistry C*, 114(27):11764–11768.

[Zhang et al., 2004] Zhang, S.-M., Zhang, C.-L., Zhang, J.-W., Zhang, Z.-J., Dang, H.-X., Wu, Z.-S., and Liu, W.-M. (2004). Preparation of Silver Nanoparticles in Room Temperature Ionic Liquids. *Acta Phys. Chim. Sin.*, 20(5):554.

Acknowledgments

Last but not least möchte ich mich bei meinen Betreuern, Kollegen, Freunden und meiner Familie für ihre Unterstützung bedanken.

Besonders möchte ich meinem Betreuer apl. Prof. Dr. Heinz Hövel danken. Vielen Dank für die anregenden Diskussionen, die Hilfe im Labor (auch in den Abendstunden oder am Wochenende) und die Unterstützung bei den Messzeiten. Seine hilfsbereite und freundschaftliche Art hat eine Atmosphäre geschaffen, in der es sich sehr gut arbeiten lies und man auch mal Rückschläge schnell verschmerzen konnte.

Bei Herrn Prof. Dr. Metin Tolan möchte ich mich dafür bedanken, dass ich meine Arbeit an seinem Lehrstuhl anfertigen durfte. An dieser Stelle auch ein großes Dankeschön an die NRW Forschungsschule für die finanzielle Förderung im Rahmen des Stipendiums "Forschung mit Synchrotronstrahlung in den Nano- und Biowissenschaften".

Herrn Prof. Dr. Thomas Weis danke ich für das Interesse an meiner Arbeit und die Anfertigung des Zweitgutachtens.

Auch möchte ich Frau Dr. Bärbel Siegmann und Herrn Prof. Dr. Kevin Kröninger für das Interesse an meiner Arbeit danken.

Den Maschinen-Gruppen des DELTA und der ESRF danke ich für die Bereitstellung der Synchrotronstrahlung, ohne die die Experimente dieser Arbeit nicht möglich gewesen wären. Auch möchte ich den Beamline Scientists Dr. Pieter Glatzel, Dr. Kristina Kvashnina (beide ID26, ESRF) und Ralf Wagner, Stefan Balk (beide BL8, DELTA) für die Unterstützung bei den XANES Experimenten danken.

Herrn Prof. Dr. Uwe Kreibig möchte ich dafür danken, dass unsere Arbeitsgruppe die Möglichkeit bekommen hat, THECLA nach Dortmund zu holen. Ohne diese Apparatur wäre diese Arbeit nicht zustande gekommen. Ich danke ihm auch für die Tipps und Ratschläge, die er mir auf Konferenzen hat zukommen lassen.

Ein besonderer Dank gilt Dr. Sabrina Hoffmann die THECLA in Dortmund in Betrieb genommen hat. Ihr, Dr. Stefanie Duffe und Stefanie Roese danke ich für die Unterstützung bei Experimenten im Labor und auf externen Messzeiten. Auch möchte ich David Odenthal, Jens-Christian Meyer und Jan Mundry für ihre Unterstützung im Labor danken.
Dr. Christian Sternemann, Dr. Michael Paulus, Dr. Johannes Möller und Julian Schulze danke ich für die Unterstützung bei Experimenten an den Beamlines BL8 und BL9 im DELTA. Hier auch ein Dank an Christoph Keutner und Dr. Ulf Berges für das Ausleihen diverser UHV Komponenten.

Herrn Thorsten Witt danke ich für die Inbetriebnahme des Schrittmotors für den Mixer und die Hilfe bei dutzenden Problemen im Labor. Für die Hilfe bei der Wartung und Beschaffung von Bauteilen möchte ich auch Herrn Georg Jülicher herzlichen danken.

Frau Monika Meuris von der Fakultät Bio- und Chemieingenieurwesen danke ich für die Anfertigung der TEM Bilder.

Herrn Rudloff und dem Konstruktionsbüro sowie Frau Kralemann und der Mechanischen Werkstatt danke ich für die Konstruktion und Herstellung verschiedener Bauteile für THECLA, sowie ihrer Hilfe bei Reparaturen.

Herrn Dirk Schemionek und Frau Gisela Pike danke ich für die Modifikation verschiedener Bauteile und die Hilfe bei Arbeiten im Präparationslabor, sowie das zur Verfügung stellen verschiedener chemischer Substanzen.

Herrn Zehner von der Firma Oerlikon Leybold danke ich für die Reparatur des Kühlkopfes.

Des Weiteren Danke ich allen Mitlgliedern das Lehrstuhls E1, die immer zur Stelle waren, wenn mal wieder Not-am-Mann war. Hier möchte ich besonders Dr. Natalie Miroslawski und Christoph Schröder danken. Ich möchte auch nicht vergessen, mich bei meinen Bürokollegen Dr. Niklas Grönhagen, Dr. Johannes Möller und Julian Schulze für das nette Arbeitsklima zu bedanken.
Ich möchte hier auch besonders den Herren Dr. Alexander Nyrow, Florian Wirkert, Thorsten Brenner und Dr. Alexander Schwamberger danken. Ihr Mitwirken hat einige unvergessliche Erlebnisse heraufbeschworen.

Mein größter Dank gilt wohl meiner Familie, die mir immer den Rücken gestärkt hat und mir bei allem zur Seite stand. Meiner Freundin Linda danke ich für ihr Verständnis, für ihre Unterstützung und dafür, dass sie meine Launen ertragen hat. Ich danke meinen Eltern für alles, was sie für mich getan haben. Hier jetzt aber alles zu nennen, würde den Rahmen dieser Arbeit sprengen.

Eidesstattliche Versicherung

Hiermit erkläre ich an Eides Statt, dass die vorliegende Dissertationsschrift — abgesehen von der Beratung durch meine wissenschaftlichen Betreuer — nach Inhalt und Form meine eigene Arbeit ist. Ich habe keine anderen als die angegebenen Quellen und Hilfsmittel benutzt sowie wörtliche und sinngemäße Zitate kenntlich gemacht. Sie wurde weder ganz noch in Teilen an anderer Stelle im Rahmen eines Prüfungsverfahrens vorgelegt.

Dortmund, November 2014

(David C. Engemann)